UNIVERSIDAD DE GUANAJUATO

DIVISIÓN DE INGENIERÍAS CAMPUS IRAPUATO-SALAMANCA

DESIGN AND ANALYSIS OF POLYMERIC INSERTS FOR ANKLE PROSTHESIS

DOCTORAL THESIS

SUBMITED AS A REQUIREMENT FOR OBTAINING THE DEGREE OF:

DOCTOR ON MECHANICAL ENGINEERING

PRESENTED BY:

HUMBERTO CORRO HERNÁNDEZ

ADVISORS:

DR. ELIAS RIGOBERTO LEDESMA OROZCO

DR. AGUSTIN VIDAL LESSO

SALAMANCA, GUANAJUATO
2020

Dedicatoria

A mis padres, Xóchitl Hernández Bautista y Humberto Corro Acosta, por su inestimable apoyo en este proyecto.

Al Ing. José Rubén Hernández Cruz y familia por su franca hospitalidad.

A Pilar, a Lupita, Melissa y al Joven, por ser compañeros solidarios en este viaje.

Y en general a todos los que hicieron posible este trabajo.

Acknowledgments

I would like to express the greatest gratitude to Consejo Nacional de Ciencia y Tecnología (CONACYT) due the received scholarship during my doctorate studies.

Also, I recognize the invaluable contribution of Universidad de Guanajuato (UG) for the use of software licenses and installations, and the economic support for derived congresses expositions and article publishing.

I am deeply grateful with my advisors Dr. Elías R. Ledesma Orozco and Dr. Agustín Vidal Lesso, for all their orientation, instruction and collaboration on this project.

For Dr. Eduardo Aguilera Gómez, Dr. Adrián Hernández Pérez, Dr. Leonel Benítez Daza, Dr. Luis Manuel Palacios Pineda, and Dr. Antonio de Jesús Balvantín García, I acknowledge their efforts and time as reviewers and members of the evaluating committee of this thesis.

I recognized the received help from Dr. Juan Francisco Reveles Arredondo and M.I. Diego Gómez Márquez during material testing.

Abstract

A new prosthesis design for total ankle arthroplasty (TAA), with an internal structure for its polymeric insert is proposed and analyzed on numerical simulation.

Engineering parameters for prosthesis designs are proposed and discussed. Physiological load conditions for ankle joint are applied for numerical simulation on a finite element analysis (FEA), considering experimental data for modeling the polymer material behavior.

Performance of total deformation, strain, safety factors and equivalent stress of structured prosthesis are compared versus a common solid model and literature findings for market-available prosthesis.

Results showed that the proposed structured design can operate safely on simulated cases, having a diminished stress state in comparison with precedent TAA prosthesis. Thus, it is a good insight for future development.

Previous side work that could not satisfy the project needs, but still with potential applications on biomechanics is also exposed.

Index

List of Figures

List of Tables

Work overview

This doctoral thesis presents the devising, designing and development of a total ankle arthroplasty (TAA) prosthesis. This logical order is followed on chapter redactions.

First chapter is dedicated to the state of the art and theoretical framework. After the obligated review of ankle anatomy, benchmarking of market-available prosthesis, and study of the main causes for prosthesis failure, found to be related with stressing and premature wear of sacrifice component on TAA prosthesis.

Second chapter verses about the use of Ultra-High Molecular Weight Polyethylene in prosthesis fabrication as material of fundamental importance. Carried essays on samples are reported, and obtained data is analyzed on third chapter for a proper material model adjustment.

As it was found that excessive stress was the main cause for ankle prosthesis failure, some possible concepts for avoiding this effect were considered on fourth chapter, namely fluid damping and a honeycomb array of negative stiffness dampers. Although these were not used on the final iteration, they could be useful on other applications and thus reported.

After finding the best approach for the ankle prosthesis design, through application of computer-aided design (CAD) software a design proposal was generated. Detailed description of this prosthesis is found on fifth chapter.

For the sixth chapter, a finite element analysis (FEA) is used on the aforementioned CAD model, considering the experimental data of third chapter for the material model, with physiological load conditions for ankle joint are applied for numerical simulation.

Performance of total displacement, strain, safety factors and equivalent stress of structured prosthesis are compared versus a common solid model and literature findings for market-available prosthesis.

Obtained results are encouraging, as the feasibility of the concept is validated, and thus allowing the justification and development of a future associated project for manufacturing and evaluating of a physical prototype.

Chapter 1 – Literature review

In this chapter, some basic definitions and preliminary concepts needed for the problem comprehension are explored; having a clear focus on ankle anatomy.

After this obligated introduction, the ankle joint replacement state of the art is approached. The main concerns and development fields are analyzed, establishing a parting point for the general thesis development.

From this review, it was found that premature wear and excessive stresses on total ankle arthroplasty (TAA) are major issues on the intervention final performance. So, a projected development for a solution which could diminish these events is needed and should be proposed as the main objective of this work, with the correspondent list of required partial objectives.

1.1. Introduction

Osteoarthritis (OA) as a pathology involves the wear on the cartilage that allows bone movement, causing stiffness and pain on the involved joint. It is estimated that 15% of the adult world population suffers any adverse effects related to OA, with 1% of said global group affected on ankle joint [1-2]. For reference, a worldwide estimate of 250 million (3.3%) for combined knee and hip OA cases is estimated [3-4], thus ankle OA having a relatively important weight on the overall cases.

Predisposition for OA rises with the presence of certain factors, being positively correlated with age and obesity. It has been established that half of the population above 60 years shows OA or another arthritis-related disease on foot and ankle, even in absence of symptoms [5]. World Health Organization (WHO) projections estimate that in year 2050 there will be 130 million people with OA symptoms, being 40 million seriously disabled by this cause [2]. The number of years lived with disability caused by general OA have risen 75% on the period 1990-2013 [6]

For Mexico, census established an elder population on that bracket of age of 10.7 million people, with an inferred rise up to 36.4 million on 2050 [7], many of them being affected with OA.

In economic terms, coping with OA can represent an emolument up to $5700 USD each year due the use of medical and non-medical resources [8]. It becomes clear that the disease is already an existing problem which will aggravate on future in terms of impacted population.

Early stages of OA can be treated with some solutions linked to changes on lifestyle, physical therapies and the use of analgesics. However, for advanced OA, surgical procedures are mandatory. Quality of life for affected people is susceptible for bettering with the use of prosthetic implant on joint, diminishing pain, allowing the patient to accomplish daily tasks with comfort and safety.

Joint replacement is well-known as a medical procedure on many countries, having a steadily rising demand [9]. Only in United States of America, an increment of 137% and 601% for hip and knee replacement by year 2030 is estimated [10]. Cyphers for ankle joint are not given, but the same ascending trend can reasonably be extrapolated, as more recent reports forecast that the global orthopedic devices market projections show a rising trend on the overall global orthopedic market compound annual growth rate of 5.22% during the period 2017-2021 [11] and expected to exceed $53 USD billion by 2024 [12].

On a local level, previous work and an important market exist on Mexico. Aggregated joint reconstruction reached by year 2004 the 25.4% of medical devices and orthopaedical implants consume [13]. Having direct presence of key regional players, a strong distribution

network, and a well-established healthcare infrastructure, North America will lead the orthopedic prosthesis growth [11].

It should be noticed that ankle joint replacement has had a later development in comparison with similar knee and joint interventions due the related complexity, the higher importance of soft tissue interaction, and the inherent joint instability [14-15]. As a result, ankle intervention is less common, having greater opportunity areas within many of the market-available joint replacements, with new contributions being more possible.

As the joint replacement is being done at earlier ages [10,11], new challenges related to the more intense activities that prosthesis should endure, linked to a more active lifestyle, and for much longer periods arise. Therefore, the necessity for creating and implementing new prosthesis models intended for these operation conditions becomes evident.

Related to their later development, there are fewer studies focused on long-term effects on total ankle replacement; however, a correlation on the overall results, the surgical technique and previous experience, and health conditions of the patient has been observed [14-15].

As a general fact, preexistent prosthesis models still have issues with gait modification, premature wear and undesired stress transmission to the rest of the lower member [16], problems that end on prosthesis loosening and foot damage [14-17]. Root cause of aforementioned situations is directly linked to changes on load distribution and energy transmission inside the system.

A more accurate understanding of this problem should be achieved with a general review of ankle joint constitution and function.

1.2. Anatomy and biomechanics of the ankle joint

Ankle (Figure 1.1) is the distal joint of lower limb, the one which relates leg and foot movements on a sagittal plane [18].

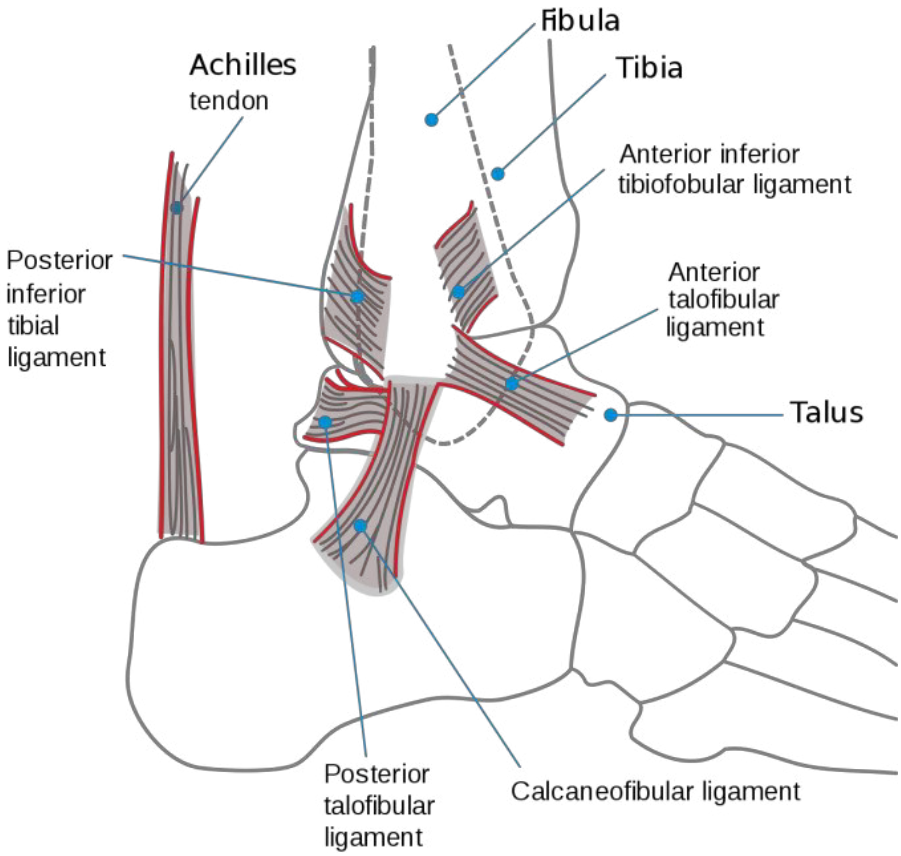

Figure 1.1. Extern lateral view of ankle joint [19].

It is a very closed joint, fitted, which significant range limitations, since in monopodal support it supports the entire weight of the body, even increased by the kinetic energy when the foot contacts the ground at a certain speed during walking [20].

The proper ankle joint is integrated by tibia and fibula (on leg) and talar bone (on feet). Tibia and fibula conform a joint pocket where talus trochlea fits (see Figure 1.2 for reference).

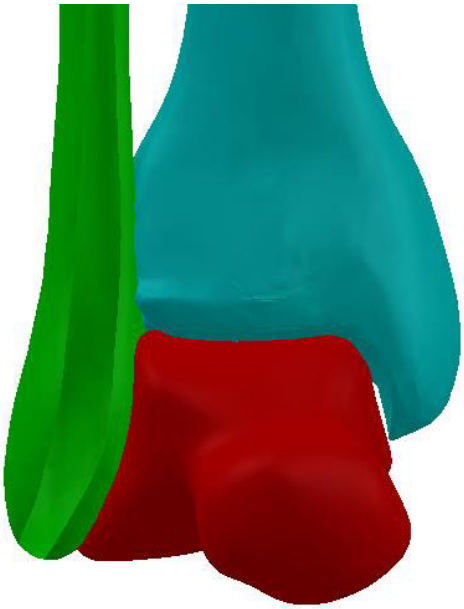

Figure 1.2. Frontal view of the bones on talocrural joint [21].

Among these bones, a damping tissue (cartilage) is found. Cartilage also works as a lubricated surface that allows for smooth joint bone movement.

Average contact area for ankle joint cartilage is of 350 mm^2, a clearly lower value compared to the average surface found on knee (1100 mm^2) or hip (1200 mm^2) joint. If knee joint receives a load equivalent to thrice the body weight during normal operation, the one found on ankle joint can be five and a half the body weight value [20,22]. Another fundamental difference found on ankle cartilage is its very regular and small thickness (1-1.7 mm) [23], still enough to absorb generated impact while walking, jumping and running.

The ankle joint complex consists of three main axes (seen on Figure 1.3) which are interrupted approximately in the hindfoot. When the foot is in a reference -neutral- position, these three axes are perpendicular to each other.

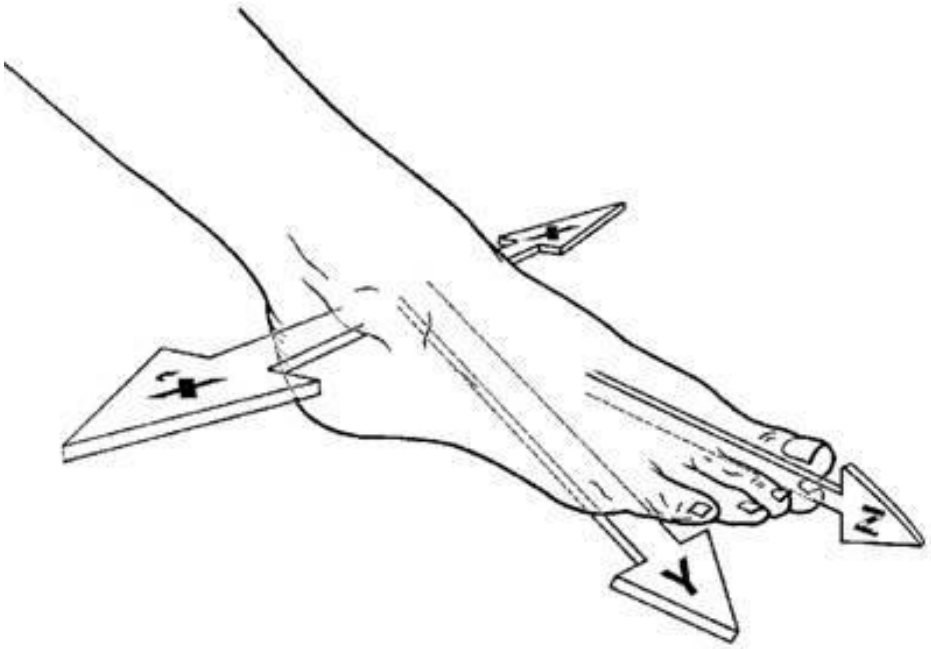

Figure 1.3. Main axes of ankle joint complex [17].

Flexion-extension movements of the foot that are performed in the sagittal plane (parallel to Z axis) are conditioned by the transverse axis XX' which passes through the two malleoli, corresponding to the talocrural joint axis.

The longitudinal axis of the leg Y is vertical and is responsible of the adduction-abduction movements of the foot, which are carried out in the transverse plane. Axial rotation of the flexed knee makes feasible these movements.

The orientation of foot sole is conditioned by the movement of longitudinal axis of the foot Z, being either directly downwards, outwards or inwards [20].

Although it is classified as restricted, ankle joint has a lot of mobility. Cadaveric studies have found average measured angles from normal position of 14.7° on dorsal flexion, 28.2° on plantar flexion, 13.8° on inversion and 5° on eversion (as seen on Figure 1.4)

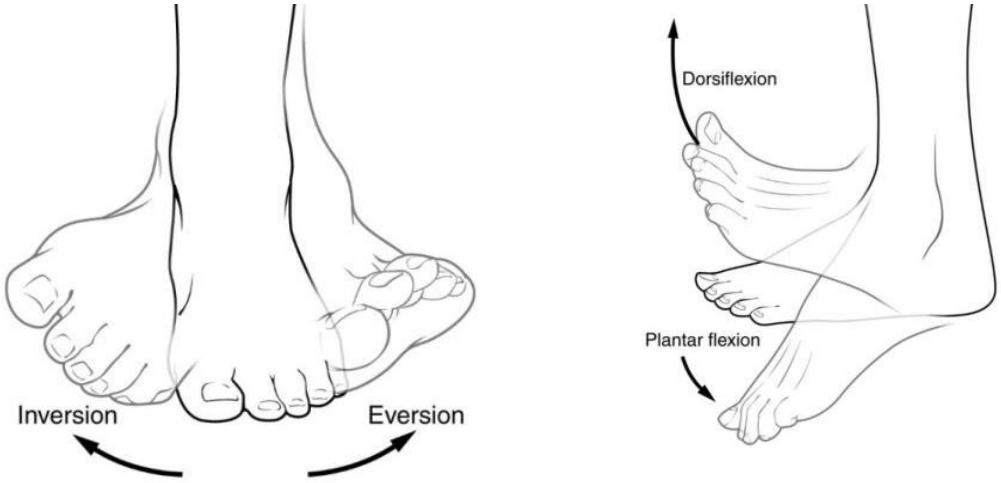

Figure 1.4. Movements of ankle joint [20].

Talocrural joint can be compared to a simple mechanical model, as seen on Figure 1.5.

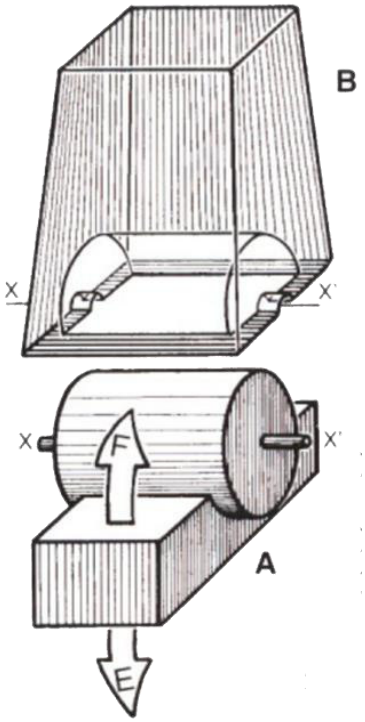

Figure 1.5. Simple mechanical model of talocrural joint [20].

The lower part is a simplified version of the talus, which supports a cylindrical surface with a large transverse axis XX'. The block on the upper part, corresponding to the lower portion of the tibia and fibula, whose contact surface has a hole in the form of a cylindrical segment.

The solid cylinder, fitted in the hollow cylinder, and held laterally between both flanks of the upper part, can perform bending and extension movements around the common axis XX'. In the anatomical reality the solid cylinder corresponds to the pulley of the talus composed of three parts: an upper surface and two lateral surfaces, the joint facets.

Ankle is considered a rolling joint with high congruency. Its stability is given by the presence of ligaments, tendons and muscles that crisscross above the bones [20].

The ligaments of the talocrural joint are composed of two main ligamentous systems - external and internal lateral ligaments- and two accessory systems - anterior and posterior ligaments- as shown on Figure 1.6.

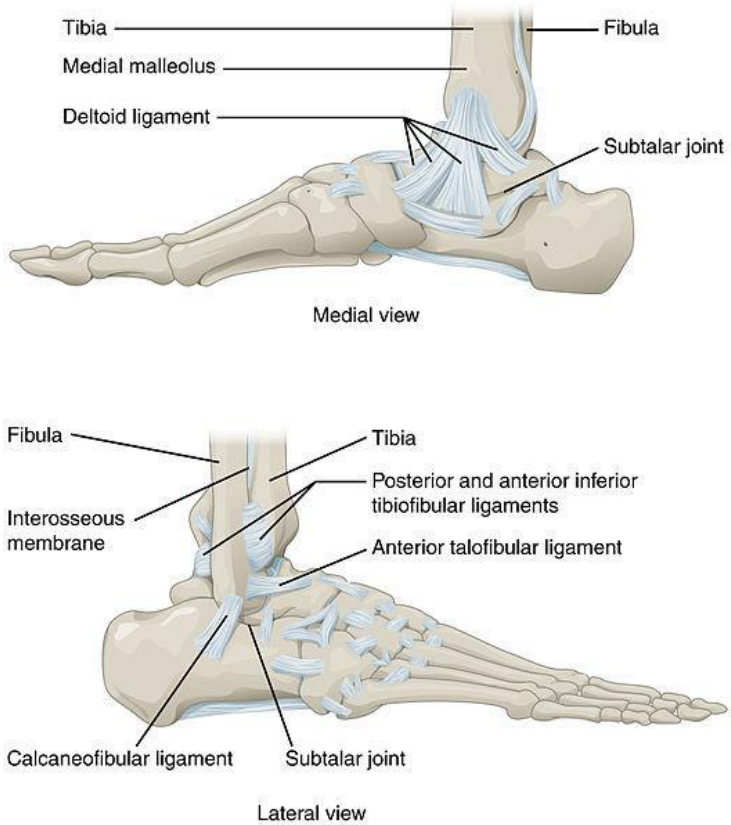

Figure 1.6. Ligaments on ankle joint [24].

The lateral ligaments, on each side of the joint, are constituted by powerful fibrous fans whose apex are fixed in the corresponding malleolus, close to the XX' axis, and whose periphery is expanded by the two bones of the superior tarsus.

The external lateral ligament (LLE) is formed by three bundles, two of them are directed to the talus and the other remaining to the calcaneus:

The inner bundle, adhered to the anterior edge of the peroneal malleolus, is directed obliquely downward and forward to insert itself into the talus, between the external face and the opening of the tarsal sinus.

The middle bundle starts in the vicinity of the most prominent point of the malleolus to be directed downwards and backwards and inserted in the external face of the calcaneus. The external talocal calcaneal ligament runs along its entire lower edge.

The posterior bundle originates in the medial aspect of the malleolus behind the articular facet, to be directed horizontally inward and slightly backwards and inserted into the posteroexternal tubercle of the talus. Its position and direction make it more visible in the posterior plane, extending itself through a small ligament called talar calcaneus posterior

Two inferior peroneotibial ligaments are spilt from the external malleolus: the anterior and the posterior.

The internal lateral ligament (LLI) is divided into two planes, superficial and deep. Deep plane is constituted by two tibiofacial grooves: the anterior bundle, obliquely downward and forward, is inserted into the internal branch of the talar yoke.

The posterior bundle, obliquely downwards and backwards, is inserted in a deep pit located below the internal face; its more posterior fibers are fixed in the posterointernous tubercle.

The superficial plane, very extensive and triangular, forms the deltoid ligament. From its tibial origin, it is expanded by a continuous inferior insertion line in the scaphoid, the internal border of the glenoid ligament and the lower calcaneal process. Thus, the deltoid ligament, as is the case with the LLE middle bundle, has no insertion in the talus.

The anterior ligaments and posterior of the talocrural are simple capsular thickenings. The anterior obliquely joins the anterior margin of the tibial surface and the branch of the

posterior bifurcation of the talar yoke. The posterior is formed by fibers of tibial and peroneal origin that converge towards the posterointernal tubercle of the talus, which with the posteroexternal tubercle, constitutes the limits of the deep flexor digitorum of the big toe.

With these anchorage of soft tissues, ankle joint is fundamental for locomotion, enduring body weight during gait, and the additional kinetic energy resulted from feet-floor contact during racing or jump reception [17].

1.3. Total Ankle Arthroplasty (TAA)

Manifestation of illness or physical damage on ankle joint generates serious limitations on movement and chronic pain in detriment of a patient life quality. As it was mentioned early, OA involves articular cartilage joint wear, causing stiffness and pain. OA is also known as degenerative articular illness, arthrosis, osteoarthrosis or hypertrophic arthritis [2,25].

Up to 60% of all OA cases in ankle joint are of pos-traumatic origin, with clinical signs of pain and dysfunction often lagging years or decades behind the initiating injury [26]. Other predisposition-related factors for OA are overweight, joint unbalance and hereditability [25].

As illness evolves, bones impact among each other and are bone spurs are formed [25].

TAA was firstly practiced on the decade of 1970 [14]. However, during a long time, results were considered inferior to the obtained ones of ankle joint induced ossification by means of fixing mechanical elements or ankle arthrodesis. Comparisons show that in theory, none of these interventions are better to the other in terms of physical performance [27]. Still, it is affirmed that TAA with a recent-design prosthesis could keep original cinematic while ankle arthrodesis can reduce up to 70% of the required mobility on sagittal plane [28], the advantage of TAA being obvious in terms of remaining range of motion.

TAA, also known as ankle joint implant or ankle total replacement, requires the exposition of articulation by a single frontal or lateral cut, making a careful separation of tendons, nerves and sanguine vessels to extirpate damaged bone and cartilage.

From this point, required operations can change with the TAA prosthesis implanted; on general terms, damaged tissue on tibia and talus is removed on that order, and their artificial replacements are anchored to the remaining bone with mechanical devices or fixation cement on earlier developments [14]. After that, a softer third piece, called sacrifice element, is assembled with the best possible fit and alignment (some models have this element imbedded on tibia element). Tendons and soft tissues are put on place again and wound gets sutured [29-30] as seen on Figure 1.7.

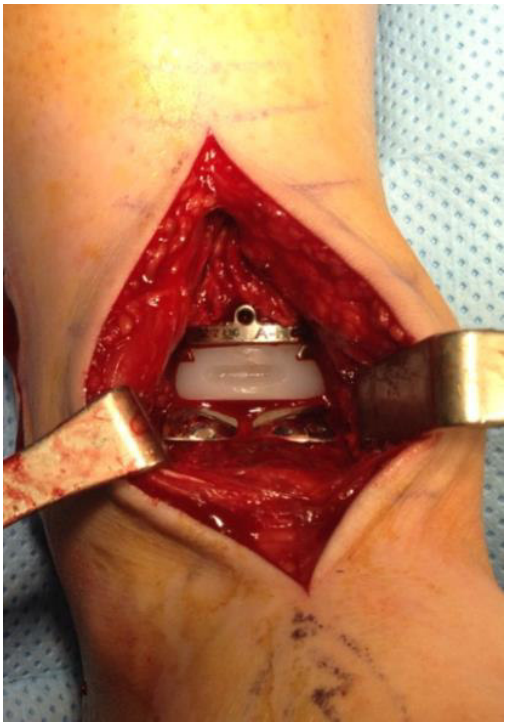

Figure 1.7. TAA surgical intervention. AOFAS [3].

As any surgical practice, complications from anesthesia, excessive blood loss and infection are possible. For specific adverse sequels, joint weakness, joint stiffness and instability, nerve and blood vases damage, bone fracture or allergic reaction to prosthesis had been found [29,31-32]. Incomplete, erroneous and late diagnosis can be the source of human

mistakes. Another common side effect for this intervention is implant loosening due induced osteolysis [17, 31-32].

Mean age for TAA patients is about 60 years, lower than mean ages for hip (68) and knee (69) replacements [15]. As it was mentioned, fewer long-term reports on this operation have been done. The best estimate for a ten-year prosthesis survival is of 89%. However, up to 23% of these cases have a noticeable change on affected tissue density on a period of 4.4 years [14].

In summary, TAA has been developed primarily on Europe, with a more recent application on USA. It has been established as a safe procedure, with very few instanced of complications like infection (3.2%) or the need of later interventions (0.7%) [33-34].

Even with these advances, TAA results are heavily dependent on surgeon's ability and applied technique. Observed tendencies show that ligament balance is a key factor for success [15]. During TAA side interventions as osteotomies, bone fusions or additional tendon transferences are quite common [35]. This encourages the use of a previous evaluation on joint deformity and its previous fixture, if possible.

Surgical technique factors, such as implant alignment, size, cutting area, among many others should also be analyzed and studied for a better knowledge on the role they have on TAA, having short and medium-term effects on it [36]. Some of them can be resumed to prosthesis design related factors.

1.4. Prosthetic designs for TAA

Prosthesis intended for TAA have passed for a multitude of changes. First models had a very basic hinge-like configuration, according to the main movement of plantar flexion and dorsiflexion; thus, the lateral movement was not possible [14]. This represented a severe operative ailment, as change of direction during gate or walking on irregular surfaces require this kind of motion [20]. Turnarounds can represent up to 25% of steps on an average day of walking [37].

Even with this known fact, most of the past TAA prosthesis designs favored sagittal plane movement. With no eversion or inversion allowed, stress levels on prosthesis rose and so did the wear [14]. Newer models took on consideration natural movement to avoid this situation. Nowadays, these bettered models coexist with older ones, discontinued but with following still given.

On a broad view, TAA prosthesis can be classified on two fundamental types: two-element and three-element ones [14], with the main difference being integration or isolation of the sacrifice component (marked in red) respecting of tibial component as seen on Figure 1.8:

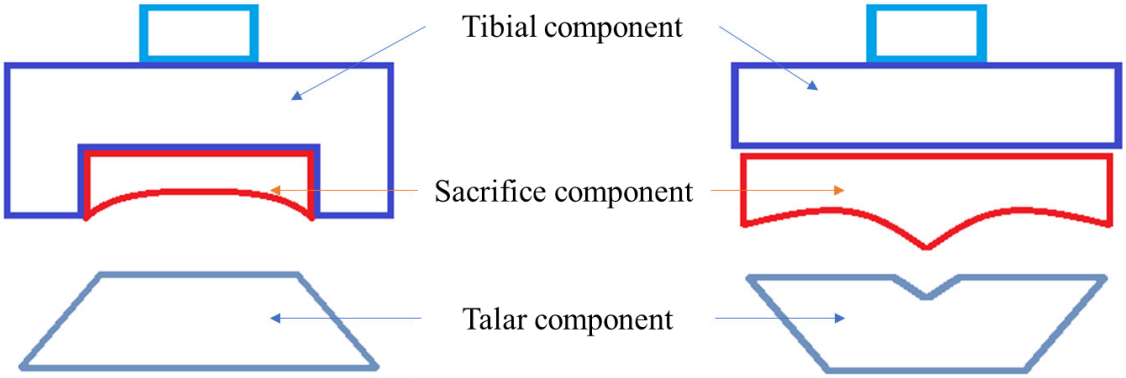

Figure 1.8. Schematic comparison of two-element (left) and three-element (right) ankle joint prosthesis.

The first assemble has a very stable configuration. This reliability has made the two-element TAA prosthesis the most commonly used one [14]. By the other side, the limitation on degrees of freedom and the lack of congruence have the undesired consequence of generating higher stresses on the joint, with the resulting wear.

Figure 1.9 show some of the most remarkable available models for two-element TAA prosthesis.

a) Agility™ [38] b) INBONE® [39]

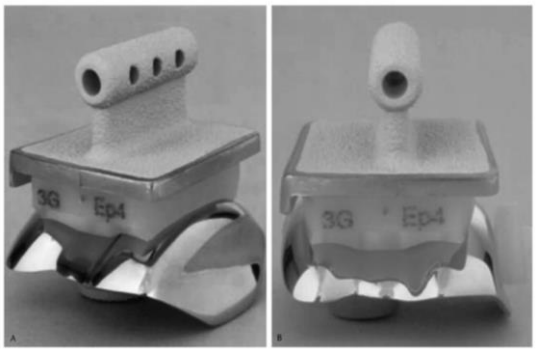

c) Salto-Talaris® [40]

Figure 1.9. Some commercially available two-component TAA prosthesis.

Agility™ has had the dominance of American market. As late as 2007, it was the solely admitted TAA prosthesis by Food and Drug Administration (FDA) [14].

In Agility™ model, talar component is not completely congruent with sacrifice element, thus slight rotation of the later is allowed. Also, for a better prosthesis anchorage, distal tibiofibular syndesmosis must be fused.

INBONE® prosthesis solves the tibial fixing problem with the use of a steam incrusted on tibia [12], but natural variability of mechanical properties of bone tissues should also be addressed to avoid prosthesis loosening [31].

The TAA Salto-Talaris® two-element prosthesis was developed for American market from the three-element original design [14]. Its recent introduction (2006) is the main cause of the lack of abundant literature on it long-term performance.

Main three-component TAA prosthesis designs are shown on as part of the Figure 1.10. Their development and use have been limited to Europe until last decade.

a) STAR™ [41]

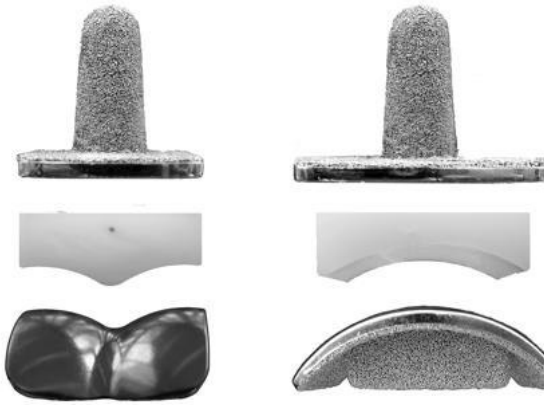

b) Buechel-Pappas [42]

c) Ramses® [43]

d) HINTEGRA® [44]

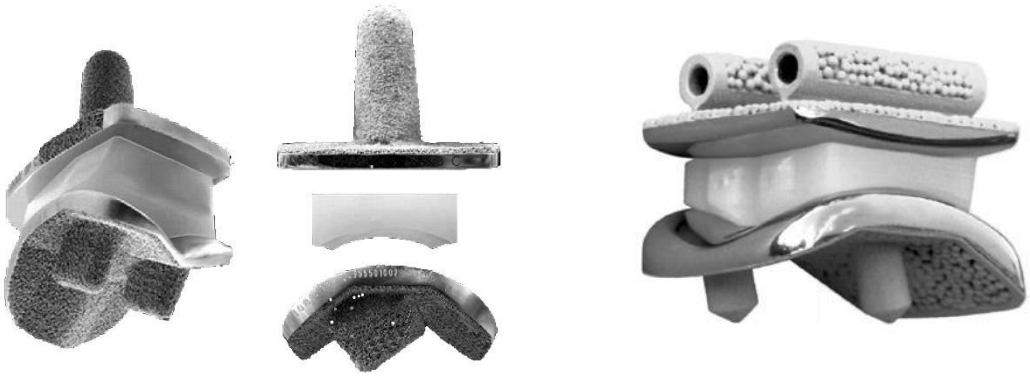

e) Mobility™ [45] f) BOX® [46]

Figure 1.10. Some commercially available three-component TAA prosthesis.

STAR™ (Scandinavian Total Ankle Replacement) prosthesis has remained virtually unmodified for 20 years. Its design allows flexion, extension, and some rotations on the sacrifice component, improving longevity and wear resistance [14, 47].

This prolonged acceptance and usage history allows the existence of many long-term result studies. A survival rate of 78% of implants five years after operation was reported for the very first recipients of STAR™ prosthesis; later, it rose to 86% of survival rate due the acquired experience of surgeons [48]. Even so, these numbers were noticeably lower than survival rates on knee or hip implants [12-13, 47].

Later studies on 200 patients showed survival rates of 93% after five years, and 80% after ten; most of the failures could be linked with a high degree of joint deformation before operation. As a side effect, patients also showed ligament rearrangement to a normal state [41].

Buechel-Papas prosthesis was originally conceived as a two-component prosthesis, then developed to a three-component one [14-15]. Its main distinction is the use of Ultracoat® coating on talar and tibial components for a diminished wear. It also allows lateral movements of inversion an eversion.

Ramses was one of the first three-components prosthesis models ever developed, intended for the possibility of having lateral movements. Its talar component surface has a spheroid shape; with more degrees of freedom that other intended prosthesis models [14, 43]. A survival rate of 100% after two years is reported [49], but also the obligatory use of fixation cement for mechanical anchorage implied an excessive bone loss during implantation.

HINTEGRA® prosthesis is a Swiss development with a different fixation proposal, using surgical screws to join both tibia and implant [44]. However, a main disadvantage is the lack of inversion and eversion moves [14].

For Mobility™ prosthesis, it was developed as a modern derivation of Buechel-Pappas design after the experience gained with TAA interventions [45]. Having a relatively new appearance, their long-term results are not clear, but a survival rate of 97% after three years is reported, and an average mechanical performance [45].

BOX® prosthesis was developed with the specific goal of minimize patient pain during movement [46], considering the compatibility of ligaments and soft tissues, looking for an isometric behavior of lateral and medium sides fibers during passive movement [14].

In contrast with its precursors, BOX® design was not limited to the mimic of original intact geometry of tibia and talus, but it was focused on developing a mechanism that favored the normal behavior of ligaments. This particular function allowed the increase on both the flexion range and useful life. Test on this prosthesis shown a survival rate of 97% after three years of use [46] having a good early income.

As shown above, stress levels inside TAA prosthesis, especially on sacrifice component, have been matter of major and continuous concern. Some comparatives on the issue are summarized on Table 1.1, so it can be concluded that design and geometry do have impact in magnitude and localization on generated stresses.

Table 1.1. Contact pressure for different TAA prosthesis [50]

Prosthesis	Study	Axial load (N)	Localization	Contact pressure (MPa)
Agility™	FEM	3330	Talar surface	26-36 (peak)
Agility™	FEM	3330	Center	20-24 (peak)
Agility™	Cadaveric	700	Not indicated	5.6 (average) 21.1 (peak)
BOX®	FEM	1600	Tibial surface	6.4 (average) 10.3 (peak)
BOX®	FEM	1600	Talar surface	5. 6 (average) 16.1 (peak)
STAR™	FEM	3650	Edges	20
STAR™	FEM	3650	Upper and inner surfaces	8-10

Resuming, for three-component TAA prosthesis, the middle sacrifice component has more degrees of freedom. However, it depends on soft tissues to keep its stability, or the surface of the talar element should be altered to allow the limited sliding of the piece, despite the anatomical reality.

In correlation to this division, two principal approaches on prosthesis design are used. The first approach consists on the faithful replication of the joint geometry, with the disadvantage of using materials whose mechanical properties are widely different from the natural ones, thus modifying the dynamical behavior of the joint, being the source of excessive stress concentrations, which lead to the prosthesis possible failure due premature wear.

The other option available relies on keeping the mechanical behavior of the joint even when original shape is altered. For example, the use of a spherical joint on talar component allows for a better conservation of degrees of freedom even when talus has a radically different geometry. It should be noticed that in this case, the soft tissues can be stressed in excess [14] because of load transmissions from the original joint.

Another distinctive element for TAA prosthesis is the tibial and talar fixture on bone. Surgical cement has been used with regularity. Other designs are expected to keep on position with only mechanical anchorage, as it happens with steamed prosthesis.

A matter of great concern is the application of new materials. Nowadays, most commercial TAA prosthesis are elaborated on titanium (Ti) and chrome-cobalt (CrCo) alloys, well-known for their use on bioengineering applications; with variations and surface treatments being optional. For sacrifice components, the use of UHMWPE can be considered as mandatory [14,51].

With the discussion of this relevant information about ankle joint, TAA and TAA prosthesis evaluation, clear objectives can be formulated for determining the guide and scope of this work.

1.5. Objectives

- Main objective

Design and build a total ankle arthroplasty (TAA) prosthesis prototype in which geometric configuration and material choice allow for energy absorption during its operation.

- Specific objectives

I. To make a comparison (benchmarking) among the prosthetic models available in the market in terms of characteristics, capabilities and performance.

II. Design and analyze a system that dissipates and stores energy efficiently through mechanical elements within the physical limitations of ankle joint.

III. Implement the previous design to a prosthetic model for total ankle arthroplasty.

IV. Generate a CAD model of the prosthesis with the integrated system.

V. Develop characterization of the biocompatible material to use.

VI. Generate a structural finite element analysis (FEA) to assess the performance of the proposed prosthesis model.

VII. Manufacture a rapid prototype of the design for experimental testing and comparison with the finite element model.

VIII. Dissemination of the results through the publication of articles and / or exhibition in conferences

1.6. Projected development

Once presented the problem background and objectives, following scheme seen on Figure 1.11 shows in broad strokes the proposed methodology

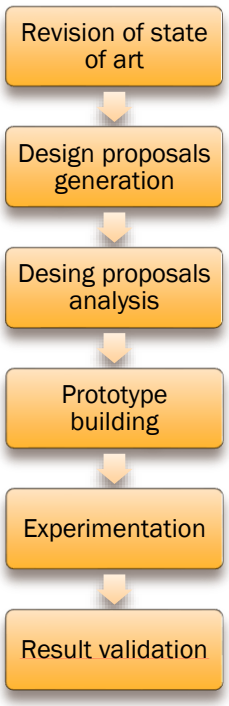

Figure 1.11. General methodology of the project.

Each step is described in more detail:

1. The review of the state of the art focuses on the study of a) prostheses present in the market, whose performance has been monitored and b) patents related to the problem posed. Another aspect of the study will be the application of systems or elements that absorb

mechanical energy and whose adaptation to a prosthesis is feasible. A joint analysis of the information collected will give suggestions on how to combine both elements.

2. From the point above one or more design proposals are generated. It is important to compare the performance between the generated options, as well as the possibility of creating those designs physically, including the selection of the material and the manufacturing process.

3. Through the analysis of finite elements, the operation and performance of the proposed solution is evaluated. The iteration at this point is not ruled out according to the simulation results themselves. A priori, displacement, deformation, stress and buckling analysis are considered. The characterization of the material to be used is an additional element to cover, as it feeds the simulation model.

4. The creation of one or several rapid prototypes. It is expected to use 3D printing as the main method, but the use of machining or other available technique is not ruled out.

5. The fundamental thing is to corroborate through experimentation the behavior observed in the simulations of point 3, subjecting the prototype to tests analogous to virtual analyzes. It should be added that there are standards to test the performance of prostheses, so they must also be followed.

6. Finally, the validation of the results and their synthesis will be the basis for the writing of the thesis, articles, and other derivatives.

Table 1.2 shows a breakdown of the activities at each step of the research process.

Table 1.2. Objective breakdown.

General objective	Particular objective	Specific objective
Design and build total ankle arthroplasty (TAA) prosthesis prototype in which geometric configuration and material choice allow energy absorption, reducing wear and its impact to the rest of the lower limb.	Make a comparison between the prosthetic models available in the market.	Identify the most common prosthetic models in the market
		Identify the main characteristics and working principles of these models
		List the strengths and weaknesses of each model
	Design and analyze a system that dissipates and stores energy efficiently.	From the previous study, propose a denture base geometry
		Find solutions for energy absorption and dissipation
		Evaluate the possible solutions to find the most efficient
		Adapt the most efficient solutions for energy absorption to the base geometry of the prostheses
		Create a geometric prosthesis model with the chosen solution.
		Propose one or more manufacturing methods for the chosen geometry
	Analyze the performance of the proposed prosthesis model	Obtain the mechanical properties of the material to be used - Characterization
		Determine the number and type of elements most suitable for numerical analysis
		Perform the numerical analysis of the various design proposals
		Perform a sensitivity analysis
		Choose one or two models with better performance for your construction
	Manufacture a rapid design prototype	According to the chosen manufacturing method, look for available facilities and machinery
		Reach an agreement for manufacturing
		Carry out prototype manufacturing

1.7. Chapter conclusions

The optimal performance of ankle joint is fundamental for life quality on a patient. OA is a chronic degenerative disease that interferes with the joint natural functionality. For advanced stages of the illness, surgical intervention (TAA) has been implemented with mixed results.

In contrast to similar operations, TAA has not had an extensive continuous development. Rising demand for this intervention and the need for achieving best results are areas of opportunity where valuable additions to the state of the art can be done.

By the aforementioned reasons, the generation and implementation of an energy absorbing system inside the TAA prosthesis design is justified, with the objective to extend its operative life and diminishing their adverse effects.

Eventually, even if the focus of the work is on ankle joint, the same principle could be applied to other prosthesis and mechanical devices in order to have the effect of extend their useful life and serving as an advancing point for new biomechanical projects.

Chapter 2 – Mechanical characterization of Ultra-High Molecular Weight Polyethylene (UHMWPE)

In this chapter, a brief description for the biocompatible material of use on the sacrifice prothesis component is given.

Having a long tradition of use on prosthetic developments, Ultra-High Molecular Weight Polyethylene (UHMWPE) characteristics have been reported on previous research. The following review is focused on the required specification for its use on biomechanical applications, and its behavior on such conditions.

After this theoretical introduction, the overall description and details on the mechanical tests applied to the available material are reported. Tensile, compressive and complementary tests were carried on for obtaining the required information for future material model adjustment. Stress-strain curves are obtained and shown as part of these results.

Finally, some information related to material fatigue is referred from literature as the corresponding tests could not be properly applied.

2.1. Introduction

Ultra-High Molecular Weight Polythylene (UHMWPE) is a thermoplastic, semicrystalline polymer which is built on homogeneous ethylene monomers [52] (as seen on Figure 2.1)

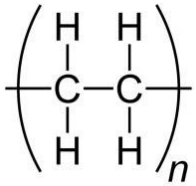

Figure 2.1. UHMWPE chemical formula.

The extreme length of its carbon chains (around 2-6 millions of atomic mass unities) [53], and the corresponding molecular structure of UHMWPE allow the existence of both crystalline and amorphous phases (as seen on Figure 2.2)

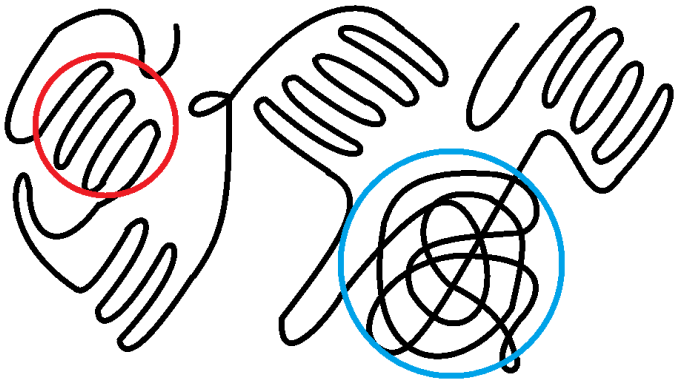

Figure 2.2. UHMWPE molecular structure.

The crystalline phase (as seen on the red circle) contains chains folded into highly oriented lamellae, with the crystals being orthorhombic in structure. These lamellae are 10-50 nm thick and 10-50 μm long [52]. These lamellae are oriented randomly within the amorphous phase (as seen on blue circle) which links individual lamellae to one another [54].

This condition is the origin of physical phenomena such as viscoelastic behavior on small deformations, distributed fluency and viscoplastic flow on higher loads, and a noticeable stiffness rise before rupture. The material behavior is also heavily influenced by the strain rate and temperature: a slower strain rate and/or lower test temperatures both increment UHMWPE stiffness [55].

The configuration generates a material that is quite resistant to impact and wear, being the resin with less loss of volume due to this cause. [52,56].

In addition to its mechanical properties, the UHMWPE is very resistant to corrosion and has one of the lowest coefficients of friction in relation to most plastic materials [51]. Being also a non-toxic and biocompatible material [57], it is a great material for prothesis building.

UHMWPE is obtained by a process of polymerization. of ethylene (C_2H_4) with the aid of hydrogen (H_2) and titanium tetrachloride ($TiCl_4$) as a catalyst. The resulting powder can be processed by compression molding, extrusion, gel spinning or sintering [58].

By means of the first process, sheets are obtained. The most common dimensions found are 1-2 m wide and 2-4 m long, with a thickness of 30-80 mm. If extrusion process is used, the resulting product are bars with diameters of up to 290 mm; although the most commonly handled bars are found in the range of 20-80 mm [58]

In any case, UHMWPE is machined for later use in various applications. However, the material is sensitive to feed rates, tooling speed, and heat build-up during the procedure; the lack of control over these variables can change their original mechanical properties or cause manufacturing defects [59]. UHMWPE products from various manufacturers can be significantly different as far as their molecular structure and mechanical properties are concerned. Those differences can be expected to increase after implantation [60].

UHMWPE mechanical properties are also affected by sterilization [56] and aging for its application on biomechanical devices [61]. The later occurrence obligates to ensure a good performance on this applications, thus leading to the production of surgical grade material.

2.2. Surgical grade UHMWPE

Since its molecular configuration can be modified by crosslinking of molecules and the addition of complementary elements, UHMWPE can be better referred as a family of materials rather than a single, unique material.

In order to give a certain UHMWPE powder a surgical grade qualification, it must comply with certain purity requirements, avoiding contamination with waste generated during its polymerization [58].

The maximum values allowed for both ASME and ISO standards are given in Table 2.1:

Table 2.1. Surgical grade UHMWPE component requirements [57].

Resine type	**1**	**2**	**3**
Comercial name	**GUR 1020**	**GUR 1050**	**1900H**
Maximum allowed ash level (mg/kg)	150	150	300
Maximum allowed Titanium (Ti) level, (ppm)	40	40	150
Maximum allowed Aluminum (Al) level, (ppm)	40	40	100
Maximum allowed Calcium (Ca) level, (ppm)	50	50	50
Maximum allowed Chlorine (Cl) level, (ppm)	20	20	90

The chemical characterization is generally given by the manufacturers of the material, but it is possible to corroborate it through the analysis of trace elements and Fourier transform infrared spectroscopy [57,61-64].

Apart from these purity requirements, there is also an internal classification for the UHMWPE used in surgical applications, according to the additional processes applied on them [65-66]:

• **Conventional surgical grade UHMWPE**, which has not been irradiated for sterilization with a radiation amount greater than 40 kilogray (kGy)

• **XLPE**, or high crosslinking UHMWPE, in which the radiation dose is higher than the previous one. This facilitates the cross-linking of the polymer, as this phenomena increases resistance to surface wear [67]. However, oxidation caused by formation of free radicals can favor material degeneration. The latter effect can be mitigated by annealing at 130-135°, a temperature near to the melting point of the crystals of the material.

The procedure causes a decrease of strength, lessening the ability of the material to withstand stress and resistance to an impact load without failure [68]. Despite this phenomenon, XLPE has been taking a prominent role on prosthetic applications [60]

• **VEPE**, or high cross-linking UHMPE enriched with vitamin E, which is also irradiated with a dose above the limit of 40 kGy, but at the same time it is added with α-tocopherol as

an antioxidant element [69]. It has been found that wear particles from VE blended UHMWPE elicited a reduced biological response compared to conventional UHMWPE. However, other chemical and mechanical changes have been observed [70].

• **Other** less common types of UHMWPE that do not conform to the previous classification should be considered, such as those obtained from lighter chain polymers, those that are porous or have received superficial treatments to reduce their wear.

It is expected for surgical grade UHMWPE to have superlative mechanical properties to those of other types of polymers [67], and that within them there are also differences and particularities [65], hence the importance of material characterization for design.

As seen on Chapter 1, UHMWPE is an essential component of prostheses for arthroplasty, since its mechanical behavior mimics that of the cartilage it replaces. Although alternatives have been sought such as polyether ether ketone (PEEK) [71] regular or reinforced [72], polyurethane (PU) [73] and others, the pieces of UHMWPE remain as an overwhelming majority.

2.3. Sample manufacturing

Since the linked mechanical properties of a specific type of UHMWPE are required for its use in design, it is necessary to have the methodology to obtain them.

As a previous consideration, a summary for the most common mechanical tests for UHMWPE can be found on Table 2.2.

Table 2.2. Available mechanical tests for UHMWPE [64].

Test Resume		Available norm
J-Integral Test	The released energy by propagating a crack made to a sample under a stable voltage load is calculated.	ASTM D6068
Tensile Test	A characteristic specimen is stretched until its rupture to obtain a stress-strain curve.	ASTM D638
Compression Test	A characteristic specimen is compressed until failure or rotation. A stress-strain curve is also obtained.	ASTM D695
Fatigue Test	The propagation of a crack made in a test tube under a load of oscillating tension is observed, accounting for number of cycles	ASTM E647
Creep Test	The change in stress on a test piece under constant load is observed.	ASTM D2990
Impact Test	The characteristics of a mark made by an actuator that impacts on a test sample are measured.	ASTM D256
Small Punch Test	Biaxial deformation test on a disc is measured.	ASTM F2183

From this catalog, the most important and relevant tests for the final objective are chosen. Feasibility within the actual resources and required specifications were also considered for the project development.

The single most important limiting factor was the material availability, as not only the mechanical characterization but the prototype building must be done on a single rod of surgical grade UHMWPE (Figure 2.3).

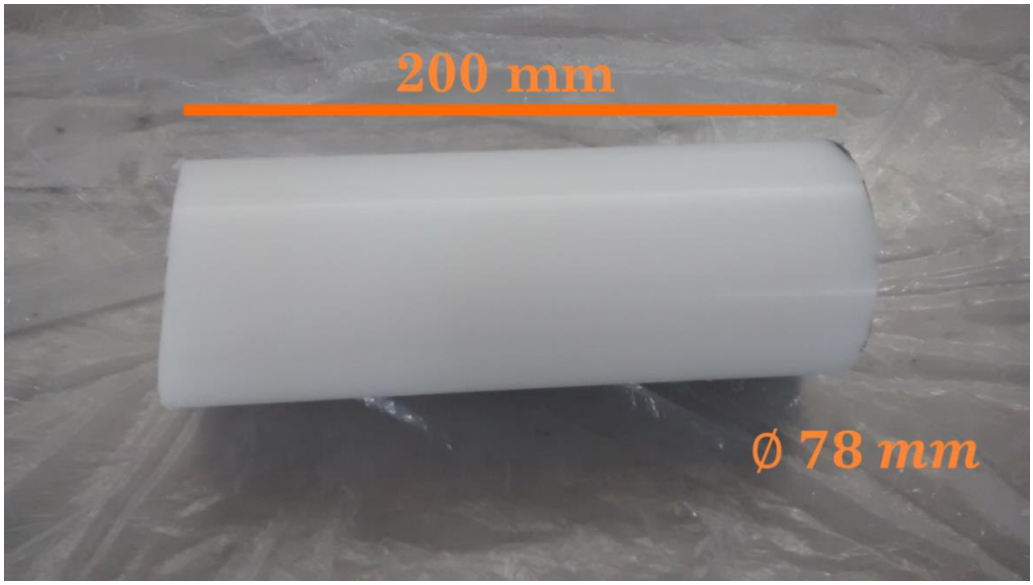

Figure 2.3. GUR1050 bar used for mechanical testing.

GUR1050 or medical grade Lennite® is produced from premium resins in accordance with ASTM specification F648 and International Standard ISO 5834-1 for surgical implants [74]. This material is used mostly for total joint replacements on hip and knee, among other medical devices and various implants, due for being biocompatible and having a great resistance to wear [52, 75].

Tensile test was chosen, referring to the ASTM D638M Standard Test Method for Tensile Properties of Plastics [76]. Normative indicates the type of equipment used, the loading conditions, the type and dimensions of the specimen, and the treatment of the results obtained. Figure 2.4 shows the respective geometric configuration:

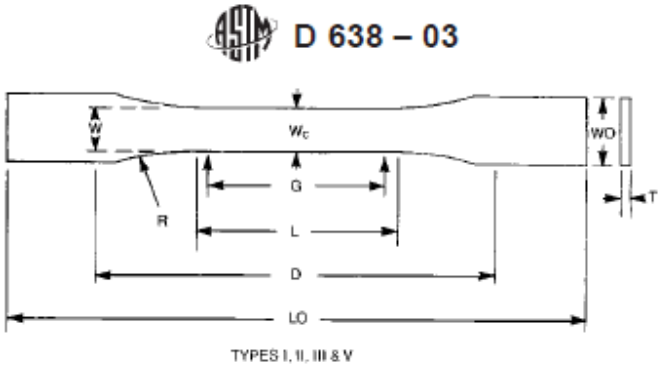

Figure 2.4. ASTM D638 sample nomenclature [76].

The nomenclature for each of the relevant dimensions is also observed: the total length (Lo), the total width of the specimen (Wo), the effective width of the specimen (W) and thickness (T). Type V sample dimensions were chosen, as shown (Figure 2.5):

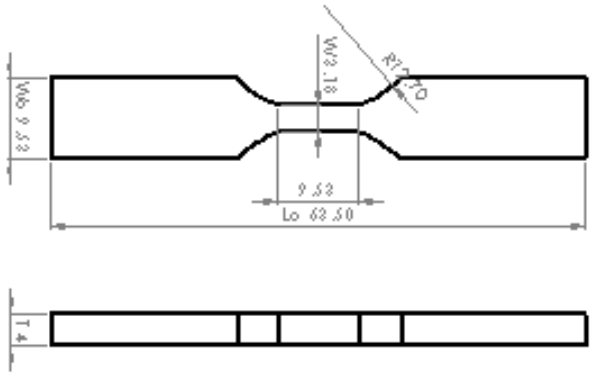

Figure 2.5. Tension sample model.

In comparison, compression sample has a much simpler geometry, a prismatic shape with square base with an edge of 12.7 mm and a height of 25.4 mm, (see Figure 2.6) according with the norm ASTM D695 Standard Test Method for Compressive Properties of Rigid Plastics [77].

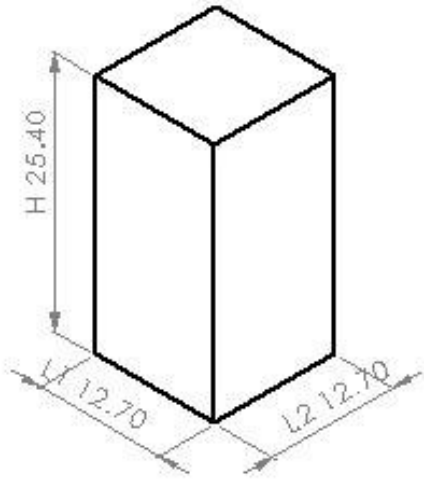

Figure 2.6. Compression sample model [77].

Due to the technical requirements for each test, at least five specimens must be worked in the axial direction of the polyethylene bar and so many in the perpendicular direction, taking in consideration any possible anisotropy.

The high number of specimens obtained refers to the need to confirm or rule out a possible anisotropy of the material as well as the repetitiveness and reliability of the tests.

Figure 2.7 below shows the original sample manufacture planning for the rod. The cylinder was divided into disk-shaped and other flat remnant sections so the desired geometry could be machined from these pieces. The available tools forced to have a wide tolerance on the previous cuts, carrying out the reduction to the desired thickness by means of numerical control.

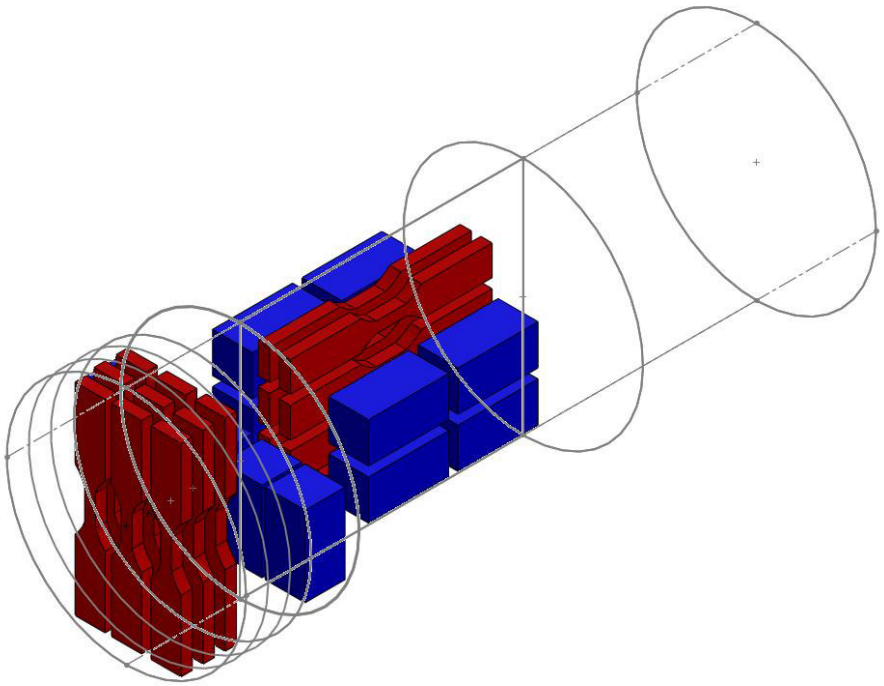

Figure 2.7. Manufacturing planning for tension and compression samples.

The parts were machined in a Fadal VMC 3016 vertical machining center (Figure 2.8) with a 12.7 mm drill bit for the cylinder section and a 1.5875 mm drill for cutting the silhouette. The speed of advance was of 25.4 mm / min, the speed of penetration of 12.7 mm / min. The spindle carried a speed of 2000 RPM.

Figure 2.8. Fadal VMC 3016 vertical machining center [78].

The operation of the lathe to cut each piece was carried out in intervals both to remove the detached material as well as to avoid the overheating of the piece [59]. The manufacture of each group of pieces per section (Figure 2.9) took a net time of 2 and a half hours.

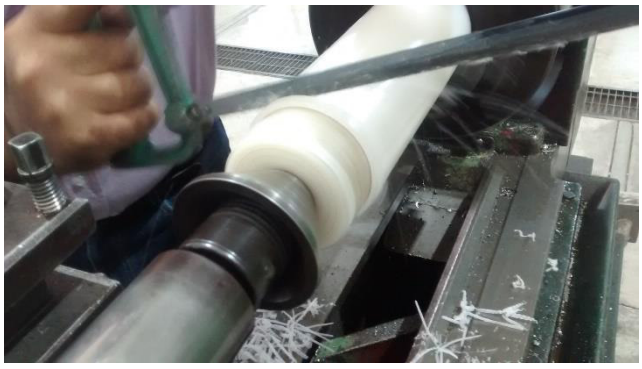

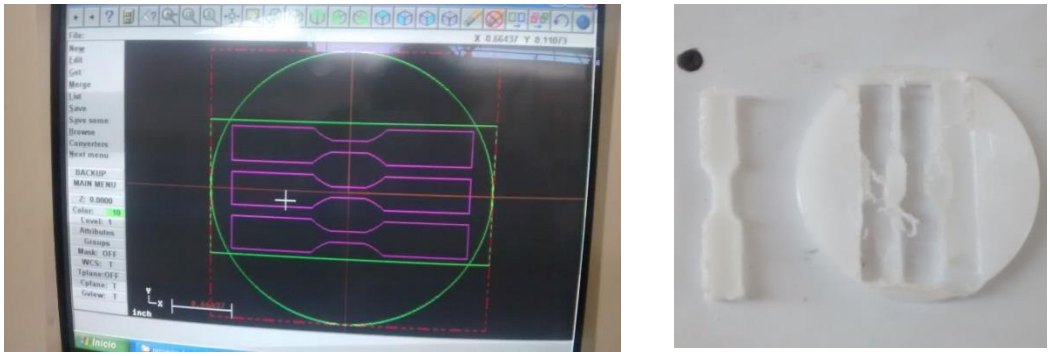

Figure 2.9. Manufacturing of a tension sample.

It is observed that the separation of the finished piece of the material requires a neat polish, first with a knife and then with sandpaper of grades 1 and 0. Although most of the samples meet the dimensional tolerances as seen on subsequent sections, there is a relatively high variability due this cause.

Both tensile and compressive tests were carried out on an Instron® 8802 machine, a hydraulic servo test system shown on Figure 2.10 below.

Figure 2.10. Instron® 8802 Fatigue Testing System [79].

The procedures for tension and compression are described on the subsequent sections.

2.4 Tensile test

The degree of crystallinity of UHMWPE is known to strongly influence several of its tensile mechanical properties such as Young's modulus, yield stress, strain-hardening rates, work of fracture and ultimate tensile properties [80]

UHMWPE is a material with a great capacity of elongation on tension (up to 400% of the original length) [56] However, as the intended application of the project will not allow for those extreme values, the results must be focused on the early stages of elongation.

Table 2.3 shows the dimensions established by the referred norm ASTM D638 and the dimensions of each test sample.

Table 2.3. Tensile samples.

#	Extraction		Lo (mm)	Wo (mm)	W (mm)	T (mm)	D (mm)	Nominal working area (mm^2)
Norm value			**63.50**	**9.53**	**3.18**	**4.00**	**25.40**	12.720
Upper limit			63.50	---	3.68	4.00	---	---
1	Disk	1	63.78	10.39	4.09	4.18	24.78	17.096
2	Disk	1	63.81	9.94	3.77	3.95	24.81	14.892
3	Disk	2	63.96	9.90	3.29	3.33	24.96	10.956
4	Disk	2	63.80	9.92	3.57	3.34	24.80	11.924
5	Disk	2	63.76	9.96	3.57	3.39	24.76	12.102
6	Disk	3	63.88	9.94	3.45	3.96	24.88	13.662
7	Disk	3	64.06	9.99	3.42	3.76	25.06	12.859
8	Disk	3	63.93	9.87	3.44	3.63	24.93	12.487
9	Plate	1	64.05	9.89	3.61	3.8	25.05	13.718
10	Plate	1	63.89	9.90	3.53	4.03	24.89	14.226
11	Plate	1	64.04	9.56	3.46	3.59	25.04	12.421
12	Plate	1	64.11	10.03	3.44	3.96	25.11	13.622
13	Plate	1	64.01	9.91	3.70	3.84	25.01	14.208
14	Plate	2	64.00	9.75	3.66	3.00	25.00	10.980
15	Plate	2	64.10	10.00	3.75	3.00	25.10	11.250
16	Plate	2	63.80	10.00	3.50	3.20	24.80	11.200
17	Plate	2	64.30	9.75	3.75	3.33	25.30	12.488
18	Plate	2	64.00	10.00	2.90	3.00	25.00	8.700

For the identification of the specimens, the order of manufacture was respected (Figure 2.11).

The references of Disk and Plate are linked with the original piece cut of the material rod used for the sample manufacturing and determine the main direction (axial and perpendicular) of the test sample.

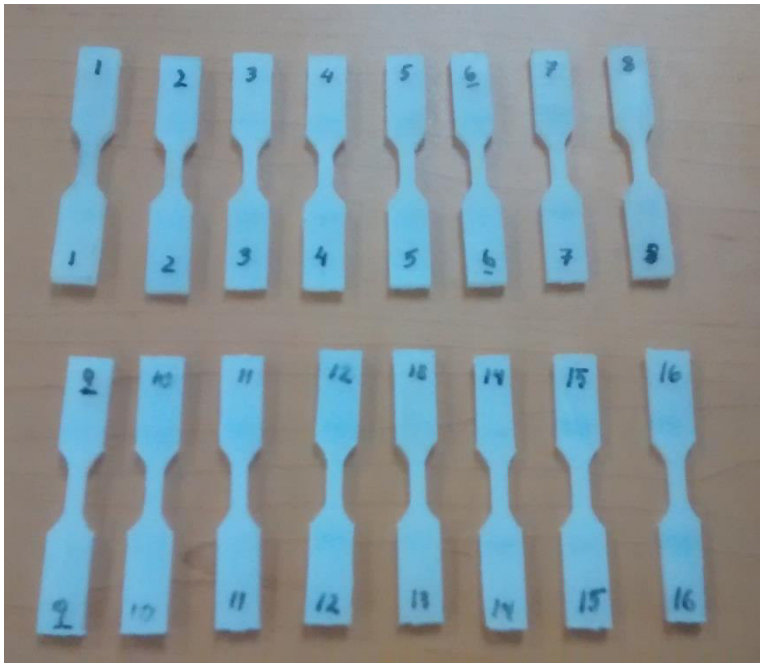

Figure 2.11. Tensile samples before test.

The specimens 0 (of a polymer different from the material to be characterized and eccentric geometry), 17 and 18 (not shown on Figure as they did not met the norm standards) were run as a preliminary test with a stretch of 10 mm / min.

As a result of this test, some drawbacks were detected and solved. The fastening problems caused by the specimen rotation were solved by adding a piece of the residual UHMWPE between the clamps (Figure 2.12). A speed adjustment was also considered, with a working speed of 7 mm / min (-25%), specified in ASTM D638.

Figure 2.12. Clamping of tensile sample for test.

The stretching of the test piece was then carried out at 0.1242 mm / s, which is equivalent to a deformation rate of 0.0130 / s.

Figure 2.13. Tensile samples after test.

Stress-strain curves generated for each specimen are shown as test results (Figures 2.14,2.15). Due to the impossibility of instantaneously measuring the change in the cross-sectional area of the specimen, both the stress and the deformation are of the engineering type.

Each individual stress-strain curve is identified with the prefix ED and the number assigned to the sample on Table 2.3.

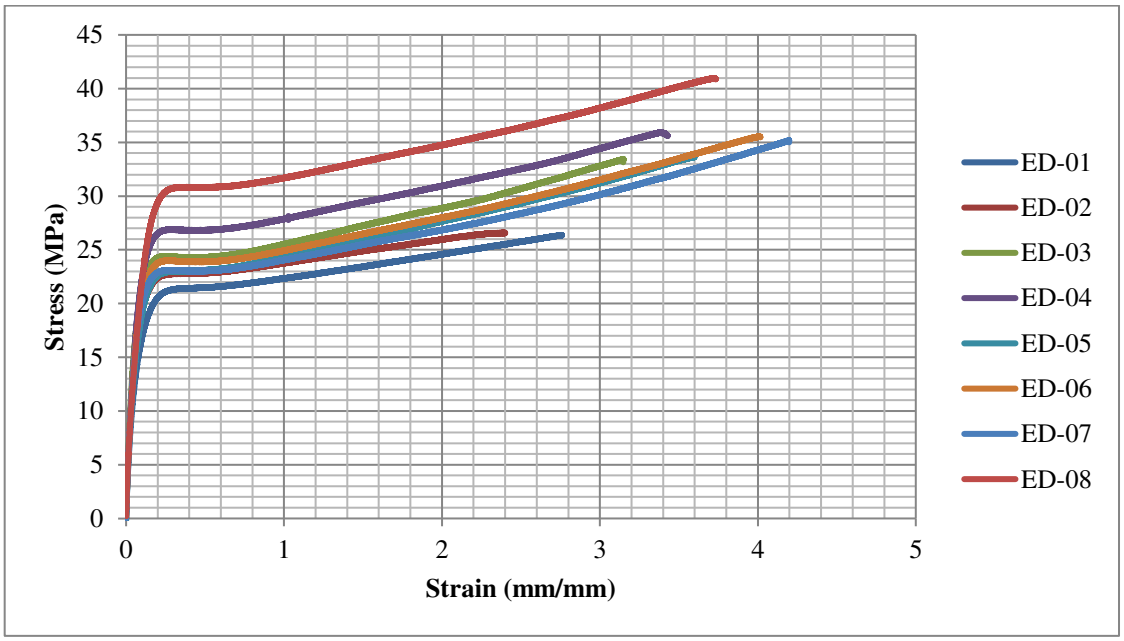

Figure 2.14. Engineering stress-strain curves for perpendicularly oriented tensile samples.

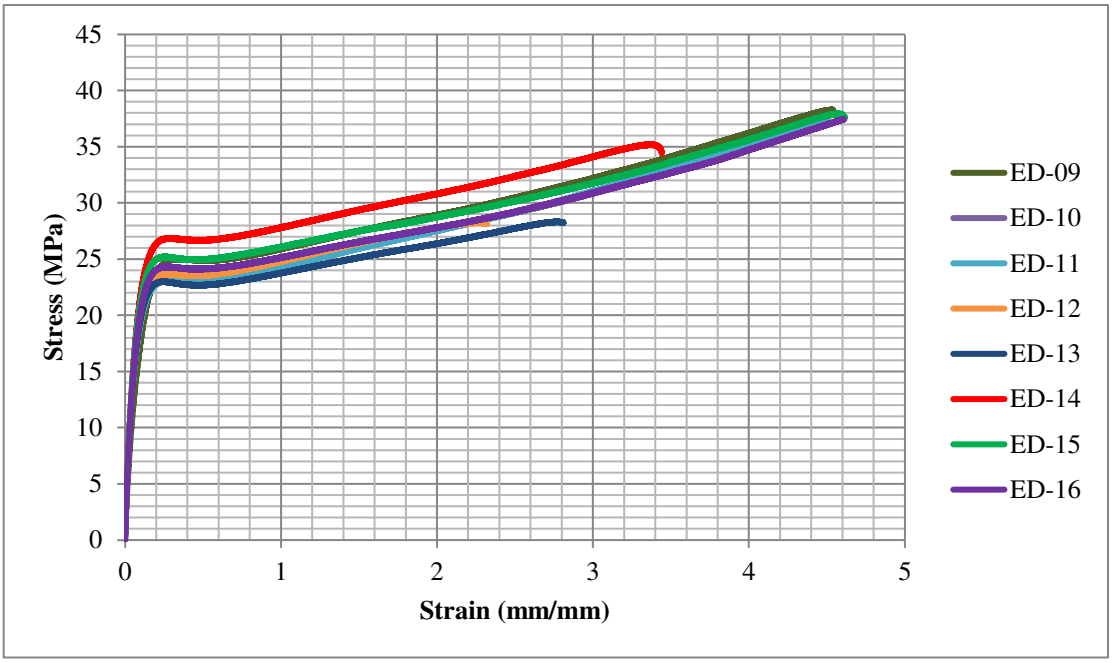

Figure 2.15. Engineering stress-strain curves for axially oriented tensile samples.

A quick look at the deformation stress curves show an expected behavior of all the specimens, as backed on earlier works [56,64,81-82], although the values of yield stress and rupture stress are more variable.

This happens for the two batches of specimens, those obtained with axial and perpendicular orientation. Then it is possible to establish that the working direction of the material does not influence the performance of the specimen (thus being an isotropic material)

The average yield stress was around 24-25 MPa, with 20% deformation. The effort to the average failure occurred around 35-37 MPa with 450% deformation

2.5 Compression test

Regarding the specimens for the compression test, an analogous process to the one of tensile samples was carried out. As seen on Table 2.4, they are also identified for sample tracking.

Table 2.4. Compression samples.

#	Extraction		Ho (mm)	L1 (mm)	L2 (mm)	Nominal working area (mm^2)
Norm value			**25.40**	**12.70**	**12.70**	**161.290**
1	Disk	1	25.50	13.00	12.66	164.580
2	Disk	1	25.75	13.50	12.50	168.750
3	Disk	1	26.00	13.00	12.80	166.400
4	Disk	1	26.00	13.00	13.50	175.500
5	Disk	1	25.90	13.00	12.80	166.400
6	Plate	1	25.80	13.10	12.66	165.846
7	Plate	1	25.75	13.00	12.66	164.580
8	Plate	1	25.66	13.10	12.66	165.846
9	Plate	1	26.00	13.10	12.70	166.370
10	Plate	2	25.90	13.00	12.75	165.750
11	Plate	2	26.00	13.00	12.66	164.580
12	Plate	2	25.80	13.00	12.50	162.500
13	Plate	2	26.00	12.66	13.00	164.580

Due to the consideration of isotropy from the previous test, fewer specimens were required for the compression test [77].

The pieces presented a lower geometrical variability in comparison to the tension samples; in contrast, they required finer adjustments for flatness, again by means of a fine sanding. This assured a better quality on results. Finished probes are seen on Figure 2.16

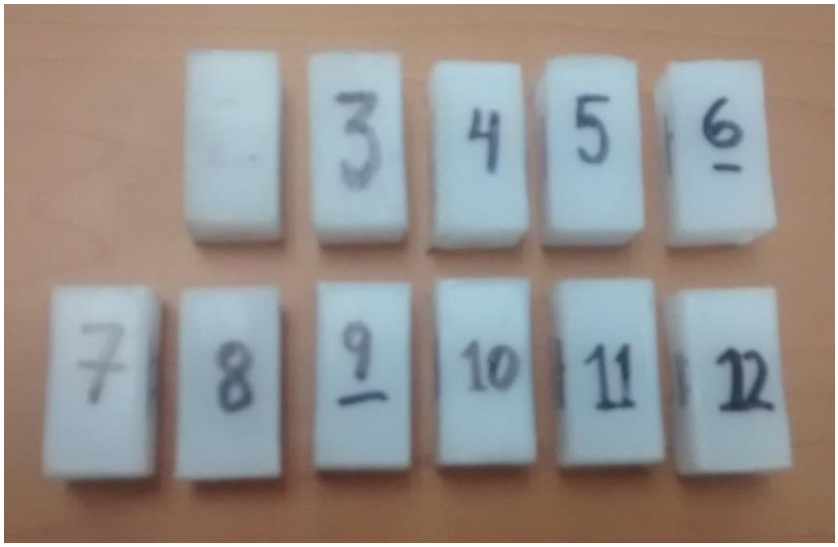

Figure 2.16. Compression samples before test.

The compression of the test sample was done at a speed of 0.0216 mm / s, deformation ratio of 0.0008 (mm/mm) / s. Compared to the stress test, the deformation occurs much more slowly and that gives importance to certain viscoelastic properties that in the other test did not manifest themselves in an obvious way.

It is observed that there is no direct clamping of the specimen for testing, as seen on Figure 2.17:

Figure 2.17. Load appliance on specimen during compression test.

The final displacement of the upper face is of 7.62 mm, allowing for an engineering strain of 0.30 in axial direction. Strain rate of test is fixed and was calculated at 6.6 $x10^{-4}s^{-1}$.

The failure of the material was caused by rotation and buckling of the specimen in all cases, as shown in Figure 2.18.

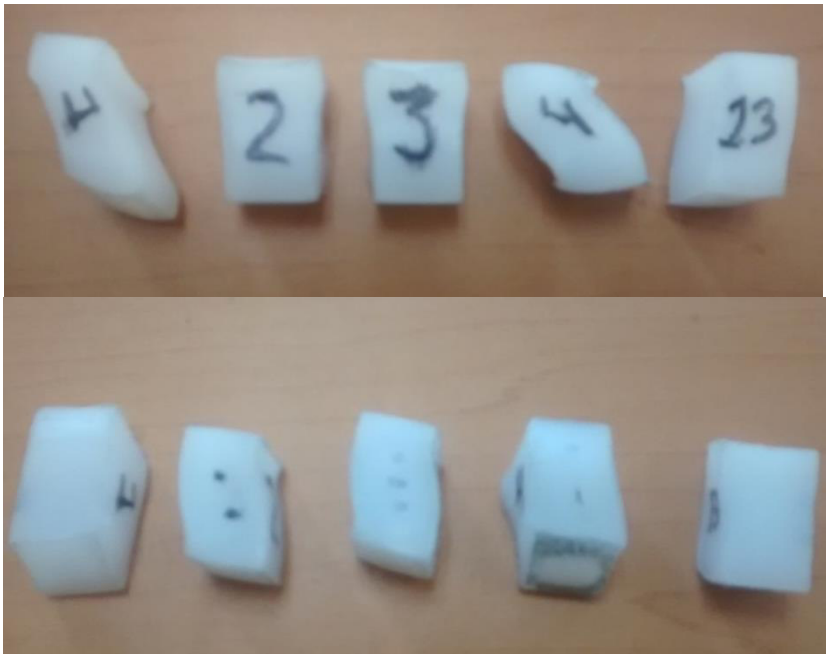

Figure 2.18. Compression samples after test.

As in the previous test, for each specimen the following engineering strain-deformation curves were generated. Each test piece is identified with the prefix PB and the corresponding manufacturing order.

Unlike the previous test, it is noteworthy that only five specimens were used, since the material was assumed to be isotropic [77].

The original readings of the measured load on device were denoted by a negative sign. The curves were adjusted to show the effort as a positive value as seen on the following Figures.

For Figure 2.19, an abrupt fall on stress lecture caused by specimen rotation and the increment of contact area is evident. Thus, these results are only useful under a strain of 0.3 or lower, being still a relevant range for the overall project.

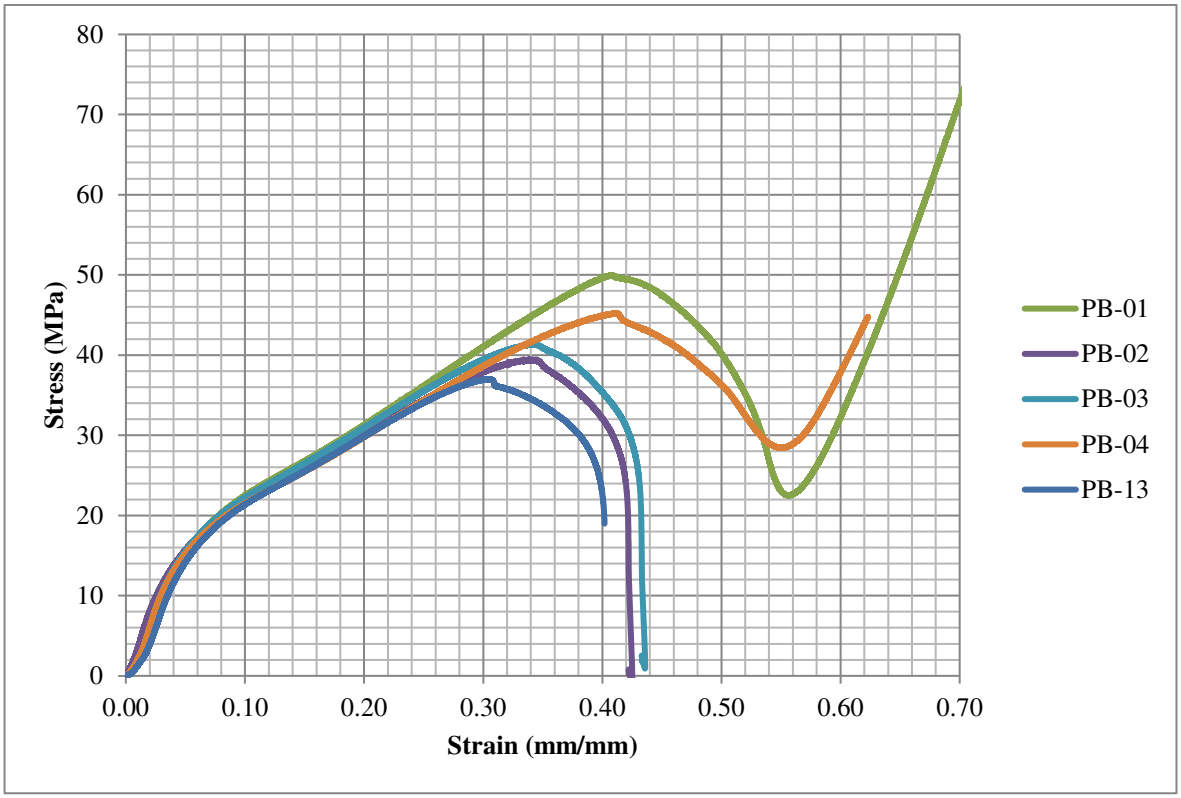

Figure 2.19. Engineering stress-strain curves for compression samples.

It is also observed that the supported efforts are greater than those obtained in the elasticity tests, hinting to a clear difference on tension and compression strength.

Resuming, results for test are reliable up to 30% compression, with a maximum stress value close to 35 MPa before failure. Due to the sought application, this value provides a large design space.

However, some questions raised from this test performance, concerning the transition between elastic and plastic deformation on UHMWPE on the first stages of deformation, as it could not be devised on the original curves. In order to get the corresponding answers, some non-standardized compression tests were used.

2.6 Additional test derived from compression samples

To complement this lack of insight on elastic behavior, an additional test was carried out to check the elasticity of the material. Due to the goal of creating a wear-resistant design that absorbs mechanical energy, it was decided to find the maximum allowable, non-permanent deformation of the material on a sample.

For this, the compression test was adjusted in such a way that the loading and unloading of the specimen occurred while linearly increasing the deformation to which it was subjected by the actuator in 0.5 mm intervals, from 0 to 5 mm. Expected strain will be kept under 19.68%.

Figure 2.20 shows the force registered by the actuator on one specimen as a time function:

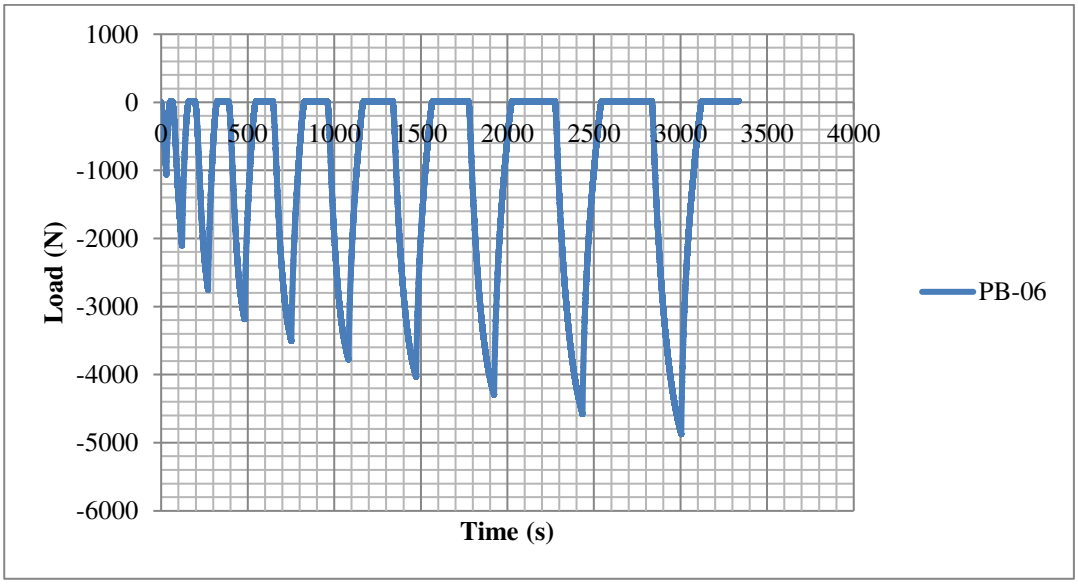

Figure 2.20. Load curve on a compression sample.

As the piece is in compression, load is denoted as negative on previous Figure. As the actuator compressed the sample, the registered force increased near to 5000 N. The progressively longer intervals with zero load value indicate the lack of physical contact of sample and testing machine caused by deformation and the consequent dimensional change.

Considering a known and constant deformation area, the engineering strain-deformation diagram, shown in the Figure 2.21, is generated:

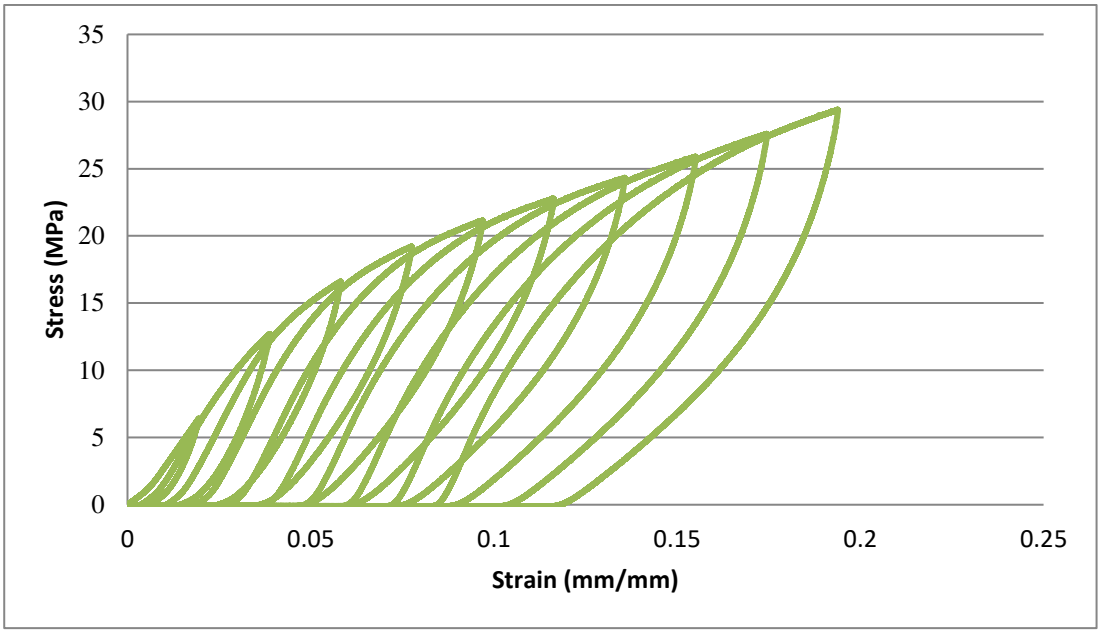

Figure 2.21. Engineering stress-strain curve for loading and unloading a compression sample.

Under the proposed conditions, the stress-strain curve shape resembles the one obtained by simple compression. However, it is also noted that the charges and discharges of the specimen do not start from the same starting point. It is then inferred that the material does not have a perceptible purely elastic zone, because in each iteration, the actuator does not start from the established zero value but considers a deformation that has occurred. It is possible to infer that the viscoelasticity described for UHMWPE is important in the actual compression conditions.

It is also probable that the hysteresis and the restitution of the material were not perceptible on the test, and there is no restitution time between deformations. However, both samples were measured again after a 24 hours period, and both had returned to their original dimensions.

2.7 Fatigue on UHMWPE

Fatigue is the structural and progressive damage that occurs in a material subject to cyclic loading, originated from microstructure changes [83]. In this process, five characteristic steps can be distinguished:

• Permanent damage due to changes in the microstructure

• Generation of microscopic cracks

• Growth and fusion of dominant cracks

• Stable propagation of the dominant crack

• Final fracture

The two main approaches to studying fatigue are the study of total life, starting from test tubes without damage, and tolerance to defects, which assumes the existence of base imperfections in the material. Polymers have specific molecular mechanisms, therefore fatigue tests to total life rarely fail evidently as would a mechanical material and therefore the second approach is preferred [83].

The proposal for future work is to submit the developed prosthesis assembly to simulations of fatigue by means of finite element analysis, therefore it must be considered in the corresponding material model.

Among the most reported analyzes for UHMWPE in the literature is obtaining the number of cycles that takes the propagation of crack in a test tube under an oscillating load [83] making direct reference to geometries of the ASTM standard E647 Standard Test Method for Measurement of Fatigue Crack Growth Rates [84]

The existing ASTM standard for fatigue is usually focused on its formulation to metallic materials, being applicable to rigid polymers. In the case of ASTM E647, the type specimen is shown in Figure 2.22:

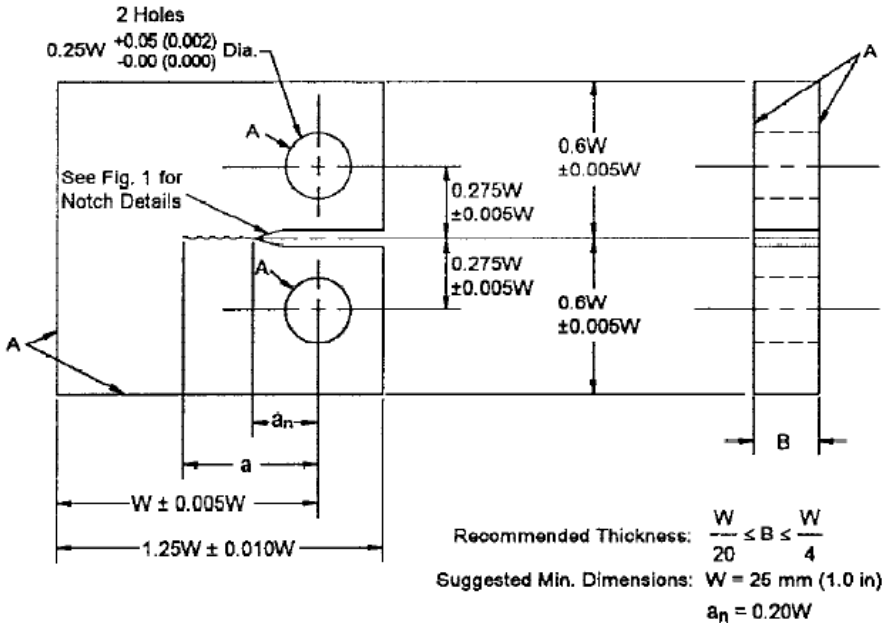

Figure 2.22. ASTM E647 Fatigue sample [84].

The basic sample form is that of a rectangular block. For the case of the smallest specimen, the maximum dimensions would be 30 mm effective length W 31.25 mm base, 30 mm height and a thickness that was 1.25 to 6.25 mm. The diameter of the corresponding holes is 6.25 mm.

This implies that existing compression samples could not be reworked to obtain the new shapes.

Referencing more fatigue studies on UHMWPE, Baker et al (2000) [61] used the proposed dimensions for GUR 415, moistening the specimens with water at 37 ° C to simulate the conditions of the human body. The load was applied following a sinusoidal function with a 5 Hz cycle. The stress ratio (maximum stress over minimum applied) was 30 for compression (0.22 to 6.5 MPa).

Kozak et al [85] used slightly larger dimensions for GUR150, with effective length W = 40 mm. The difference of applied loads was 371 N and a ratio of 0.1 with a frequency of 3 Hz for sinusoidal function at a temperature of 37 ° C. Ansari et all [86] applied proposed

minimum dimensions, with load applied with a sinusoidal function at 5 Hz frequency, with incremental loads maturing the ratio of 0.1. The room temperature was used.

All the references used Paris equation (Eq. 2.1) to relate the crack propagation rate as a function of the intensity range of the stress.

$$\frac{da}{dN} = C(K_{max} - K_{min})^m \tag{2.1}$$

Where a is the crack length, N the number of load cycles, $K_{max} - K_{min}$ the force intensity range factor, C and m material parameters.

Fortunately, there is a reference of an experimental *S-N* curve for GUR1050 to compression by Pruitt et al on UHMWPE Material Handbook [83]. Reference is shown on Figure 2.23.

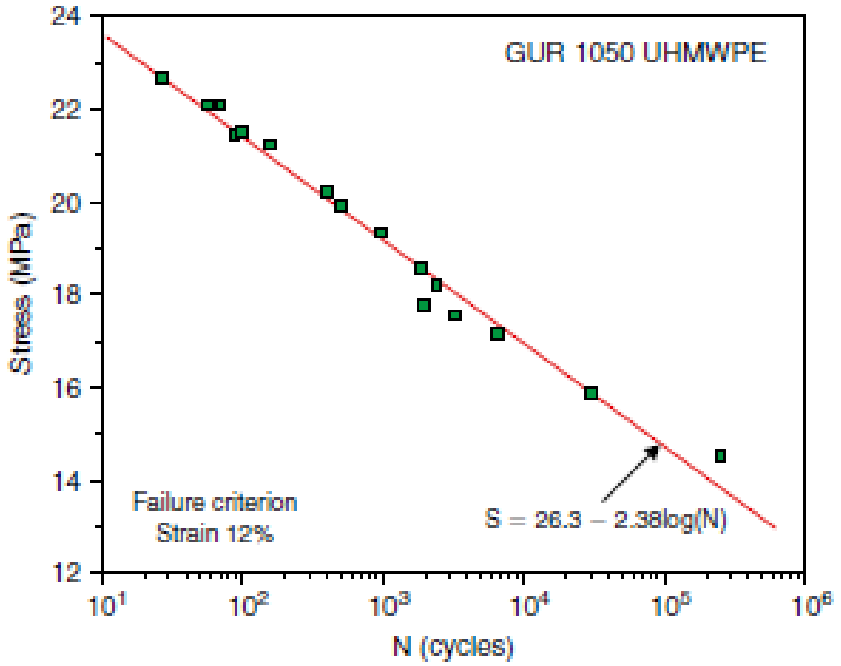

Figure 2.23. Experimental S-N curve for GUR 1050 UHMWPE [75].

Data analysis generated a correlative equation among maximum failure stress (denoted as S) and number of operative cycles (N) (Eq.2.2)

$$S = 26.3 - 2.38Log(N) \tag{2.2}$$

It is also observed that the admissible deformation for design on material is limited to 12%, as a greater value would make the model assumptions incorrect.

From the perspective of the analysis by finite element, considering that the material corresponds to the one that has been used and the state of compression, and its coincidence with other experimental values, this curve can be more useful to implement it in the simulations already done, at least as a first approximation.

2.8 Discussion

The previous testing development gave some vital insight needed for the project. Although commercial grades of UHMWPE suffer more structural alterations as compared to laboratory grade ones [87], the use of the former material is closer for a future built of orthopedic devices.

About material choice, even when highly crosslinked and enriched UHMWPE is considered as the state-of-the-art material of choice for TAA and equivalent interventions [88], it should be reminded that older models are still in use for earlier patients, and the evolution of polymer wear on prosthesis is better reported, whereas the failure of sacrifice components on TAA is more expected on a system within certain operation time.

For a comparison on the most similar conditions, it could be devised if a proposed, purely mechanic solution for stress reduction on polymer is feasible. Chosen conditions are considered enough for design on UHMWPE.

Statistically, the ASTM norm following assures the minimum number of samples in order to have useful results [76,77]. Additional samples were employed on these tests. Indeed, the

variation of engineering stress-strain results was within expected range on previous reports. However, as noticed on Figures 2.14 and 2.15, perpendicularly oriented samples on tension stress values are slightly more scattered than their axially oriented counterparts. The proposed explanation is that some of the former probes were the first ones manufactured, with more variation as the machining conditions were adjusted for a better processing.

A representative curve was elaborated by averaging equally distributed strain values; however, it was considered better to use a representative real curve for the following data adjustment, even when there was a clear overlap among stress-strain curves.

Taking in account the process of UHMWPE manufacturing effects on molecular chains, the bar extrusion could have influenced on reporting the polymer behavior as isotropic [89]. However, this assumption is also made in previous literature [55], reinforcing the conclusion of the experimental data. Even so, this must be taken into consideration on possible manufacturing process effects for the designed concept building.

For design purposes, an insight for a clear transition on the elastic and plastic zone on GUR1050 was needed, avoiding permanent deformation on TAA sacrifice component. References for this regimen change were not clear for the engineering-strain curves and an adaptation on the compression test was used. Albeit the proposed test did not used a direct reference or normative, it allowed for a better idea of how the material reacts to slow compression, expected to be found on normal TAA prosthesis operation.

It was found that material did experience deformation, but a later recovery of samples after a 24-hour period was also found. When the original stress is taken away, the accumulated back stresses on the molecular chains will cause the polymer to return to its original form. A clear boundary among reversable and irreversible creep deformation has been reported for tension samples around 15 MPa of engineering stress [90] This should be taken on consideration for possible solutions on energy dissipation for sacrifice components on TAA prosthesis design.

2.9 Chapter conclusions

UHMWPE is an important material family from an engineering point of view, especially in biomechanics. This implies that some specific considerations must be taken while modeling it in order to correctly reflect its unique properties and behavior.

Mechanical tensile and compressive tests were performed on GUR1050 samples in conformity with ASTM norms. It was established that GUR1050 is fundamentally isotropic, probably due effects of rod extrusion. As a result, engineering stress-strain curves were obtained. Calculated yielding stresses were of 25 MPa on tension and 35 MPa on compression.

In addition to these, supplementary tests were carried, with a more particular focus on its elastic properties. If the material is subject to strain higher than 2% it will not recover instantly, but in a variable period, being not completely elastic. However, that deformation was neither considered as a plastic, as relaxation effects must be taken on account, and a posterior restitution.

For fatigue tests, the project will rely on a yielding stress and number of cycles relation based on a previous work on GUR1050 samples on compression. As the reported conditions are very close to the future operation of sacrifice component, this mathematical approximation can be used within reliability.

Chapter 3- Material model implementation for UHMWPE

In the previous chapter, a series of mechanical tests on surgical grade Ultra High Molecular Weight Polyethylene (GUR1050) were reported. The adjustment of obtained data to different material models and its implementation to finite element analysis (FEA) tests is thus presented.

As a preamble, a brief description of the available material models, their physical signification, advantages and disadvantages is presented. After this review, selected material models are adjusted and evaluated in comparison with the original tensile and compressive tests for validation, at least for the first stages of obtained stress-strain curves.

The material models with a closer approach to the experimental data will be used for design and analysis of polymeric inserts on the sacrifice component of the total ankle arthroplasty (TAA) prosthesis.

3.1. Introduction

As seen on previous mechanical tests, UHMWPE mechanical behavior is clearly non-lineal, strain dependent and influenced by operating conditions [55]. Strain rate sensitivity, relaxation, creep and recovery at room temperature are observed as viscoelastic material properties of the polymer [91]

UHMWPE components used in prosthesis are subjected to complex loading conditions during service life, which lead to internal changes on material constitution. This mechanism plays a role on change of UHMWPE mechanical properties [92]. For example. an increase in elastic modulus and a decrease in the elongation to failure, ultimate stress and toughness has been related to oxidation [93]

If a physical phenomenon can be mathematically described, it can be simulated with the application of numerical techniques. Simulation of UHMWPE is limited by many assumptions if a simpler material models is used [55]. However, if chosen wisely, their use

can give accurate answers for a specific problem [94-97] where these approximations are close enough to the real described phenomenon on the polymer.

Simpler models are not well suited for assumption of cyclic loading, for determining the time-dependent response to loading, or for prediction of large deformation behavior leading up to failure [55].

In contrast, several robust, non-linear material models specifically designed for UHMWPE have been developed [55,98-99] reflecting how the loading rate affects the stress–strain, creep, and relaxation response by applying mathematical basis of rheological models [100]. Their main disadvantage for use is that they require a lot of experimental tests in order to make a fit, and a precise adjustment can be hard to get [55].

For TAR designs, simulation of axial force and contact stress is primordial [101] having a distinct nonlinear elastic response on this situation [102]. It is expected that design will operate on compression rather than tension, but the existence of the later could not be discarded early. As UHMWPE behavior can vary due working conditions, both situations must be taken on account.

As each material model has its own strengths, weakness, and applications, from the most simplified to the most complex ones, some of them are adjusted with the available data shown on Chapter 02 and compared for future use on simulation of more complex geometries, such as the one of the projected sacrifice component of TAA prosthesis.

3.2. Chapter nomenclature

a	Pressure dependence of Flow
a_i	Relative moduli parameter for Prony series
$\overline{B_i^*}$	Cauchy-Green deformation tensor
Ci	Material constant
Ci	Parameter i for Mooney-Rivlin material model
Cii	Parameter *ii* for Mooney-Rivlin hyperelastic model

d	Compressibility parameter
F	Deformation gradient tensor
I	Identity matrix
I_i	Invariant *i* of the Cauchy-Green tensor
J_i^e	Determinant of deformation gradient tensor for network *i*
k_B	Boltzmann constant
E	Young Modulus
N	Number of chains on Arruda- Boyce model
L^{-1}	Inverse Langevin function
m	Stress exponential
m_i	Stress exponential for network *i*
n	Number of chain segments on Arruda-Boyce model
SSR	Sum Square Residual
t_i	Relaxation time parameter *i* for Prony series
W	Strain energy density function
x	Independent variable
y	Dependent variable
β	Inverse Langevin function of polymer chain
β_0	Slope of lineal regression
β_1	Intercept of linear regression
μ_i	Shear modulus of network *i*
κ	Bulk Modulus
λ_i	Locking stretch of network *i*
ν	Poisson Ratio
σ_i	Stress state in network *i*
σ_y	Yielding stress

3.3. Material models theory

A material, or constitutive, model is a mathematical representation of the expected behavior of a given material in response to an applied load [103]. This is a crucial component for the use of numerical solutions for a system analysis. If the chosen constitutive model is correct, it is expected to find a simulated mathematical prediction of the studied component.

In an overall view, the better suited material models for UHMWPE [55] can be grouped on four general types as 3.3.1) linear elastic, 3.3.2) hyperelastic, 3.3.3) plastic and 3.3.4) specialized polymeric models.

3.3.1 Linear elastic model theory

The simplest approach available for a material model is the use of an isotropic linear elastic material model (LE) [104]. The only needed parameters are Young Modulus E and Poisson ratio ν. Both can be easily obtained from the mechanical tests data.

In certain controlled situations, such as very small strains, a lack of thermal effects and monotonic loads, the use of LE models for UHMWPE is considered valid [55,94]. As the problem proposes some restricted conditions inside the ankle joint the use of LE approximation should be taken in consideration.

From the shown engineering stress-strain curves, a simple approximation can be done. Young Modulus can be calculated as the estimated slope of the linear regression analysis of the data, following equation 3.1:

$$y = \beta_0 + \beta_1 x \tag{3.1}$$

Being E equivalent to β_1 and β_0 must be neglectable.

About Poisson ratio, both the experimental tests and literature agree that UHMWPE is nearly incompressible, with an effective value of $\nu = 0.46$ [105]

3.3.2 Hyperelastic models theory

A hyperelastic material is a type of constitutive model for ideally elastic material for which the stress–strain relationship derives from a strain energy density function. The hyperelastic material is a special case of a Cauchy elastic material [106].

Hyperelastic behavior has been reported as being the dominant one for UHMWPE on medium strain (20-50 %) [55]. It is expected to find the lower part of the range during operation of sacrifice component of TAA prosthesis, so these kind of models should be reviewed.

One of the most recurred hyperelastic models for polymers is the Mooney-Rivlin (MR) model. The related strain energy density function (as seen on Eq. 2) is a linear combination of two invariants of left Cauchy-Green tensor [106-107].

$$W = C_1(\bar{I}_1 - 3) + C_2(\bar{I}_2 - 3) \tag{3.2}$$

Material parameters C_1, C_2 must be derived from experimental data.

By the other side, the polynomial model (POL) is a more general version of the hyperelastic model, in which the deformation energy density function is a polynomial of two invariants of the left Cauchy-Green tensor

$$W = \sum_{i,j=0}^{n} C_{ij}(\bar{I}_1 - 3)^i(\bar{I}_2 - 3)^j \tag{3.3}$$

Which can be added with a volume dependence for a compressible material. However, it was established UHMWPE is nearly incompressible and thus is not needed.

The Ogden model is a hyperelastic model developed to describe the relationship between large deformations and the stress of materials such as rubber and biological tissues. Considering the incompressibility of the material, the deformation energy density function is defined by the main tensions (main stretching):

$$W(\lambda_1, \lambda_2) = \sum_{p=1}^{N} \frac{\mu_p}{\alpha_p} \left(\lambda_1^{\alpha_p} + \lambda_2^{\alpha_p} + \lambda_1^{-\alpha_p} \lambda_2^{-\alpha_p} - 3\right) \tag{3.4}$$

In the simplest case, this function can be reduced to the aforementioned MR model.

Yeoh material model was developed to work with incompressible elastomers, with high non-linearity. Unlike previous models, it is considered that the energy deformation density function only depends on a deformation invariant, that it can be expressed in a generalized equation:

$$W = \sum_{i=1}^{n} C_i (I_1 - 3)^i \tag{3.5}$$

Thus, being reduced to a polynomial model.

In overall, hyperelastic models are easy to calibrate, and are available for most of commercial finite element codes. Mayor limitations are that pure hyperelastic models only allow for monotonic loading of materials, do not reflect effects of viscoelasticity or hysteresis during cyclic loadings [108].

3.3.3 Plasticity models theory

The term plasticity is used to describe the elastoplastic behavior of a material that has been loaded beyond its yield strength, being permanently deformed after said load is removed [109].

As seen on the original probes and additional compressive test on Chapter 02, these were permanently deformed after they reached an engineering stress of 20-25 MPa, with highest values linked to compression than tension. Measured values are near or under the registered peak values for sacrifice components on commercially available TAA prosthesis [50] meaning that they could be permanently deformed during operation.

Even as early work on classical plastic theory for UHMWPE on orthopedic applications has found that expected permanent strains upon unloading are frequently overcalculated [110], the possibility of structural compromise, and the aim to identify a possible failure are enough for the use of non-linear models.

Although these models were formulated for metallic materials, these can be used on polymers. It should be considered that polymeric materials on large strain tend to exhibit both plastic and viscous effects, as implied by a rate-dependent material [111].

The first of the proposed constitutive models was the bilinear isotropic hardening (BIH) one (Figure 3.1), which has implicit a rate-independent plasticity. Isotropic hardening states that the yield surface of a material expands uniformly during plastic flow [107].

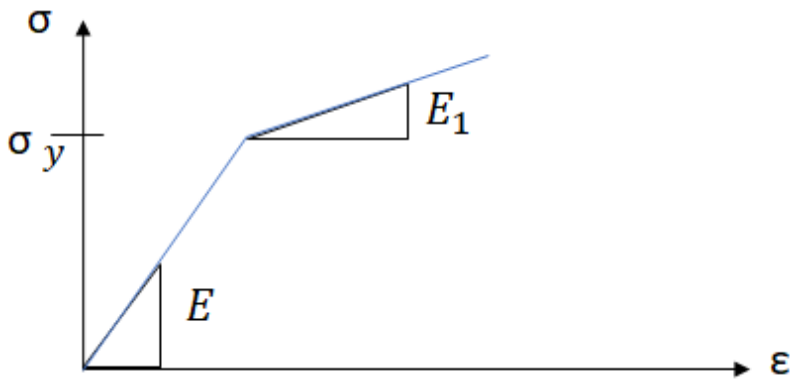

Figure 3.1. Uniaxial stress-strain curve for BIH model [107].

From the original data set, an abrupt change of the stress-strain curve slope can be observed. From this observation, the parameters for lineal elastic E, ν part are estimated. For the lineal plastic part, yielding stress $\sigma_y$and the tangent module are obtained on the same way. The tangent modulus cannot be less than zero (perfect plasticity case) nor greater than Young modulus [112].

All isotropic hardening plasticity models that are based on (non-zero) isotropic hardening will exhibit a gradual increase in the yield stress with increasing plastic strain [113].

Closely related, multilinear isotropic hardening model (MIH) uses the von Mises yield criterion with associative flow rule and isotropic hardening (Figure 3.2) According to von Mises, the material is assumed to yield when the equivalent stress is equal to the current yield stress for material [112].

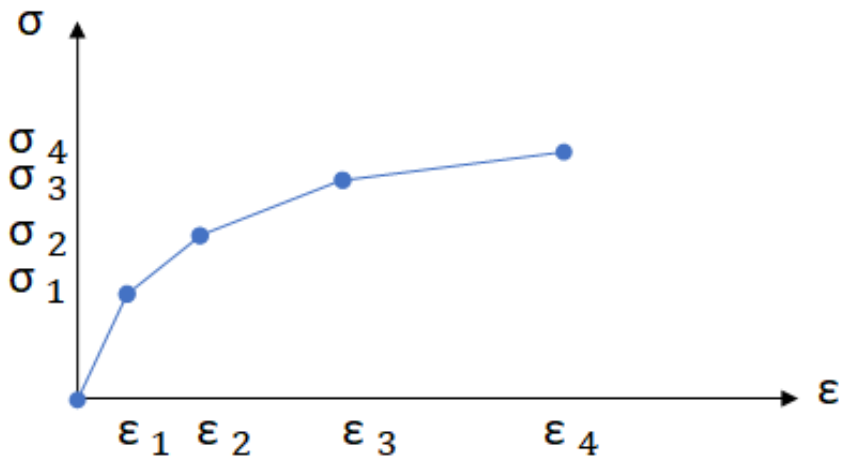

Figure 3.2. Uniaxial stress-strain curve for MIH model [107].

From stress-strain curve the parameters for lineal elastic part of model E, ν part are estimated. For the lineal plastic part, multiple yielding stress $\sigma_y$and the tangent module (using ANSYS nomenclature [107]) are calculated. The condition for its use on finite element is the need for each successive tangent modulus to be of a lesser value than the precedent [107].

Chaboche kinematic hardening (CKH) was the first material model to incorporate the strain range dependence of cyclic hardening [114], allowing for the superposition of several independent back stress tensors. CKH material model can be useful in modeling cyclic plastic behavior such as cyclic hardening or softening and ratcheting or shakedown [107].

3.3.4 Specialized polymeric models

One common denominator for the previous constitutive models is the need for certain restrictions for its application. Most of the reviewed models are most useful for monotonic loading, small or medium strain (under 30-50%), or are less reliable for cyclic analysis. From

the described physical characteristics of UHMWPE, it can be deduced that relationship of stress and strain on the most general cases should be modeled with more complex models.

As UHMWPE has the uttermost relevance for orthopedic applications, tailored constitutive models for similar polymers have been developed. Most of these specialized models are linear combinations of hyperelastic and viscous, non-linear models.

Arruda-Boyce (AB) material model is a hyperelastic constitutive model used to describe the mechanical behavior of rubber and other polymeric substances, based on the statistical mechanics of polymer chains on a representative volume using a supposition of incompressibility [115].

Rheological representation of Arruda-Boyce model is given on Figure 3.3.

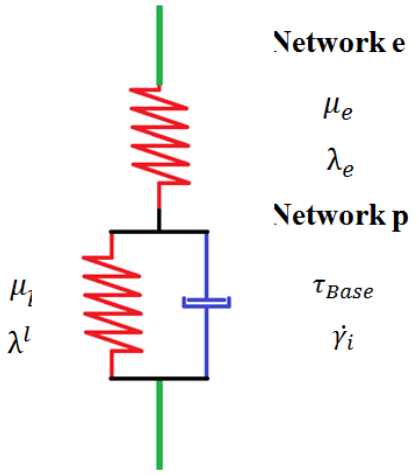

Figure 3.3. Arruda-Boyce (AB) rheological model.

Energy density is for AB model is given by Eq. 3.6

$$W = Nk_B\theta\sqrt{n}\left[\beta\lambda_{chain} - \sqrt{n}\ln\left(\frac{sinh\beta}{\beta}\right)\right] \tag{3.6}$$

Which can be expressed in an alternative form using the five terms of the inverse Langevin function [101,109].

$$W = C_1\left[\frac{1}{2}(I_1 - 3) + \frac{1}{20\lambda_m^2}\left({I_1}^2 - 9\right) + \frac{11}{1050\,\lambda_m^4}\left({I_1}^3 - 27\right) + \frac{19}{7000\,\lambda_m^6}\left({I_1}^4 - 81\right) + \frac{519}{673750\,\lambda_m^8}\left({I_1}^4 - 243\right)\right] \tag{3.7}$$

Being a better suited function for numerical solution [107]

In other idea, Bergström Boyce (BB) material model is a phenomenolical based, highly nonlinear material model used for elastomers, allowing for nonlinear stress-strain relationship, creep and rate dependence [107,116]. The rheological model is built by two connected networks, as seen on Figure 3.4.

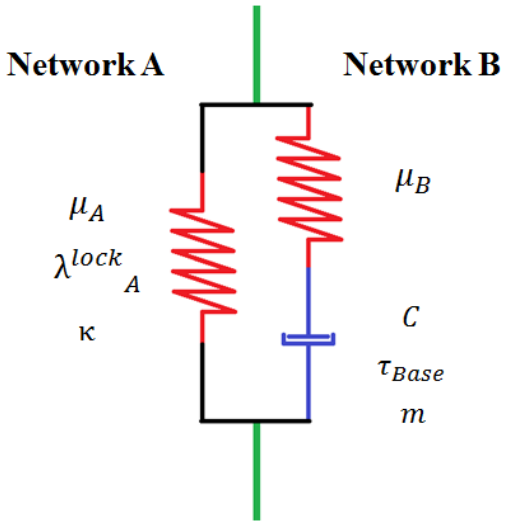

Figure 3.4. Bërgstrom-Boyce (BB) rheological model.

Stress in Network A is given by the Eq.3.8.

$$\sigma_A = \frac{1}{J^e}\frac{\mu_A}{3}\frac{L^{-1}\left[\frac{\overrightarrow{\lambda_A}}{\lambda_A^{lock}}\right]}{\frac{\overrightarrow{\lambda_A}}{\lambda_A^{lock}}} dev[\bar{B}_A^*] + \kappa[J^e - 1]I \tag{3.8}$$

While stress in Network B is calculated by Eq.3.9

$$\sigma_B = \frac{1}{J_B^e}\frac{\mu_B}{3}\frac{L^{-1}\left[\frac{\overrightarrow{\lambda_B^{e*}}}{\lambda_B^{lock}}\right]}{\frac{\overrightarrow{\lambda_B^{e*}}}{\lambda_B^{lock}}} dev[\bar{B}_B^{e*}] + \kappa[J_B^e - 1]I \tag{3.9}$$

Where $\bar{B}_i^*$ and $\overrightarrow{\lambda_A}$ depend on deformation gradient tensor F:

$$(J^e)^{-2/3}FF^T \tag{3.10}$$

$$\sqrt{tr[\bar{B}_i^*/3]} \tag{3.11}$$

The total stress response is obtained from the sum of both [116]. Viscous deformation of the model can be obtained from Eq. 9.

$$F^p = \left[F^{e\,-1}\right]F \tag{3.12}$$

Finally, the Three Network Model (TNM) was developed to cope with thermoplastics simulation. The microstructure of the material is represented with three structural domains (Figure 3.5) intended to capture a non-linear, time and temperature dependent response of a material [99].

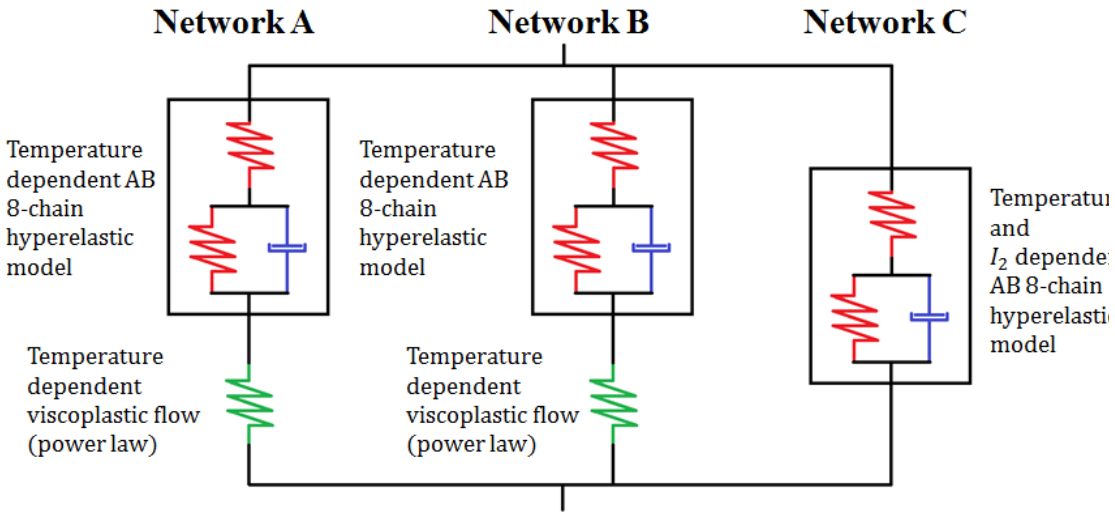

Figure 3.5. Three Network Model (TNM) rheological model.

Stress state is calculated for each network with the following mathematical expressions (Eq. 3.13-15):

$$\sigma_A = \frac{1}{J_A^e}\frac{\mu_A}{\overline{\lambda_A^e}}\left(1+\frac{\theta-\theta_0}{\hat{\theta}}\right)\frac{L^{-1}\left[\frac{\overrightarrow{\lambda_A}}{\lambda_A^{lock}}\right]}{L^{-1}\frac{1}{\lambda_A^{lock}}}dev[\bar{B}_A^*]+\kappa[J_A^e-1]I \tag{3.13}$$

$$\sigma_B = \frac{1}{J_B^e}\frac{\mu_B}{\overline{\lambda_B^e}}\left(1+\frac{\theta-\theta_0}{\hat{\theta}}\right)\frac{L^{-1}\left[\frac{\overrightarrow{\lambda_B}}{\lambda_B^{lock}}\right]}{L^{-1}\frac{1}{\lambda_B^{lock}}}dev[\bar{B}_B^*]+\kappa[J_B^e-1]I \tag{3.14}$$

$$\sigma_C = \frac{1}{1+q}\left[\frac{\mu_C}{J\lambda^{lock}}\left(1+\frac{\theta-\theta_0}{\hat{\theta}}\right)\frac{L^{-1}\left[\frac{\overrightarrow{\lambda_B}}{\lambda^{lock}}\right]}{L^{-1}\frac{1}{\lambda^{lock}}}\right]dev[\bar{B}^*\,] + \kappa[J_A^e-1]I + q\frac{\mu_C}{J}\left[I_1\ \bar{B}^*\ -\frac{2I_2}{3}I-(\bar{B}^*\,)^2\right] \tag{3.15}$$

The effective deviatoric flow rate is given by the following power-flow equations (Eq. 3.16-3.17)

$$\dot{\gamma}_A = \dot{\gamma}_0\left(\frac{\tau_A}{\widehat{\tau_A}+aR(p_A)}\right)^{m_A}\left(\frac{\theta}{\theta_0}\right)^n \tag{3.16}$$

$$\dot{\gamma}_B = \dot{\gamma}_0\left(\frac{\tau_A}{\widehat{\tau_B}+aR(p_B)}\right)^{m_B}\left(\frac{\theta}{\theta_0}\right)^n \tag{3.17}$$

3.4. Material model adjustment for tensile test

As seen on Chapter 2, UHMWPE can be greatly elongated during a tension test. Even if projected application would be on compression rather than tension, this possibility should not be discarded, and thus the correspondent material model adjustment is done.

General shape of sample is shown on Figure 3.6, where the distinction among the working zone and fixing zone is cleared.

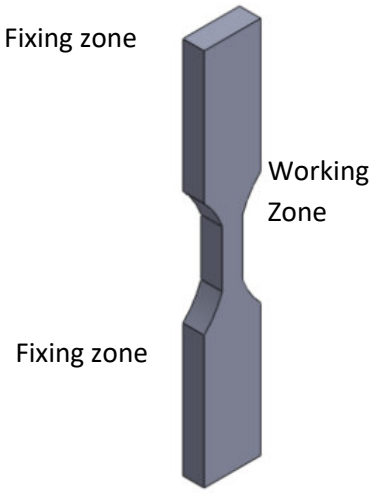

Figure 3.6. Tensile sample geometry.

Dimensions are referred as the ones of a V Type Probe for ASTM D638M Standard Test Method for Tensile Properties of Plastics [76]. Effective working zone length is of 9.53 *mm*.

For the numerical discretization of the domain, geometry allows the use of a swept mesh, with SOLID185 hexaedrical elements, as shown on Figure 3.7 below:

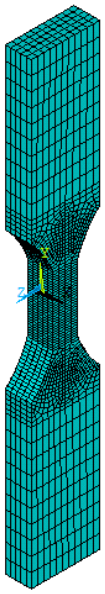

Figure 3.7. Finite element tensile sample.

The FEA model for tensile probe has 21422 nodes and 4285 elements. The narrower part of the probe is the most relevant, being meshed with more densely packaged elements. Results will be referred to its gravity center.

In equivalence to the conditions present during tensile test, the chose boundary conditions (Figure 3.8) were a fixed support on the lower fixing zone, while the facets of the upper fixed zone were displaced on axial direction 1.9 mm, thus indicating a 20% strain. This was related with an abrupt shift on stress-strain curve slope on experimental data.

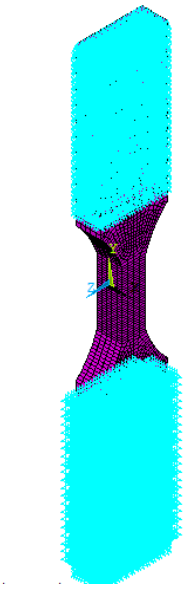

Figure 3.8. Tensile sample boundary conditions.

Eight stress values corresponding with equidistant strain are chosen from the stress-strain curves and averaged. Then, the probe closer to the average (ED-11) is evaluated as the most representative and the linked stress-strain values are used for material model fitting. Table 3.1 resumes data.

Table 3.1. Tensile test data for adjustment (20%).

Time (s)	Load (N)	Displacement (mm)	Engineering Strain (mm/mm)	Engineering Stress (MPa)
1.91	106.76	0.24	0.02	8.59
3.82	171.91	0.48	0.05	13.84
5.01	199.75	0.63	0.07	16.08
8.68	251.95	1.08	0.11	20.28
10.00	262.47	1.25	0.13	21.13
11.73	272.41	1.46	0.15	21.93
13.25	278.51	1.65	0.17	22.42
15.00	282.78	1.91	0.20	22.77

3.4.1 Linear elastic models results for tension

UHMWPE as a material manifests a lot of non-linearities on the chosen adjustment range. However, a linear elastic (LE) model could be used when expected strain is minimum. For this approach, the selection of equally distanced points for strain under 5% and the consequent regression revealed a Young modulus value $E = 256.82\ MPa$ (Table 3.2)

Table 3.2. Tensile test data for small strain adjustment (5%).

Time (s)	Load (N)	Displacement (mm)	Engineering strain (mm/mm)	Engineering stress (MPa)	LE stress (MPa)
0.60	40.51	0.10	0.01	3.26	1.99
1.55	89.38	0.19	0.02	7.20	5.08
2.49	130.27	0.29	0.03	10.49	8.38
3.21	154.16	0.38	0.04	12.41	10.79
3.93	174.76	0.48	0.05	14.07	13.21

Another advantage for this approximation is that tension and compression have equivalent stress values for the same present strain, as seen on respective Figure 3.9. The main drawback on this model choice is the restriction of a maximum available strain of 5% for any UHMWPE component in prosthesis.

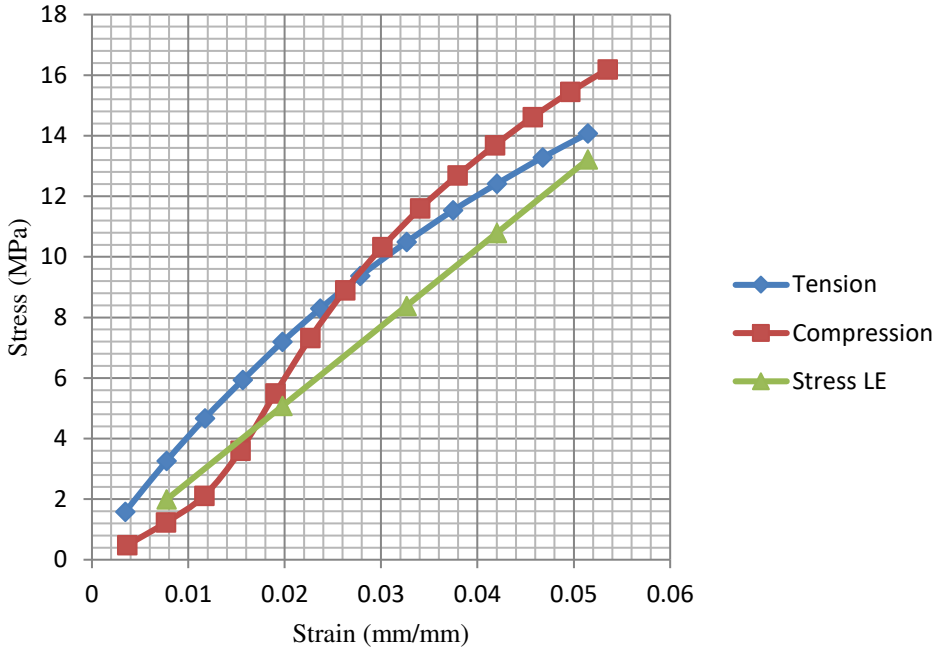

Figure 3. 9. Stress-strain curves for small strain in tension and compression (5%).

In contrast, average error is high (21.54%), with a higher bias on the smaller strain points for tension and higher strain points of compression.

3.4.2 Hyperelastic model results for tension

As many hyperelastic models were available, multiple fits could be achieved with any of the aforementioned models. It was found that a third order polynomial model (POL-3) and two Mooney-Rivlin models with 3 and 9 parameters (MR-3, MR-9, respectively) ones had the best fit. Related parameters are registered on Table 3.3. Results are evaluated on Figure 3. 10 and Table 3.4.

Table 3.3. Estimated parameters for hyperelastic models.

POL-3		MR-3		MR-9	
Parameter	Value	Parameter	Value	Parameter	Value
C10	-7.8378E+008	C10	-3.83E+08	C10	-7.8378E+008
C01	8.6694E+008	C01	4.55E+08	C01	8.6694E+008
C20	2.1935E+010	C11	1.38E+08	C20	2.1935E+010
C11	-4.6333E+010	d	0	C11	-4.6333E+010
C02	2.5205E+010			C02	2.5205E+010
C30	1.1826E+006			C30	1.1826E+006
C21	-1.6145E+007			C21	-1.6145E+007
C12	-5.3992E+009			C12	-5.3993E+009
C03	3.1543E+009			C03	3.1544E+009
d_1	1E-012			d	1E-012
d_2	1E-012				
d_3	1E-012				

Table 3.4. Experimental data vs Simulation results (hyperelastic models).

Engineering Strain (mm/mm)	Engineering Stress (MPa)	POL-3 stress (MPa)	MR-3 stress (MPa)	MR-9 stress (MPa)
0.02	8.59	5.3907	6.0861	6.3324
0.05	13.84	9.9458	11.248	9.9445
0.07	16.08	14.73	12.61	12.398
0.11	20.28	18.168	18.316	16.698
0.13	21.13	22.845	21.029	19.798
0.15	21.93	21.482	23.398	22.244
0.17	22.42	22.763	25.367	23.409
0.20	22.77	24.144	26.684	24.14

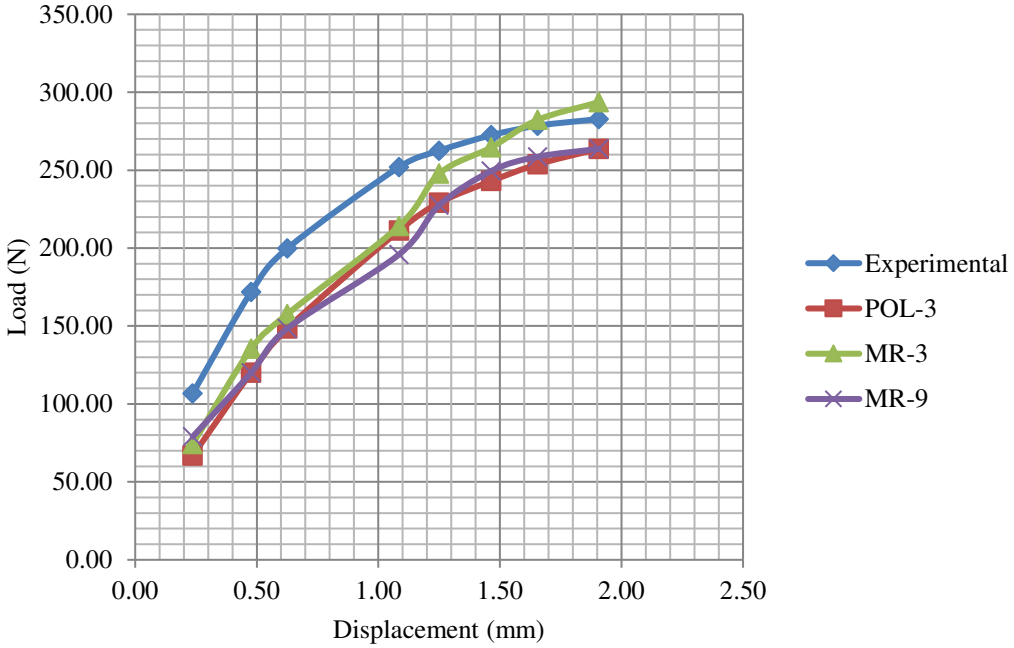

Figure 3.10. Experimental data vs Simulation results (hyperelastic models).

Corresponding average error is 12.75% for POL-3, 14.59% for MR-3 and14.15% for MR-9, any of them being useful for describing stress-strain relationship on UHMWPE on a uniaxial tensile test.

3.4.3 Plastic models results for tension

The evaluation of the three available plastic models was done. During numerical simulation, both bilinear isotropic hardening (BIH) and Chaboche kinematic hardening (CKH) model came to instability due high element distortion. Consequently, the FEA was interrupted and only partial results were analyzed on Table 3.5 and Figure 3.11.

Table 3.5. Experimental data vs Simulation results (plastic models).

Engineering Strain (mm/mm)	Engineering Stress (MPa)	BIH stress (MPa)	MIHstress (MPa)	CKH stress (MPa)
0.02	8.59	3.72	2.06	3.71
0.05	13.84	5.77	3.86	5.77
0.07	16.08	8.2	4.79	8.19
0.11	20.28	13.03	6.51	13.02
0.13	21.13	15.37	7.09	16.25
0.15	21.93	X	7.51	X
0.17	22.42	X	7.91	X
0.20	22.77	X	8.025	X

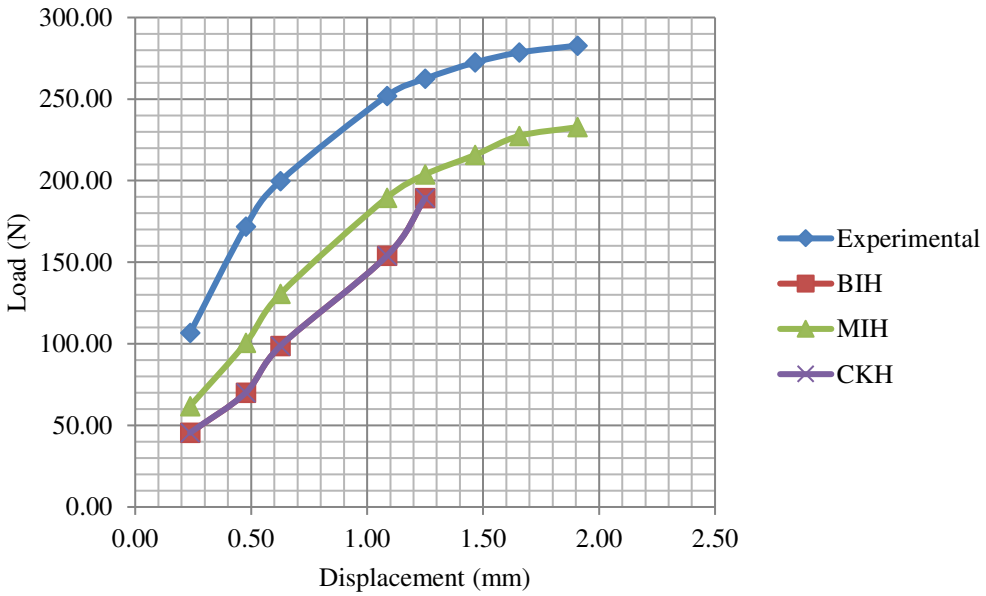

Figure 3.11. Experimental data vs Simulation results (plastic models).

Apparently, MIH is closer than other models. In spite of this, estimated average error is of 68.49%, too high for any practical use. The overall conclusions of these sections show that in tension hyperelastic effects are dominant on the material.

3.4.4 Specialized polymeric model results for tension

In order to test these specialized polymeric models, the tension, compression and relaxation test available data was used to fit the model. First ones were obtained from the use of software MCalibration®, and so was the codification for each model for ANSYS15®.

The material model for Arruda-Boyce (AB) model is implemented in ANSYS15® with the parameters shown on Table 3.6. For Bergström-Boyce (BB) model, used codification is shown on Table 3.7:

Table 3.6 Calculated AB parameters.

Parameter	Value
C_1	64.73
λ_μ	3.2359 E 07
d	0

Table 3.7. Codification for BB model in ANSYS.

Codex line	Physical interpretation
TB, BB, 1, , , ISO	!Activate ISO table for Bërgstrom-Boyce data
TBDATA, 1, 5.72e6	!Shear modulus muA
TBDATA, 2, 100	!Define material parameter N0=(lambdaAlock)2
TBDATA, 3, 1.18e8	!Shear modulus muB
TBDATA, 4, 100	!Define N1=(lambdaBlock)2
TBDATA, 5, 2.8e-123	!Define material parameter
TBDATA, 6, 0	!Define material parameter c
TBDATA, 7, 16.29	!Define material parameter m
TB, BB, 1, , , PVOL	!Activate table PVOL for Bërgstrom-Boyce data
TBDATA, 1, 1.25e-9	! 1/K, being K Bulk modulus

As BB was intended for modeling UHMWPE both in tension and compression, the parameters will be the same for the correspondent adjustments.

AB results for tension could not be achieved due numerical instability, so only BB model results are declared on subsequent Table 3.8 and Figure 3.12.

Table 3.8. Experimental and numeric stress values. BB model.

Engineering Strain (mm/mm)	Engineering Stress (MPa)	BB stress (MPa)
0.02	8.59	3.5
0.05	13.84	8.5185
0.07	16.08	10.2
0.11	20.28	18.474
0.13	21.13	19.99
0.15	21.93	24.59
0.17	22.42	24.586
0.20	22.77	27.241

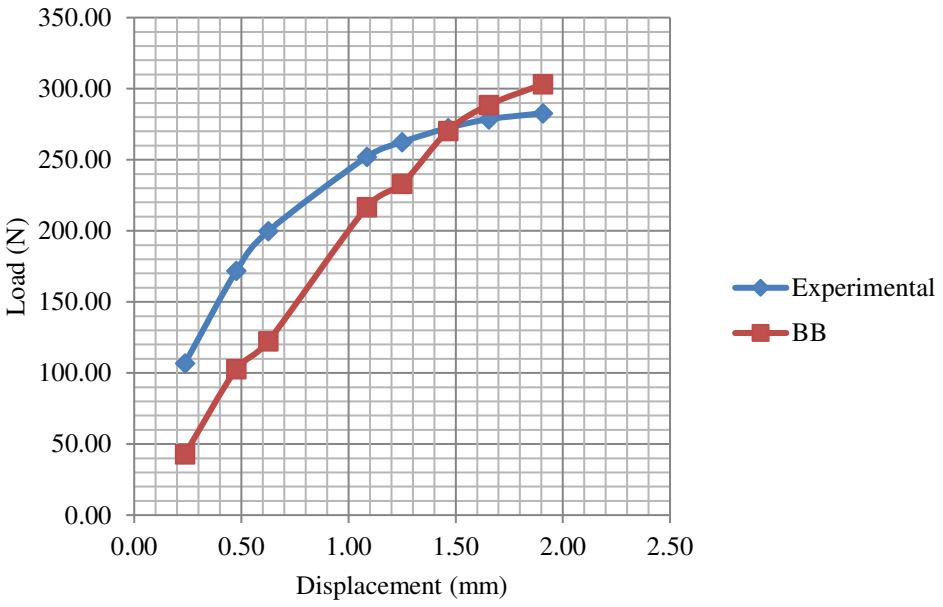

Figure 3.12. Experimental data vs Simulation results (BB).

Average error for BB model is of 29.72%. This value is higher than that of previous models and is slightly more time-consuming. By the other hand, the adjustment of compression test data could give a better insight of the model programming and performance.

3.5. Material model adjustment for compressive test

As seen on Figure 3.13, the probe has a square base with an edge of 12.7 mm and a height of 25.4 mm, based on ASTM D695 Standard Test Method for Compressive Properties of Rigid Plastics [77]. This geometry allows the use of a swept mesh, with SOLID185 hexaedrical elements [107], having a highly regular distribution, with 9581 equidistant nodes and 2000 elements.

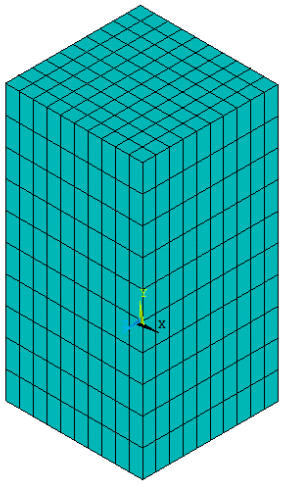

Figure 3.13. Finite element compression sample.

For the chosen boundary conditions, the bottom surface of the probe was fixed, and a vertical displacement applied to the upper surface (Figure 3.14). The final displacement of the upper face is of $7.62\ mm$, allowing for an engineering strain of 0.30 in axial direction. Strain rate of test is fixed and was calculated at $6.6\text{x}10^{-4}s^{-1}$.

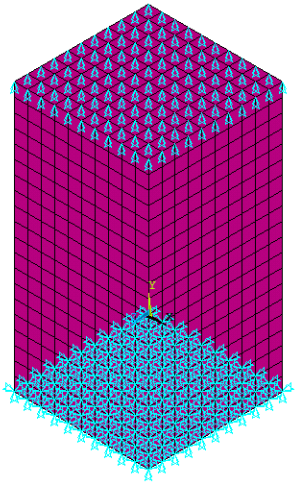

Figure 3.14. Compression sample boundary conditions.

Seven stress values corresponding with equidistant strain are chosen from the stress-strain curves and averaged. Then, the probe closer to the average is evaluated as the most representative and the linked stress-strain values are used for material model fitting.

Table 3.9 summarizes the reference information related to PB-03 probe.

Table 3.9. Compression test data for adjustment (30%).

Time (s)	Load (N)	Displacement (mm)	Engineering Strain (mm/mm)	Engineering Stress (MPa)
6.03	117.40	0.254	0.01	0.71
54.01	2403.76	1.27	0.05	14.45
114.03	3622.79	2.54	0.10	21.77
173.98	4339.72	3.81	0.15	26.08
234.01	5076.17	5.08	0.20	30.51
294.05	5832.41	6.35	0.25	35.05
354.03	6502.67	7.62	0.30	39.08

The data is registered only to a compressive strain of 0.30, just before rotation of the probe was observed. As a logical consequence, the use of the derived material models will be valid until the strain limit is surpassed.

This inconvenience is diminished as the model is intended to simulate permanent joint prosthesis models that cannot be excessively deformed by several reasons, such as anatomical restrictions of bones and soft tissues

Results are reported in aggregated graphs and tables for an easier comparison.

In each case, the simulations had the expected results, with a relatively uniform stress distribution excluding maximum peaks on the lower corners, as is in intended from the test probe geometry. A true-scale sample of the probe geometry deformation and the corresponding near-uniform stress distribution at the end of the compression test is shown on Figure 3.15.

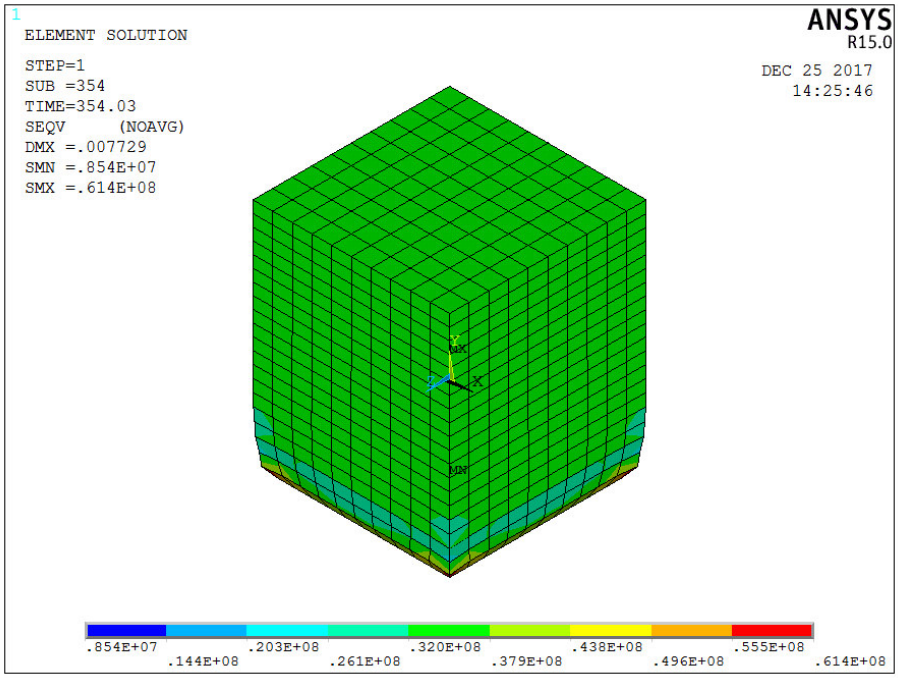

Figure 3.15. Von Mises Stress final state for compression probe (LE).

Specific load-displacement curves and Tables featuring measured stresses at the geometric center of probe are provided.

3.5.1 Linear elastic models results for compression

In certain controlled situations, such as very small strains, absence of thermal effects and monotonic loads, the use of linear elastic (LE) model is considered valid for UHMWPE [93,95] so, this model was taken on consideration for simulation.

The choice of a linear model for a highly non-linear behavior can be justified also as being a mean to find the maximum strain on which non-linear effects are dominant for UHMWPE in compression

As a linear approximation, it should be reminded that a lot of essential mechanical properties of UHMWPE are missing, such as the viscoelastic ones. In this idea, relaxation and creep tests done in previous work is reported.

Following similar test conditions, a compression probe was subject to a load slowly applied at a fixed strain rate of $0.008s^{-1}$, enough to cause 5% of strain and an initial stress of 18 MPa. Then the probe was allowed to relax for 2000 s.

Acquired experimental relaxation curve from a representative sample is shown on Figure 3.16:

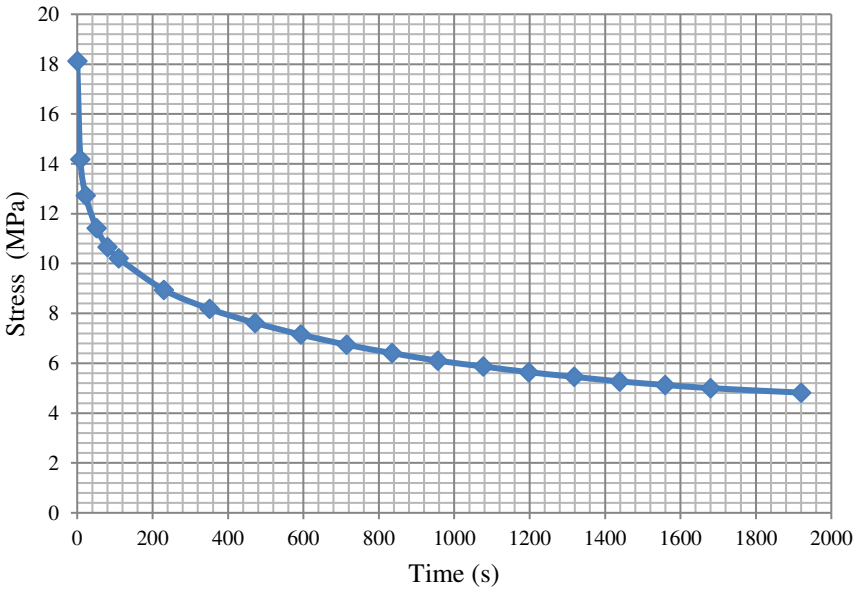

Figure 3.16. Relaxation curve of a compression sample.

A better representation of UHMWPE behavior on LE models is feasible by the addition of viscoelastic effects [102]. These material properties can be represented by springs and dampers in parallel or in series [117]. Prony Series have been used in an efficient numerical method in the time domain to relate relaxation and creep function on UHMWPE and similar polymers [118]

From the curve adjustment of ANSYS ® Mechanical APDL, it was found that seven Prony terms are required for a valid fit of relaxation curves (as shown on Table 3.10)

Table 3.10 Calculated Prony terms for shear and bulk response.

Prony term	Shear response	Bulk response
a1	0.12	1.27E-06
t1	841.11	0.61
a2	0.10	1.22E-06
t2	3.80	789.00
a3	0.11	0.34
t3	841.14	793.75
a4	0.08	0.01
t4	3.79	43005.00
a5	0.13	0.19
t5	23.24	60.90
a6	0.13	0.01
t6	98.90	43005.00
a7	0.10	0.23
t7	841.13	5.30

Then, the original LE model is added with a generalized Maxwell solid formulation [18] and so it will reflect the relaxation observed for GUR1050. Thus, the new material model is labeled as linear elastic with relaxation (LER).

Relaxation tests also showed that the material could recover completely from a compression strain of 5% after a period of 24 hrs.

Both experimental stress values and the ones calculated on simulations are shown on Table 3.11.

Table 3.11. Experimental data vs. Simulation results (linear elastic models).

Engineering Strain (mm/mm)	Experimental stress (MPa)	LE stress (MPa)	LER stress (MPa)
0.01	0.71	0.65	0.57
0.05	14.45	5.81	4.14
0.10	21.77	12.27	7.95
0.15	26.08	18.73	11.38
0.20	30.51	25.19	14.71
0.25	35.05	31.65	17.82
0.30	39.08	38.11	20.80

As the material model fit was made with stress-strain curve, the evaluation of mean error will be made with the measured experimental load the force reaction of the fixed end of the simulation model for each assigned strain value.

As seen on Figure 3.17, the estimated mean error is about 28.00 % for LE model, with the immediate conclusion that a lineal elastic model is not enough to reflect the material behavior on the actual work conditions.

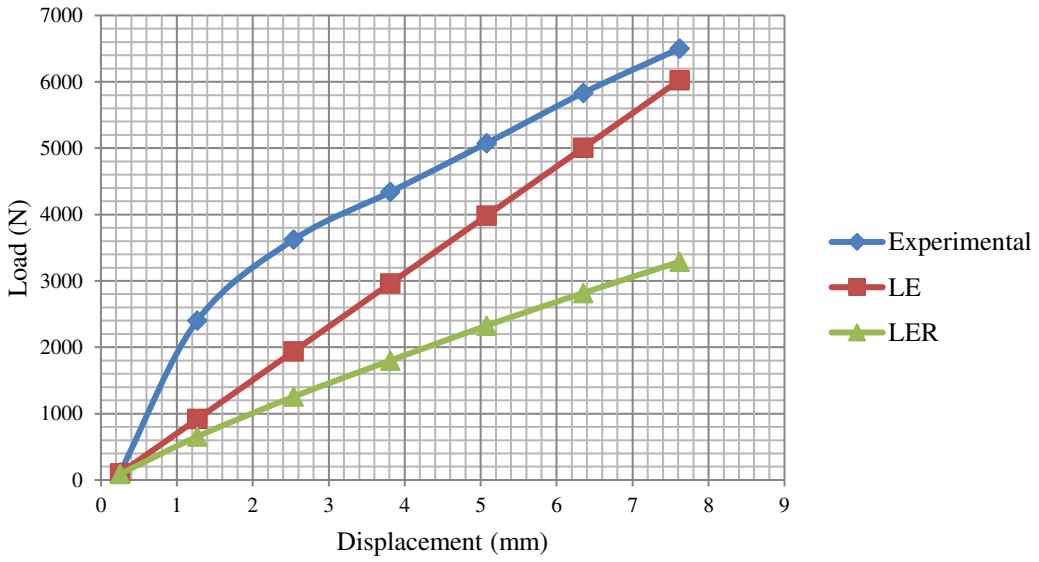

Figure 3.17. Experimental data vs Simulation results (Linear elastic models).

The estimated mean error for LER model is about 53.51%, thus it can be inferred that in the actual test conditions and strain levels, viscoelastic effects are negligible.

3.5.2. Hyperelastic models results for compression

A five-parameter Mooney-Rivlin (MR-5) material model was successfully fitted on the original data. However, the generated material model is of a great instability, and no simulation was completed before finding a pivot warning on numerical solving.

It was found that hyperelastic models for UHMWPE work much better on tension rather than compression. It is also stated than additional test results such as biaxial, shear, and volumetric stress-strain response should have been carried to give a better, more stable fit [107].

3.5.3 Plastic models results for compression

First tested plastic model was bilinear isotropic hardening (BIH) one. The needed parameters for lineal elastic information are estimated as $E = 289\ MPa$; $\nu = 0.46$. For the lineal plastic part, yielding stress is $\sigma_y = 14.15\ MPa$ and the tangent module $E = 95MPa$.

It should be noted that an abrupt change in stress-strain curve slope does not necessarily indicate the yielding point. However, loading and unloading tests described on Chapter 02 support the idea.

From early results, it was found that certain plastic models needed more accurate data on the lower levels of strain. Complementarity test data of Table 3.12 was used for the use of a multilinear isotropic hardening model (MIH) fit.

Table 3.12. Compression test additional data.

Time (s)	Load (N)	Engineering Strain (mm/mm)	Engineering Stress (MPa)
6.03	117.40	0.01	0.71
18.03	568.36	0.02	3.42
30.04	1395.43	0.03	8.39
41.99	1977.96	0.04	11.89
54.01	2403.76	0.05	14.45

Taking both sets of values on Tables 3.9 and 3.12, the instantaneous Young Modulus was calculated. These should be consecutively smaller in order to work on the running simulation. Legacy element SOLID45 was used in order to support the material model [107].

Measured stress values for plastic models are shown on Table 3.13. Calculated and experimental load curves are shown on Figure 3.18.

Table 3.13. Experimental data vs Simulation results (plastic models).

Engineering Strain (mm/mm)	Experimental stress (MPa)	BIH stress (MPa)	MIH stress (MPa)	CKH stress (MPa)
0.01	0.71	1.55	0.93	1.53
0.05	14.45	13.84	14.08	13.73
0.10	21.77	19.48	22.16	17.35
0.15	26.08	24.61	27.00	20.52
0.20	30.51	29.88	32.00	23.67
0.25	35.05	35.05	35.05	26.82
0.30	39.08	40.22	35.05	29.95

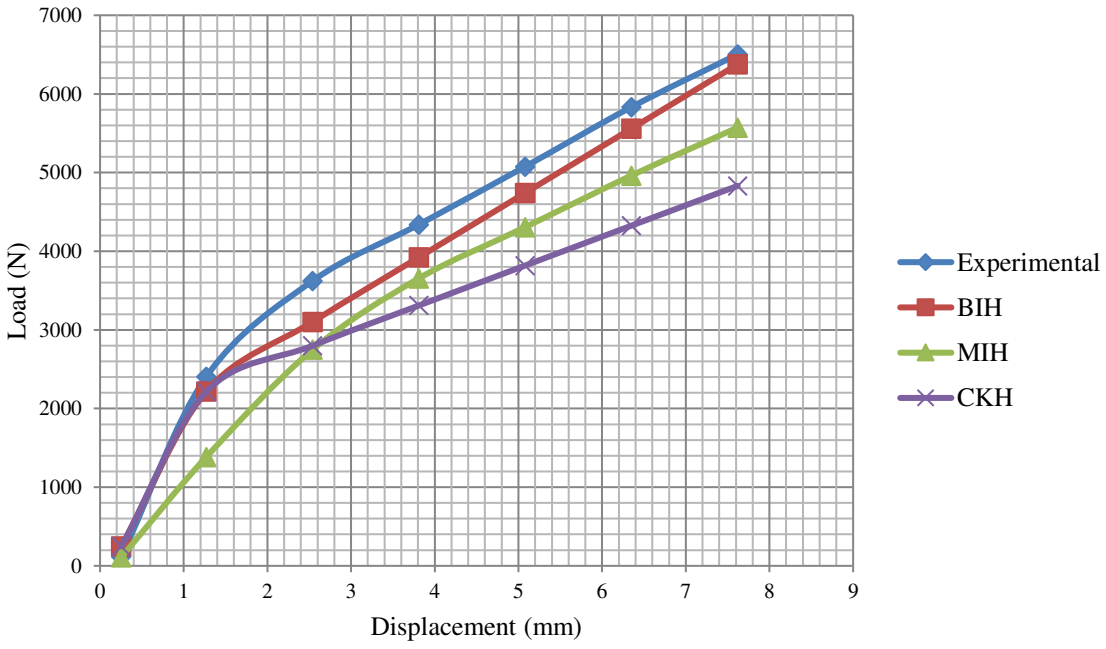

Figure 3.18. Experimental data vs Simulation results (plastic models).

BIH model has a seemingly good match with test data. Even if at first the fit seems much closer, the estimated error is about 20.10 %, lesser than any of the previous models, but still not desirable for use in design.

A closer look on the error distribution, it is seen that the first lineal part has an estimated stress value of twice the measured one, that being responsible of the great margin of error. However, this value drops drastically with the strain.

Taking only the plastic part of stress-strain curve, fit has a margin of error of 04.23%, acceptable for use.

By the other hand, load estimation of MIH had a distributed mean error of 19.04 %, but has a noticeable drop at the estimated reaction force on the higher levels of strain.

The results for the last model show a great discrepancy (average error of 34.42%) and thus the inadequacy of using CKH model. Even so, it can be concluded that plastic models are a better approach for the compressive test and problems with similar boundary conditions.

3.5.4 Specialized polymeric results for compression

More robust material models based on the molecular mechanisms of UHMWPE and other rubber-like polymers are available and were also tested on this work. Table 3.14 and Figure 3.19 summarize the information.

Arruda-Boyce (AB) and Bergstöm-Boyce (BB) model are implemented in ANSYS15® with the respective code shown on the Table 3.7.

Table 3.14. Experimental data vs Simulation results (specialized polymeric models).

Engineering Strain (mm/mm)	Experimental stress (MPa)	AB stress (MPa)	BB stress (MPa)
0.01	0.71	0.70	1.97
0.05	14.45	6.68	17.84
0.10	21.77	15.45	37.37
0.15	26.08	26.71	42.04
0.20	30.51	42.15	43.50
0.25	35.05	64.60	45.09
0.30	39.08	99.05	46.85

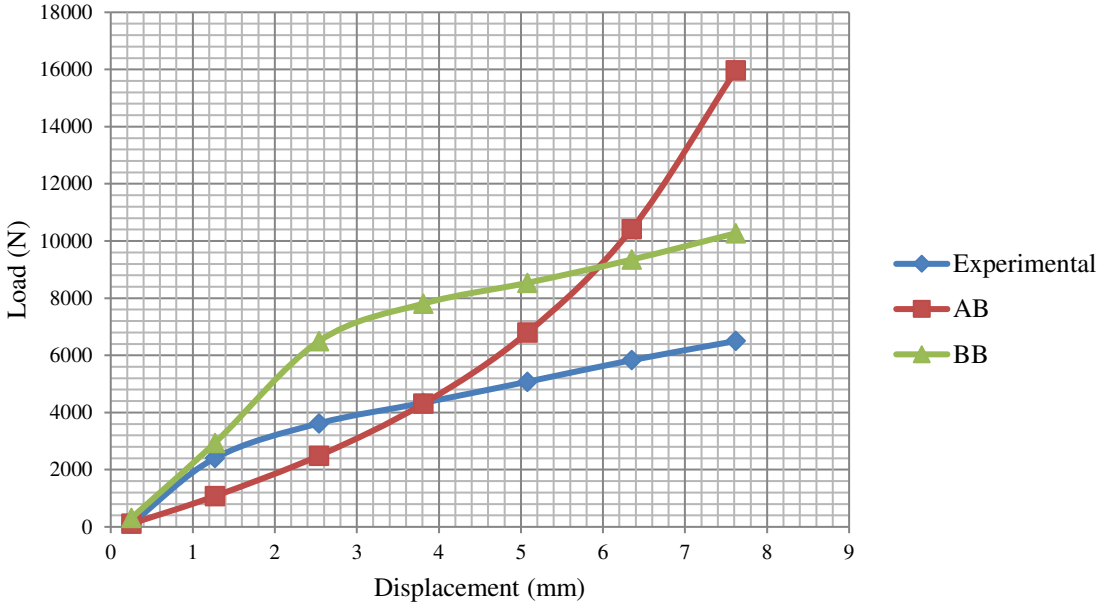

Figure 3.19. Experimental data vs Simulation results (specialized polymeric models).

From the comparison, it is clear that the AB fit is not near to the original data, having a mean error of 49.81 % and a clear load overcalculation trend for a large deformation. For BB model it is seen that stress is heavily over calculated, even when the qualitative trend of it is similar. Mean error is estimated as 76.39 %.

During the first iterations, the origin of this value difference was looked on coding issues, incompatibility, lack of unit consistency, and wrong parameter assignment. However, those were discarded as error sources.

Overall results of these specialized rheological models show that compression and relaxation data must be complemented with additional tests for a better fit, including changes on load rate and biaxial tests. Absence of data on thermal effects on UHMWPE behavior could have influenced on the inconsistencies, especially for BB, in which thermodynamical consistency of the internal material evolution law is needed for a valid numerical solution [119], even when project application would not allow for an ample range of thermal variation.

3.6. Discussion

Parting from the fact that many constitutive equation models had been attempted on literature, it should be addressed that UHMWPE behavior has different approximations depending on the available working conditions, with emphasis on the search of more robust models which could be less restrained by this limitations, especially on a polymer of such interest in bioengineering and medicine applications.

As the main interest of this work is the development and design of a TAA prosthesis, the approached solution attempted was the use of one or many simple models available for dissociated possible loading conditions (tension and compression). Certain additional restrictions then should be added for design in GUR1050 components in order to keep the material model as valid and thus the obtained results significant as future development.

Most of evaluated models had a qualitative behavior that showed coincidence with the general trend of stress and strain relationship on experimental data. Mean average error was used as a quick comparison parameter among constitutive material models.

The overall high mean errors reported on the previous sections show discrepancy of simulation results and experimental data. Additionally, the distribution of error is almost uniform on models probed on tension. In contrast, models tested on compression are much closer on predictions on lower strain values (< 0.1) and the error increases above that limit, with the material model failure for increased strain (0.2 on tension, 0.3 on compression). This could impose a closer range of allowed strain on a possible mechanical solution on TAA design. As the ankle joint previously generates a strict restriction on displacements and deformation, there is not concern for excessive parameters restriction.

Inquiringly, the more complex models did not show better results in terms of quantitative results, with stress lectures much higher than the experimental ones. These required multiple data sets of different test on multiple load rates for a better adjustment. Obtained results seems to imply a better fit of a rather simple model on the test conditions applied on samples. The main implication is that chosen material models should be used on similar conditions during simulation. However, from the anatomical review done on Chapter 1, the later

conditions are closer to be ones expected to be found on TAA prosthesis operation, with a predominance of an axial load and compressive effects. An additional positive side effect of a simpler material model choice is the possibility of use on complex design geometry on UHMWPE while keeping a low demand on computational resources.

By the other side, if the use of a model that reports a higher stress value still could add to the safety factor of the design, while being detrimental in case of optimization of polymeric inserts. The choice was to reject completely the use of these, at least without additional sample testing.

Being the model with the better performance, and being closer to the intended operation conditions for TAA prosthesis, bilinear isotropic hardening (BIH) model was studied with additional data (Table 3.15, Figure 3.20)

Table 3.14. Data for revisited BIH model

Engineering Strain (mm/mm)	Experimental stress (MPa)	BIH stress (MPa)
0.010	0.71	1.55
0.025	8.38	7.80
0.050	14.45	13.84
0.075	19.60	19.24
0.100	21.77	19.48
0.125	24.40	21.52
0.150	26.08	24.61
0.175	28.70	26.53
0.200	30.51	29.88
0.225	33.30	31.28
0.250	35.05	35.05
0.275	37.60	36.35
0.300	39.08	40.22

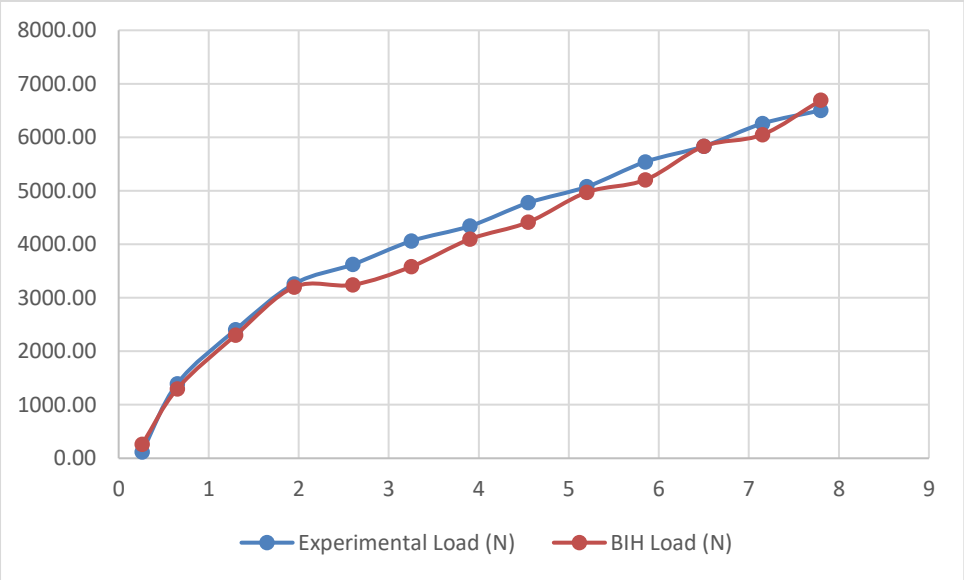

Figure 3.20. Experimental data vs Simulation results (revisited BIH model).

New estimated average error is 13.94 % Excluding the first atypical value, it falls to 5.24%

3.7. Chapter conclusions

UHMWPE is an important material family especially in biomechanics. This implies that some specific considerations must be taken while modeling it in order to correctly reflect its unique properties and behavior.

In order to find the best fit for a given set of data obtained from a GUR1050 sample tension and compression test, multiple material models were adjusted and simulated.

In general, stress values obtained by simulation are not so close to the experimental data. As the testing conditions are heavily controlled, some simplifications were at first considered as valid but showed as being excessive.

Linear elastic models are not useful for mimicking GUR1050 behavior unless strain is very low (under 5% at least), load being monotonic and the strain rate not very low. Caution is advised for the use of this model, mostly recommended for small UHMWPE components on an assemble on which they have a small role.

For the more complex models, such as hyperelastic or specialized rheological, limited data was a drawback that affected the possible implementation for the simulation model, even when thermal effects were not taken in consideration. In spite of this, hyperelastic models have a close fit to the behavior of UHMWPE on tension.

Plasticity is an effect that should be taken in consideration for a strain up to 0.2 on tension and 0.3 on compression with the implications of a security limit for design in polyethylene

From the results, the use of a third order polynomial (POL-3) model is recommended for tension under a constant strain rate. Bilinear isotropic hardening (BIH) model is recommended as it was found as the best fit for GUR1050 in compression under a constant strain rate. As the intended application for an implant inside a constrained joint, it is expected to have a predominantly compressive behavior of the prosthesis component, the later model is closer for the intended material behavior if a numerical model is applied.

The obtained models are intended for some quick analysis of complex geometries on moderate strain.

Chapter 4- Early designs for a damping system on total ankle joint prosthesis

Iteration in design is a common occurrence. Generated solutions for a particular problem must be tested for feasibility and efficiency.

During the brainstorming for a compatible damping system for sacrifice component of a total ankle replacement prosthesis, at least two promising ideas were developed and tested by means of finite element analysis.

First attempt for obtaining this characteristic was the use of a damping fluid -either liquid or gas- interacting with the solid inner surface of complex chamber structures inside the sacrifice component model, causing drag and improvement on energy dissipation.

Second attempt also required the use of inner structures in honeycomb cell patterns with inherent negative stiffness, enabling a large amplification of their damping and recoverability capabilities within a limited space.

For both cases, obtained results could not stand with designment requirements and limitations for a safe operation within the human ankle joint. Even so, these results can have other potential applications and are made available, and the design findings were used on the definitive process.

4.1 Introduction

In physical systems, damping is produced by processes that dissipate the energy stored in them [120], generally in the form of heat.

There are different types of damping: Coulomb, viscous and hysteretic damping. Coulomb damping is caused by kinetic friction between sliding dry or surfaces. If the heat is dissipated due to the movement of bodies in a liquid medium, it is a case of viscous damping in which

the damping force is proportional to velocity. When a solid is deformed, if heat is dissipated by internal friction it is called as hysteric or solid damping. [121]

In the context of the working problem, each mechanism could be seen a solution for diminishing sacrifice component wear and excess energy channeling to lower limb.

For a perfectly elastic material, the energy utilized to deform the solid is stored within with no dissipation of energy. In contrast, the work done to deform the viscous fluid is dissipated as heat during the irreversible flow. Due their molecular properties, semicrystalline polymers have an intermediate behavior better described as viscoelastic [121] influenced by loading type and velocity, and surrounding conditions.

As it has been established, material limitations due ankle anatomical constrains are present.

4.2 Chapter nomenclature

a_t	Acceleration vector
E	Young Modulus
E_k	Kinetic energy
F_t^{ext}	Applied external force vector
F_t^{int}	Internal forced vector
f_i	Inner force
G	Shear modulus
h	Cell pattern curved beam maximum height
K	Bulk Modulus
l	Cell pattern curved beam length
M	Mass matrix
n	Amount of substance in moles
P	Pressure
R	Gas constant
T	Absolute temperature

t	Time
u_i^s	Displacement field
V	Volume
v_i^s	Velocity field
V_f	Final block speed
V_i	Initial block speed
V_m	Minimal block speed
$w(x)$	Height of the cell pattern horizontal beam as a function of position
x	Given position of the cell pattern curved beam
Γ	Domain boundary interface
Δt	Time step
δ_{ij}	Kronecker delta
ε_{ij}	Elastic strain tensor
θ	Cell pattern curved beam thickness
λ	First Lamé parameter
ν	Poisson ratio
ρ	Fluid density
π	Pi value
$\sigma_{ij,j}$	Stress tensor
τ_{ij}	Shearing stress tensor
Ω_f	Computational fluid domain
Ω_s	Computational solid domain

4.3 Fluid-Solid Interaction theory

Cartilage tissue has a very high percentage of water (roughly 80%) with a primordial role on its load-carrying capacity due frictional resistance to flow and pressurization [122] Naturally, viscous behavior has been reported for cartilage, and the idea for a fluid-based damping for TAA sacrifice component seems consequent.

This idea is sustained by the preexistence of transtibial prosthesis designs with this working principle. At least one pneumatic foot-ankle prosthesis has been developed [123], showing capable of providing an appropriate range of motion and biomimetic mechanics.

However, it should be considered the natural limitations of an internal prosthesis. The interaction with the enveloping ankle tissues, and structure of the full prosthesis assemble obligate for consideration of how fluid and solid interact and are influenced by each other.

Fluid structure interaction (FSI) is defined as the interaction of some movable or deformable structure with an internal or surrounding fluid flow [124]. Being inherently complex problems, these are forcibly analyzed by means of physical experiments or numerical simulation [125]

The general methodology of first reduced -and thus, numerically efficient- FSI methods corresponded to dynamic sub structuring procedures adapted to fluid-structure modal analysis, working with a solid tank partially filled with compressible fluid. A variational modal interaction scheme was proposed, allowing the use of the acoustic eigenmodes of the liquid in a rigid motionless enclosure and the hydroelastic modes of the enclosure for a three-field mixed variational formulation [126]

Later emphasis has been put on nonlinear models, enhanced physical understanding of FSI problems and the use of reduced-order models, time linearization, and methodologies drawn from dynamical system theory. [127]

FSI can be classified according to the numerical procedure used:

a) Monolithic: the solution of the solid part and the liquid part is given together (in the same matrix)

b) Partition: the fluid and the solid are resolved in separate fields. This is the most common approach in commercial software. FSI in partitioning requires periodic linking between the solid and liquid part (interface).

Another classification derives from the treatment of the finite element model meshes:

a) Conformal mesh method: The interface is defined as a physical limit and the meshes coincide with each other.

b) Non-conforming mesh method: The interface is restricted according to the mathematical model used.

The available software for FSI analysis (ANSYS) uses the non-conforming mesh method [107]. Taking in account the domain Ω, the external boundary Γ, $\overline{\Omega_s}$ the solid structure and $\overline{\Omega_f}$ the fluid, and the interface is denoted as Γ_s (Figure 4.1)

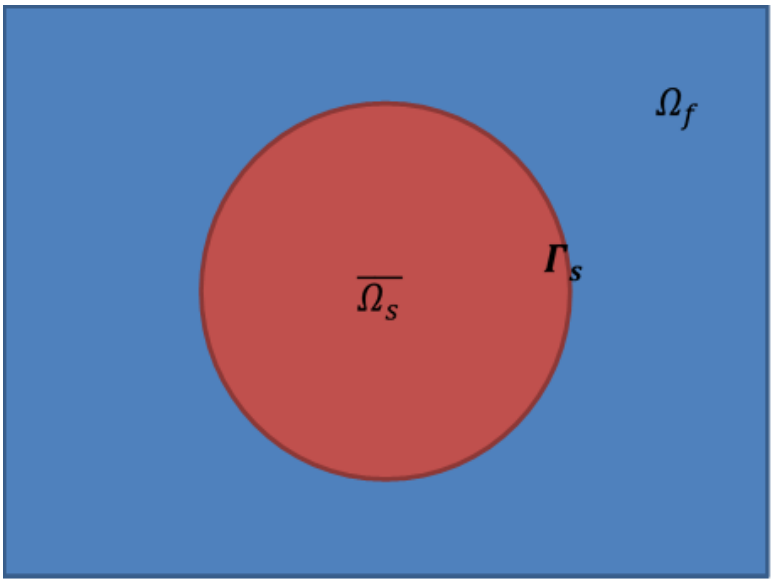

Figure 4.1. Schematic Fluid-Solid Interaction.

By the principle of D'Alembert Eq. 4.1 can be established

$$\rho \dot{v}_i - \sigma_{ij,j} + f_i = 0 \tag{4.1}$$

For the structural domain in Lagrangian formulation:

$$\rho^s \dot{v}_i^s - \sigma_{ij,j}^s + f_i^s = 0 \text{ for each } \overline{\Omega_s} \tag{4.2}$$

Velocity v_i^s is defined the material derivative of the displacement field u_i^s :

For a linear elastic material, the stresses can be obtained by means of the Lamé constants and the unitary deformations:

$$\sigma_{ij}^{s} = \lambda \delta_{ij} \varepsilon_{ij} + 2G\varepsilon_{ij} \tag{4.3}$$

$$\varepsilon_{ij} = \frac{1}{2}\left(u_{i,j} + u_{j,i}\right) \tag{4.4}$$

$$G = \frac{E}{2(1+\nu)} \; ; \; \lambda = \frac{E\nu}{(1+\nu)(1-2\nu)} \tag{4.5}$$

For the fluid part it can be established:

$$\rho^{f} \dot{v_i^{f}} - \sigma_{ij,j}^{f} + f_i^{f} = 0 \text{ for each } \overline{\Omega_f} \tag{4.6}$$

What is described in Eulerian formulation (Eq. 4.7):

$$\dot{v_i^{f}} = \frac{dv_i^{f}}{dt} = \frac{\partial v_i^{f}}{\partial t} + v_i^{f} v_{i,j}^{f} \tag{4.7}$$

If the fluid is considered as Newtonian, the internal efforts are determined by the following set of equations:

$$\sigma_{ij}^{f} = -p\delta_{ij} + \tau_{ij} \tag{4.8}$$

$$\tau_{ij} = 2\mu(e_{ij} - \delta_{ij} e_{kk}/3) \tag{4.9}$$

$$e_{ij} = (v_{j,i}^{f} + v_{i,j}^{f}) \tag{4.10}$$

The static pressure p is necessary to ensure the incompressibility of the fluid. Non-sliding condition at the boundary of both domains is expressed:

$$\begin{cases} v_i^{s} = v_i^{f} \\ \sigma_{ij}^{s} n_i = \sigma_{ij}^{f} n_i \end{cases} para\ \Gamma_s \tag{4.11}$$

In the available finite element software, the part of the fluid is formulated by the transient state Navier-Stokes equations in a conservative fashion [107].

For nonconforming meshes, the solution of the constitutive equations is achieved by means of Lagrange multipliers drifted from terms of the fluid equations.

Using the method of immersion, force terms are added in the equations relative to the fluids to represent the interaction of the structural part, avoiding the updating of the mesh.

In ANSYS, the so-called FSI force is used, which represents the effects of the border acting on the fluid [107]. It is computed explicitly from the structure to obtain the velocity of the fluid. The condition of non-slip is imposed. The fluid equations are solved for the domain with a fixed Eulerian mesh and the boundary in motion is calculated separately.

$$\rho^s \dot{v_i^s} - \sigma^s_{ij,j} + f_i^s = 0 \text{ for each } \overline{\Omega_s} \tag{4.12}$$

$$\rho^f \dot{v_i^f} - \sigma^f_{ij,j} + f_i^f = 0 \text{ for each } \overline{\Omega_f} \tag{4.13}$$

The following conditions must be followed on Γ_s :

$$u_i^s = u_i^f \tag{4.14}$$

$$\dot{u_i^s} = \dot{u}_i^f \tag{4.15}$$

$$\ddot{u}_i^s = \ddot{u}_i^f \tag{4.16}$$

Based on virtual work principle and Lagrange multiplicator theorem, equations for fluid and solid domains are combined in a unique equation:

$$0 = \int_{\overline{\Omega_s}} \left(\rho^s \dot{v_i^s} - \sigma^s_{ij,j} + f_i^s\right)\delta u_i^s dv + \int_{\overline{\Omega_f}} \left(\rho \dot{v_\iota} - \sigma_{ij,j} + f_i\right)\delta u_i dv + \int_{\Gamma_s} \bar{\lambda}_i(\delta u_i^s - \delta u_i) dv \tag{4.17}$$

Where $\bar{\lambda}_i$ is estimated Lagrange multiplicator for Γ_s , representing the generated force by FSI.

In the original formulation by Peskin, structure has no volume and $\overline{\Omega_s} = \Gamma_s$, $\overline{\Omega_f} = \Omega$. The equation 4.17 is rewritten as:

$$0 = \int_{\Gamma_s} \left(\rho^s \dot{v}_i^s - \sigma_{ij,j}^s + f_i^s + \bar{\lambda}_i\right)\delta u_i^s dv + \int_{\overline{\Omega_f}} \left(\rho \dot{v}_i - \sigma_{ij,j} + f_i - \bar{\lambda}_i L(\Gamma_s)\right)\delta u_i dv \tag{4.18}$$

Where

$$L(\Gamma_s)\begin{cases}1, x \in \Gamma_s \\ 0, x \notin \Gamma_s\end{cases} \tag{4.19}$$

is defined as a delta function. The remaining two independent equations are written:

$$\rho^s \dot{v}_i^s - \sigma_{ij,j}^s + f_i^s + \bar{\lambda}_i = 0 \tag{4.20}$$

$$\rho \dot{v}_i - \sigma_{ij,j} + f_i - \bar{\lambda}_i L(\Gamma_s) = 0 \tag{4.21}$$

The value of $\bar{\lambda}_i$ is obtained on eq. 4.20 to enter it into eq. 4.21, which is then solved to obtain the movement of the fluid. $L(\Gamma_s)$ is a continuous function, but it can be replaced by a discrete function or the FSI force interpolation of the structural domain on fluid domain [107].

4.4 Fluid damping approach

In a two-way transfer FSI analysis, the computational fluid dynamics (CFD) analysis results, such as forces, temperatures, heat flows, or heat transfer coefficients and near wall temperatures at the fluid-structure interface are transferred to the mechanical model and applied as loads. Within the same analysis, the subsequently calculated displacements, temperatures, or heat flows at the fluid-structure interface are transferred back to the CFD analysis [107]. Figure 4.2 is included as a visual reference.

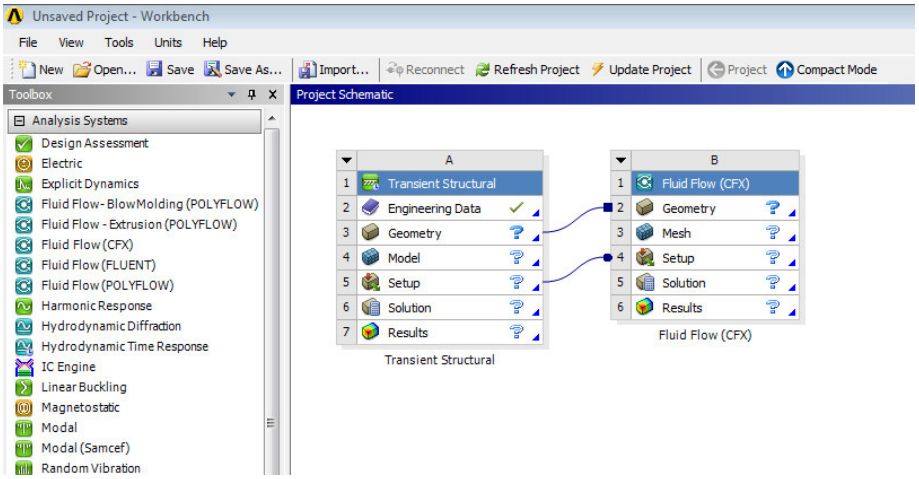

Figure 4.2 Two-way FSI on ANSYS Workbench®.

With this mathematical understanding of the interaction of a solid shell with an inner fluid, some increasingly complex chambered models (seen on Figures 4.3-4.5) were tested for a two-way FSI analysis.

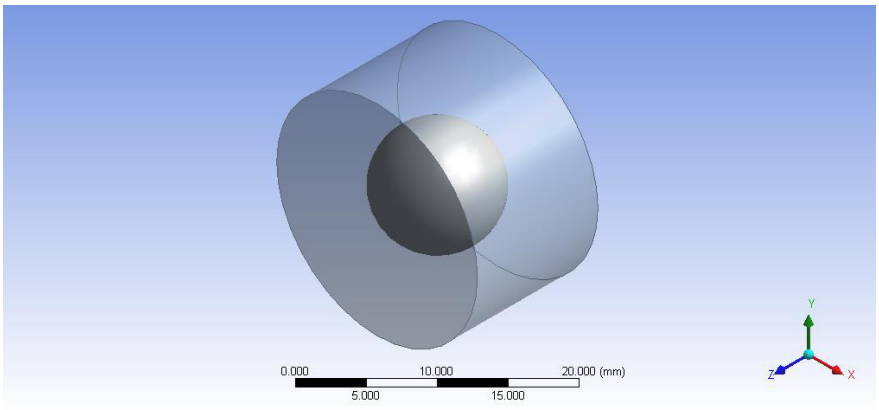

Figure 4.3. First approach for a fluid-damped insert design (Model A).

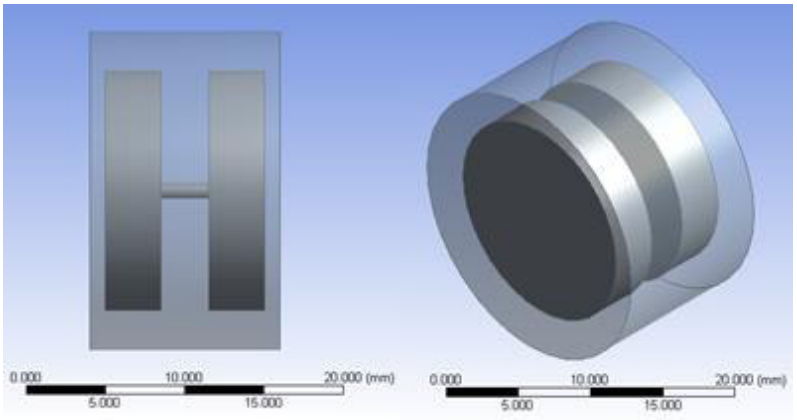

Figure 4.4. Second approach for a fluid-damped insert design (Model B).

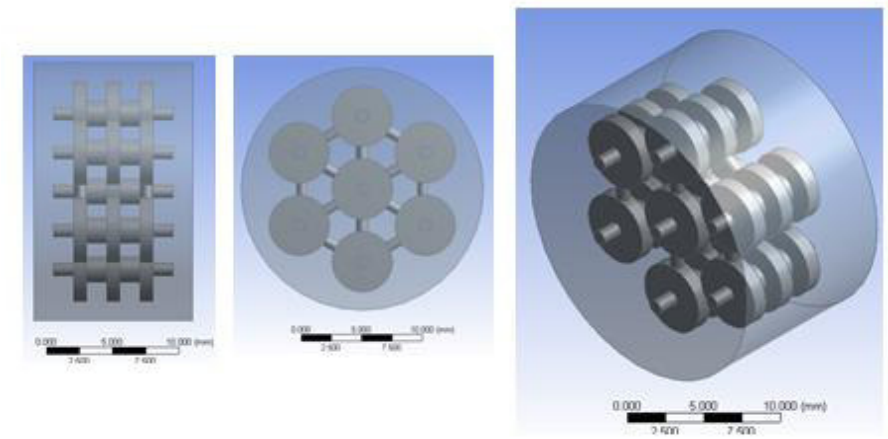

Figure 4.5. Third approach for a fluid-damped insert design (Model C).

The base cylinder for all models has 20 mm in diameter and 12 mm in height. Dimensions were chosen taking in consideration a probable insert size for a sacrifice component of a TAA prosthesis.

The spherical cavity of model A is located on the geometric center of and is 10 mm in diameter. Model B and C follow similar patterns, having thinning zones among the centered multiconnected chambers, intended for a forced fluid flow.

As a first approach, the simpler constitutive models were used. For fluid, the ideal gas model on 300K, isothermal consideration was used. It must be remembered that in most usual

conditions (for instance at standard temperature and pressure), most real gases behave qualitatively like an ideal gas [128]. Shear transport stress was applied. This implies an air-filled design for the insert.

For the solid component, an isotropic linear elastic model was used, with material parameters shown on Table 4.1:

Table 4.1. Material properties for first approach of fluid-damped insert design.

Young modulus	1100	MPa
Poisson ratio	0.42	–
Bulk modulus	2291.7	MPa
Shear modulus	387.3	MPa
Yielding strength	20	MPa
Ultimate strength	50	MPa

This choice for a simpler model, rather than bilinear isotropic model (BIH) was done for avoiding excessive complexity as a first step on a series of iterations. Solid part of the insert was modeled using hexaedrical, eight-node elements, referred by the software as SOLID164 elements (seen on Figure 4.6).

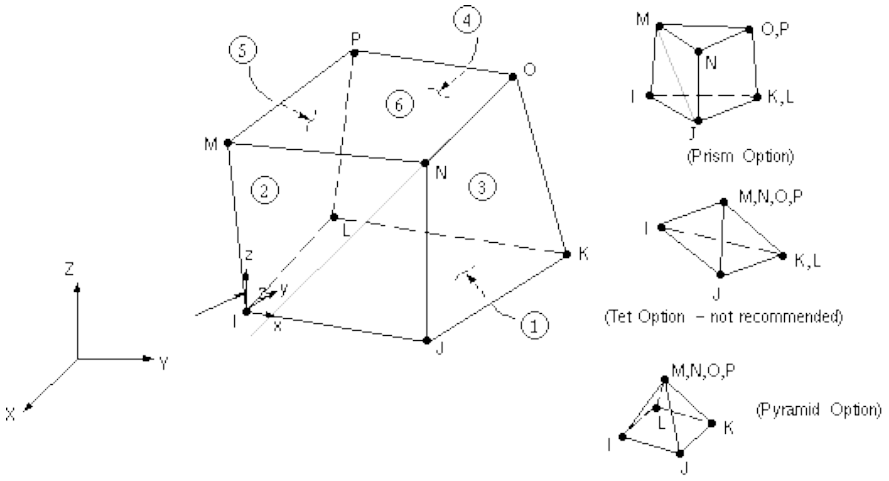

Figure 4.6. SOLID164 element [107].

For the FEA analysis, an adaptive timestep Δt was used, with an initial size of 0.05 s, and a variable range of 0.05-0.1 s

The overall volume is compressed 3 mm in the dimension of the axis, equivalent to 25% of the initial length. It starts at 0.1 s and develops completely at 0.9 s. The complete simulation time is of 1 s. The compression ratio was chosen as more moderate compressions did not had the desired effects.

FEA results were divided on fluid-related and solid- related. Table 4.2 resumes the former, along with some statistics about discretization

Table 4.2. Fluid finite element analysis statistics.

Parameter	Model A	Model B	Model C	
Gas nodes	1324	5556	48377	#
Gas elements	605	27667	226550	#
Initial Gas Volume	516.61	6533.81	2152.79	mm^3
Final Gas Volume	437.16	1004.90	331.10	mm^3
Final Gas Pressure	119.65	123.80	154.13	KPa
Gas volume reduction	15.38%	18.92%	34.31%	
Pressure growth	18.09%	22.19%	52.12%	

As seen on previous Table, gas volume within the insert is reduced during compression. On the other hand, gas pressure rises (Figure 4.7) from the initial value, equivalent to the atmospheric pressure nominal value of 101,325 Pa

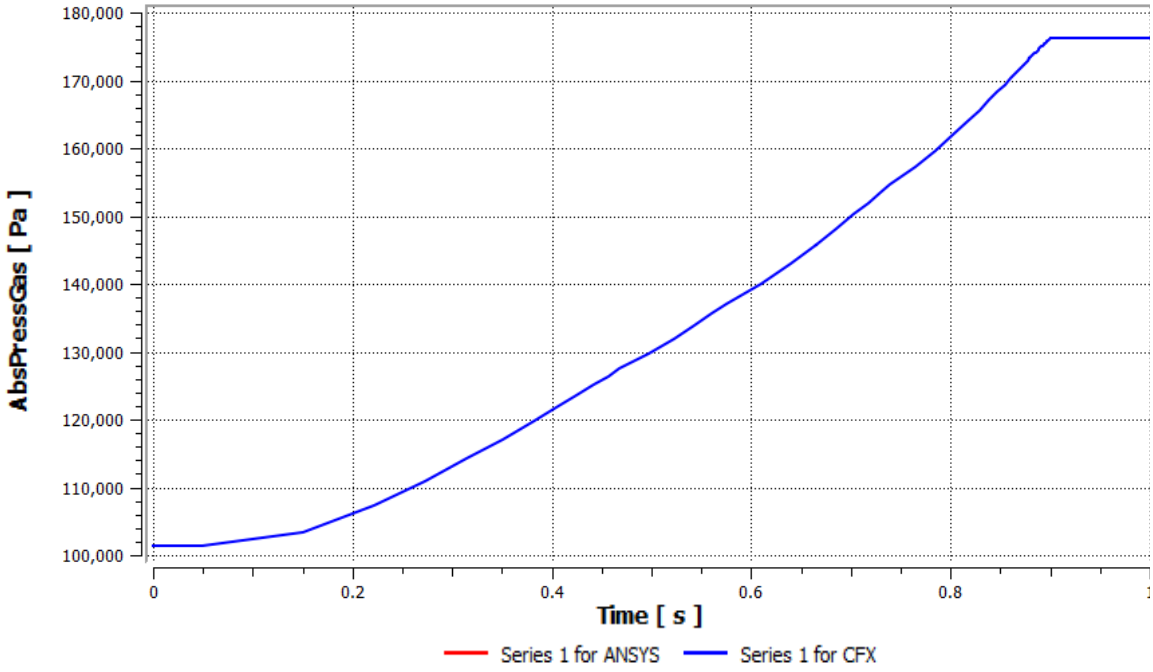

Figure 4.7. Pressure change on Model A insert.

Following the ideal gas law (Eq. 22)

$$PV = nRT \tag{4.22}$$

The product of pressure and volume must remain constant. The value calculated at the beginning for the constant PV is 0.05305 $Pa(m^3)$ for Model A, 0.66199 for model B and 0.218124 for model C. Estimated error in three cases is less than 1.00%

Figure 4.8 shows that pressure is evenly distributed on the inner fluid.

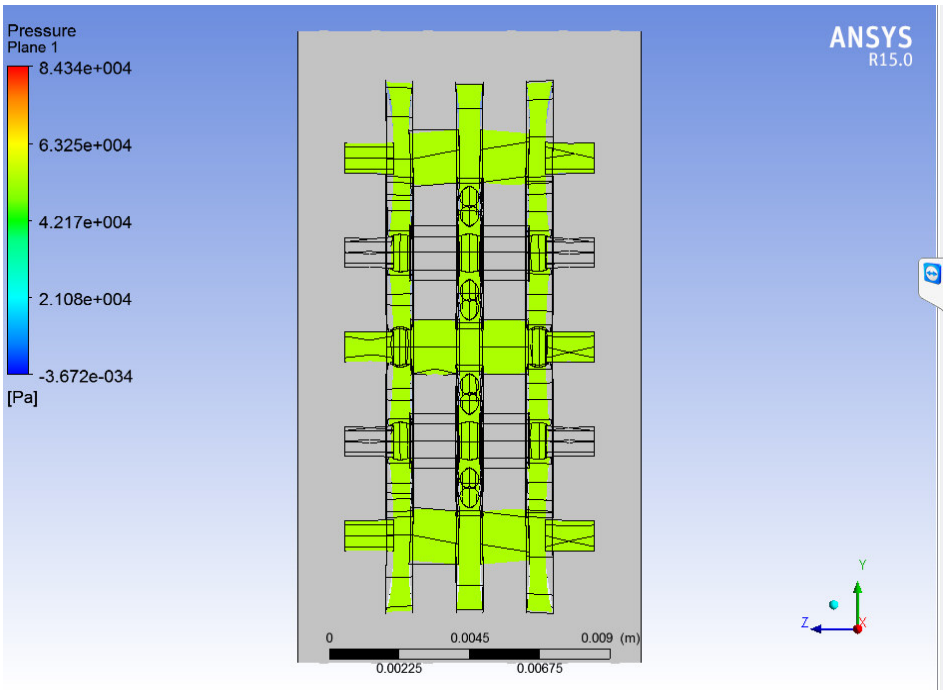

Figure 4.8. Final pressure on Model C insert.

Solid-related results are expressed on Table 4.3 and Figure 4.9. In this case, available results are strain and von Mises stress.

Table 4.3. Solid finite element analysis statistics.

Statistics	Model A	Model B	Model C	Units
Solid nodes	3709	5574	23709	#
Solid elements	2048	3130	14236	#
Maximum strain	0.1467	0.135226	0.3882	mm/mm
Maximum von Mises stress	29340.0	148.7	427.0	MPa

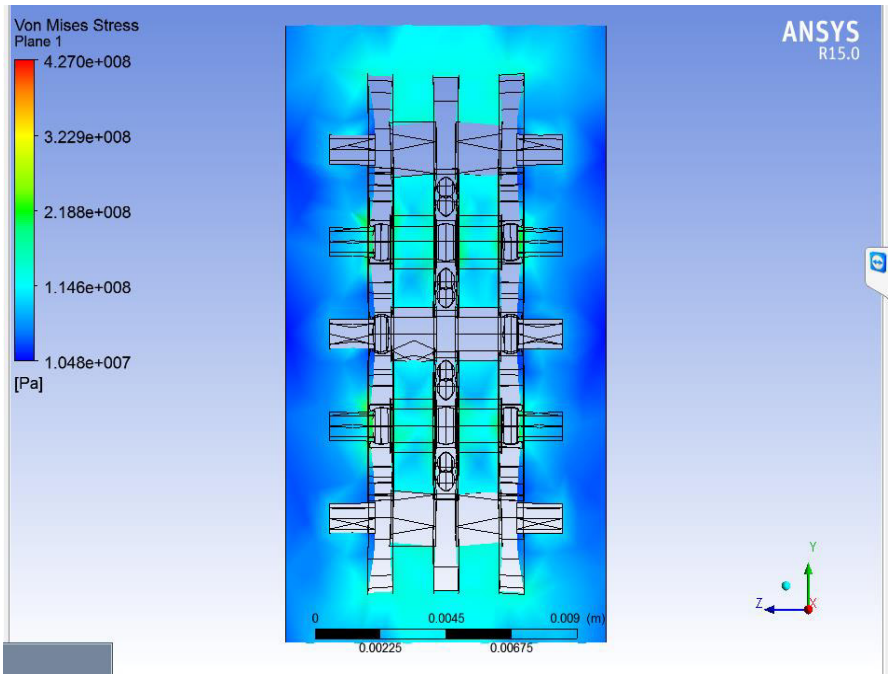

Figure 4.9. Stress on solid part of Model C.

These results reveal some serious problems. Maximum von Mises stress exceeds by orders of magnitude the breaking stress of polyethylene (50 MPa). Linear approximation done with constitutive equations is not valid anymore. This problem is inherent to the problem formulation. Any other material model for the solid part of insert would have similar results.

4.5 Discussion on fluid damping

Even when the idea of a damping fluid inside a TAA prosthesis design seemed at first feasible, the rise of certain complications during development and the obtained negative results obligate for abandoning this approach. Even so, some discussions about the root causes of this failure are explored.

As a primeval idea, the use of a liquid (water, synovial fluid), a gas (air) or a mixture of both as a damping fluid were equally considered. On the first cases, viscous damping was expected, caused by energy losses as they occur in a fluid forced through a series of small openings inside the inner chamber of the cylinder base. The use of multiple chambers was

attempted in order to provide more interaction surface among fluid and solid components of the intended prototype. However, this was not assured for the use of a liquid phase, turning interest on gas as a damping fluid.

Ideal gas assumption was made as a preferred approximation for simplicity on the concept testing. Human body has a very limited range of temperature (36.1-37.2 ºC) [129], so temperature effects on fluid behavior were discarded. Pressure changes were considered of more importance, as the lower limb is subject to variable loads on relatively short amounts of time. Future additional effects on prosthesis sterilization should also be explored.

The use of magnetorheological damping fluids has been tested on knee prosthesis [130], to cope with the same fundamental problems of excessive loading and gait pattern alteration. However, the main difference with TAA prosthesis is that the former device is not implanted inside the body, as is the project case, and thus the materials are not subject to the necessities of biocompatibility, and the possibility of corrective maintenance is kept.

The use of elastomers or rubber-like materials as a capsule rather than UHMWPE seems more practical, as evaluated on the initial simulation results. In contrast, ankle conditions surrounding the intended damping device and material limitations for TAA prosthesis were determinant for the search for new approaches on energy dissipation.

4.6 Negative stiffness damping

As the previous approach was not successful, other damping options should be considered. The second approach is referred to the use of negative stiffness.

Negative stiffness is understood as the occurrence of a force in the same direction as the imposed deformation in a certain element, in contrast with the usual phenomena [131-132]. This can be explained as most of these elements have been previously buckled or strained, thus they store internal energy, assisting rather than resisting deformation [133].

It is known that heterogeneous systems with one constituent of negative stiffness are predicted to give rise to high damping and stiffness [134]. The use of this kind of dampers has been mostly applied on vibration control [135-136], being commercially available for several years [137].

These characteristics have been of interest in such applications as damping and vibration control [131, 133]. Some previous attempts to apply negative stiffness on orthopedics had been attempted as a mean to better stiffness tenability on prosthetic limbs [138-140], diminishing the applied energy amount on them in search for safe and comfortable operation. The use of a cell pattern with negative stiffness, however, has not been yet reported for these biomedical applications.

Previous work by Correa et. al. [141-142] was focused on the use of a slender bar in a post-buckled "S" shape constrained laterally to give stability at a unique position becoming the base of a cell pattern structure (Figure 4.10) capable of restitution after a large deformation.

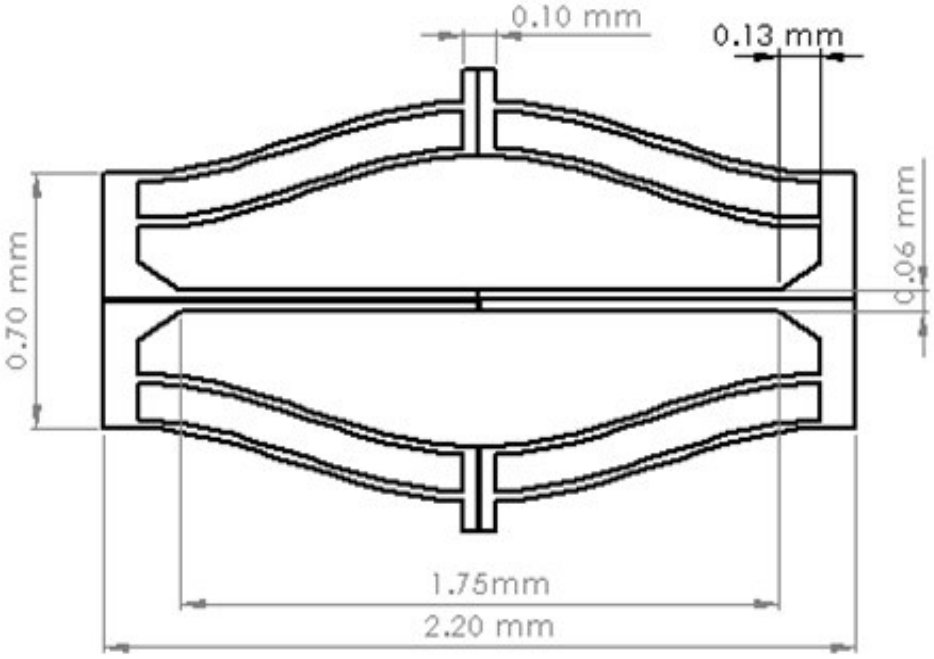

Figure 4.10. Cell structure.

Curve shape is given by the Eq. 4.26

$$w(x) = \frac{h}{2}[1 - Cos(\pi \frac{x}{l})] \tag{4.23}$$

The generated curve has only one stable position when deformed [141-142], creating the desired effect of negative stiffness and allowing its following recovering.

Preliminary 2D test were used to ensure the correct work of the structure simulation. Dimensions of the 2D structure were based on the aforementioned works of Correa [141-142]. For simulation boundary conditions of this 2D model, the bottom edge of the structure is kept fixed, and a frictionless contact between block and structure is added.

Considering the effects of its intended displacement, contact regions between the curved beams edges were added. The existence of large deformations and self-contact within the structure turns the problem into a non-linear case, despite the material model used [107]. Table 4.4 shows the adjusted material constitutive model on Chapter 03.

Table. 4.4. BIH material model properties.

Parameter	Value	Units
Young Modulus	289.00	*MPa*
Poisson ratio	0.46	---
Tangent modulus	14.15	*MPa*
Yielding stress	95.00	*MPa*

Using the verified symmetry for a better use of computational resources, the model is divided in half, and a condition of symmetry is defined. Then, a square block was built above the model, in order to simulate a falling object that will compress the structure (see Figure 4.11).

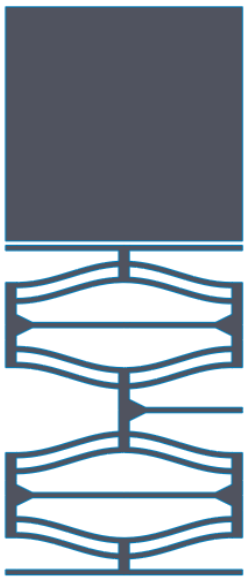

Figure 4.11. 2D half-structure with falling block model .

Domain discretization was realized with PLANE 162, a 2D explicit planar solid element type.

ANSYS Explicit STR solver is used for explicit dynamics solution; which is based on a Lagrangian formulation of ANSYS AUTODYN solver [107]. The equilibrium equation system is solved using the central differential method. Accelerations at time t are given by Eq. 4.24

$$\{a_t\} = [M]^{-1}\left([F_t^{ext}] - \left[F_t^{int}\right]\right) \tag{4.24}$$

Nonlinearities such as contact are included on the internal force vector. Velocities and displacements are evaluated with Eq. 4.25 and 4.26

$$\left\{V_{t+\Delta t/2}\right\} = \left\{V_{t-\Delta t/2}\right\} + \{a_t\}\Delta t_t \tag{4.25}$$

$$\{u_{t+\Delta t}\} = \{u_t\} + \left\{V_{t+\Delta t/2}\right\}\Delta t_{t+\Delta t} \tag{4.26}$$

Geometry is update by adding the displacement increments to the initial geometry [107].

The equations become uncoupled and can be solved directly. This solution is stable if time step is smaller than critical step size [143].

Used time step was of 2.5 milliseconds, up to a total simulated time of 50 milliseconds.

The speed of the block before and after impact was taken as a direct measure of the energy absorbed [144]. In this case, the initial block speed (at t = 0 s) is assigned directly. The final block speed (at t= 5e-02 s) is obtained from the last set of simulation results. Absolute values are used.

Applying the software capabilities of parametric design, five different initial block speeds were used on this preliminary test, the matching results are shown on Table 4.5.

Table 4.5. Reduction of speed for a block falling over an energy absorbing 2D structure.

Initial block speed (*m/s)*	Final block speed *(m/s)*	Reduction percentage of kinetic energy
0.875	0.503	66.95%
1.0	0.810	34.39%
1.125	0.420	86.06%
1.250	0.544	81.00%

4.7 Negative stiffness approach

With these positive results, two options for shock absorption patterns were proposed mostly based on the original design, with a heavy change on scale and array in order to develop an energy absorption system with a feasible use on biomechanics, particularly on prosthesis design. These 3D models are now labeled as Model A and Model B (as seen on Figures 4.12 and 4.13).

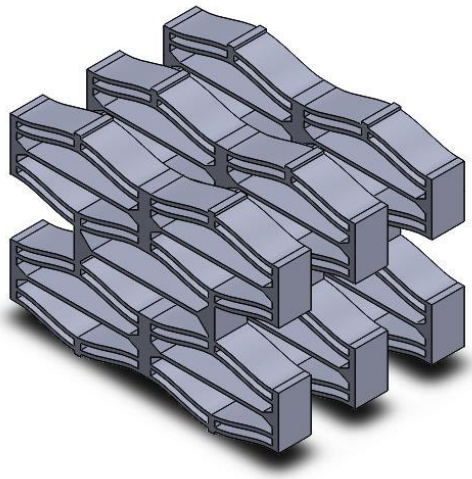

Figure 4.12. Model A original configuration.

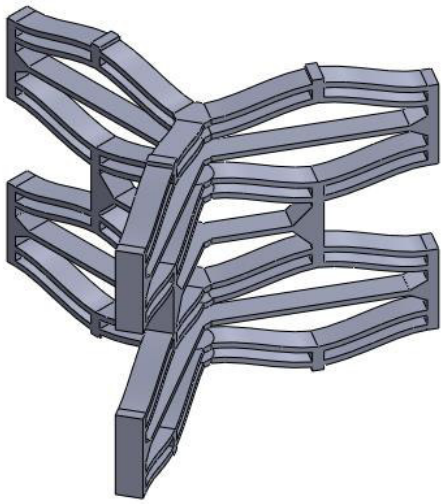

Figure 4.13. Model B original configuration.

Each one has a different approach, using a linear and a radial array. For comparison and intended application purposes, each model was surrounded by a thin cylindrical wall of 0.2 *mm* of thickness. This configuration affected specially the final geometry of some honeycomb cells on Model A (Figure 4.14).

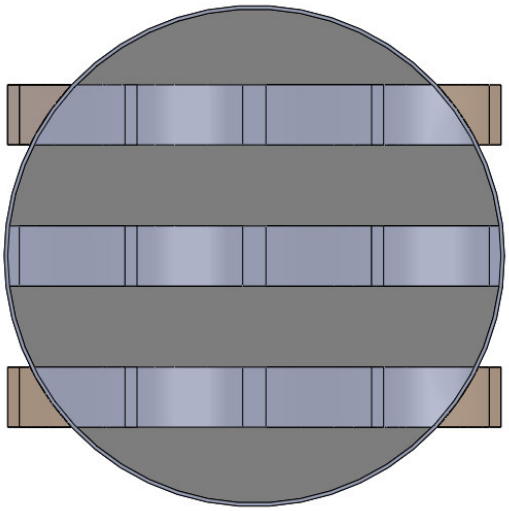

Figure 4.14. Model A modified configuration.

From the 2D analysis, it is reasonable to expect behavior symmetry for Model A. The assumption is made for Model B.

For computational efficiency during simulation, each modified model was reduced to a symmetrical half, as seen in Figure 4.15.

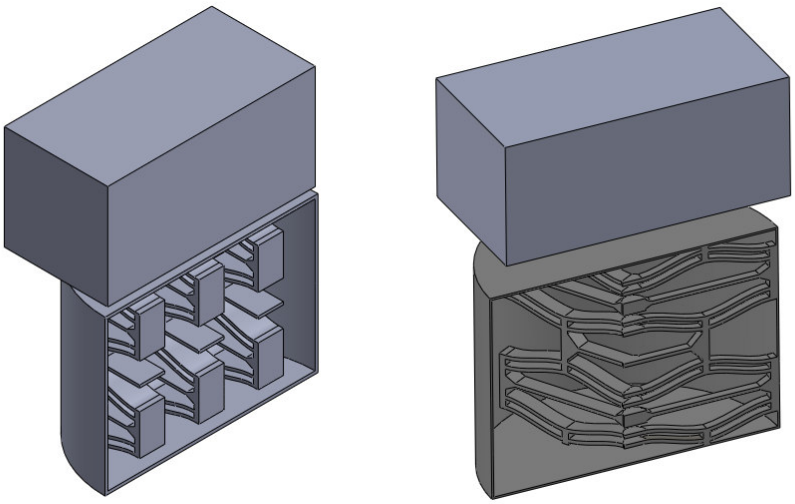

Figure 4.15. Tested computational models for each simulation.

Material properties of these 3D models are shared with the original PE 2D structure, and the same stress limits apply.

For boundary conditions, the bottom surface of the cylindrical wall was fixed, in addition to the symmetry condition.

During the early 3D tests, it was found that each falling block needed to give a single uniform impact on the upper surface of the structure to avoid inertial side effects and side pandering. This was achieved by giving the falling block the same maximum width than the tested structures, which are close but not fully identical due their different conformations. Thus, the mass for each impacting block is slightly different. As the comparison of kinetic energy loss for each block is given on percentage values, this should not be a concerning issue for energy absorption evaluation.

Frictionless contacts were added on each of the curved beams horizontal surfaces, as these are responsible of negative stiffness effects.

Finite element SOLID164 was used in both models, with a tetrahedral dominant shape in structure [107].

The overall dimensions, calculated mass and the characteristic of the meshing are listed on Table 4.6.

Table 4.6. Dimensions and meshing characteristics of tested models.

	Model A	Model B	Units
Maximum width*	14.20	12.72	*mm*
Maximum height*	10.20	12	*mm*
Maximum depth*	14.20	12.72	*mm*
Beam height (h)	0.68	0.68	*mm*
Beam length (l)	6.34	6.10	*mm*
Beam thickness (θ)	1.7	0.69	*mm*
Volume	152.6	176.66	mm^3
Mass	1.449E-04	1.678 E-04	*kg*
Number of nodes (meshing)	7424	10196	--
Number of elements (meshing)	20871	28782	--

*Dimensions referred to the symmetrical half models shown on Figure 4.15

As these models were expected to be more rigid, the speed for test was increased to 10 *m/s*, giving the block much more kinetic energy, thus allowing for a better observance of the speed reduction. As the objective of simulation is to test the overall concept the choice of magnitude change is arbitrary high in order to have a robust design.

The change on block speed also allows the use of a smaller time step of 1.5 milliseconds, and a shorter simulation time length of 5 milliseconds.

During the result review, it was noticed that the block speed decreased consistently after the contact with the structure until it reached a minimum, (minimal block speed) coincident with the structure maximum deformation. After that point, the structure restitutes itself while the block experiments acceleration until it reached a stable value until the end of simulation (final block speed). Consequently, it should be assumed that some energy stored in the structure is transferred back to the block during contact.

Table 4.7 shows the summary of results for the efficiency of energy absorption.

Table 4.7. Energy absorption results.

	Model A	Model B	Units
Block mass	6.498e-04	5.586 e-04	*kg*
Initial block speed	10	10	*m/s*
Minimal block speed	4.606	2.758	*m/s*
Time of minimal block speed	2.5e-04	5.0e-04	*s*
Final block speed	6.933	5.410	*m/s*
Percentage of kinetic energy absorbed in structure	78.784%	92.39 %	--
Percentage of kinetic energy loss in block	51.933%	70.73 %	--

No issues on numerical stability were found.

For evaluation of percentage of kinetic energy absorption into the structure and the final loss of the block, the calculated speeds were used in Eq. 5, as reported with the 2D model. However, the amount of energy stored in the structure was estimated form the minimal block speed instead (Eq. 6)

$$Absorbed\ E_k = \frac{\left(V_i^2 - V_m^2\right)}{V_i^2} x100 \qquad (4.27)$$

Both designs have similar results in terms on proportional kinetic energy reduction. However, as seen by the minimal speed of the block at the time of the maximal structural compression, Model B absorbs more energy at the time of impact, albeit it returned to the block, acting as a spring.

However, the material limitations should now be considered. It must be addressed that for Model A, an additional condition of symmetry is used to show only a quarter of the original model on subsequent Figures for a clearer interpretation.

Model B is fully shown as it was solved, but with a symmetry plane view rather than an isometric one for a better comprehension of each variable distribution.

In both models, the deformation is concentrated on the top of the cylinder and the surrounding parts of the energy absorption structure (Figures 4.16-4.17). The inner structural array tends to be compressed on the upper section, with little effect on the lower part.

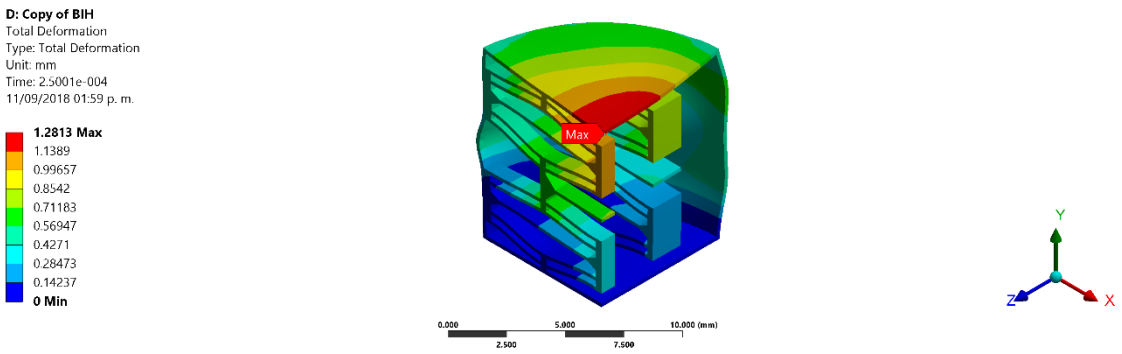

Figure 4.16. Maximum deformation of Model A.

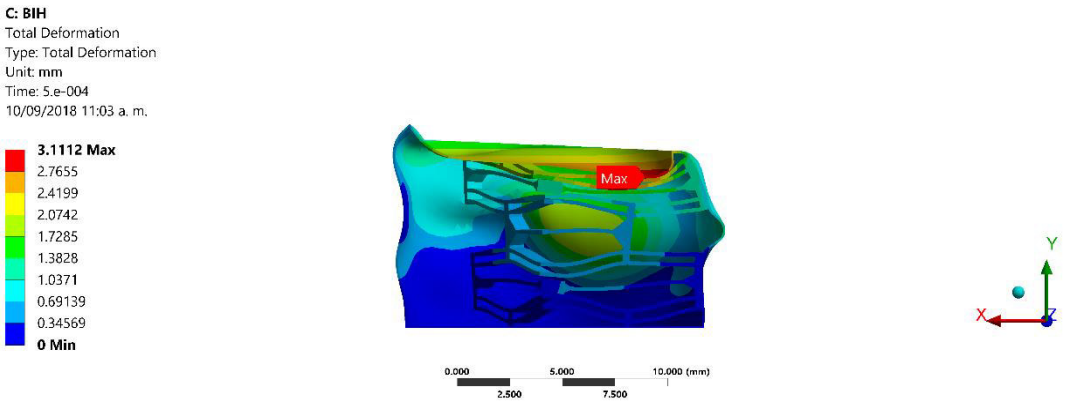

Figure 4.17. Maximum deformation of Model B.

However, as it is seen on Figure 4.18, for Model A, strain is also concentrated on the middle section of the surrounding wall. The same effect is lessened on Model B, as seen on Figure 4.19.

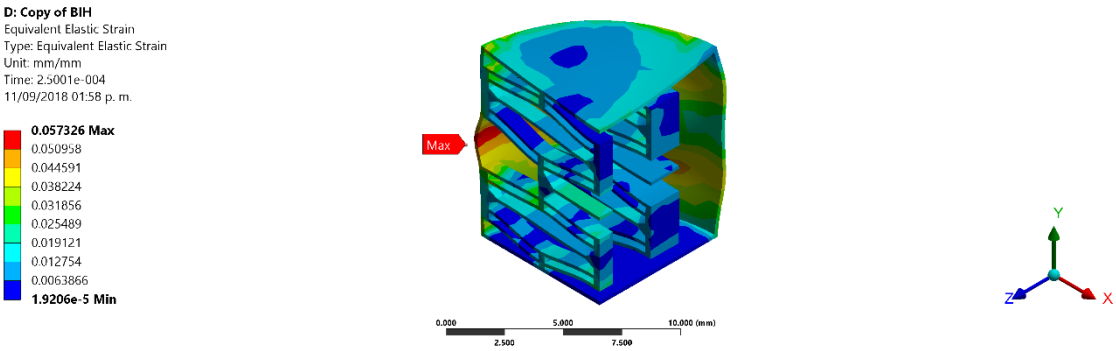

Fig. 4.18 Maximum equivalent strain of Model A.

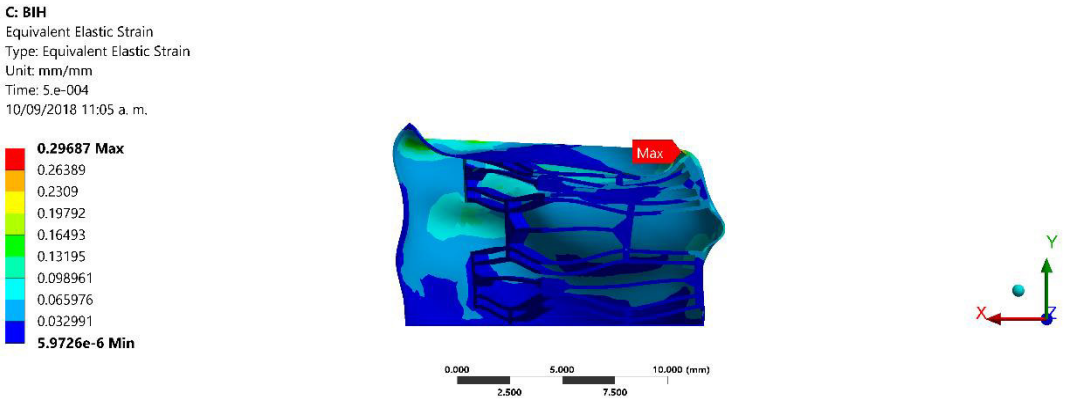

Fig. 4.19 Maximum equivalent strain of Model B.

Stress results are of great concern, as they give the limits of the safe operation of the energy absorption structure. Results are shown on Figures 4.20 and 4.21.

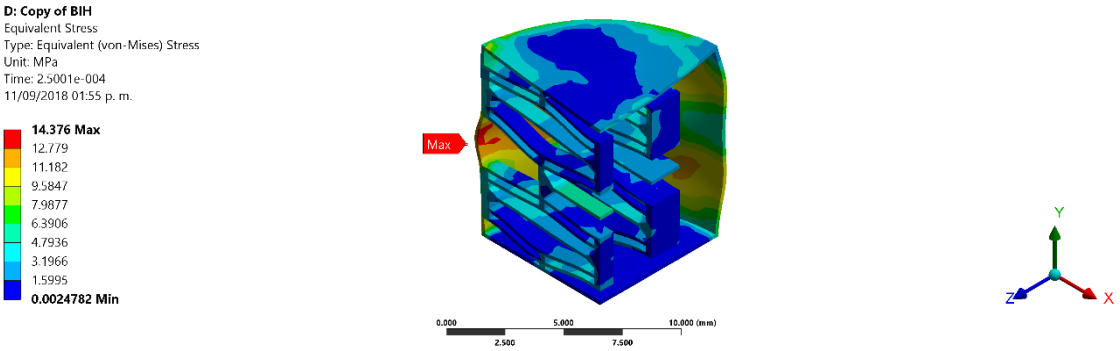

Fig. 4.20 Maximum equivalent stress of Model A.

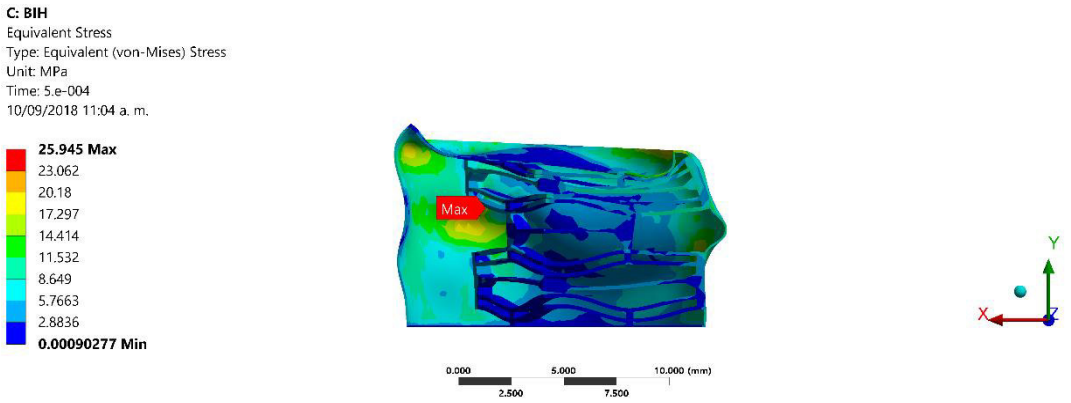

Fig. 4.21 Maximum equivalent stress of Model B.

For better clarity, Table 4.8 shows the maximum deformation, equivalent strain and equivalent von Mises stress obtained on each model during the simulation.

Table 4.8. Mechanical performance results.

	Model A	Model B	Units
Maximum deformation	1.2836	3.1112	*mm*
Maximum strain	0.57326	0.2968	*mm/mm*
Maximum stress	14.376	25.945	*MPa*

The obtained results show that some zones of the Model B are subject to high levels of stress, far beyond the established yielding limits, clearly putting the structure in a risky zone of operation and compromising its long.-term integrity. In summary, Model B is not operative on the established safety strain and stress limits.

By contrast, Model A does work as intended, and its application for a future development for energy absorption on prosthesis is feasible.

4.8 Discussion on negative stiffness

Being derived from a previous dissertation, there is much more available information for the development, use and effectiveness of a negative-stiffness honeycomb array as a source of mechanical damping. In this case, the focus lays on the possible application of this solution for a TAA prosthesis.

The first step for the possible implementation on a prosthesis prototype is scalation of the honeycomb design. As this was available for the CAD design, the only real limitation for the smallest proposed size is the availability of adequate manufacturing tools for the thinnest beam sections (0.69 mm for Model B, according to Table 4.6).

Chosen material model was crucial for concluding the operability of both designs. Previous development on this work, using the assumption of small (5%) strain and a linear elastic model as shown on Chapter 3. These material properties gave excessive stress values for the structure, surpassing the UHMWPE yielding stress [145]. Material model was also found to be invalid above said value. The use of the bilinear isotropic hardening (BIH) model corrected this wrong assumption.

As seen on the simulation results, interaction with the wall and the honeycomb array represented an unintended side effect. The purpose of these addition was to avoid structure buckling and load transmission on horizontal direction, situation that would represent an overload on the ankle joint and surrounding ligaments and soft tissues. In direct contrast, FEA results indicate that this wall interference can be vital in the desired damping effect. As

the polymeric should be inserted on the sacrifice component of the TAA prosthesis, this effect cannot be assured.

However, in a different context, this polymer honeycomb array can be used in other kind of orthopedic applications, such as external prosthesis intended for amputees, as the TAA restrictions are not the same.

4.9 Chapter conclusions

The search for a damping mechanism for extending the useful life of sacrifice components of TAA prosthesis led to the proposal of two fundamental mechanisms: use of a damping fluid and a structure with negative stiffness. Both approaches were tested on FEA analysis.

UHMWPE mechanical properties are not easily mimicked on simulation .However, with both cell pattern structures tested on compression and no thermal effects taken on account, linear elastic material model constitutes an obligated first reference point and the bilinear isotropic hardening material model is a good approximation to material behavior within these operative conditions.

The use of a surrounding wall on fluid damping and negative stiffness inserts original configuration was intended to avoid UHMWPE debris dispersion, which has been linked with joint prosthesis loosening. However, in the first case, the damping fluid cannot act unless the solid insert structure is damaged until the point of fracture. For the second case, this wall has a role as a stress concentrating zone and diminishes the damping effect of the negative stiffness beam structure. This situation is exacerbated as the inserts would have had to work inside a restricted position inside the ankle joint.

In resume, the fluid damping option was found not feasible for an internal insert. However, the idea of an inner structure inside the sacrifice component of TAA prosthesis was found as a practicable option, with some major adjustments.

It should be noticed that boundary conditions for simulation were chosen to have the most generic approach, more intended to test the overall concept rather than a fully functional prosthesis design; a better option would be the use of geometry and conditions closer to the ankle joint operation with said approach of a simpler inner structure.

Chapter 5- Tested prosthesis design

Previous chapters have dealt with material characterization and different solution proposals for the main objective of the project.

As previous input and certain references have suggested, UHMWPE wear in prosthesis could be lessened with implementation of internal gaps inside the sacrifice component structure. This focus was finally selected as the main approach in the search for a solution for a new TAA prosthesis design.

Early and modern design considerations were overviewed on theoretical approach on a benchmarking of the different TAA prosthesis. The implications for each design choice on tibial, talar and sacrifice component are justified

Using a 3D printer, a rapid prototype is elaborated. The corresponding model will used as input for a posterior finite element analysis (FEA) on the following chapter.

5.1. Introduction

The first reference to TAA dates from 1970, by Lord and Marrote using an inverted hip shaft inside the tibia and an acetabular cup cemented in the calcaneus, completely removing the talus [146]. However, the novel procedure had a worse and more unpredictable output than ankle arthrodesis, being relegated during many years.

Since then, designs have been proposed more in accordance with anatomical reality, as the understanding of ankle joint biomechanics has increased (Figure 5.1). TAA has gained relevance as reliable surgical technique for advanced cases of osteoarthritis and other related diseases [14].

Some favorable trends for TAA prosthesis performance include the use of non-constrained, three element mobile-bearing implants, non-cemented bone fixation, and surgeon specialization [14].

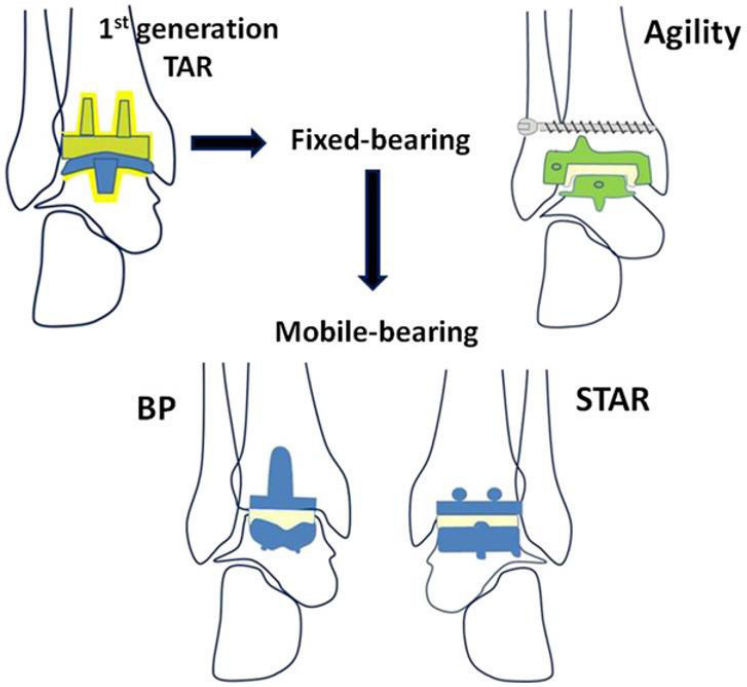

Figure 5.1. Evolution of TAA prosthesis design [14]

One limit to the scope of this work is that design will focus exclusively on TAA prosthesis, without consideration of all the required tibial and talar for preparing bones for receipt of orthopedic prostheses, and the linked surgical procedure.

5.2. Basic anatomical references

Computer Aided Design (CAD) can be defined as the use of computers to aid in the creation, modification, analysis, or optimization of a design [147]. Its role is crucial as its general implementation on many engineering fields has allowed for faster, more accurate and cheaper results

Since the anatomy of individuals is variable, a minimum and maximum range that is compatible with most of the target population must be estimated. In fact, the practice defined for commercial prostheses is to have different sizes [148] that meet this variation, with the surgeon adjusting cut and alignment depending on the patient preoperative state [149]. Personification is another recent trend on prosthesis design. Recent development in 3D

printing technology and robot assisted surgeries will be of relevance orthopedic devices industry in future [150].

In order to obtain some guidelines about prosthesis size, it is suggested to stick to the dimensions of the three-dimensional CAD model for the bones of the lower limb, seen on Figure 5.2:

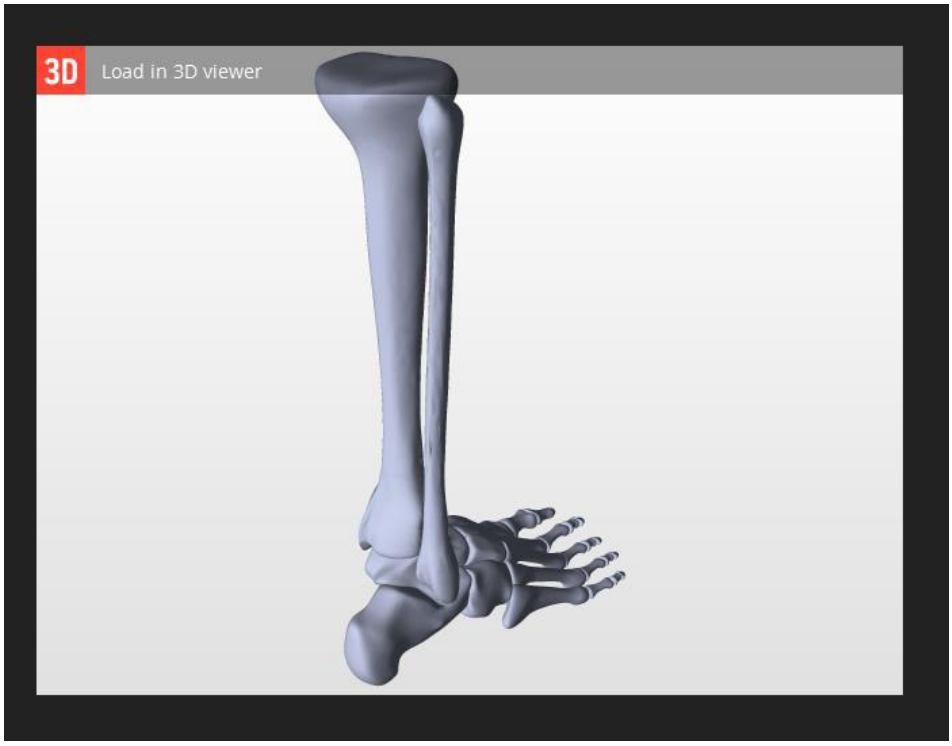

Figure 5.2 Lower limb CAD model [21].

Although the obtention of CAD model is not explained, it is inferred that it came from a patient scanning. Dimensions of the model (on millimeters) are consistent with the references for a right male leg osseous structure [151]. All bones were modeled as irregular solids, excepting tibia and fibula, which are only surfaces and were fixed for design purposes.

Approaches to the tibiotalar joint show that although it is irregular, some reference dimensions can be obtained. Note in Figure 5.3 that the surfaces are not completely congruent, as it would happen under unhealthy joint conditions [152].

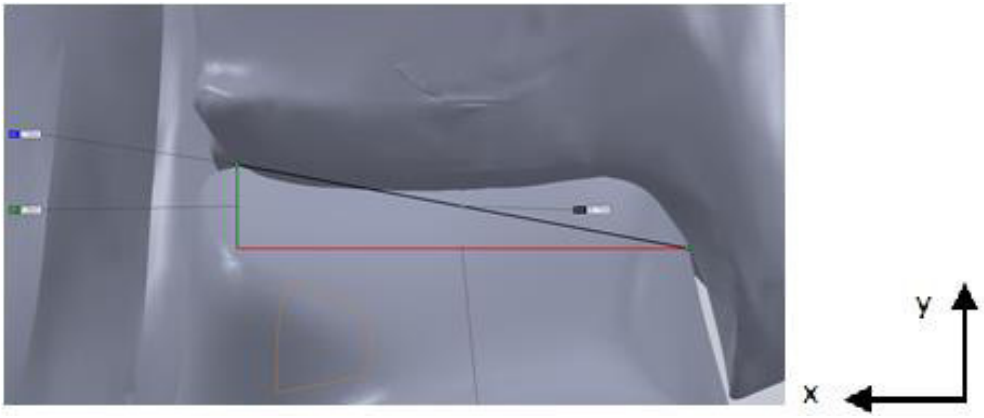

Figure 5.3. Maximum design dimensions for TAA prosthesis. Frontal view.

A distance of 35.49 mm in horizontal (red line), 6.59 mm in vertical (green line) between the highest points of the talus that is n in the joint is observed in the image.

The side view on Figure 5.4 also shows the overlap area between the tibia and the talus. There is a maximum length of 31.38 mm in horizontal (blue line), and 4.80 mm in vertical (green line).

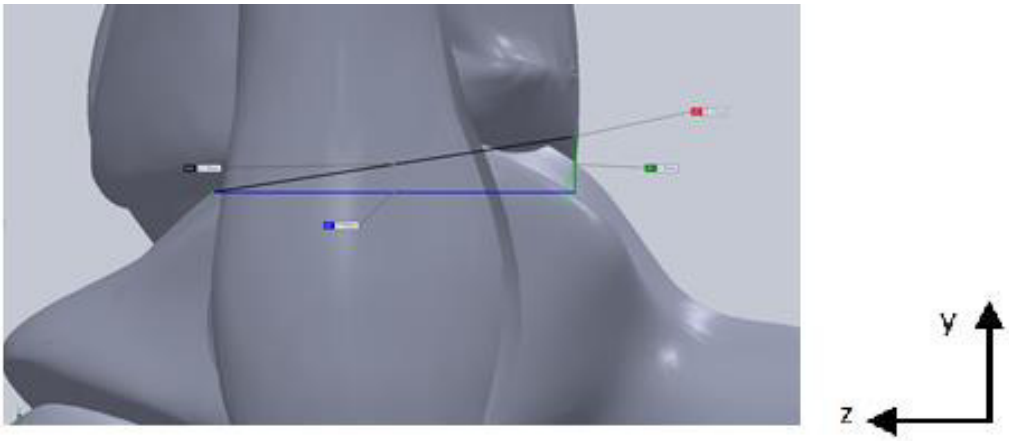

Figure 5.4. Maximum design dimensions for TAA prosthesis. External lateral view.

With a prosthesis general shape approximation as a rectangular prism, the maximum permissible dimensions for the tibia-sacrificial anchor-talus anchor assembly can be obtained.

As TAA involves the extirpation and replacement of this anatomical reality, a concept of polymeric insert must adhere to these dimensions, if what is sought is equivalent functionality. Subjacent functioning principle should be scalable, and of feasible manufacture.

The new proposed design description will be referenced by the natural subdivisions of sacrifice, tibial and talar components.

5.3. Sacrifice component

Even when other material alternatives have been searched and tested, regular and highly crosslinked UHMWPE pieces are still a sizeable majority of available prosthesis, and the established standard material for joint replacement [153], as seen on Chapter 02.

The general design for this crucial component followed the major radius curvature on astragalus upper surface, as seen on Figure 5.5.

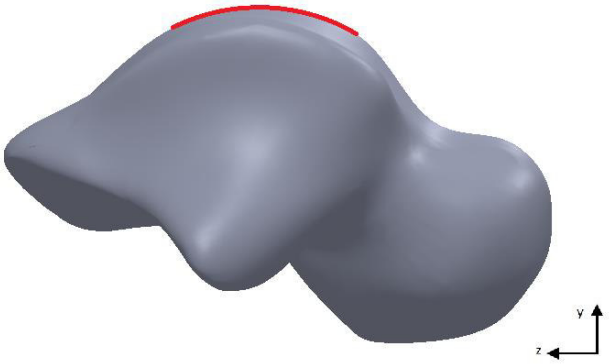

Figure 5.5. Major curvature ratio on astragalus upper surface.

This external configuration was kept even when size, damping mechanism and idea of interaction with the metallic elements of TAA prosthesis varied with time.

The main possibilities for talar subjoint contact are illustrated on Figures 5.6 and 5.7.

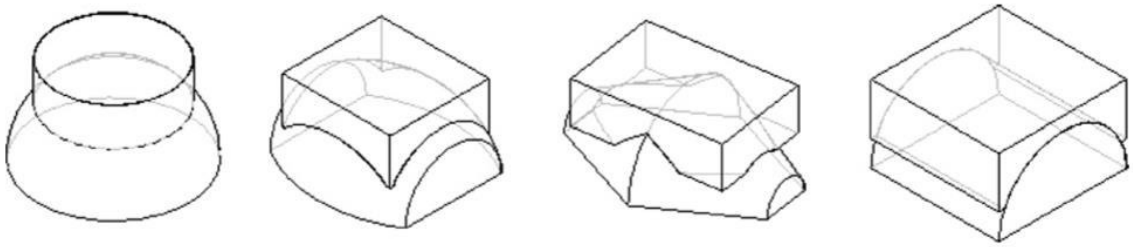

Figure 5.6. TAA congruent surfaces: spherical, sphenoidal, conical, cylindrical [14].

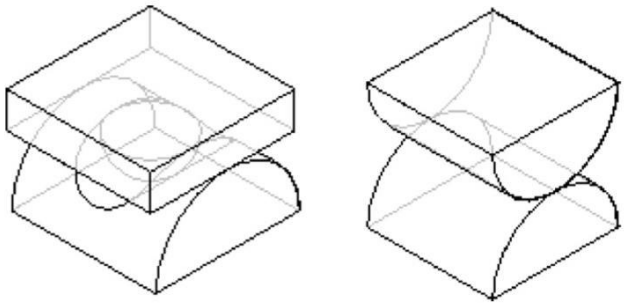

Figure 5.7. TAA incongruent surfaces: trochlear, convex-convex [14].

Congruent surfaces in the designed implants are of high importance, since the implemented load is distributed along the entire surface, increasing its wear resistance in the component. The main drawback of these configurations is the lack of lateral movements for ankle joint

Inconsistent surfaces generate stress concentrations due to the contact between the designed surfaces, this incongruence in the design causes premature wear on the components and instability; however, these are closer in degrees of freedom to the original joint [14].

It was stated on Chapter 04 the early attempts for finding a viable damping mechanism. For the definitive approach, a previous patent concession, *Shock absorbing system for knee and hip prosthesis* [154] has suggested that UHMWPE wear in prosthesis should be lessened with implementation of internal gaps. The main contribution of this design is its application on a complete TAA prosthesis model.

For the first geometry proposals for the sacrificial element (Figure 5.8), the disposition of the solid and hollow spaces had been estimated by trial and error.

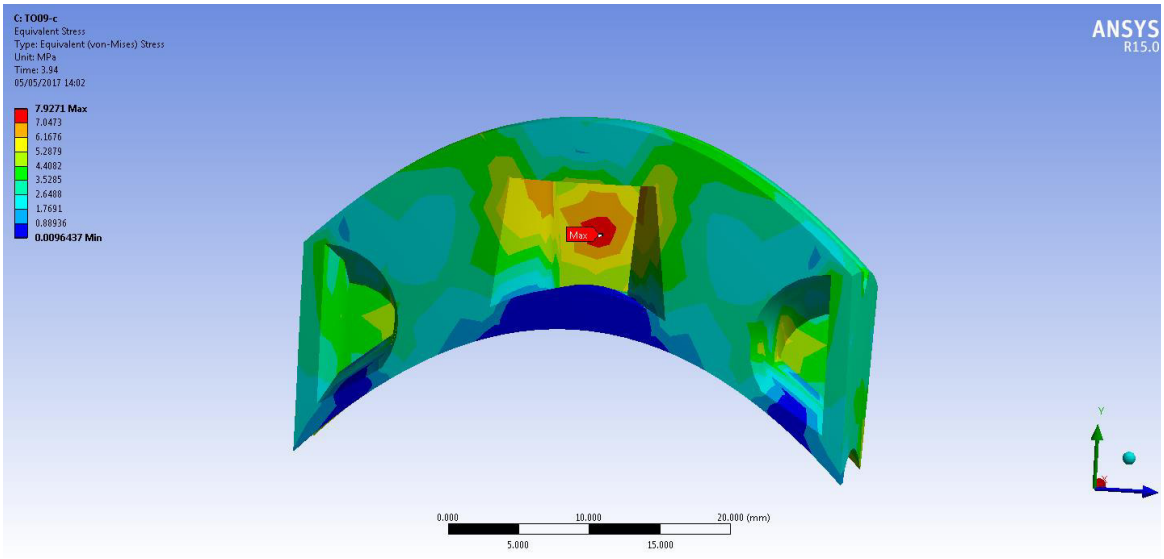

Figure 5.8. Sample of early sacrifice component geometry stress state.

This early models were tested on a linear static FEA analysis, with a linear elastic (LE) constitutive model with Young modulus $E = 256\,MPa$ and Poisson ratio $\nu = 0.46$. This previous insight was promptly replaced with the definitive bilinear isotropic hardening (BIH) model obtained in Chapter 3.

A better method for defining the inner geometry was considered, using a shape optimization tool for a more systematic and design exploration.

From a commercial shape optimizer module on ANSYS® [107], application on the basic sacrifice component shape, a regular matrix of twelve prismatic cavities was proposed as the inner structure basic configuration.

An important detail that was observed was that the Shape Optimizer module of ANSYS 15® only worked with materials with a Poisson ratio value between 0.1 to 0.4; UHMWPE is out of reach (0.46) [107]. However, it was run with a reduction of the polyethylene modulus (0.40). Later versions of the software did not have this limitation and results were qualitatively similar, validating previous findings.

As seen on Figure 5.9, the simplest approach was to use the silhouette of the central part of the original geometry of the sacrificial element to perform a 2D analysis. Plane square

elements of 0.5 mm of edge were used for the numerical solution. For border conditions the lower edge was fixed and the upper one was subject to a simple load of 3500 N in vertical component, equivalent to the maximum axial force experimented by ankle joint during gait [155]

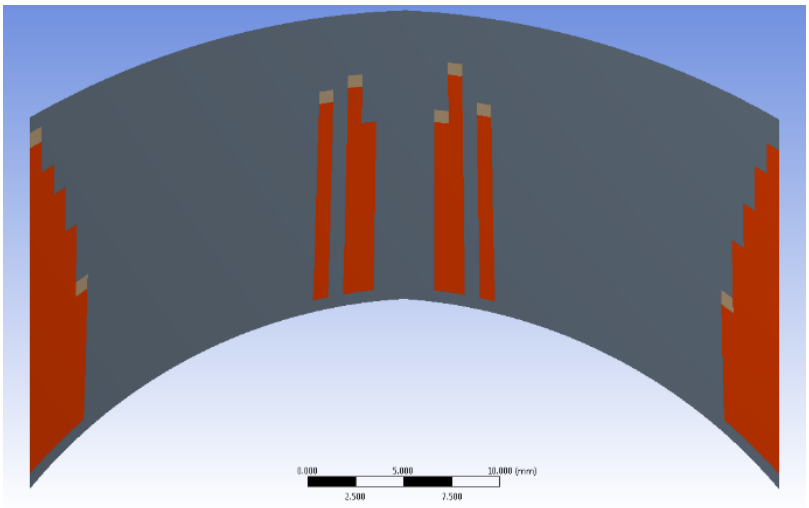

Figure 5.9. 2D silhouette for sacrifice component optimization.

The red zones on the illustration show the dispensable elements on the structure [107], with the focus on borderline and central zones. Similar results were obtained with 3D geometries and tetrahedral elements.

The general shape of sacrifice element remained almost unchanged. The main differences with advanced design were related to its interaction with tibial and talar components.

Definitive model is shown on Figure 5.10.

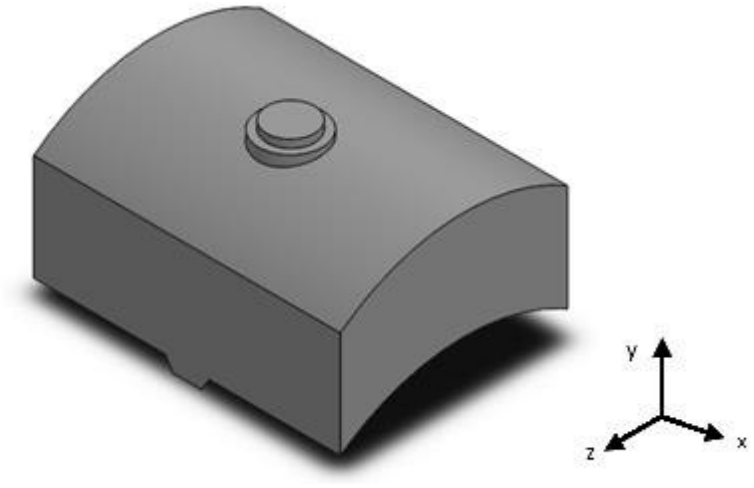

a) **Isometric view**

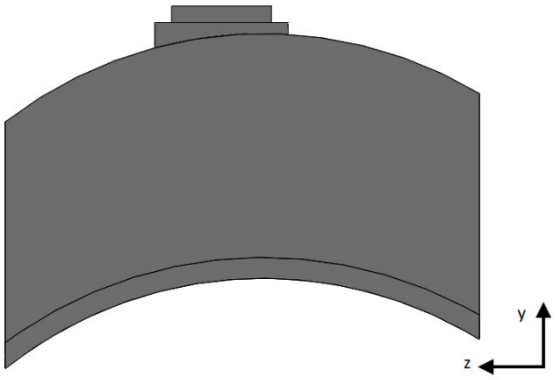

b) External lateral view

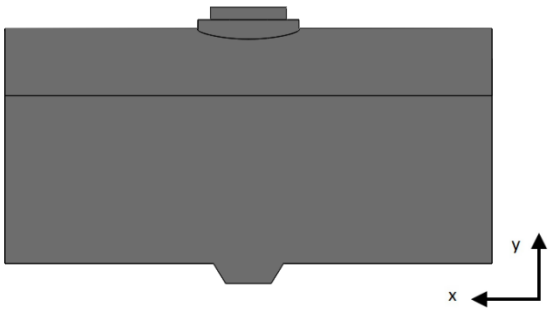

c) Frontal view

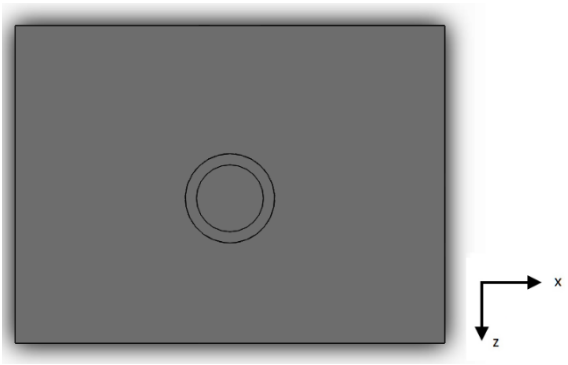

d) Upper view

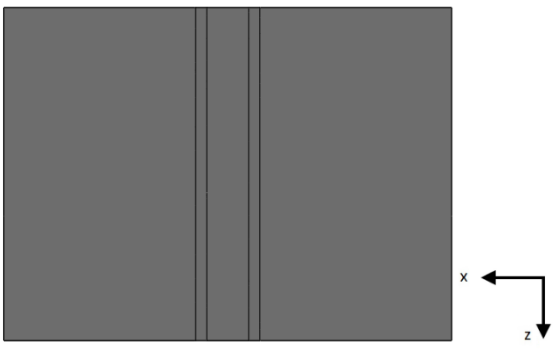

e) Bottom view

Figure 5.10. Sacrifice component.

Additional to the curve shape, it can be observed the existence of a peg on upper face. This mechanical anchorage allows sacrifice component alignment with tibial component. Tibial component is fixed to sacrifice component with a pocket, having limited displacement. However, it can slide above talar component following the plantar flexion movement of the feet [20].

On the inferior face, a guide is intended to align with talar component. In contrasts, this will give only one degree of freedom for the inferior contact zone.

Inner structuring of sacrifice component is evident on Figure 5.11. Symmetrical planes were intersected to the piece in order to show the twelve gaps inside of it:

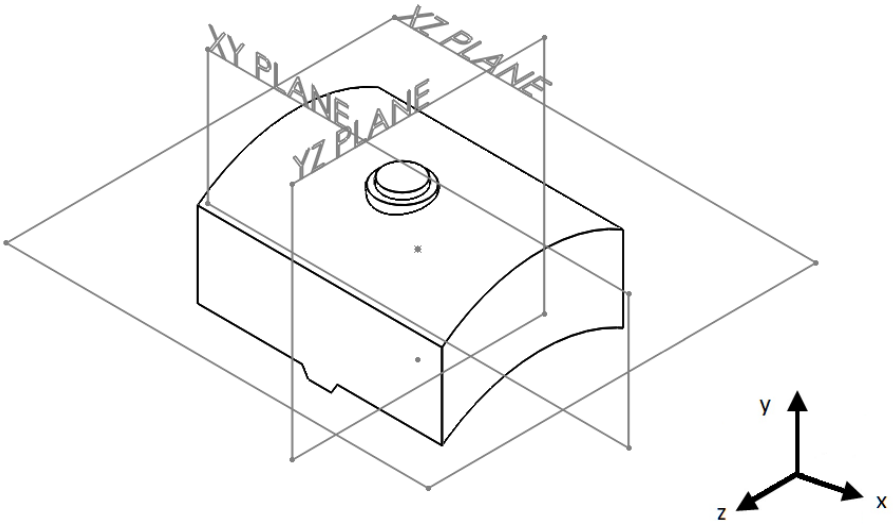

a) *Isometric view*

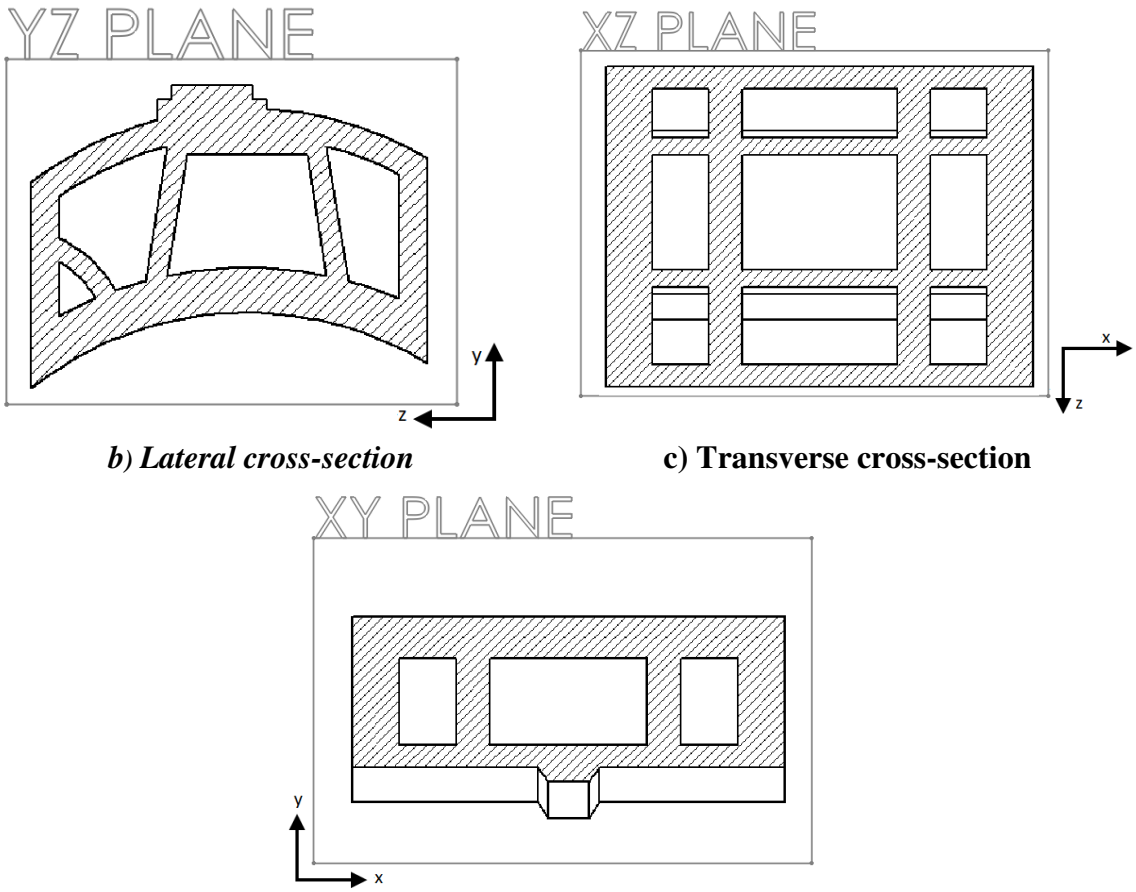

b) Lateral cross-section **c) Transverse cross-section**

d) *Frontal cross-section*

Figure 5.11. Inner structure of sacrifice component [156].

5.4. Tibial component

With sacrifice component geometry defined, the other components must be adapted to it and also to the corresponding attached bone. First one is tibial component, seen on Figure 5.12 below.

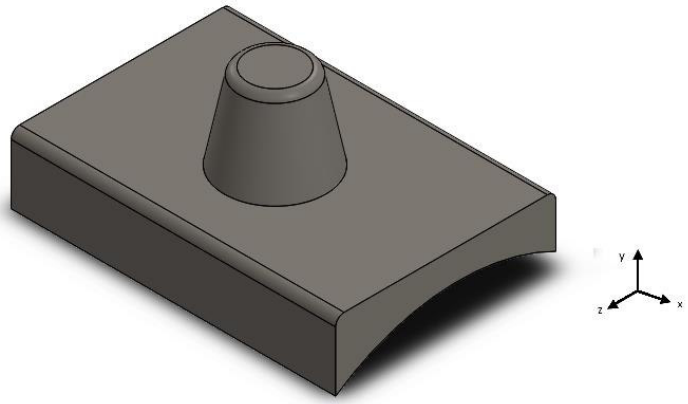

Figure 5.12. Tibial component. Isometric view.

The main body of the tibial component itself has a prismatic shape, with a flat upper face as well as the anterior, posterior, internal and external face. The inner face has a marked cylindrical concavity with a uniform radius.

It is observed in the upper part of the tibial component a spur of oblong shape, with a circular base that decreases its perimeter until a final rounding that allows its anchoring to the tibia itself (Figure 5.13). This surface can be subjected to a surface treatment to increase its roughness.

From previous information, it has been found that non-cemented anchorage with a non-constant axial width was helpful for avoiding loosening on TAA prosthesis [157]. Therefore, tibial component was designed with a fixation steam, characteristic also seen on commercial prosthesis such as Mobility™ [158] or INBONE® [159]. Steam longitude was reduced to avoid an excessive penetration, potentially detrimental for fixation [160].

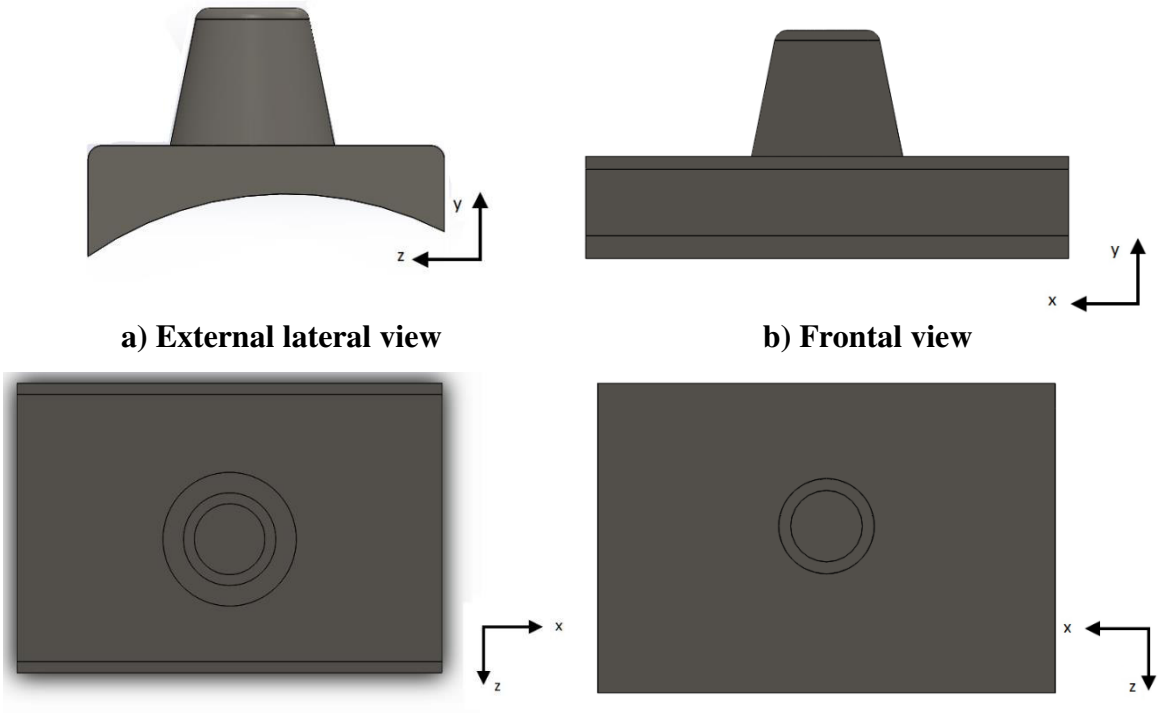

a) External lateral view **b) Frontal view**

c) Upper view **d) Bottom view**

Figure 5.13. Tibial component.

It is evident from the top view in the Figure that the spur itself is in symmetry with respect to the sagittal plane but is more aligned to the part of the tibiotalar joint rather than feet. This is clearer on full assemble.

During implantation the component is laterally restricted by the internal malleolus and the fibula. As mispositioning of the implant leads to gaps between bone and implant, and increased chances of micromotion and loosening [161], it was found an additional reason for using only one peg for tibial component anchorage.

In the lower part of the tibial component there is a cylindrical cavity that allows the partial anchoring of the sacrificial component, although it gives a certain rotation freedom on the plane parallel to the ground.

It must be addressed that most of the commercially available TAA prosthesis have metal-alloy components, being cobalt-chromium (CoCr) the most common, although other biocompatible materials such as stainless steel or titanium alloys are available [162] Even attempts on using a polymer tougher than UHMWPE have been registered [163] in an attempt to use a material with a density closer to the one of the human bone and reducing sacrifice component wear.

5.5. Talar component

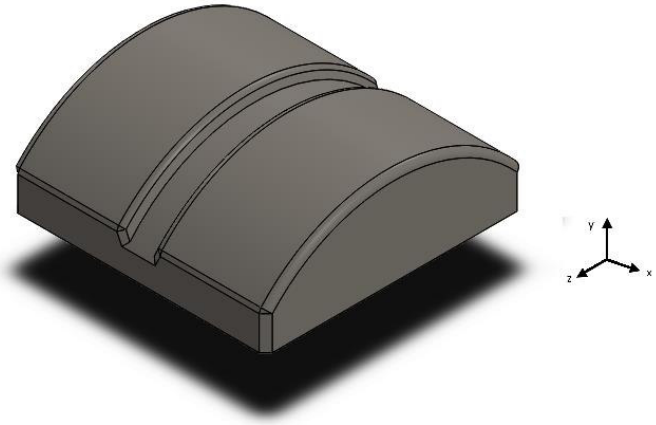

Figure 5.14. Talar component. Isometric view.

The talar element (Figure 5.14) consists of a convex cylindrical surface, congruent with the corresponding concave surface of the sacrificial component. Use of a spherical geometry in the talar was tested avoid stress concentrators while keeping lateral movement on TAA prosthesis. However, some instability was reported for that kind of designs [14]. The asseveration is supported by FEA model sliding instances.

A guide is present on its upper surface for good alignment, fundamental for a successful intervention [14,15]. So, lateral movement limitation is expected in exchange for better stability. Talar component is fixed to the talus with a steam on the bottom surface (Figure 5.15).

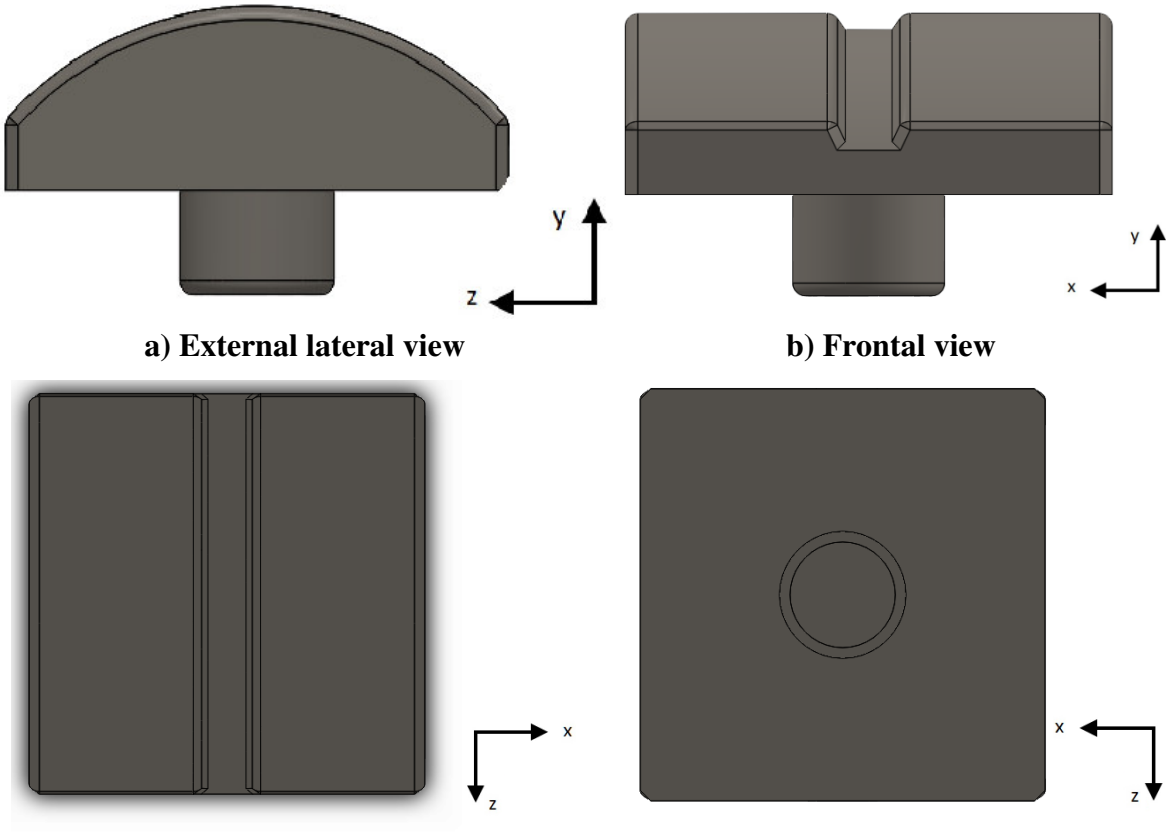

a) External lateral view **b) Frontal view**

c) Upper view **d) Frontal view**

Figure 5.15. Talar component

As it happened with the tibial component, a single spur is used for a better possibility of alignment during surgical intervention. Even so, many existent prosthesis have multiple anchorage points [161], with certain inclination such as Vantage® [164] or both as Infinity™ [148] Total Ankle Systems.

Reports of a massive talar component on TAA prosthesis show that this condition can be detrimental in case of a severely damaged bone. In some cases, it is preferable to remove the complete talus and use an artificial substitute of the overall bone [14], or the use of a custom made talar component [165]

5.6. Prosthesis final assemble

The final appearance of TAA prosthesis is shown on Figure 5.16. The proposed design has maximum dimensions of 49.48 mm in height, 38.48 mm in width and 39.00 mm in depth trying to preserve the physiological dimensions of the joint. Semi translucent sacrifice component appearance is for sake of showing the inner structure.

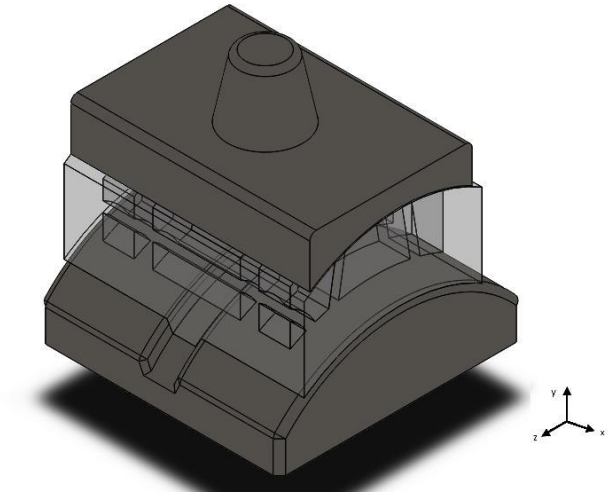

Figure 5.16. TAA prosthesis assemble. Isometric view.

Figure 5.17 shows other views of the full assemble.

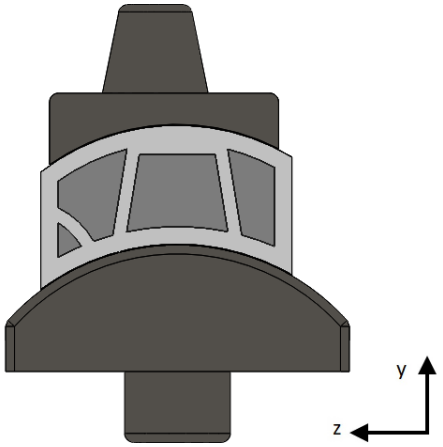

a) External lateral view

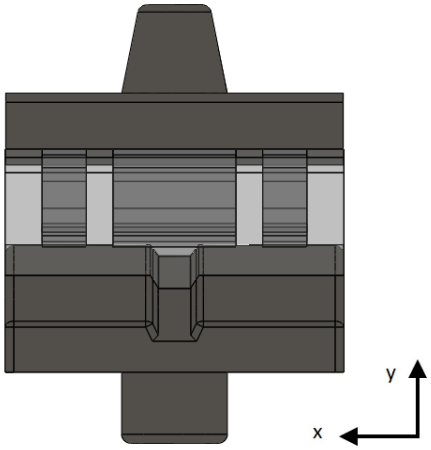

b) Frontal view

Figure 5.17. Full assemble for TAA prosthesis.

This CAD model will be used for a FEA analysis on conditions closer to the physiological ones on the next chapter.

As it has been established for TAA [14] ostectomy of tibia and astragalus is needed for prosthesis implementation. From the same CAD model, needed bone section for prothesis implanting on tibia and astragalus (Figures 5.18 and 5.19)

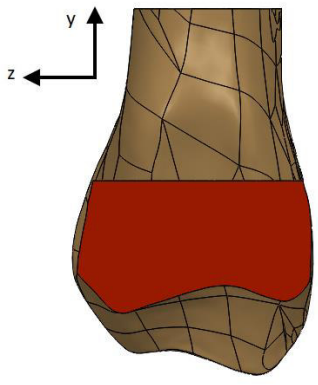

a) External lateral view

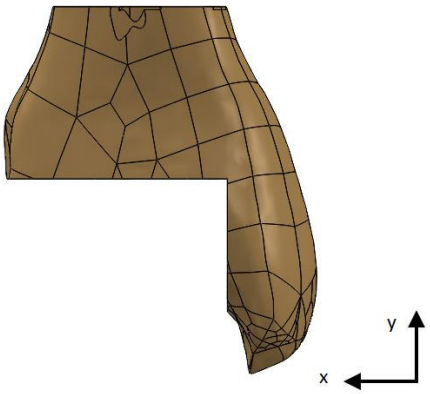

b) Frontal view

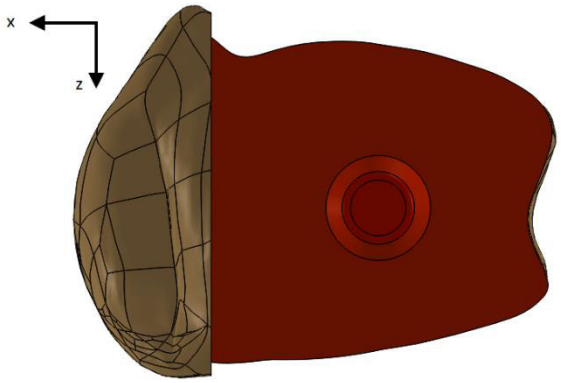

c) Upper view

Figure 5.18. Needed bone extirpation for tibial component fixing.

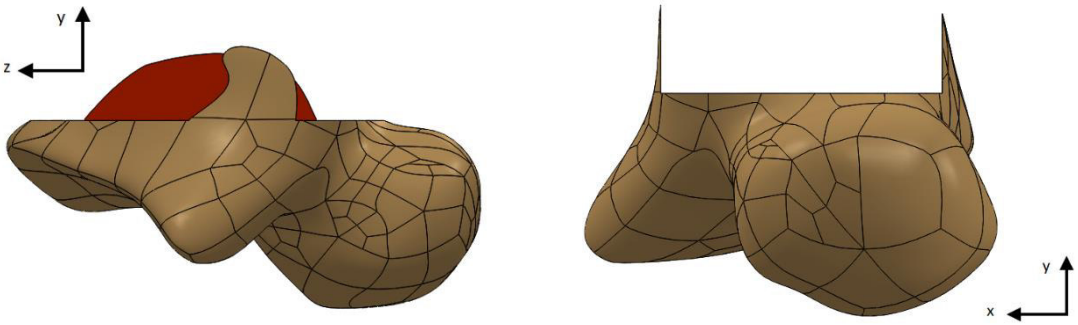

a) External lateral view **b) Frontal view**

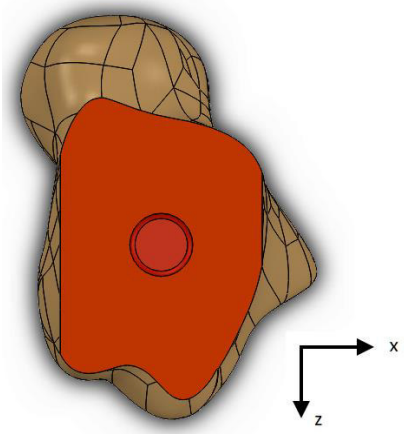

c) Upper view

Figure 5.19. Needed bone extirpation for talar component fixing.

Final situation of the prosthesis within ankle joint is shown clearly on Figure 5.20

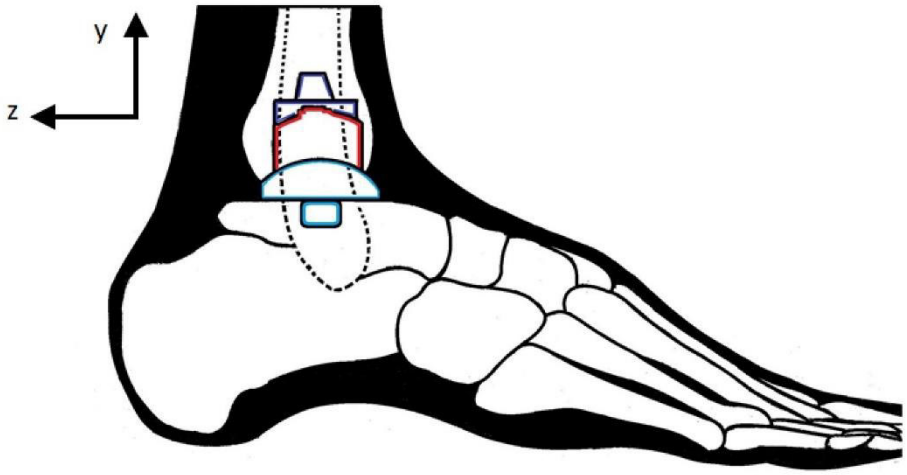

a) External lateral view

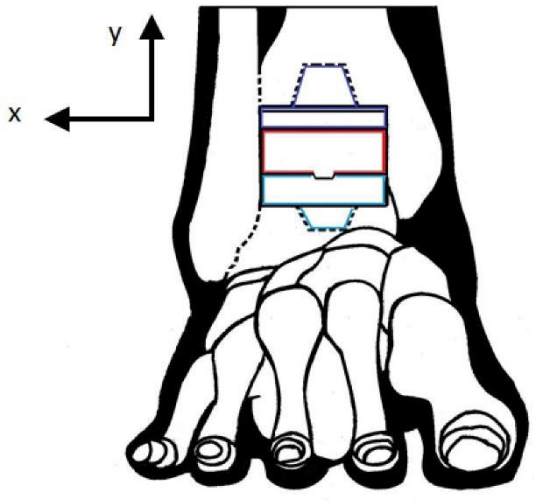

b) Frontal view

Figure 5.20. Implantation of TAA prosthesis in joint [16].

5.1. Rapid prototyping

Additive manufacturing – also known as 3D printing- is a manufacturing technique in which structures are made by the addition of thousands of minuscule layers which combine to create the product [166].

As a CAD sketch is produced, the additive manufacturing equipment reads in data from the CAD file and lays downs or adds successive layers of liquid, powder, sheet material or other, in a layer-upon-layer fashion to fabricate a 3D object [166].

In this case, even when it will be ill-suited for mechanical tests, a rapid prototype was built for assuring the TAA prosthesis intended behavior.

A Makerbot ™ Replicator equipment found on Universidad de Guanajuato- DICIS was used for building of the presented TAA prosthesis model (Figure 5.21)

Figure 5.21. Makerbot ™ Replicator [167].

Acrylonitrile butadiene styrene (ABS) was the thermoplastic of use. Tibial and talar components (Figure 5.22) were printed with 50% of density. Sacrifice component (Figure 5.23) was printed with a 100% density and in translucent material

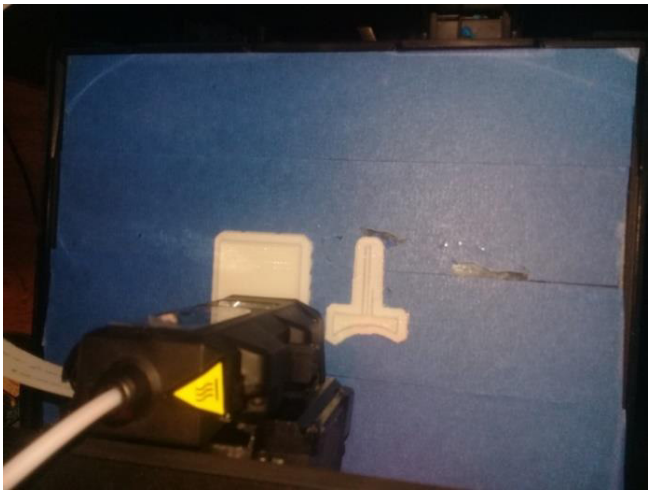

Figure 5.22. 3D printing of the rapid prototype. Tibial and talar components.

Figure 5.23. 3D printing of the rapid prototype. Sacrifice components.

The complete rapid prototype assemble is shown on Figure 5.24.

Figure 5.24. Rapid prototype of the assemble.

Even with a different, rougher material, model movement of sacrifice and talar component was smooth. Tibial and sacrifice component remained mostly fixed to each other.

The use of a rapid prototype also allowed for a glimpse of future solutions for the fabrication on design materials. Additive-manufacturing allows for creation of custom-made prosthesis by laser-melting metal powders layer-by-layer. TAA is particularly suitable for this progress because of the limited number of sizes and the poor bone stock [168].

5.2. Discussion

Main contribution of this section is the ideation of a full assemble ready for testing on a Finite Element Analysis (FEA). The reason for most recent TAA prosthesis designs not being an automatic choice of treatment is a result of the strict indications for surgery alongside the relatively high reported clinical failure rates [169]. The implementation of simulation should foresee possible issues as possible.

Insight on previous designs, taken decisions on deviations on anatomical geometry, material choice, building and effectiveness reviewed on Chapter 1 were broken down on each component of TAA prosthesis on a modular focus development.

As it has been earlier explored, the sacrifice component is the most susceptible to failure. The project is mostly oriented to the bettering of it. Being limited on material selection for its build (surgical grade UHMWPE), a search for a structural solution for stress diminishing and redistribution has been chosen.

Use of optimization tools has been previously used on other prosthetic applications, with the main goals of reduction of stress concentrations at the interface between bone and these devices [170]. Although the initial design took distance from the anatomical geometry, this focus is deliberate, in order to provide better stability to the TAA prosthesis complex.

The scope of this thesis is made on design and study of polymeric component of the TAA prosthesis. It is assumed that effects of stress on metallic components' structure is rather neglectable in terms of possible failure. However, the interaction of this components and the adjacent bones should be explored.

Chosen single anchorage on design, may not be the optimum approach for a better support. In contrast, the former disposition of a single beam allows for a quick and correct alignment of inserted components of TAA, a key condition for a successful intervention.

Rapid manufacturing was used to generate a physical model, albeit one in a material with different mechanical properties. However, while the model stability and devised degrees of freedom could be confirmed with this prototype. Concerning future manufacturing of a better suited prototype 3D printing on UHMWPE has been tested on similar applications [171], and the possibility for manufacturing tibial and talar component in other biocompatible materials remains open.

5.3. Chapter conclusions

Generation of an energy absorbing system inside TAA prosthesis is proposed to extend its structural life and diminishing adverse effects. In this development, a new prosthesis geometry design with internal damping structure is proposed.

Developed TAA model was defined as a three-element, congruent, with one anchorage point for tibia and other for talus. Material assigned for its construction were surgical grade UHMWPE for sacrifice component and a metallic alloy for the remaining ones. This constitution is typical for most orthopedic prosthesis designs.

About the inner built for sacrifice component, software for shape optimization was used among with trial and error developments, testing the isolated component under the maximum measured load for ankle joint during gait.

In order to evaluate the results, a CAD model is ready for a complete FEA analysis in working conditions closer to the ones on the ankle joint.

As a side project, a rapid prototype version of the TAA prosthesis was made. This gave an input on how the prothesis will work, even when its material properties differ significantly.

Chapter 6- Finite element analysis of ankle joint prosthesis

On the previous chapters, after many iterations, an ankle joint prosthesis model with an inner hollow structure for the sacrifice component was fully developed. In this section, it will be tested on a finite element analysis (FEA). For this end, material models and properties obtained on preceding development were used.

A set of physiological load conditions for ankle joint are applied for simulation. Results are focused on total displacement, strain, safety factors and equivalent stress. Performance of structured prosthesis is compared among a solid proposal and literature findings for market-available prosthesis.

Findings suggest that the proposed design can be operated safely on all simulated cases. Stress distribution is changed with the use of an inner structure and is susceptible for improvement.

1.1. Introduction

Finite element analysis (FEA) is a numerical method for solving engineering problems by means of its formulation as a system of algebraic equations [172]. FEA is particularly suited for structural analysis, as it allows the study of complex geometries, focus on local effects and the use of dissimilar material properties [143].

One of the earliest (1972) applications of FEA to orthopedic biomechanics was the evaluation of stresses in human bones [173]. Since then, it has been used for a variety of analysis on musculoskeletal system, particularly the interaction of cartilage on contact surface [174-176]. Healthy and affected ankle joint tissues conformation and operation had also been examined on FEA [177], with significantly useful insight of its mechanics that correlate with experimental studios, especially for stress distribution on joint surface [22,178-180].

With this precedents, market-available TAA prosthesis had been tested with FEA, isolated or in comparison, such as Zenith™ [181], Agility™ [182-184] and STAR™ [183,185] BOX® [186], Mobility™ [161,184] and SALTO® [161,162], looking fundamentally for micromovement, stress distribution and wear. Cited works were positively correlated with experimental tests in most of the cases.

This focus on simulation can give a partial validation or allowing for a more convenient analysis for the previously developed prosthesis designs, within reasonable material and time limitations.

6.2 Chapter nomenclature

F_n	Normal force on node
F_t	Tangential force on node
k_n	Normal stiffness
k_t	Tangential stiffness
x_p	Penetrating distance
x_s	Sliding distance
λ	Augmented Lagrange term
σ_{ij}	Component of stress deviation tensor
σ_v	Von Mises stress

6.3 Preprocessing

As seen on the previous chapters, the mechanical characterization of medical grade UHMWPE probes led to the use of a bilinear isotropic model (BIH) for GUR1050 on sacrifice component, with additional data accounting for the fatigue effects on the material.

By other side, the material properties of the metallic components of the prosthesis design were at first considered as a linear material model of structural steel for early design and

testing simulations. Later, these were changed for Ti6Al4 alloy, a material with a long tradition of use on orthopedics due its low density and excellent corrosion resistance [186]. Used properties were referenced by ASM Aerospace Specification Metals Inc [187]

Table 6.1 summarizes the material properties used in the respective material models.

Table 6.1. Applied material properties.

GUR1050	**Value**	**Units**
Young Modulus	289.00	MPa
Poisson Ratio	0.46	---
Yield Strength (BIH)	14.15	MPa
Tangent Modulus (BIH)	95.00	MPa
Tensile Yield Strength	20.00	MPa
Compressive Yield Strength	25.00	MPa
Tensile Ultimate Strength	45.80	MPa
Compressive Ultimate Strength	39.60	MPa
Ti6Al4	**Value**	**Units**
Young Modulus	113.80	GPa
Poisson Ratio	0.34	---
Tensile Yield Strength	880.00	MPa
Compressive Yield Strength	970.00	MPa
Tensile Ultimate Strength	950.00	MPa
Fatigue Strength	510.00	MPa

6.3.1 Boundary conditions

The simplest boundary condition available for simulating the ankle load is the application of a single axial load. A value of 3650 N was used, based on the maximum load applied to the ankle joint during normal gait by a person of 65 kg [29,155], being the recommended upper weight limit for a TAA patient [29].

This value is added to the upper surface of assemble, keeping the bottom end fixed, as it would be to the talar bone. However, this was tested only for the reference neutral position, with the feet parallel to the floor.

A second set of load conditions was taken from previous references [182,188] is thus used for further exploration of design reliability. In addition to the main axial load, lateral forces and moments are taken in consideration. Details for these loads are recorded on Table 6.2.

Table 6.2. Ankle loads used as boundary conditions.

Load conditions	Reference angle on working plane (Degrees)	Axial Load (N)	Antero-posterior Load (N)	Internal-External Load (N)	Antero-posterior Moment (N.mm)
Simple axial	0	-3650	0	0	0.00
Neutral	0	-600	-280	150	2.85
Dorsal flexion	-10	-1600	-185	-185	6.20
Plantar flexion	15	-400	-245	100	-0.10

For the later, three different positions had been named as neutral (original one), maximum dorsiflexion and maximum plantar flexion. These were configured on the CAD model, following the reference angle on working plane, as the TAA prosthesis will assume these during operation. Figure 6.1 shows clearly the different positions. Simple axial shares configuration with neutral stance

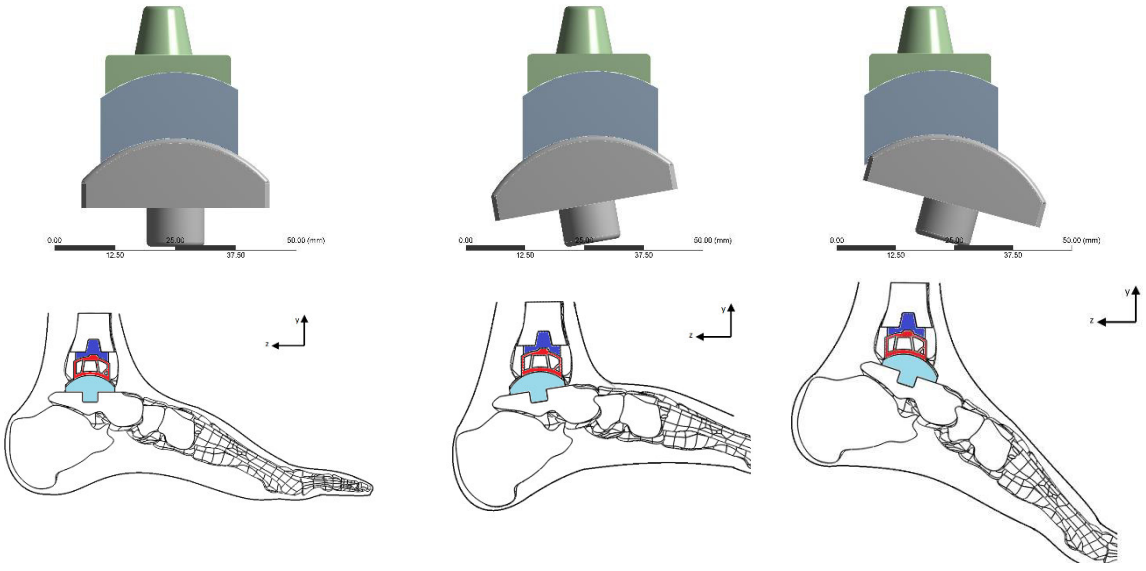

a) b) c)

Figure 6.1 External lateral view of a) neutral b) dorsiflexion c) plantar flexion position.

Complementarily, a surface displacement restriction on upper surface of tibial component was added on all models for more stability. This effect is justified as direct contact with tibia does not allow for rigid rotation of the component.

In resume, four different sets of boundary conditions are used (with the basic scheme shown on Figure 6.2) having a total of eight simulation cases, with both solid and structured sacrifice components.

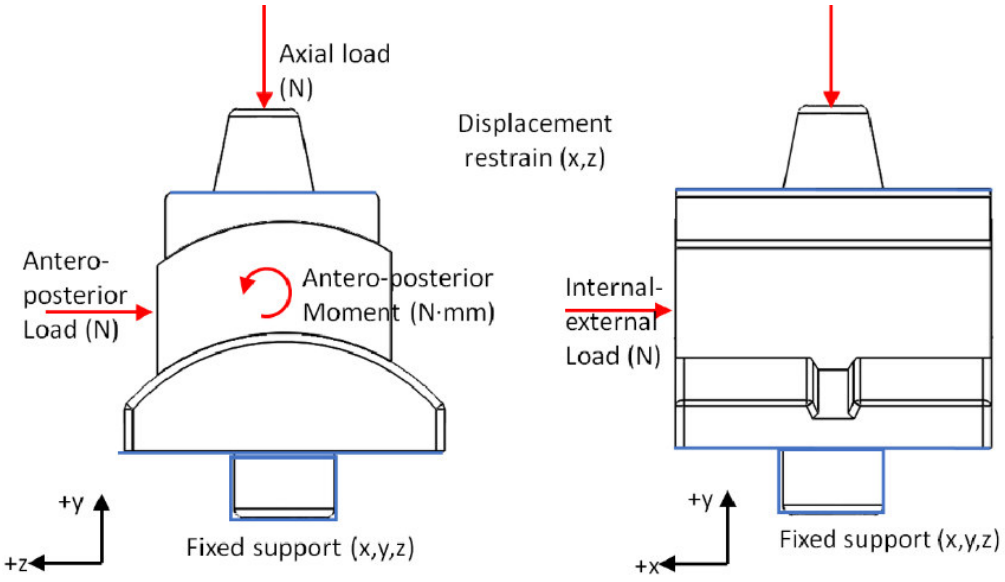

Figure 6.2. a) Applied boundary conditions [156]

The upper contact of tibial and sacrifice component was considered as bonded, as the prosthesis design is semi-constrained. The contact among sacrifice and talar component was held as a no-separation one. The difference among these contacts is settled as the former does not allow for sliding, while the later does. In both cases the tangential force applied a node is governed by the equation (Eq. 6.1):

$$F_t = k_t x_s \tag{6.1}$$

With k_t being the tangential contact stiffness, and x_s, the sliding distance that should tend to zero [107].

An augmented Lagrange formulation was added for contact detection. This is based on penalization for penetration. Governing equation (Eq. 6.2) is very similar to (Eq. 6.1), with the augmented term λ that makes the contact less sensitive for normal stiffness changes [107].

$$F_n = k_n x_p + \lambda \tag{6.2}$$

As metallic and polymeric components of the assemble have very different mechanical properties, normal stiffness factor k_n is was set to 10, and stiffness is recalculated each iteration to ensure numerical stability. reducing penetration. The main drawback of this choice was the need of additional iterations for reaching equilibrium, and the possibility of bounce on the gap among the pieces in contact [107], especially for the case of plantar flexion boundary conditions.

6.3.2 Meshing conditions

Eight-node SOLID145 elements [107] with 1.00 mm of edge were used (Figure 6.3). Size choice was settled by a combination of convergence on numerical results and computational efficiency.

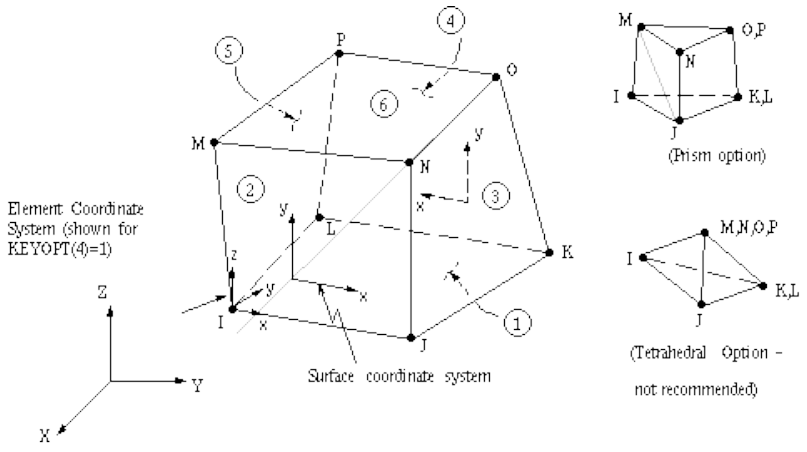

Figure 6.3. Description of SOLID145 element (ANSYS 15®) [107].

Both hexaedrical and tetraedrical elements could be used for simulation (Figure 6.4). Preliminary tests show that hexaedrical elements allow for a more uniform and sparser, less time- consuming meshing on solid sacrifice component.

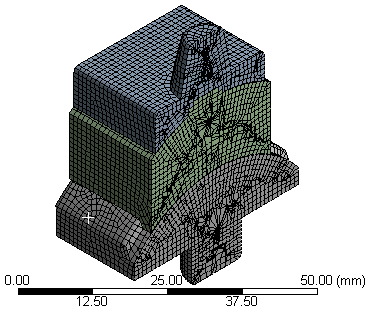

a) Solid, hexaedrical

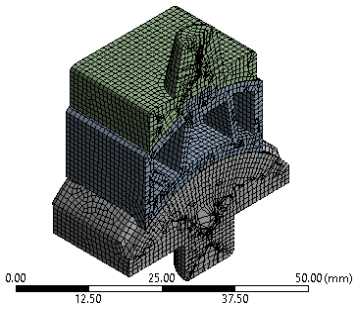

b) Structured, hexaedrical

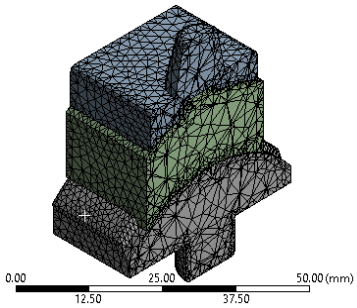

c) Solid, tetraedrical

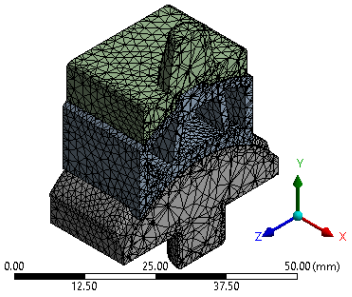

d) Structured, tetraedrical

Figure 6.4. Representative mesh quality.

However, these advantages are lost for the hollow sacrifice component, and numerical convergence tends to instability, so the later were chosen and used for the subsequent simulations.

The number of elements was kept relatively constant, on range of 330,000 elements for solid component assembles and 300,000 for structured ones Table 6.3 gives a summary of mesh properties.

Table 6.3. Summary of mesh properties for simulation cases.

Sacrifice component type	Boundary conditions case	Number of nodes	Number of elements	Abbreviation
Solid	Simple axial	473475	334054	SOSA
	Neutral	473475	334054	SON
	Dorsal flexion	474146	334553	SODF
	Plantar flexion	474072	334489	SOPF
Structured	Simple axial	435135	299832	STSA
	Neutral	435135	299832	STN
	Dorsal flexion	435806	300331	STDF
	Plantar flexion	435732	300267	STPF

Element edge size choice (1.0 mm) allowed for similar element numbers on both solid and structured sacrifice component cases. A longer element edge (1.5 - 2.0 mm) would had led to defective results as the inner elements of the structure would had had only one element on thickness.

However, to take account of the influence of smaller element sizes, a mesh sensibility analysis was reported on the following section.

6.3.3 Mesh sensibility

One of the faced inconvenient during the recursive solution of simulations was the necessity for very long lapses of simulation. Existence of contacts were a key factor for this delay. However, a mesh sensibility test must be carried, at least for the sacrifice component.

Then, the geometry of the prototype sacrifice component was subjected to the loads of the neutral boundary conditions applied directly on its surfaces (Figure 6.5):

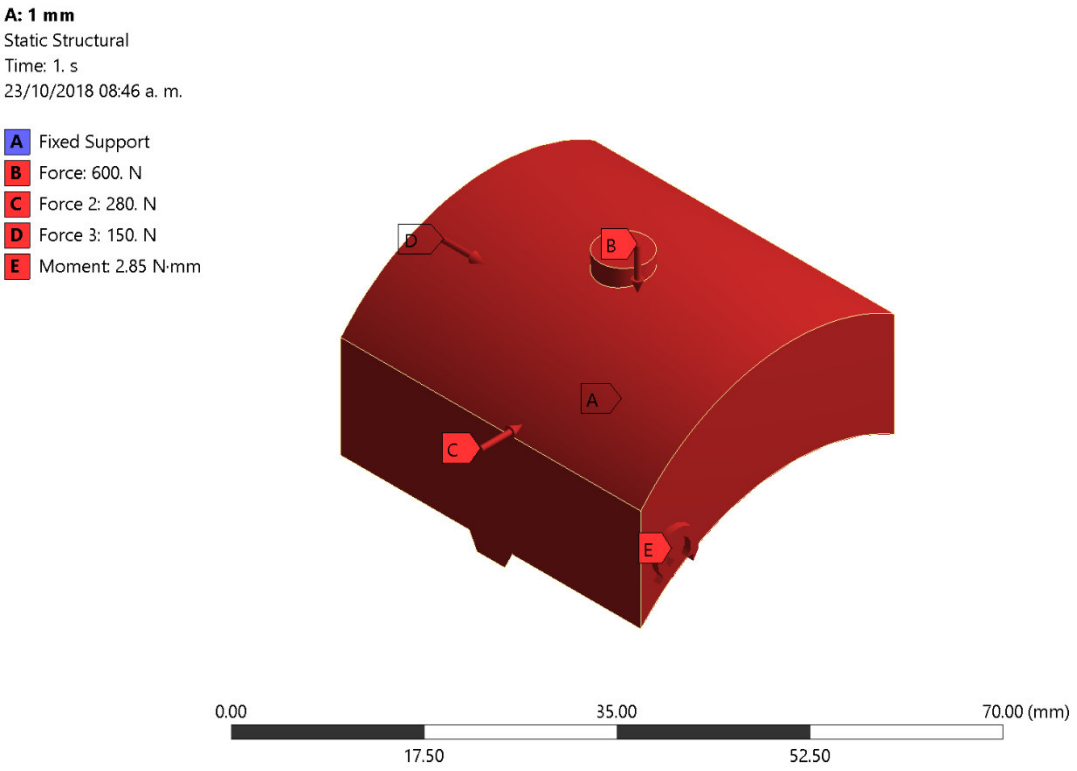

Figure 6.5. Boundary conditions for mesh sensibility analysis

Mesh changes were controlled by variation on element edge length (1.20,1.00, 0.80, 0.65, 0.50, 0.40 mm). Deformation (Figure 6.6) and equivalent stress were considered the parameters of interest.

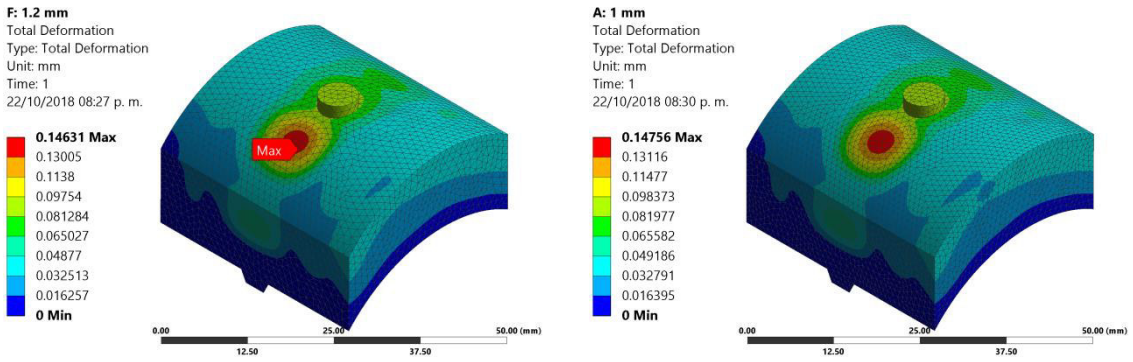

a) 1.20 mm

b) 1.00 mm (original)

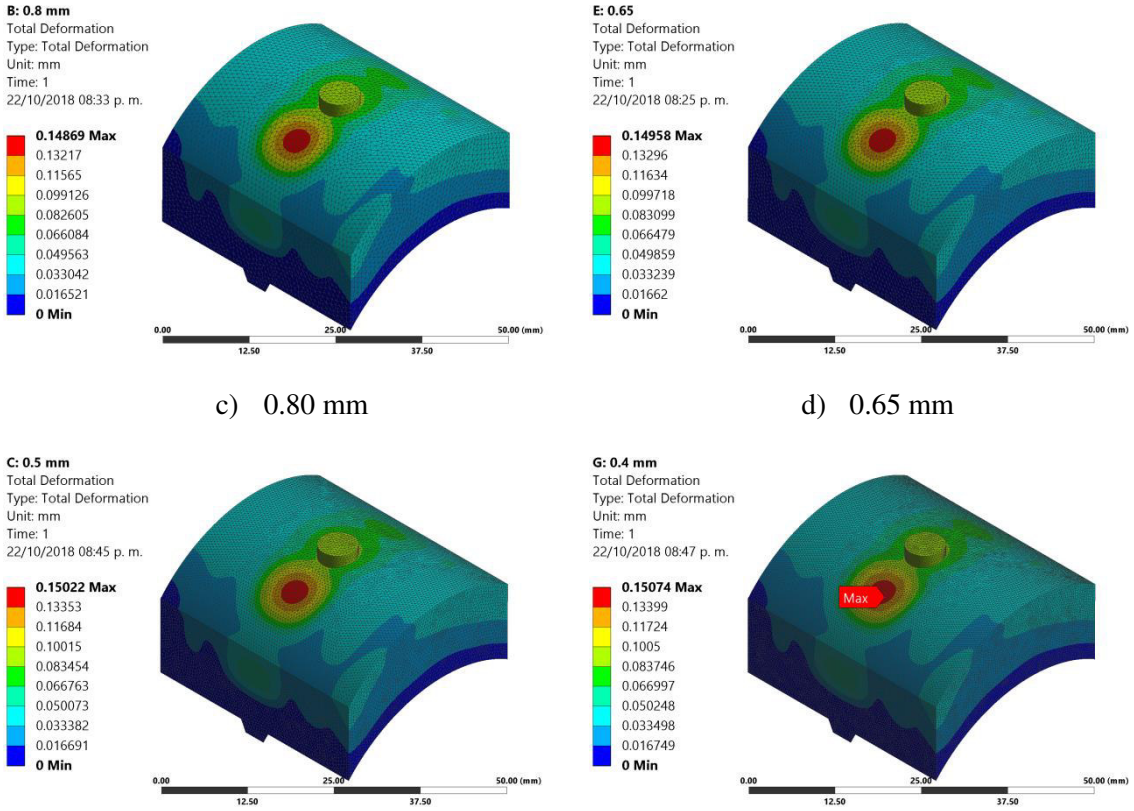

c) 0.80 mm

d) 0.65 mm

e) 0.50 mm

f) 0.40 mm

Figure 6.6. Mesh sensibility for deformation.

As seen, deformation results, in qualitative terms are identical, with the same spatial distribution. For quantitative comparison, three reference points (labeled A, B, C) are selected for data lecture. Their location is shown on Figure 6.7. A graphic relation of maximum measured deformation and mesh element number is shown on Figure 6.8 to illustrate the possible mesh sensibility.

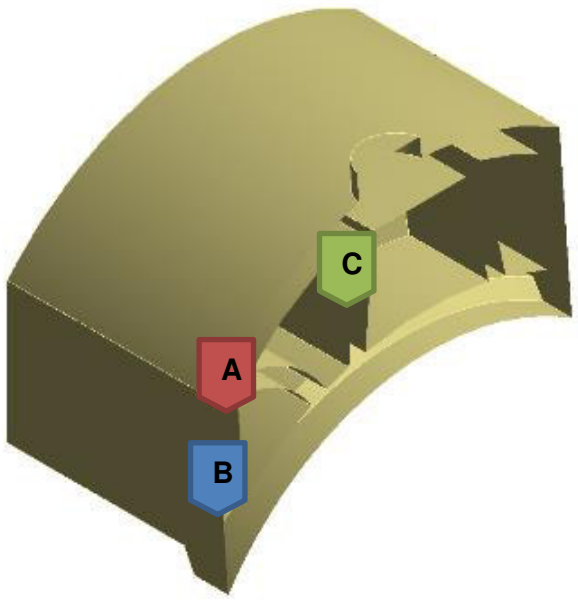

Figure 6.7. Selected points for reference on mesh sensibility.

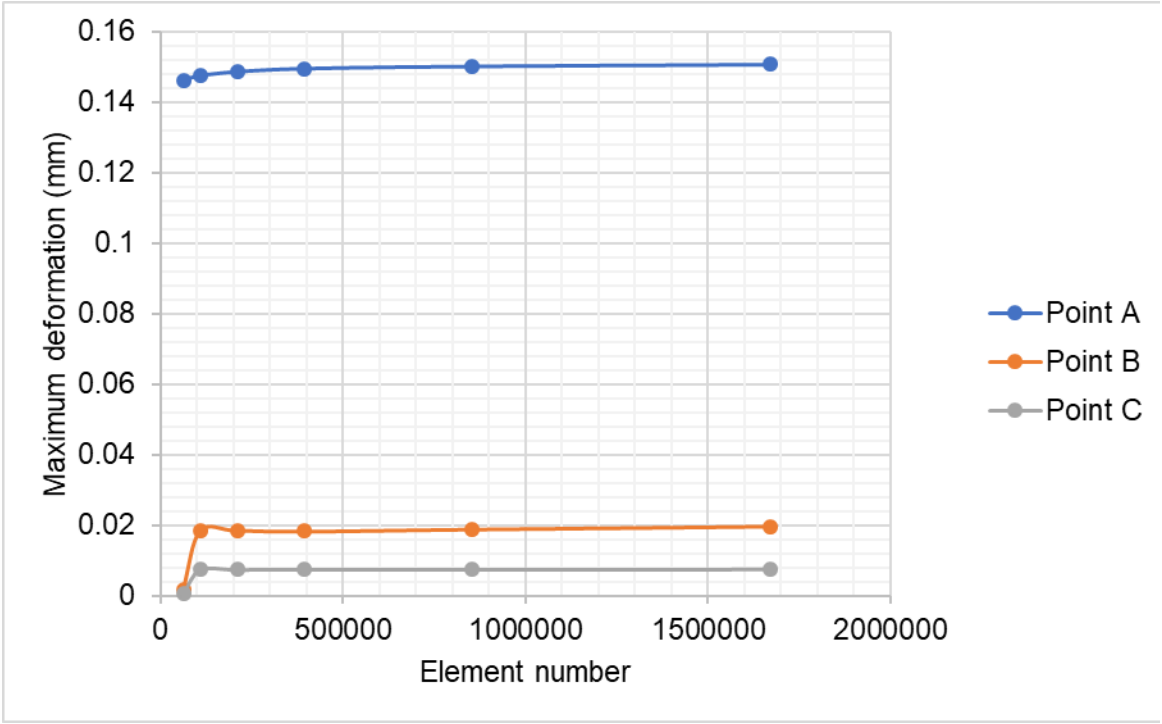

Figure 6.8. Element number vs maximum deformation.

It is found that deformation is independent of mesh element size. In contrast, as equivalent stress resulted more sensible to element size.

An additional mesh (element 0.45 mm) was used for a clearer insight. Figure 6.9 shows a view on the sagittal plane of the sacrifice component, as the maximum values are found on the inner structure of sacrifice element.

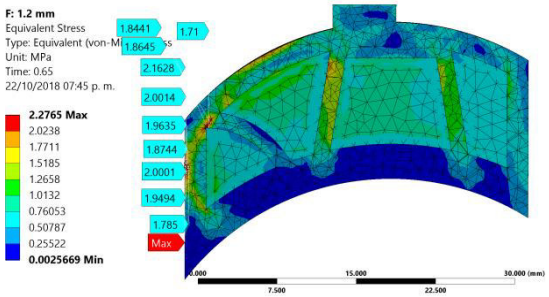

a) 1.20 mm

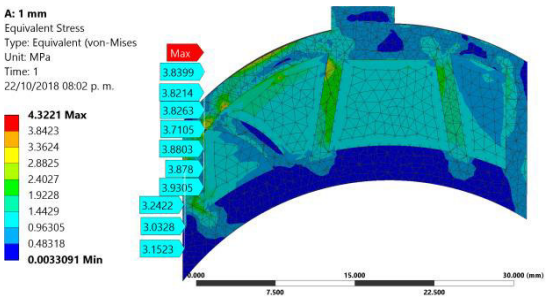

b) 1.00 mm

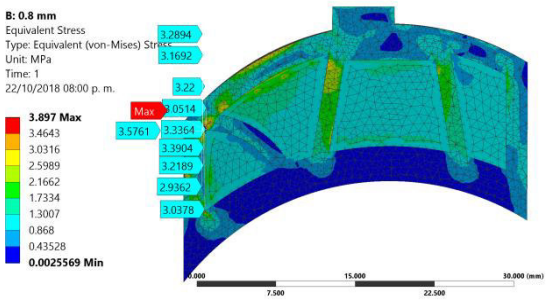

c) 0.80 mm

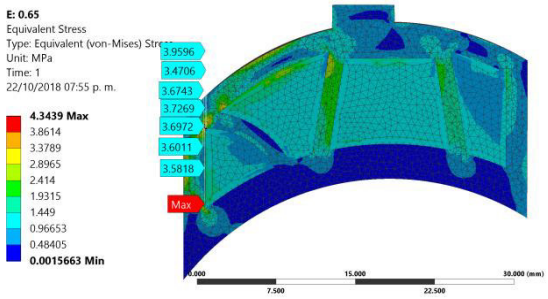

d) 0.65 mm

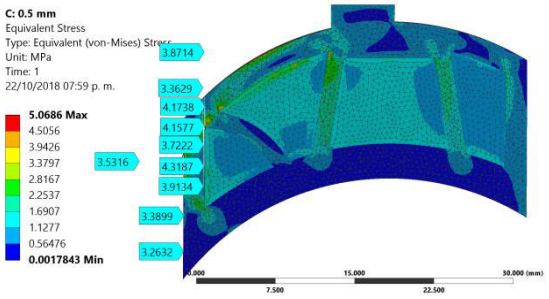

e) 0.50 mm

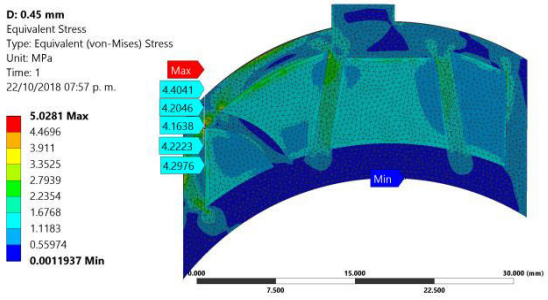

f) 0.45 mm (additional)

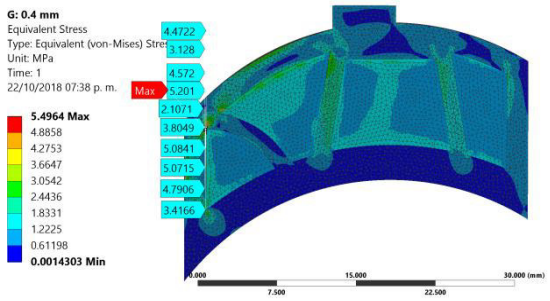

g)

Figure 6.9. Mesh sensibility for stress.

Element number influence on maximum stress value is seen on Figure 6.10.

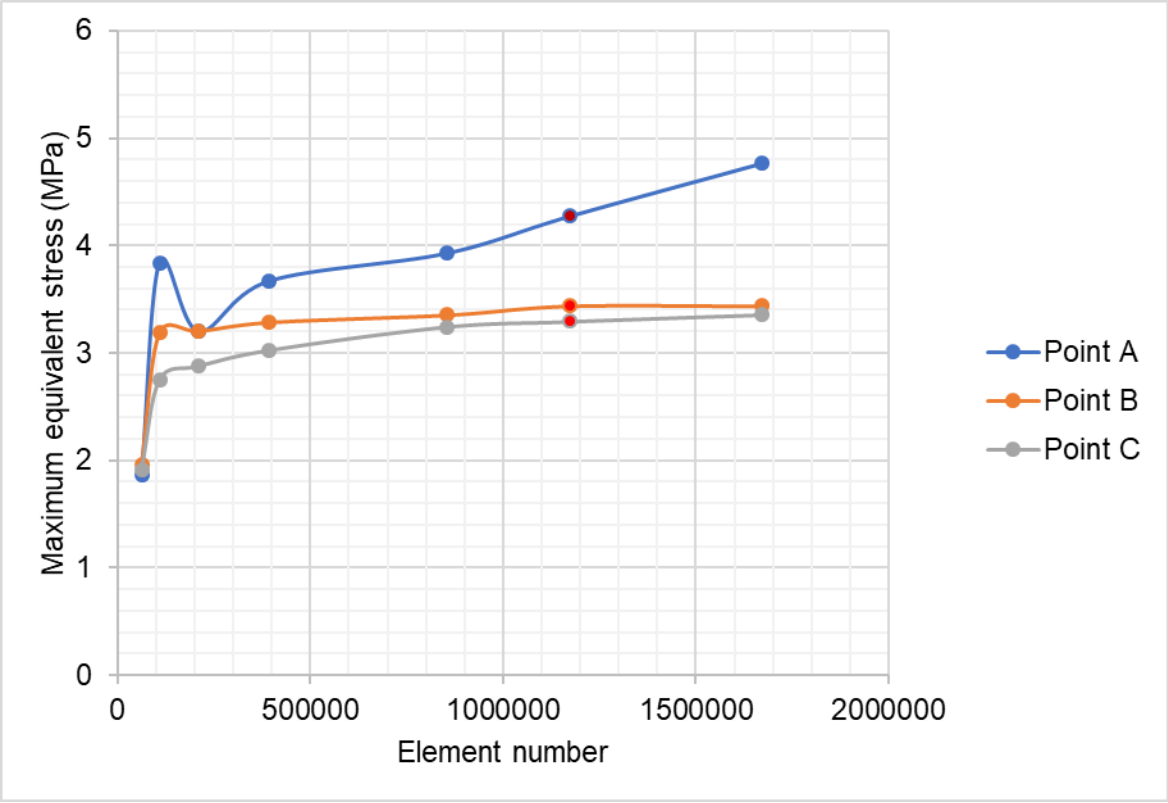

Figure 6.10. Element number vs. maximum averaged stress.

Points B and C, subject to lower stress values, are hardly sensible to reductions on element size. However, it was found that elements on the point A tended to diverge. A clear analysis of mesh quality on the size showed a tendency for acute angles and other shape oddities associated with mesh reduction.

As other undesired effect, use of smaller elements (0.65 mm and smaller) augmented solution time exponentially and did not show significant changes on results. Thus, the working element edge size was kept as 1.00 mm for the full analysis.

6.4 FEA Results

The results of interests for each component are a) maximum total deformation b) maximum equivalent strain c) maximum von Mises equivalent stress, d) safety factor. For the sacrifice component only, e) maximum strain energy, f) minimum safety factor to fatigue, and g) minimum operation cycles are examined, as the other components had a neglectable role or were not affected.

6.4.1 Total deformation

From Table 6.4 and Figure 6.11 can be inferred that geometry tends to, with independence of inner structure on sacrifice component, very similar qualitative behavior, with the dominance of axial loading effects on any position.

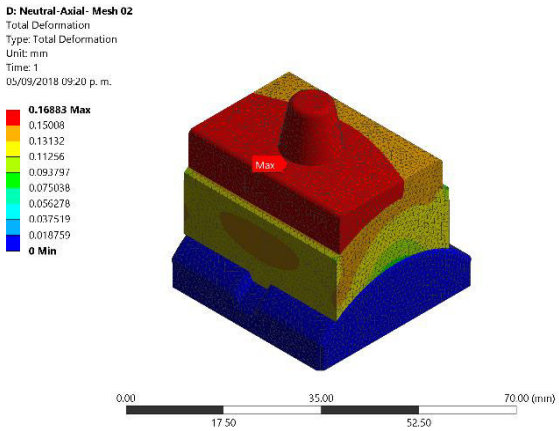

a) SOSA

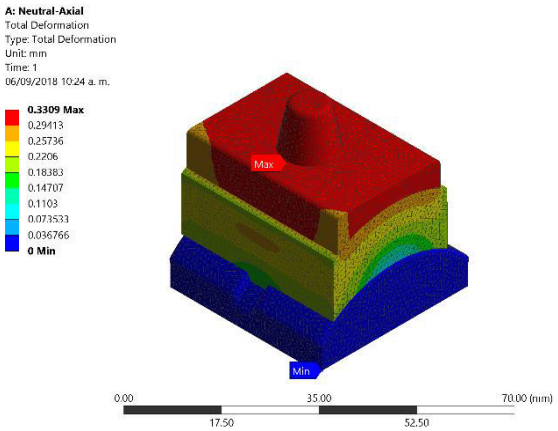

b) STSA

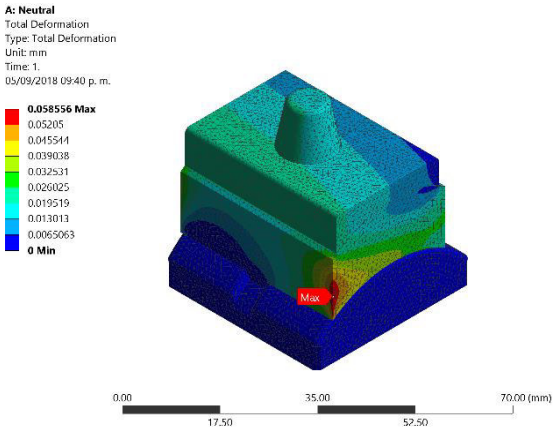

c) SON

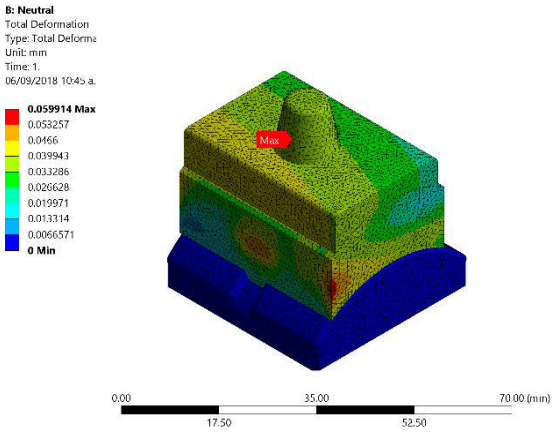

d) STN

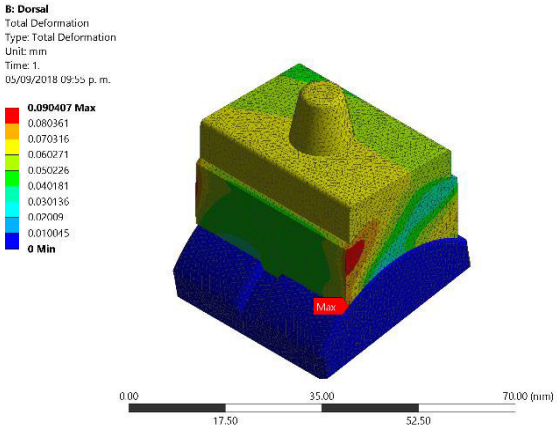

e) SODF

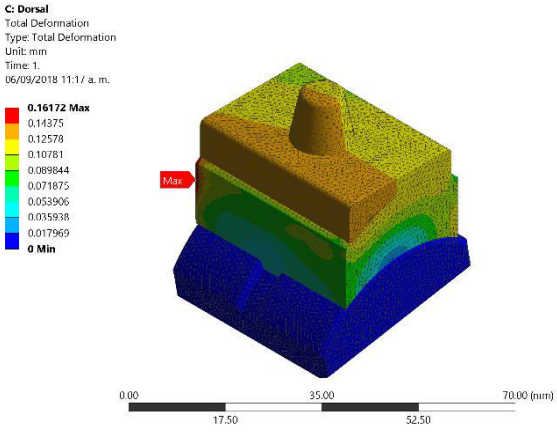

f) STDF

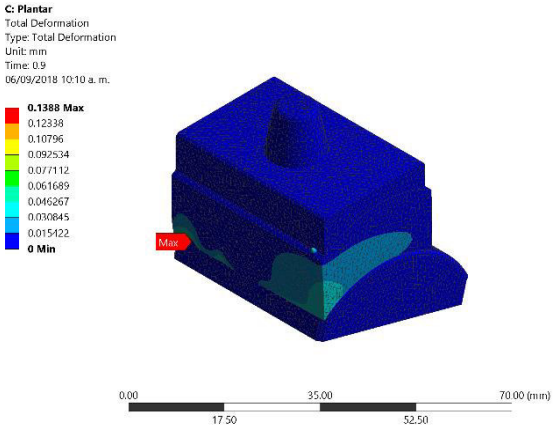

g) SOPF

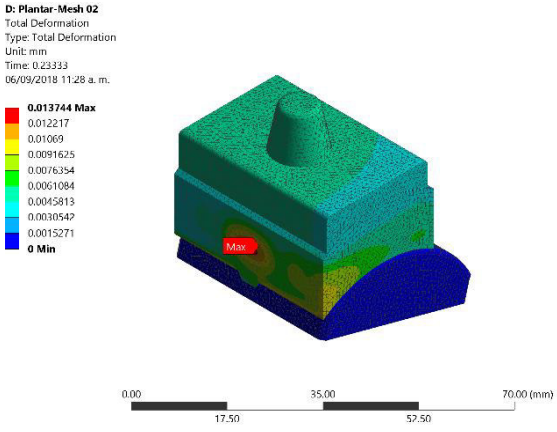

h) STPF

Figure 6.11 Assemble deformation state.

Table 6.4. Maximum deformation on prosthesis components (mm).

Sacrifice component type	Component	Simple axial	Neutral	Dorsal flexion	Plantar flexion
Solid	Tibial	0.1607	0.0256	0.0684	0.0128
	Sacrifice	0.1689	0.0586	0.0904	0.1388
	Talar	0.0006	0.0003	0.0005	0.0002
Structured	Tibial	0.3121	0.0448	0.1356	0.0245
	Sacrifice	0.3309	0.0599	0.1617	0.1808
	Talar	0.0010	0.0003	0.0008	0.0002

However, it must be addressed that maximum displacements on assembles with structured sacrifice components (0.31-0.33 mm.) can double the measured ones on solid sacrifice equivalent (0.16 mm). Talar component does not displaces noticeably (0.0001-0.0006 mm)

This is appreciated in better detail if a section of the model is done, as well with and adjustment for a common color scale for total deformation (as seen on Figure 6.12), where the hollow structure element deformation is concentrated mostly on the posterior zone of sacrifice component.

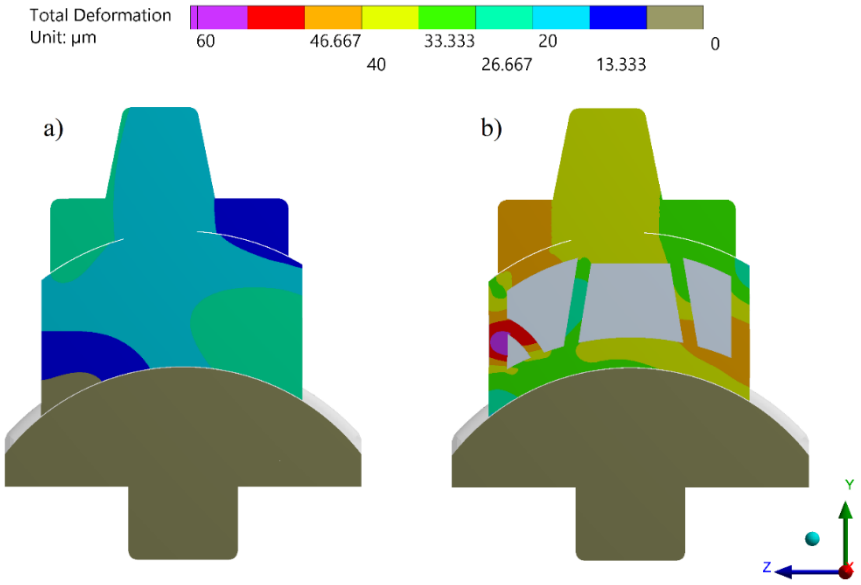

Figure 6.12 Assemble deformation state. Neutral position. Middle section [156].

It is understood that displacement lesser values are more suited, as the soft tissues could be overloaded, and the lower limb affected if the assemble has rigid motion [29,188].

Specific results for isolated components are described by subsequent Figures 6.13-6.15.

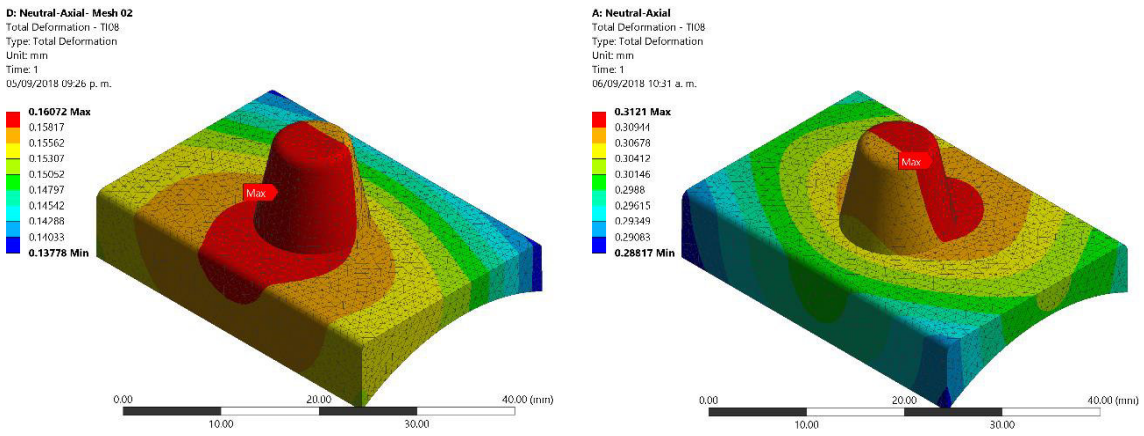

a) SOSA b) STSA

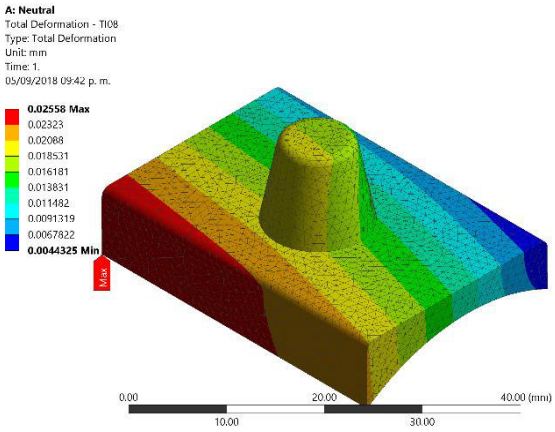

c) SON

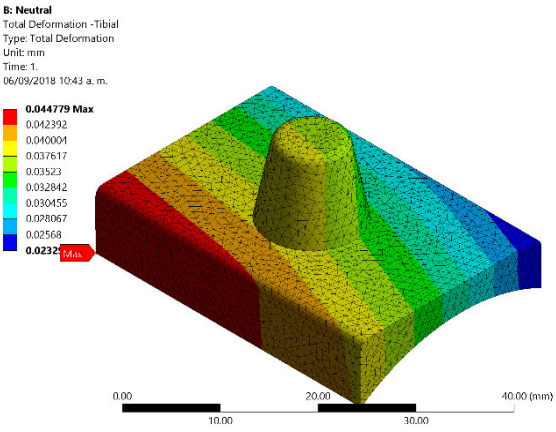

d) STN

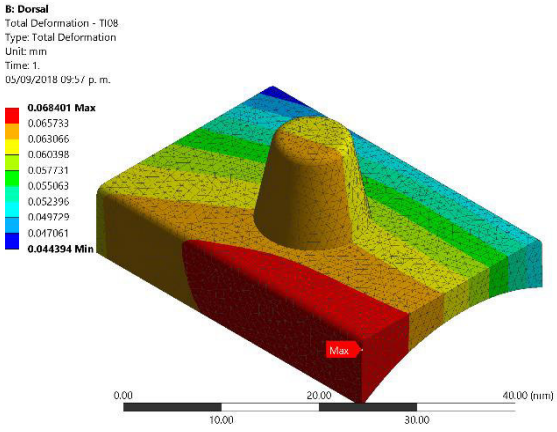

e) SODF

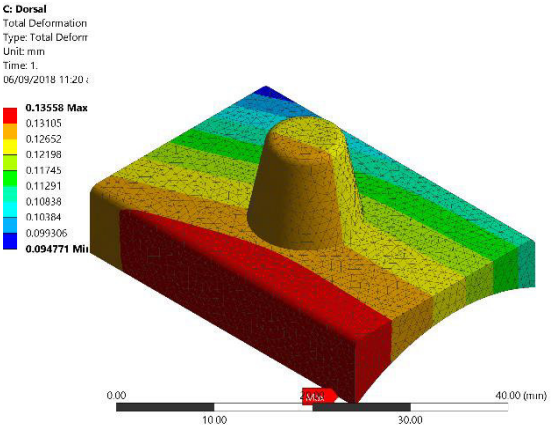

f) STDF

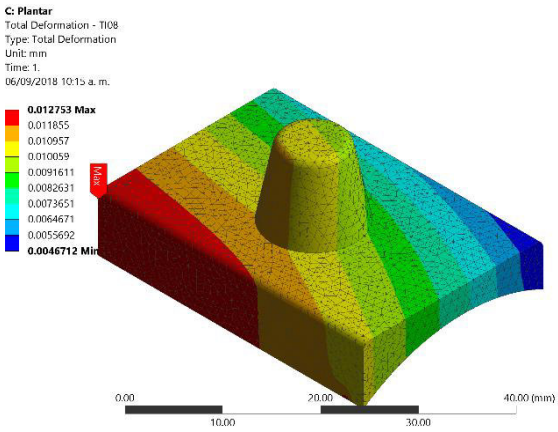

g) SOPF

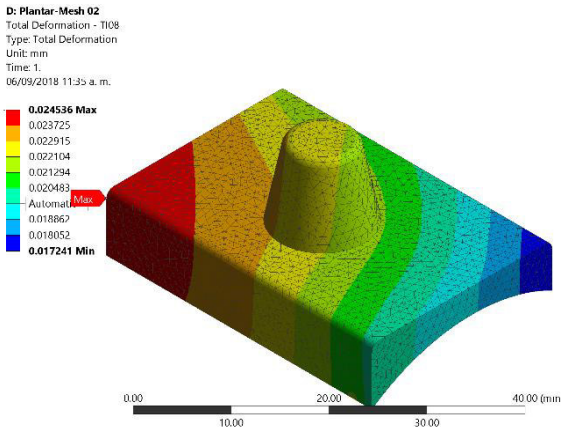

h) STPF

Figure 6.13. Tibial component deformation.

Cadaveric studies on both Agility™ and STAR™ TAA prosthesis for loaded and unloaded varieties of positions (150 and 300 N) reported maximum relative displacement of 0.5 mm for tibial component and a range of 1-1.5 mm for talar component [161]. Considering the first criteria, performance is slightly better for both solid and structured assembles.

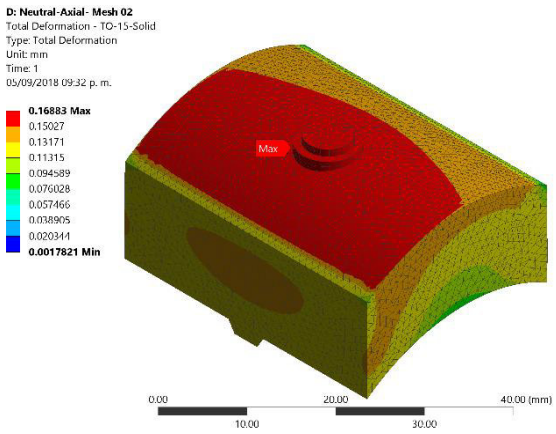

a) SOSA

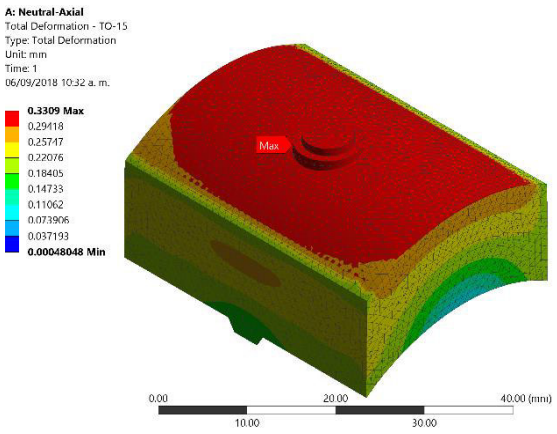

b) STSA

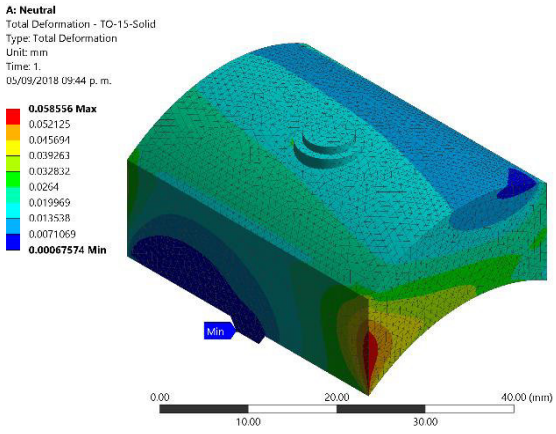

c) SON

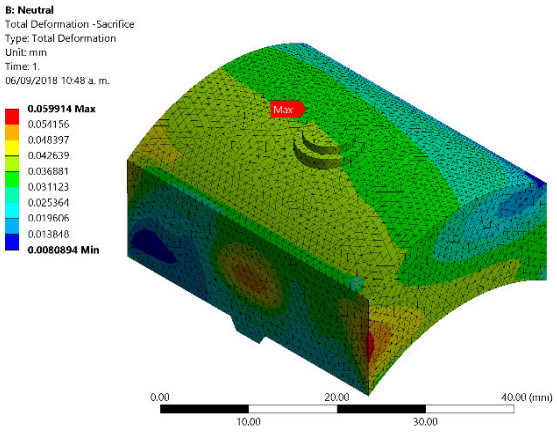

d) STN

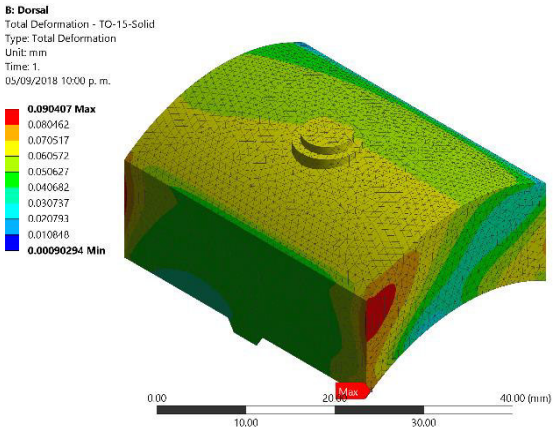

e) SODF

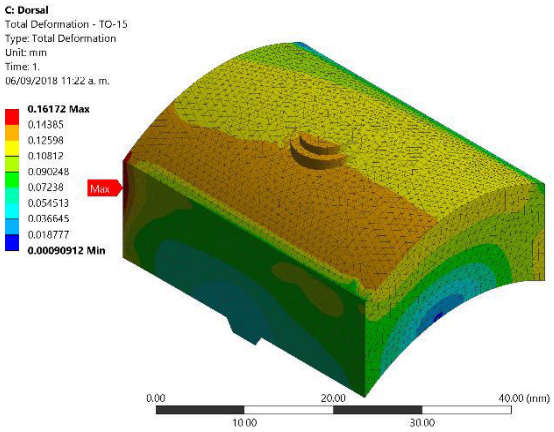

f) STDF

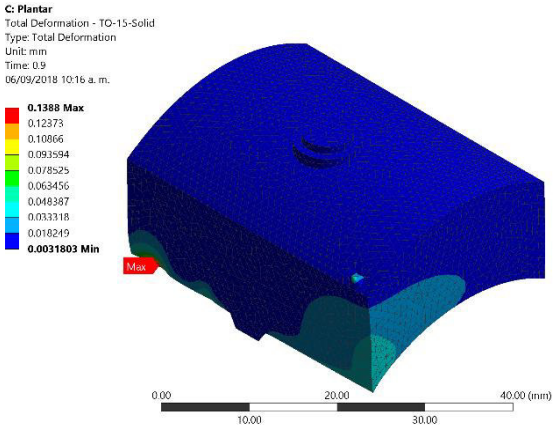

g) SOPF

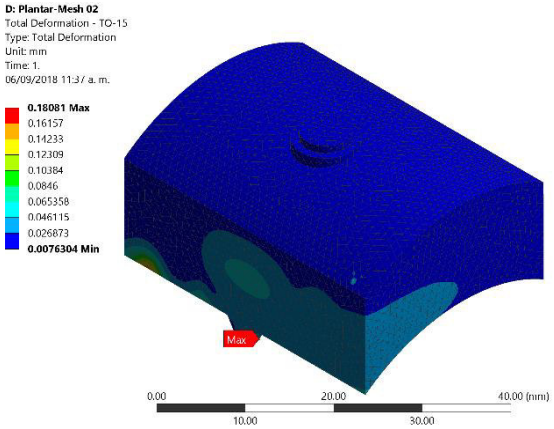

h) STPF

Figure 6.14. Sacrifice component deformation

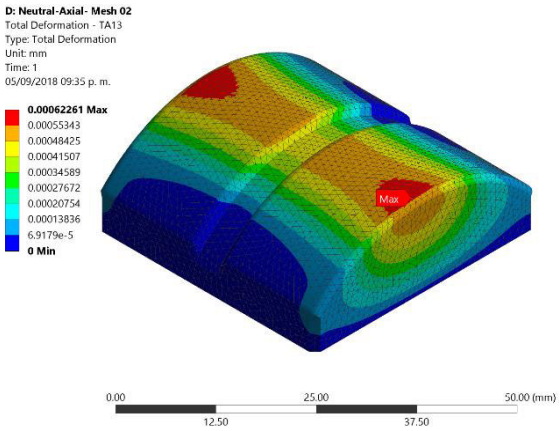

a) SDSA

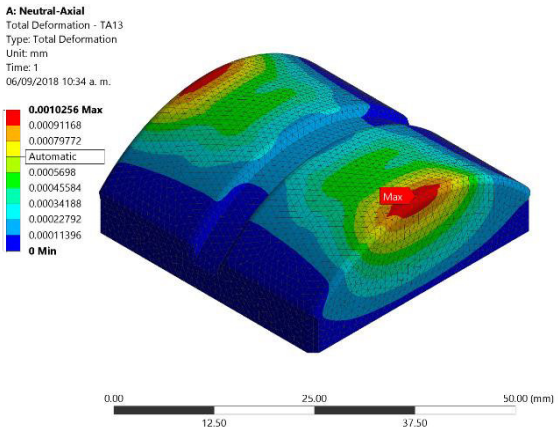

b) STSA

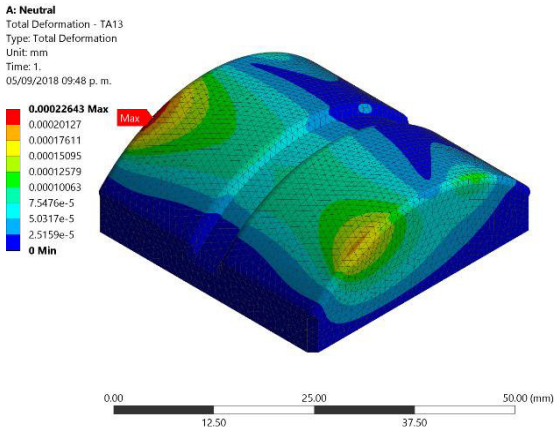

c) SON

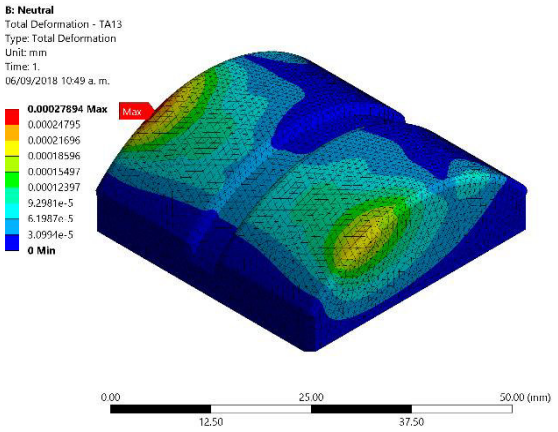

d) STN

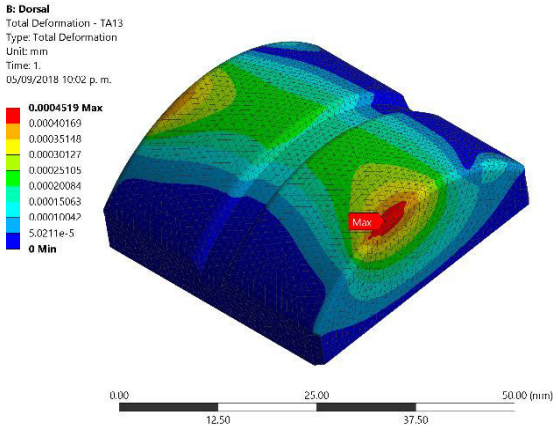

e) SODF

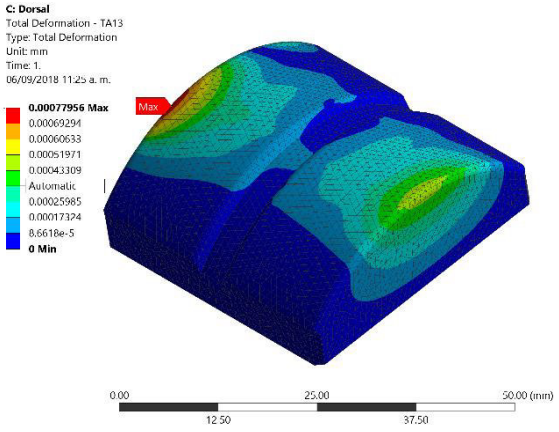

f) STDF

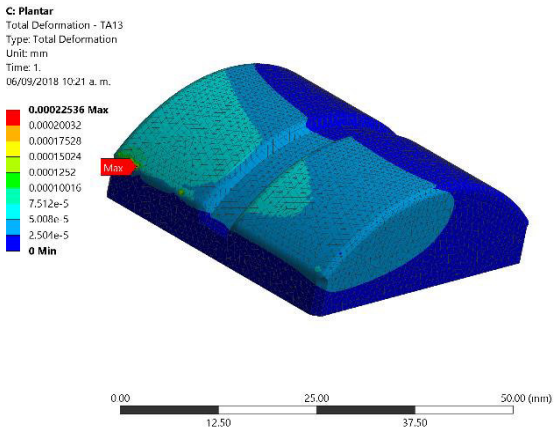

g) SOPF

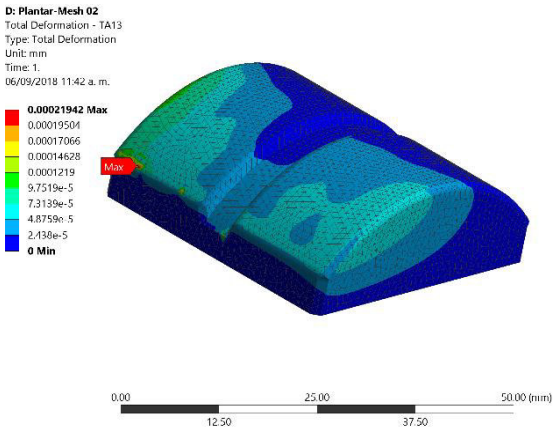

h) STPF

Figure 6.15. Talar component deformation

Other simulation works about implant micromotion on BOX®, Mobility™ and SALTO® shown peak values on the range of 0.01-0.02 mm for talar component and 0.005-0.06 mm for tibial component on neutral position [161]. Under this criteria, neither assemble has a smaller micromovement for tibial component on neutral position, but they are close.

6.4.2 Total elastic strain

Strain has similar distribution patterns (Table 6.5, Figures 6.16-6.18) to deformation, but the presence or lack of inner structure on sacrifice element do show changes on distribution.

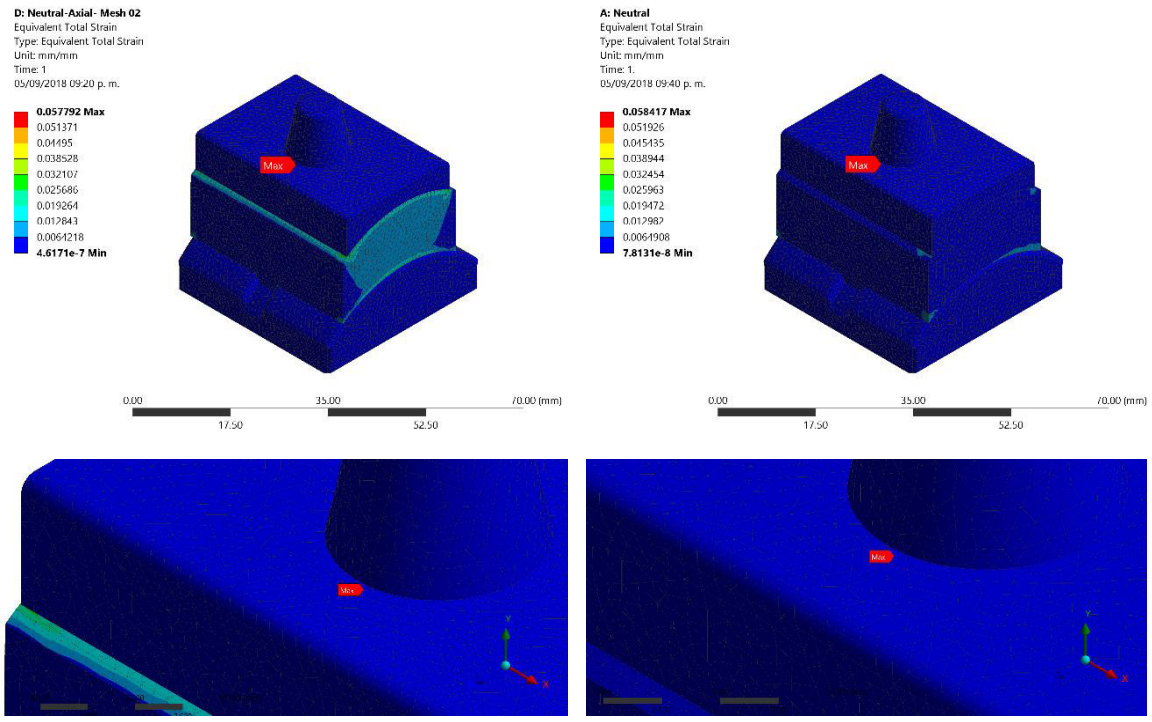

a) SOSA b) SON

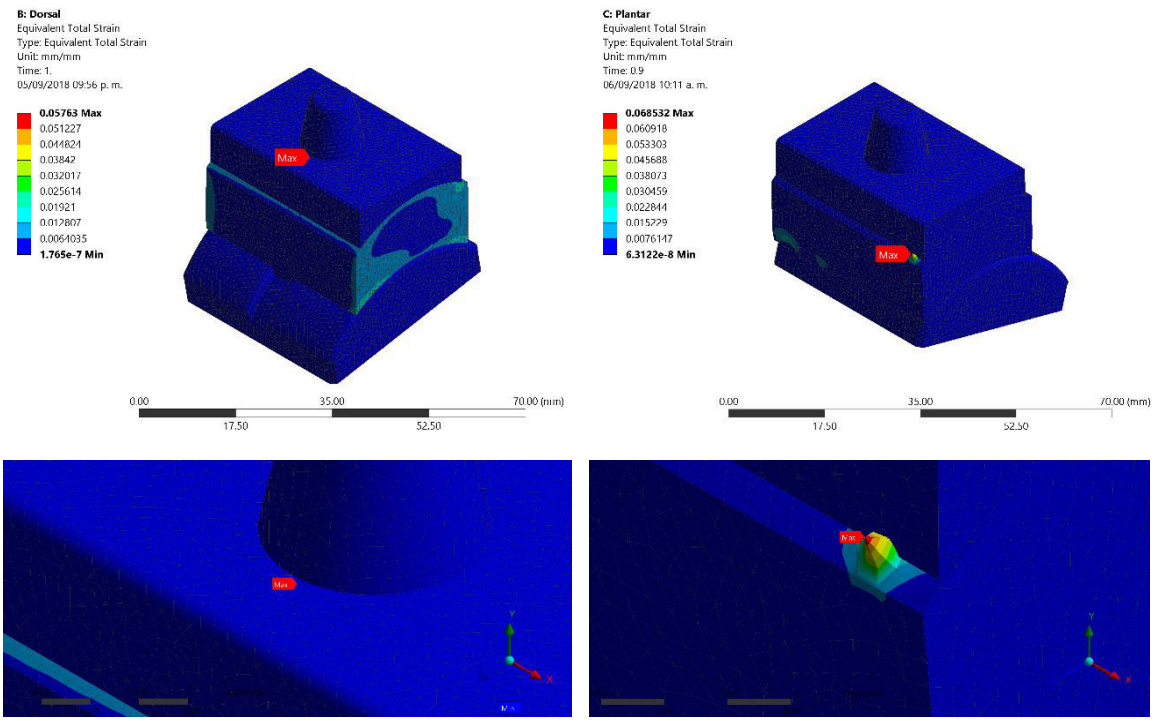

e) SODF d) SOPF

Figure 6.16. Assemble deformation state. Solid component.

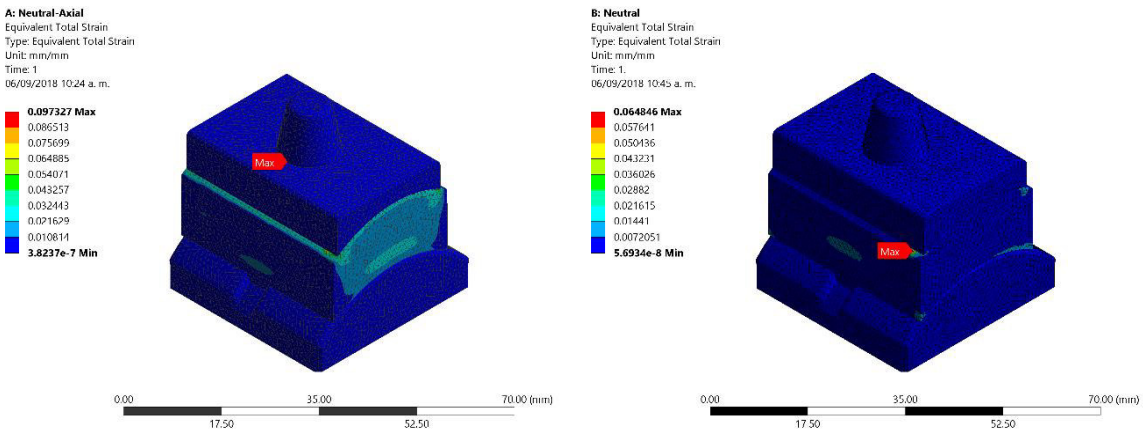

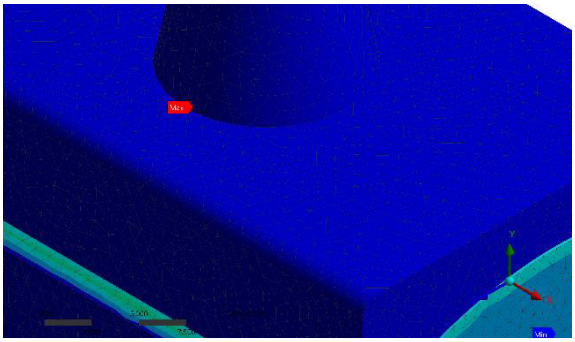

a)

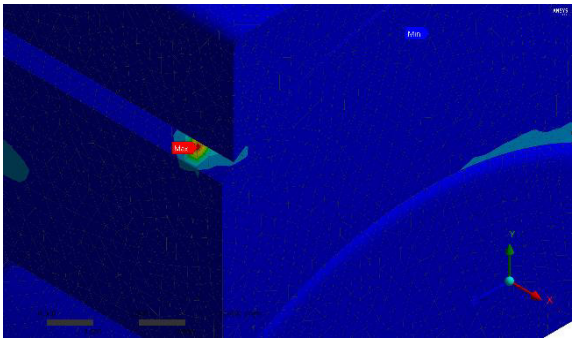

b)

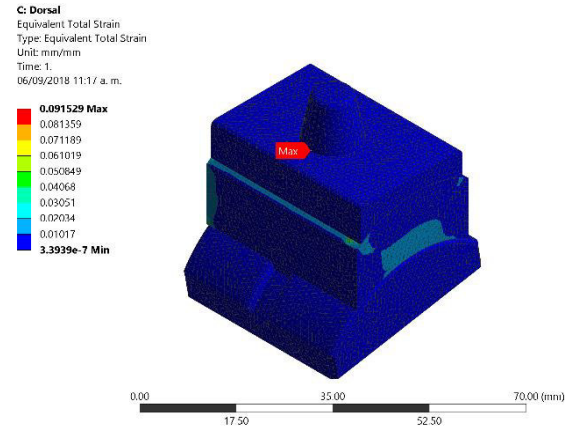

c)

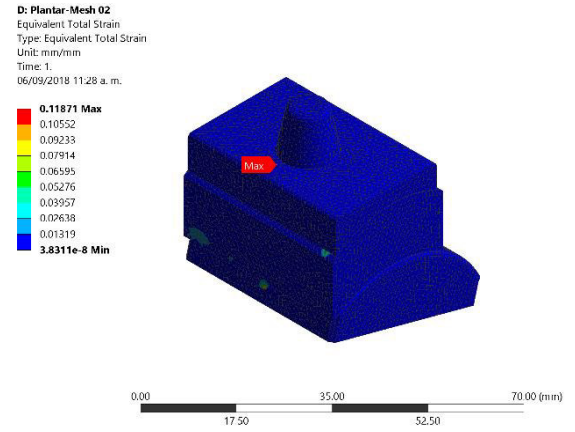

d)

Figure 6.17. Assemble deformation state. Structured component.

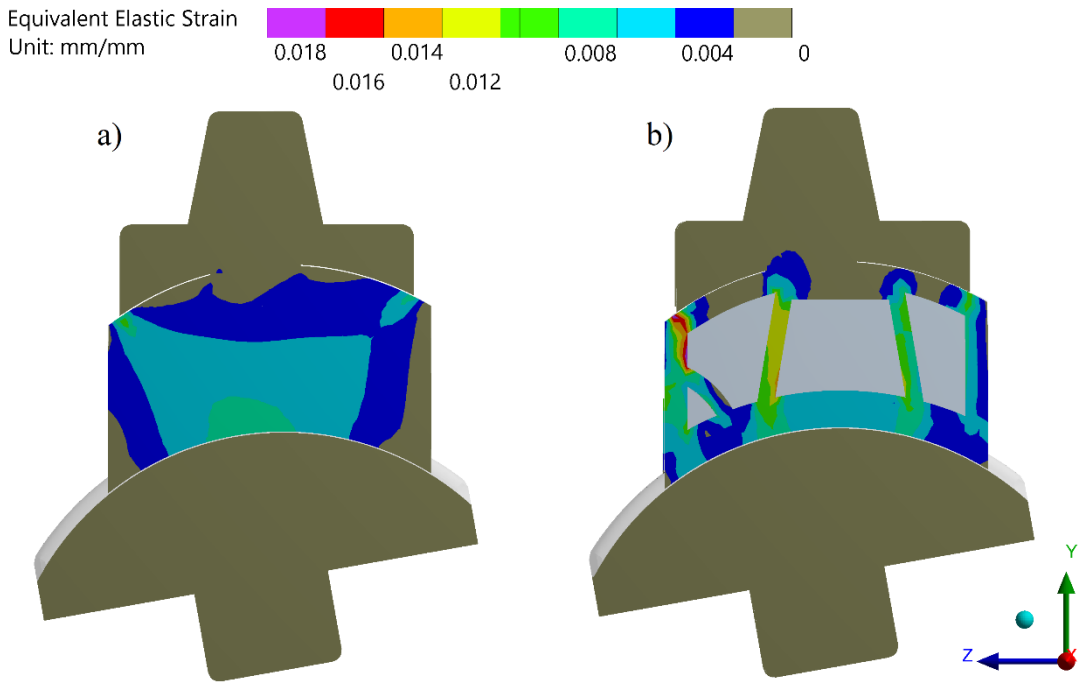

Figure 6.18 Assemble strain state. Dorsiflexion position. Middle section [156].

Table 6.5. Maximum strain on prosthesis components (mm/mm)

Sacrifice component type	Component	Simple axial	Neutral	Dorsal flexion	Plantar flexion
Solid	Tibial	0.0009	0.0008	0.0008	0.0017
	Sacrifice	0.0578	0.05841	0.0576	0.0685
	Talar	0.0001	0.00005	0.00005	0.0005
Structured	Tibial	0.0013	0.0017	0.0016	0.0017
	Sacrifice	0.0973	0.0648	0.0915	0.1187
	Talar	0.0001	0.0001	0.0002	0.0006

Tibial component (Figures 6.19 and 6.20) has a very regular behavior on both assembles and positions (0.008-0.0017 mm/mm on maximum range).

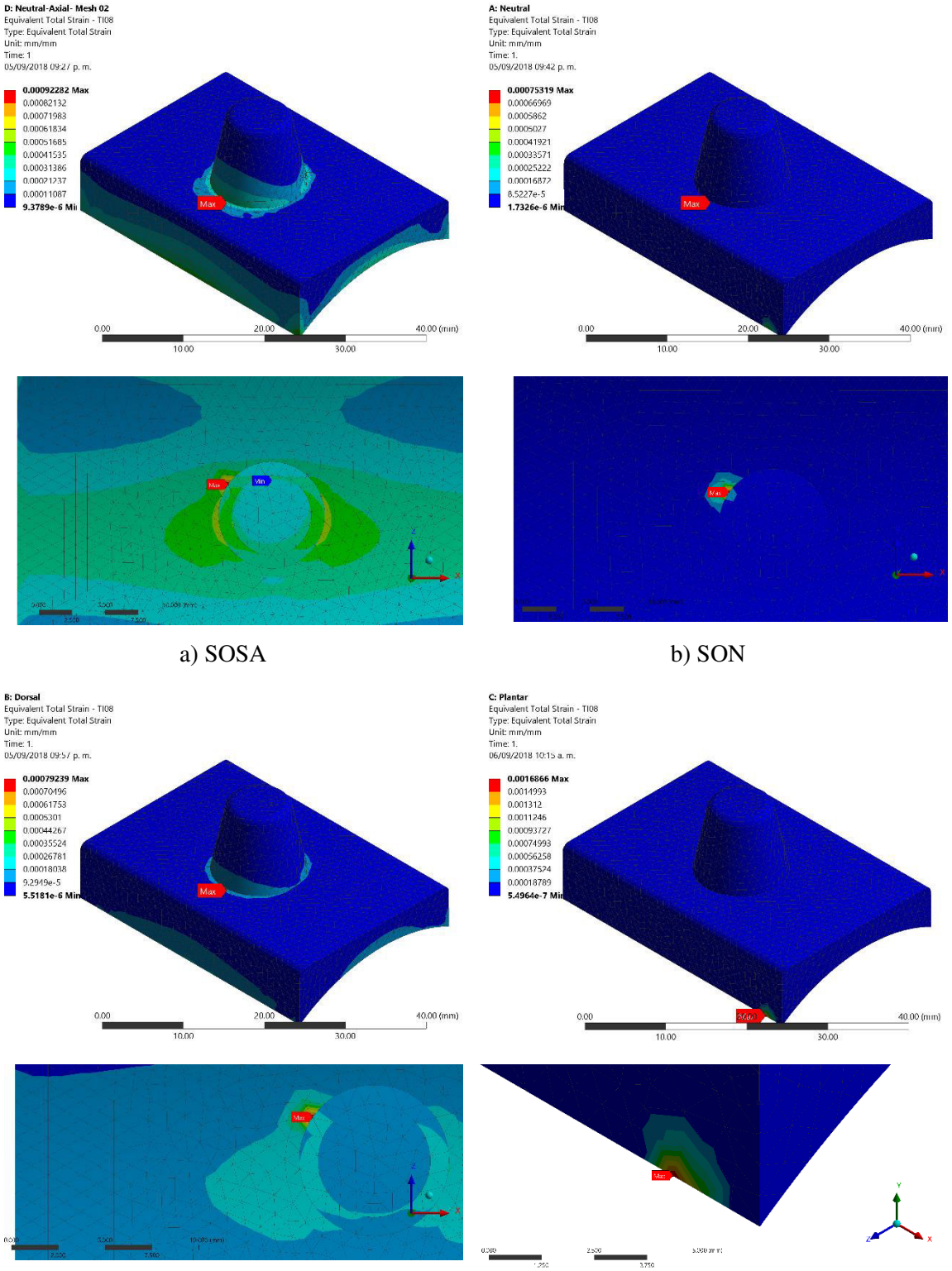

a) SOSA b) SON

e) SODF d) SOPF

Figure 6.19. Tibial component strain. Solid component

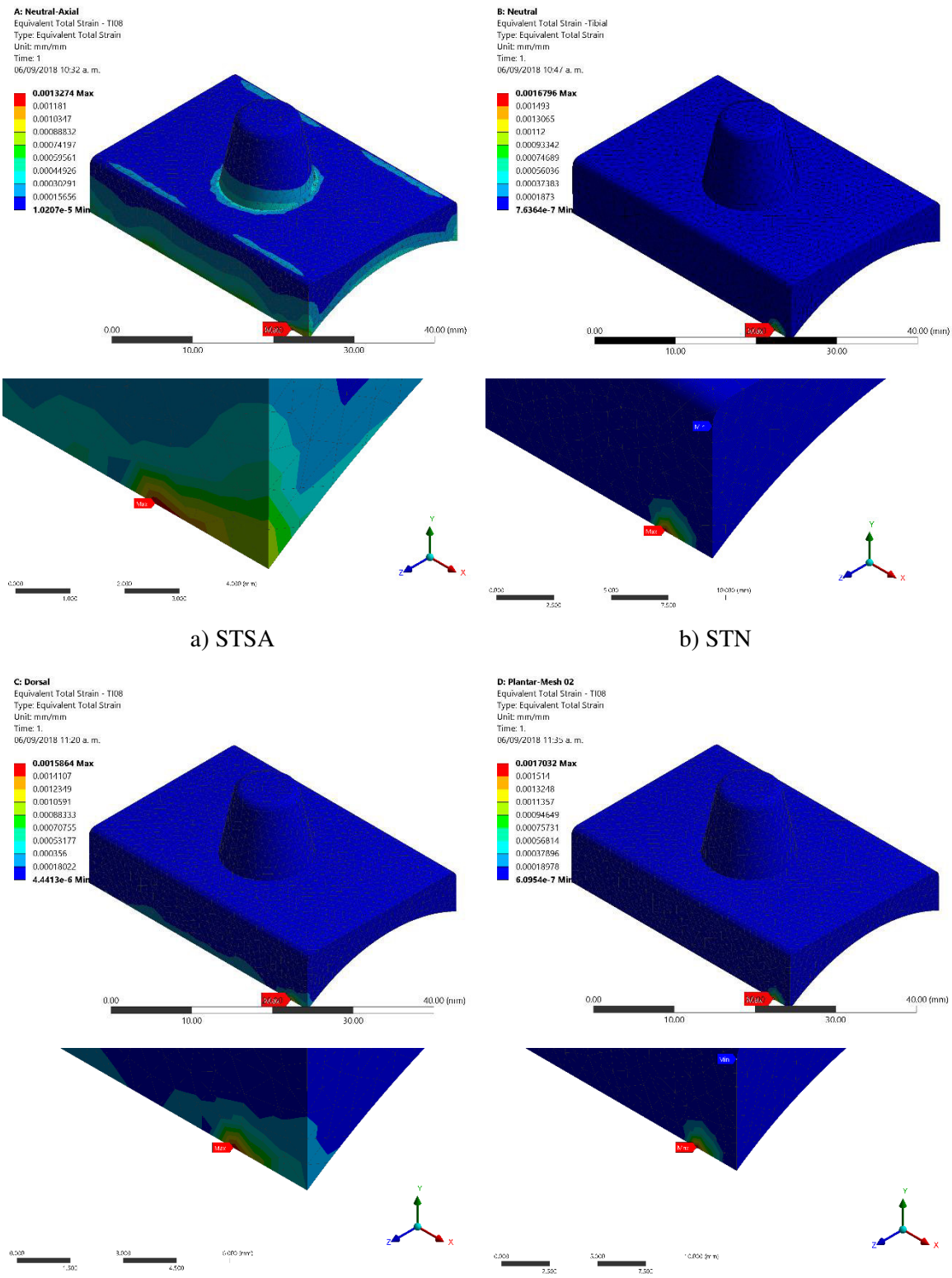

a) STSA b) STN

c) STDF d) STPF

Figure 6.20. Tibial component strain. Structured component.

In contrast, sacrifice component has the highest strain values (Figure 6.21-6.22). These are noticeable on hollow gaps edges and in contact zone with talar component.

First attempts on strain calculation for sacrifice component used a linear elastic formulation for UHMWPE, albeit it was very limiting for design options, with a maximum available strain of 5% on any proposed inner structure for insert. As seen on the lecture of Table 6.5, only a solid polymeric insert would have operated under these former strain limits.

The reference upper limit for the definitive material used came from the later material model of choice (BIH), considering a maximum admissible limit of 2 mm on displacement and a maximum strain of 12% [75] on UHMWPE component for reliable results. These new limits are not trespassed on any case.

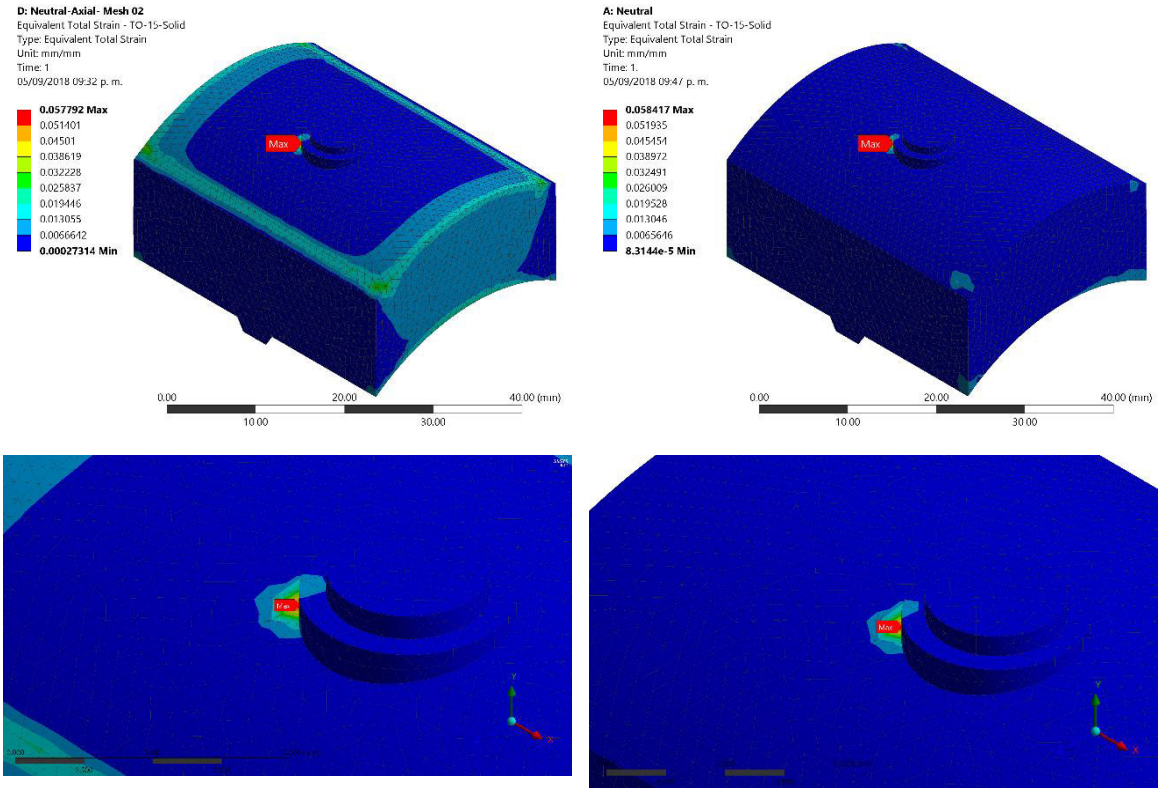

a) SOSA b) SON

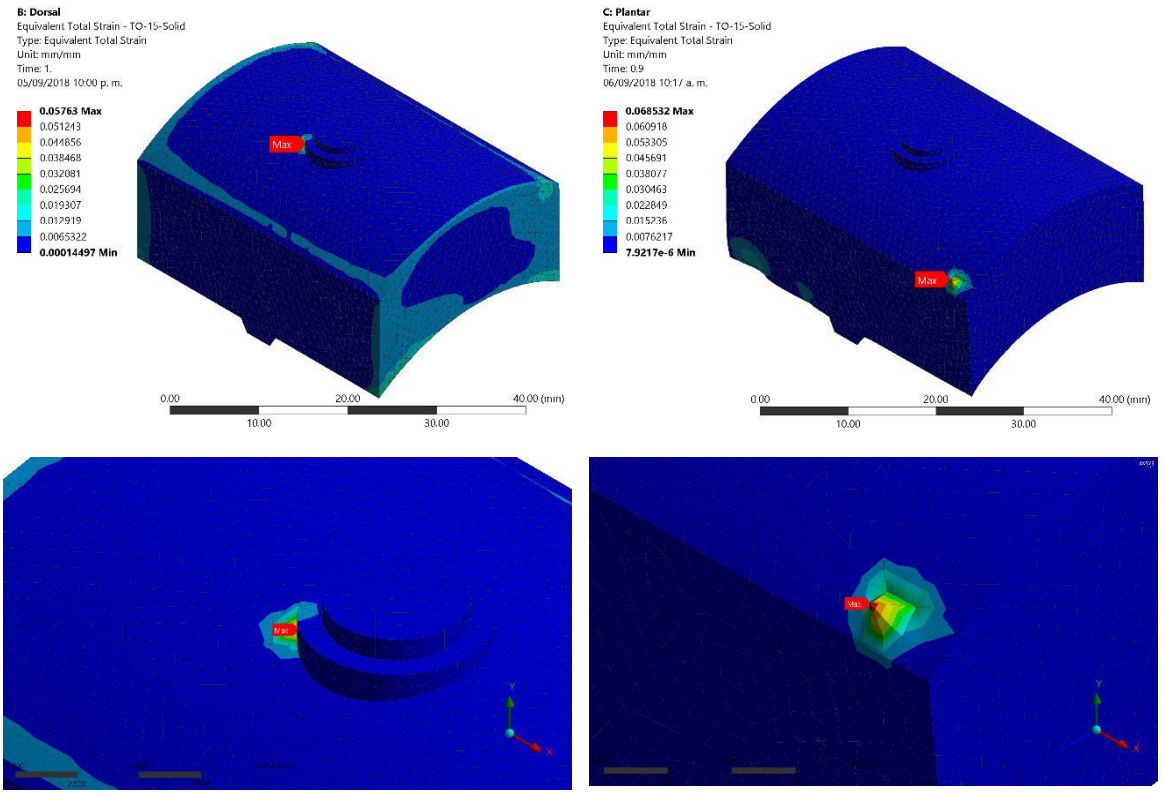

e) SODF d) SOPF

Figure 6.21. Sacrifice component strain. Solid component.

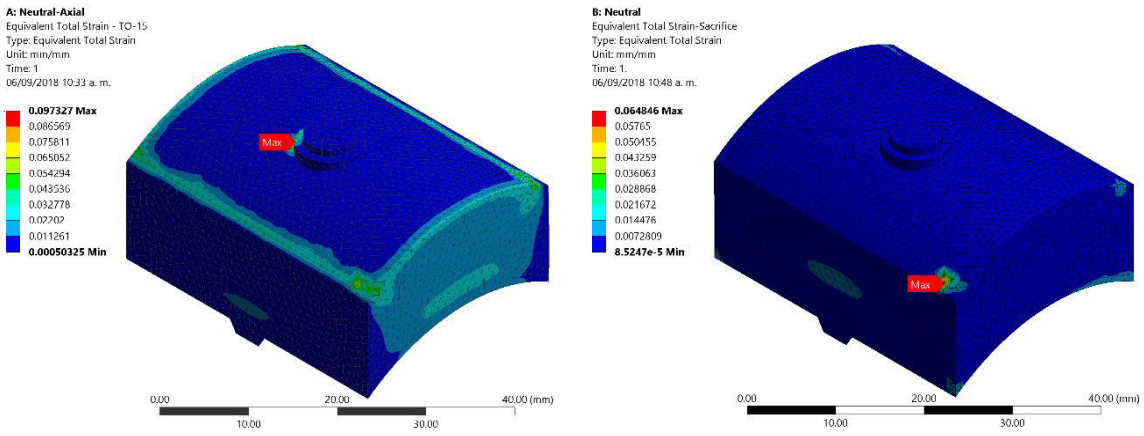

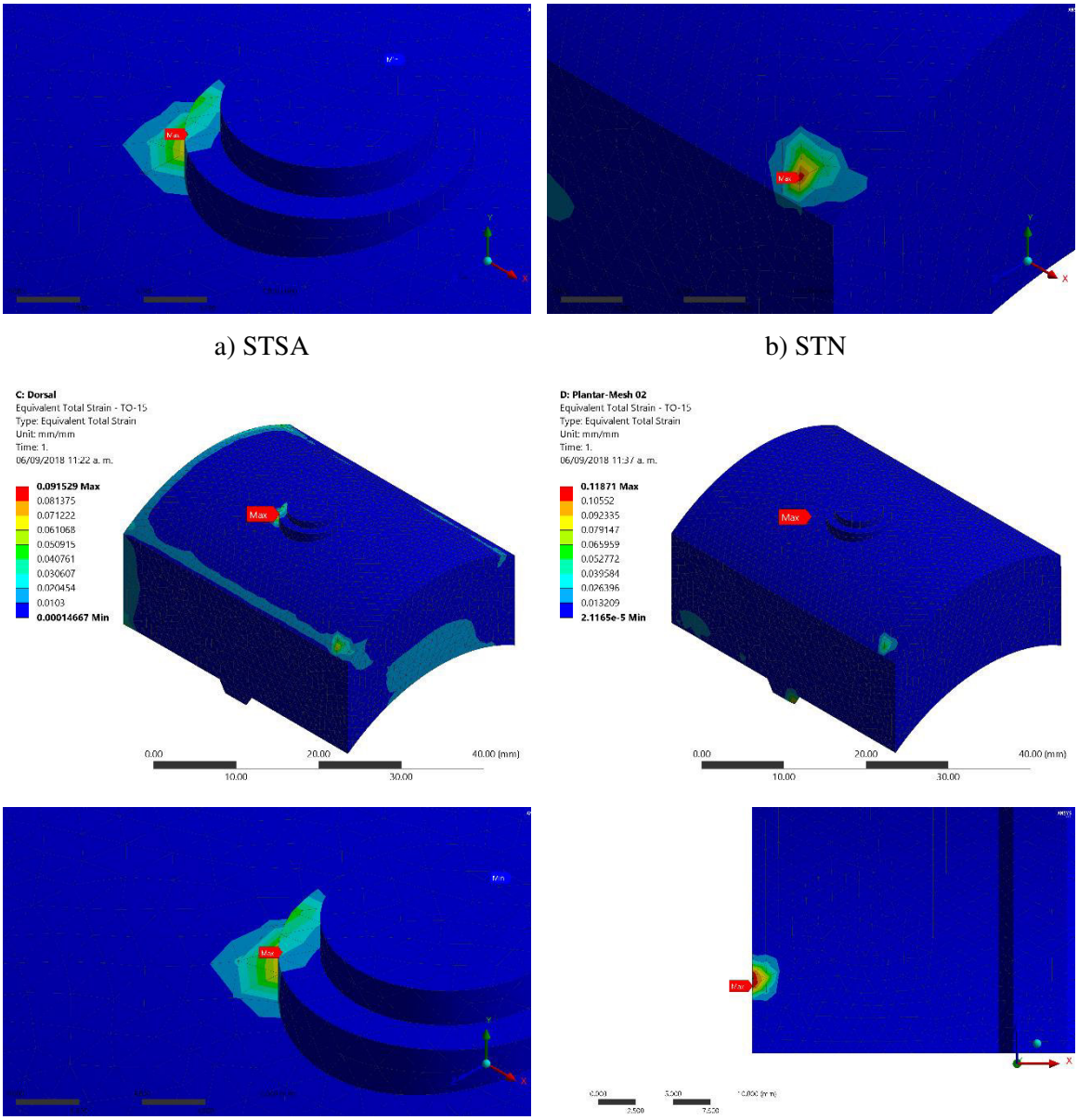

a) STSA b) STN

c) STDF d) SPF

Figure 6.22. Sacrifice component strain. Structured component.

Talar components had little deformation (Figure 6.23), on the range of 0.05- 0.1187 mm/mm. On all cases, the structured component has higher deformation values that their solid counterpart (up to 52.85% on average for all positions).

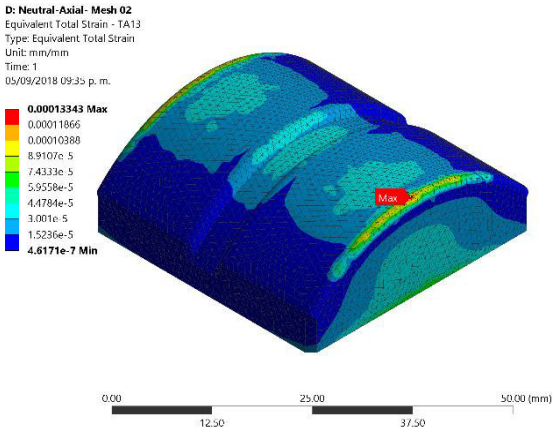

a) SOSA

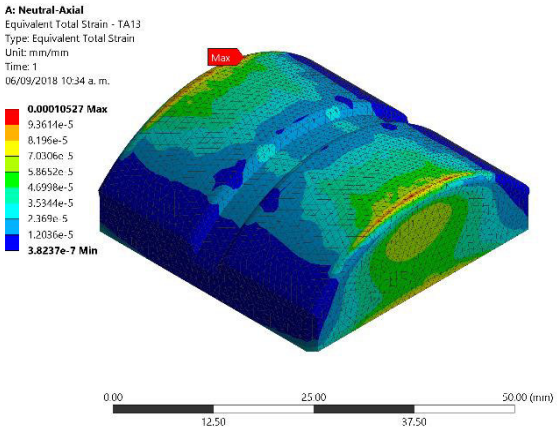

b) STSA

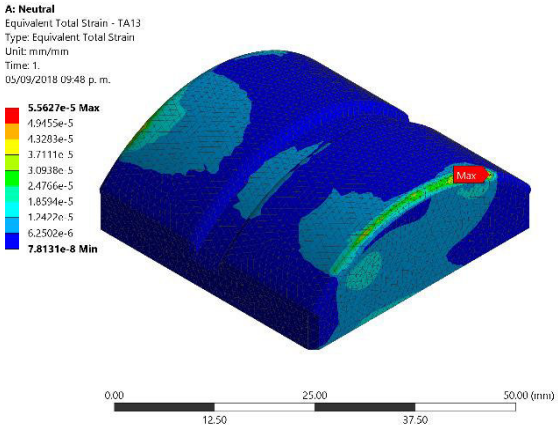

c) SON

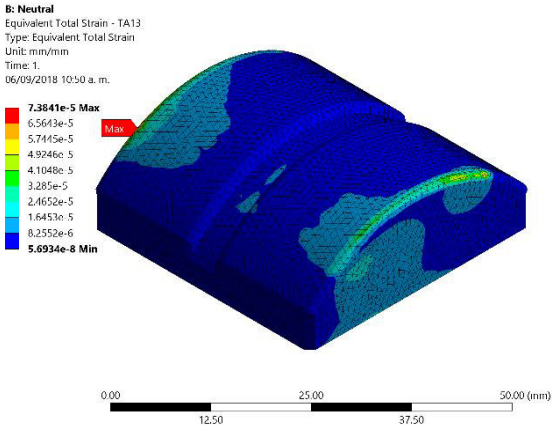

d) STN

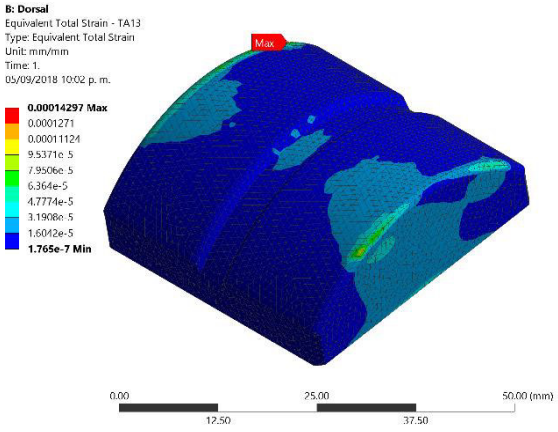

e) SODF

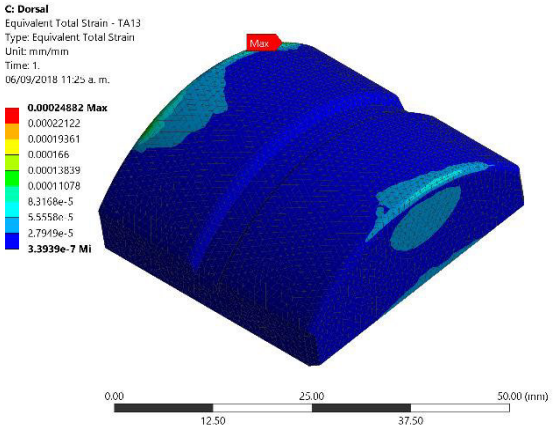

f) STDF

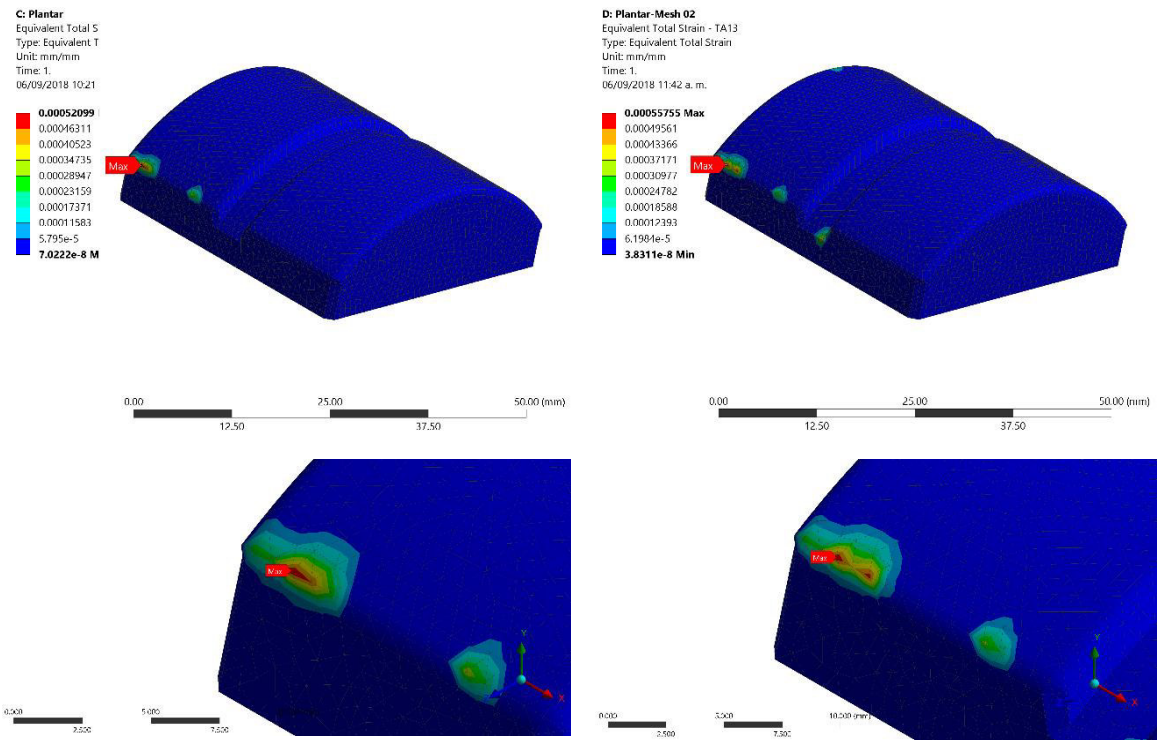

g) SOPF h) STPF

Figure 6.23. Talar component strain.

6.4.3 Equivalent stress results

Stress distribution (seen in the subsequent Figures 6.24-6.32) is more important for interpretation and comparison as most FEA carried on healthy ankle joints [22,180] or TAA cases are more common [50, 160, 185, 188-189]. The use of equivalent stresses is the common reference.

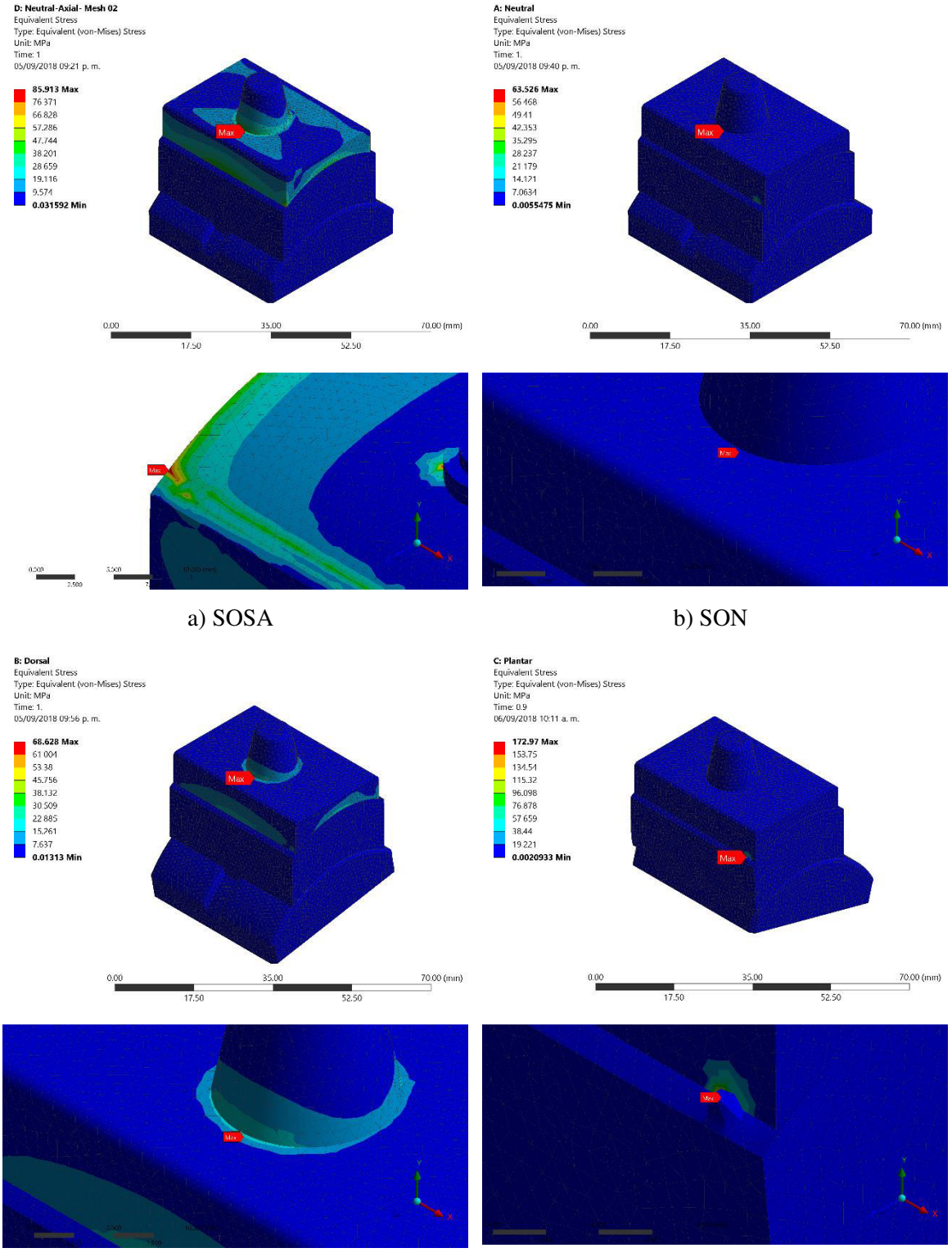

a) SOSA b) SON

c) SODF d) SOPF

Figure 6.24. Assemble equivalent stress. Solid component.

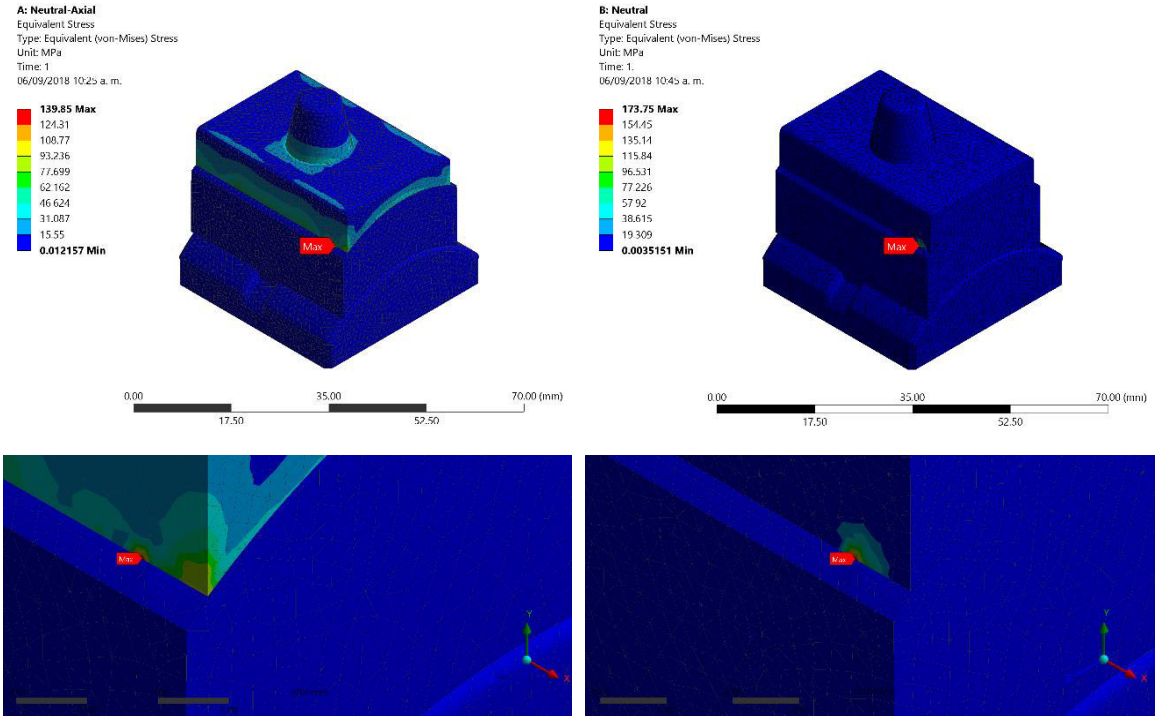

a) STSA b) STN

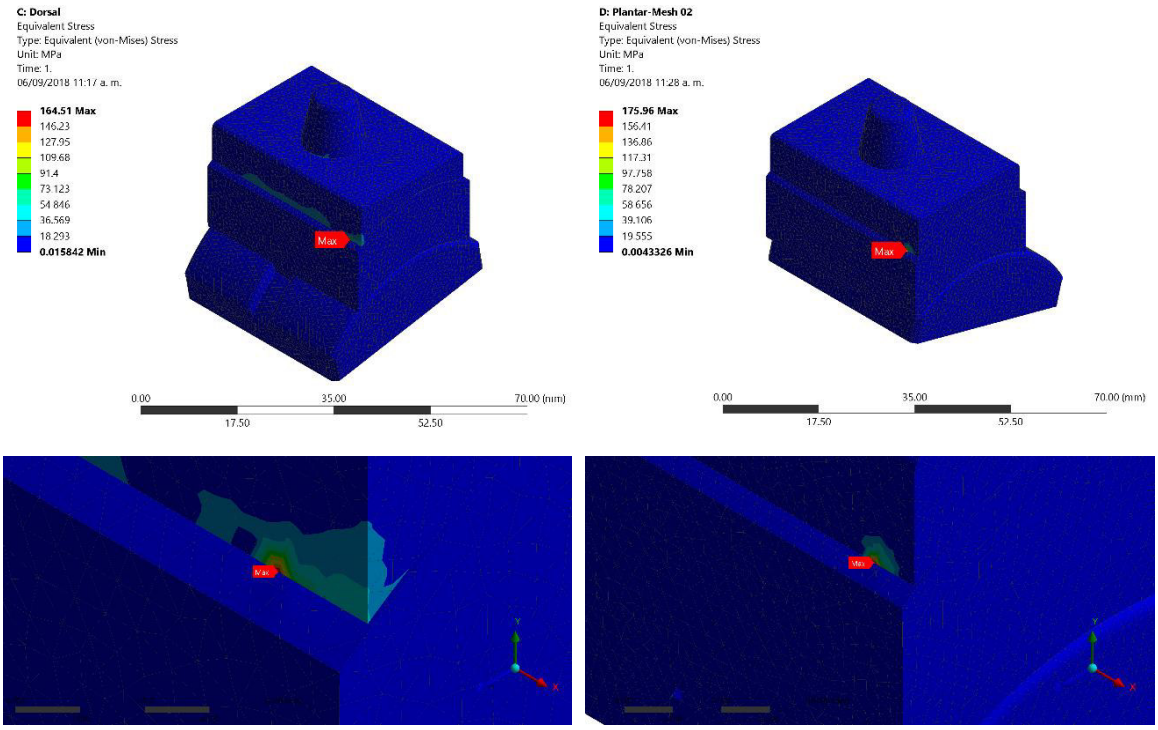

c) STDF d) STPF

Figure 6.25. Assemble equivalent stress. Structured component.

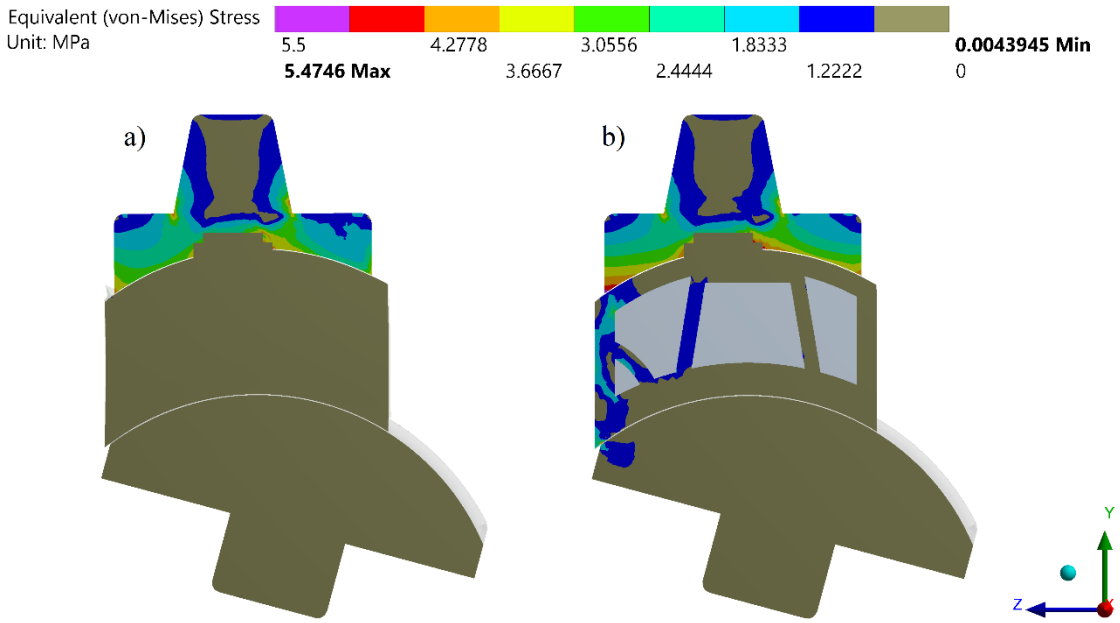

Figure 6.26. Assemble equivalent stress state. Plantar flexion position. Middle section [156].

Tibial components are subject to the highest stress values of all the assemble, as it is seen on the isolated results.

However, as the metallic components have a much higher yielding stress (970MPa), the major concern is the stress transmission to the softer sacrifice component.

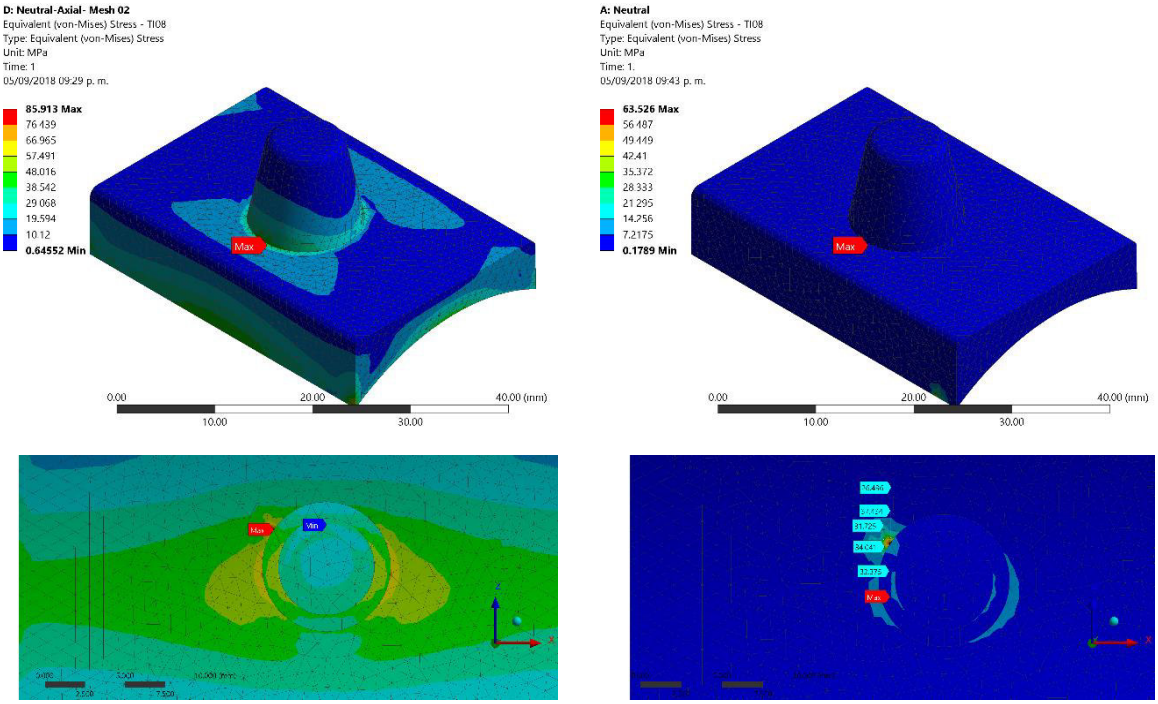

a) SOSA b) SON

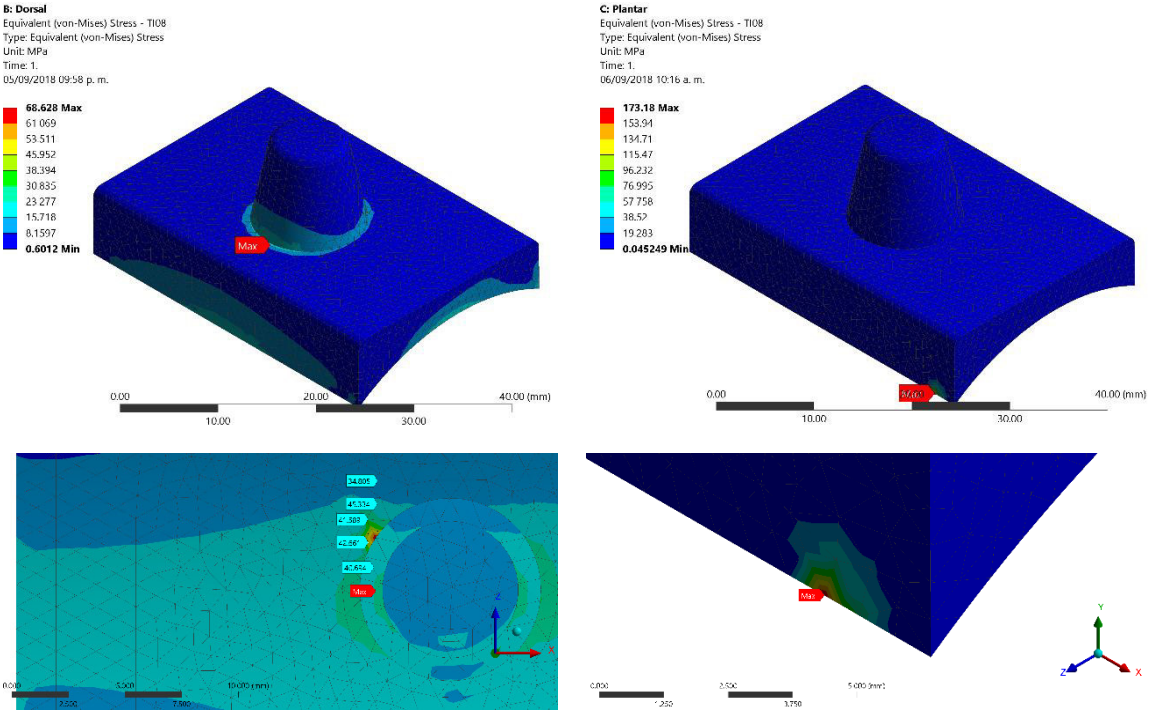

c) SODF d) SOPF

Figure 6.27. Tibial component equivalent stress. Solid component.

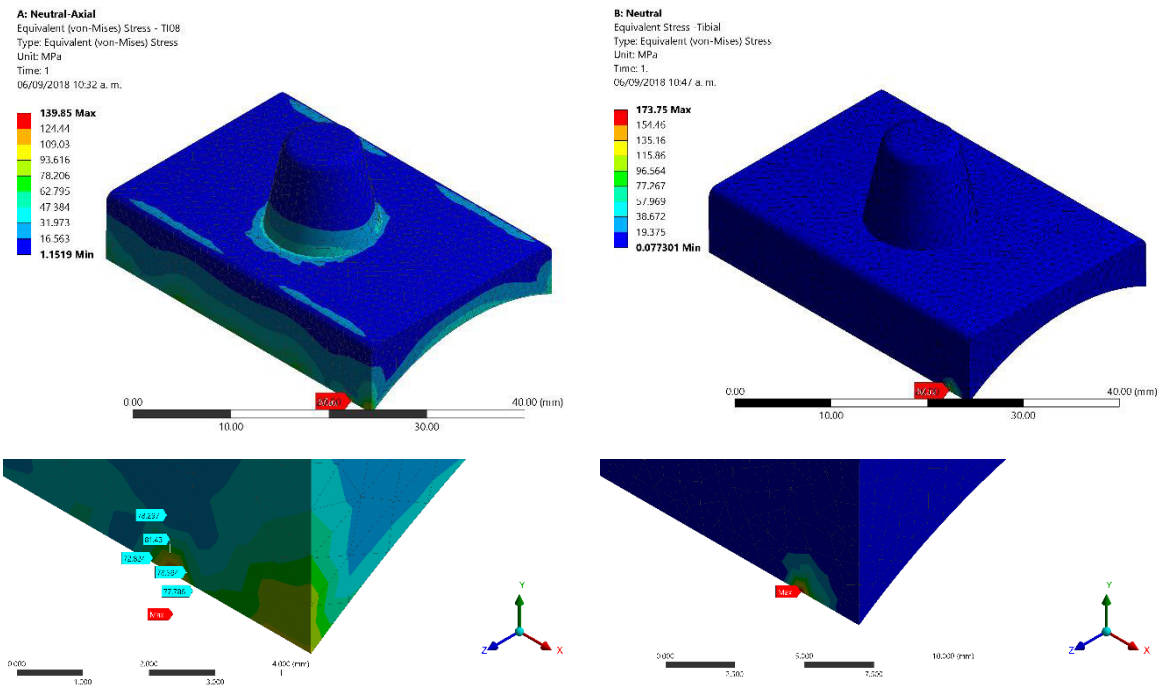

a)

b)

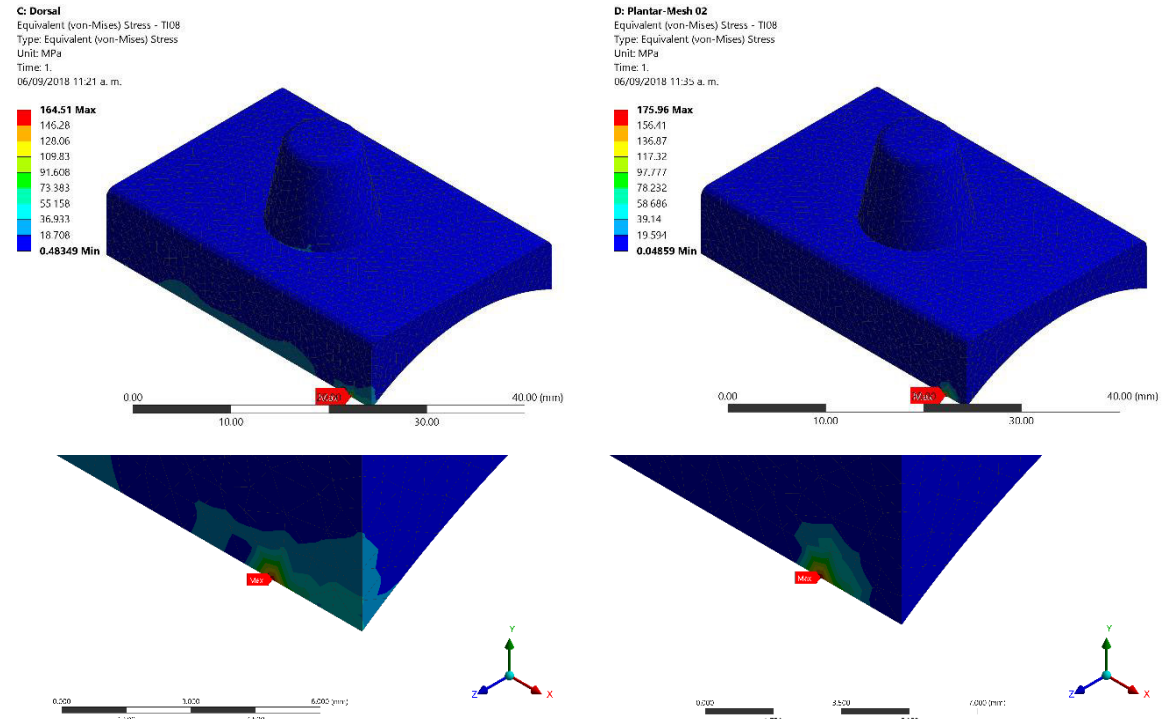

c)

d)

Figure 6.28. Tibial component equivalent stress. Structured component.

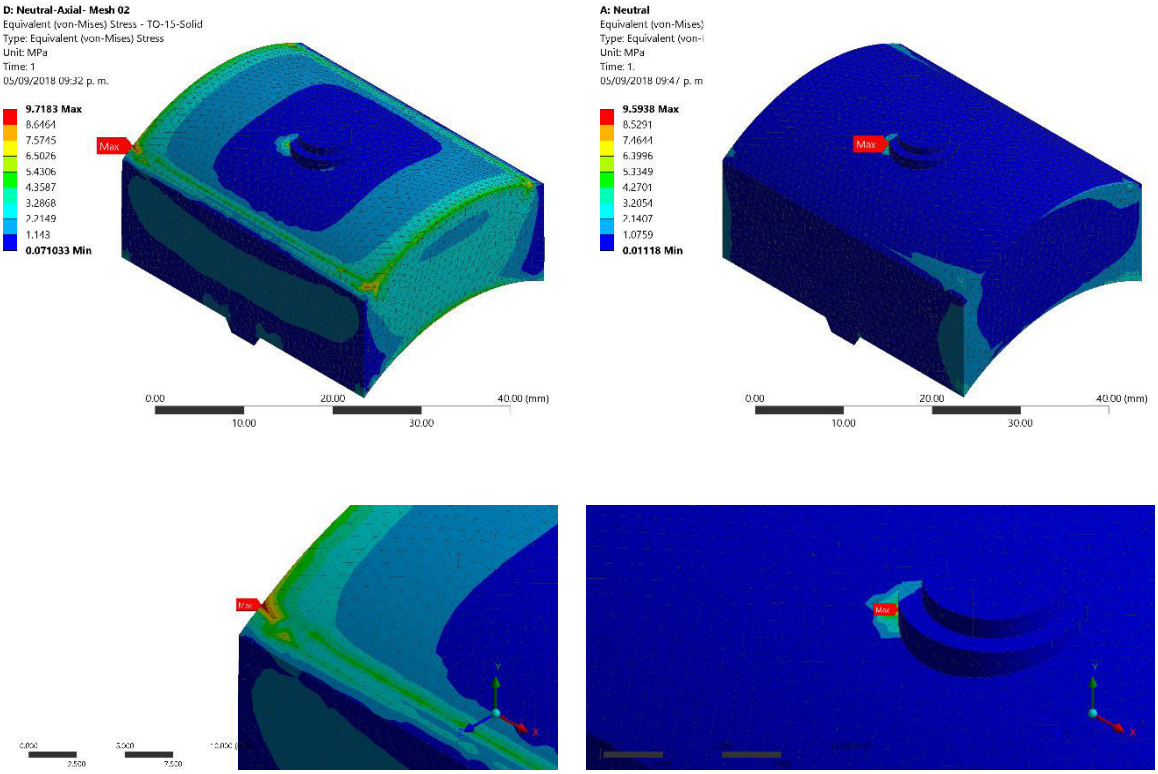

a) SOSA b) SON

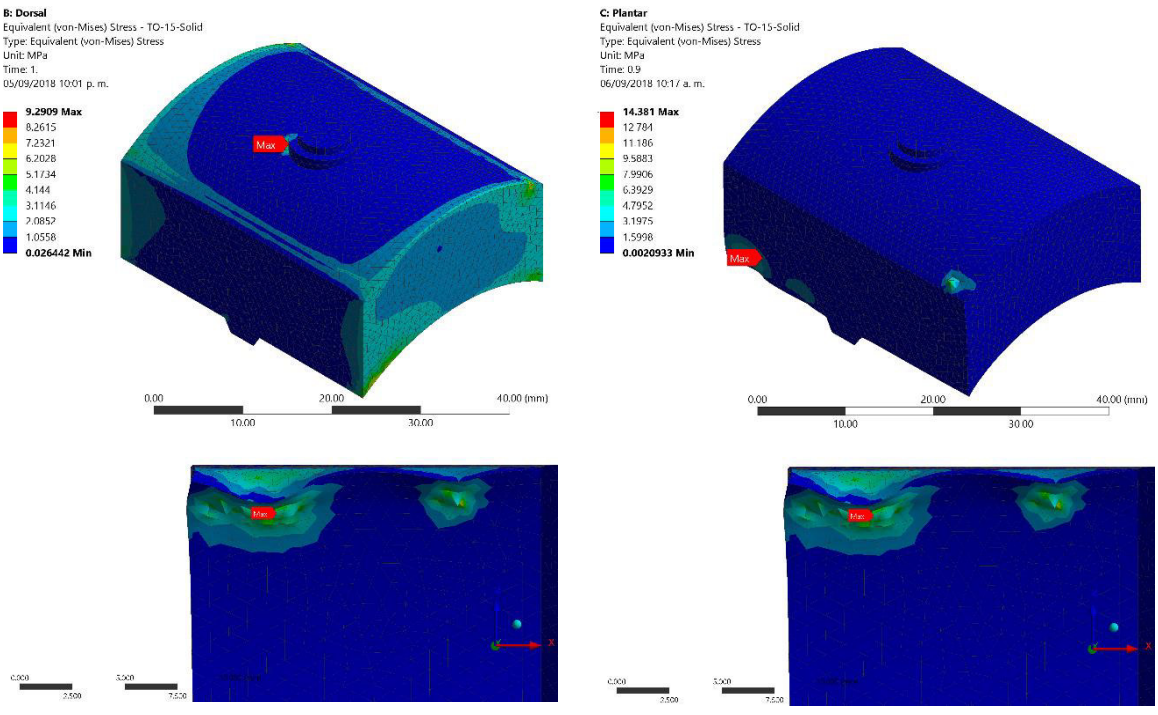

c) SODF d) SOPF

Figure 6.29. Sacrifice component equivalent stress. Solid component.

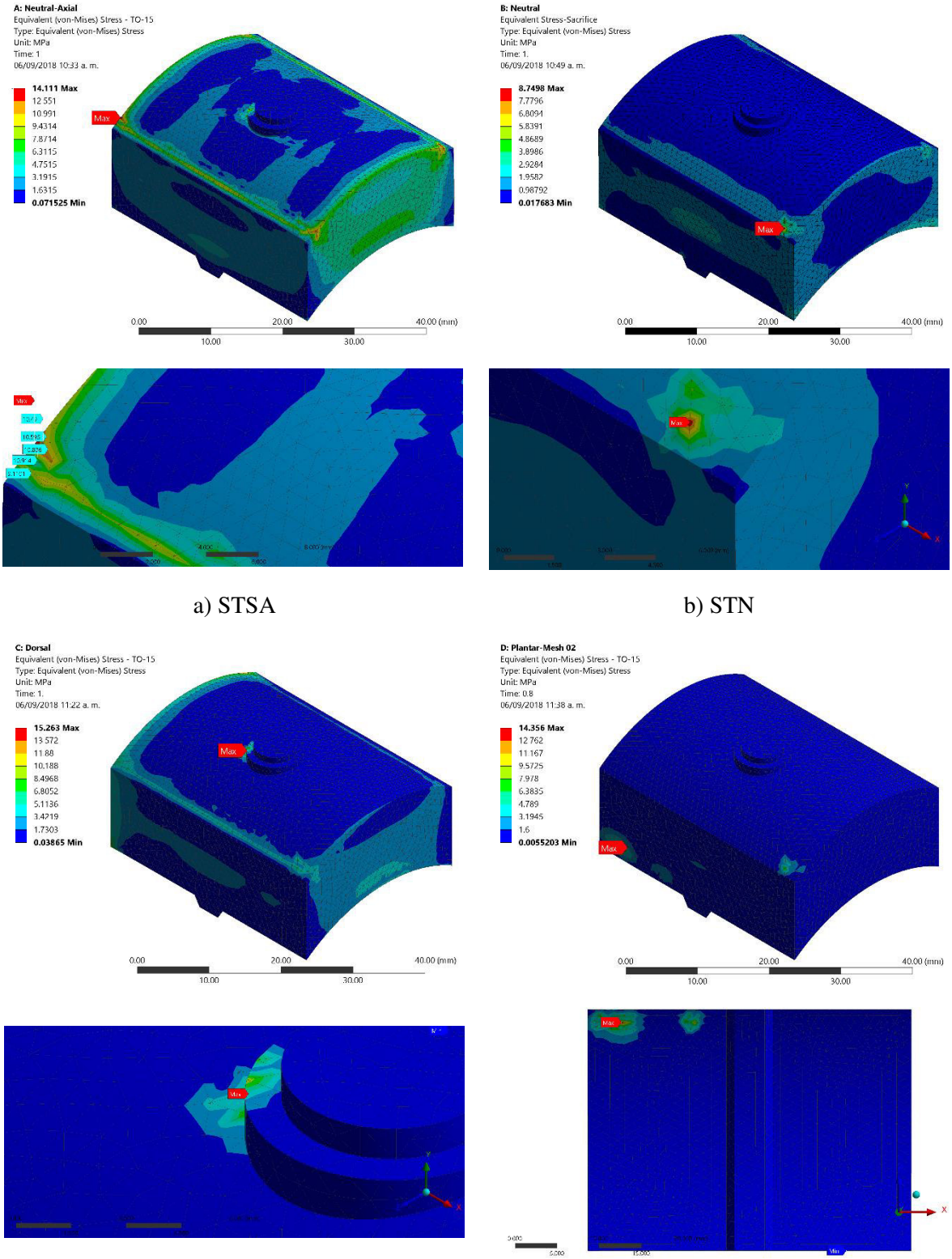

a) STSA

b) STN

e) STDF

f) STPF

Figure 6.30. Sacrifice component equivalent stress. Structured component.

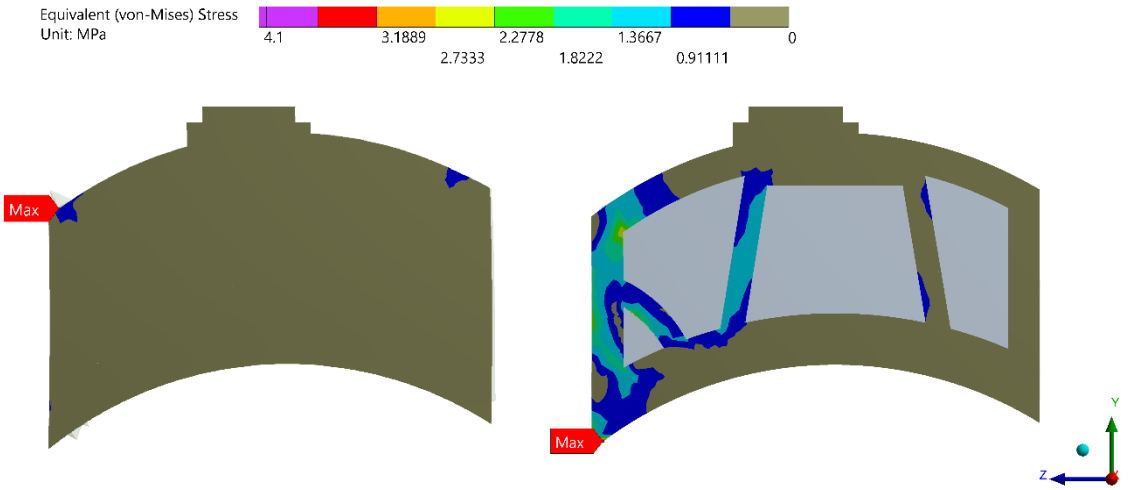

Figure 6.31. Sacrifice component equivalent stress. Plantar flexion pose. Middle section [156].

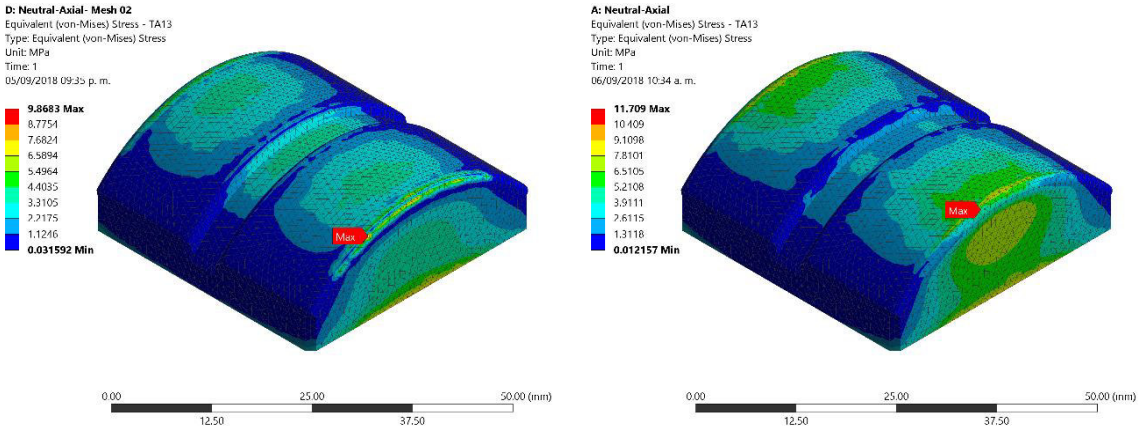

a) SOSA

b) STSA

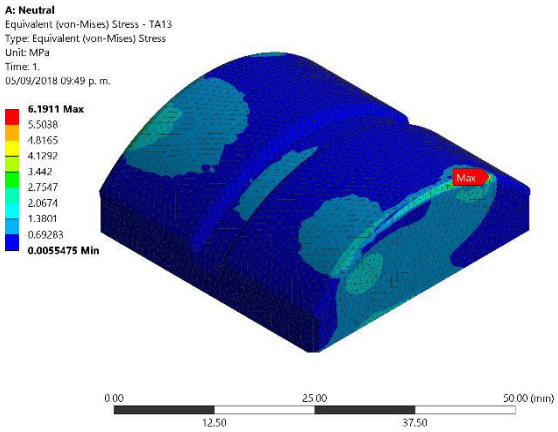

c) SON

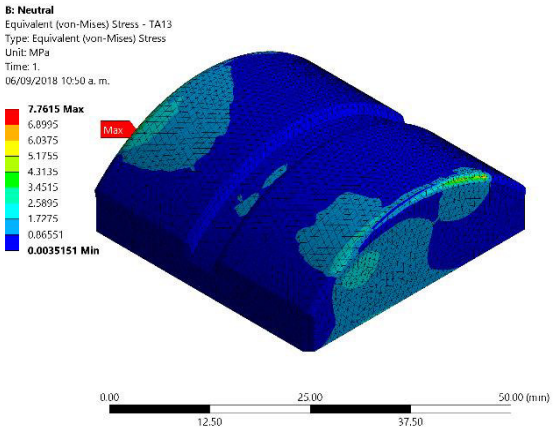

d) STN

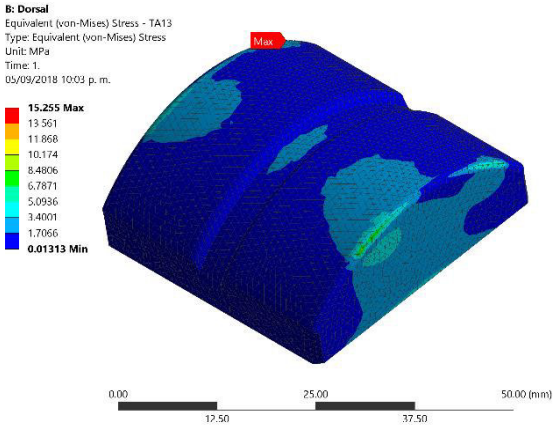

e) SODF

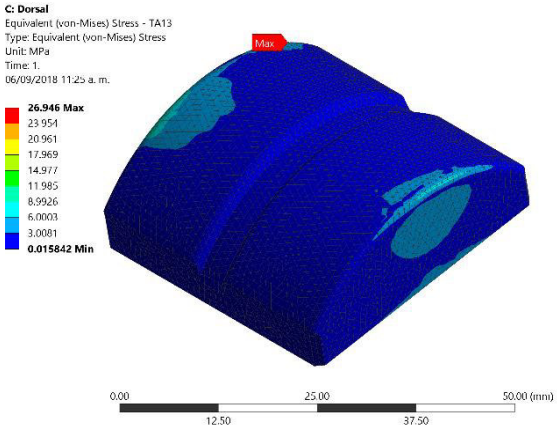

f) STDF

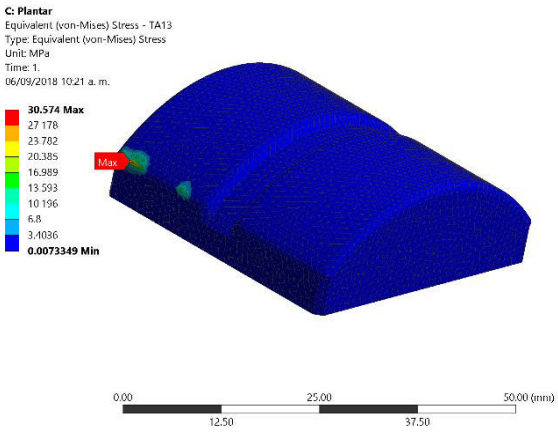

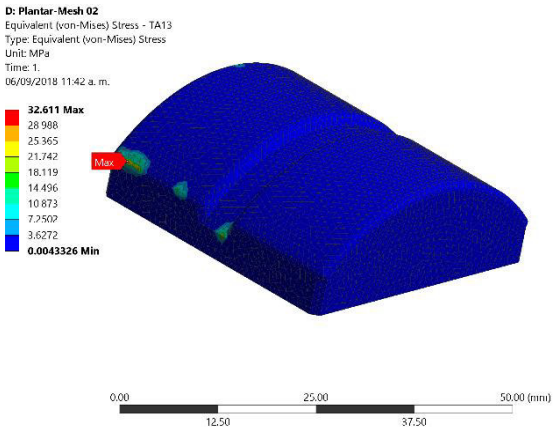

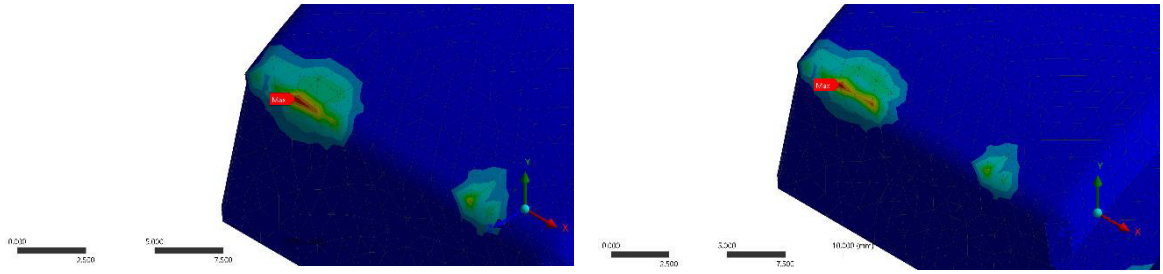

g) SOPF h) STPF

Figure 6.32. Talar component equivalent stress.

The maximum variable lectures can be misleading, as they are focused on small sections of a single element, with extreme gradient changes and no plausible physical explanation. For correction, several measures of variable value are taken from 5-6 geometrical centers of surrounding elements for an average value reflected on Table 6.6. The difference of both values comes on a range of 30-40% on all cases, but the impact of this variation is much more relevant on sacrifice component stress lectures.

Table 6.6. Adjusted maximum stress on prosthesis components (MPa)

Sacrifice component type	Component	Simple axial	Neutral	Dorsal flexion	Plantar flexion
Solid	Tibial	61.2372	32.4242	41.0166	99.3844
	Sacrifice	9.7183	9.5938	9.2909	14.3810
	Talar	9.8683	6.1911	15.2250	30.5740
Structured	Tibial	77.7462	88.6246	83.5138	108.0502
	Sacrifice	10.3890	3.9605	9.8261	9.0308
	Talar	11.7090	5.0611	15.6436	19.1960

Structured components increase the maximum stress values on all positions. Excepting contact zones, talar components tend to have low stress values. Plantar flexion pose gives the highest values for stress on sacrifice component on the contact zone with the talar component.

Having much more references, stress on sacrifice component can be compared in terms of efficiency. As it has been reported on literature and our mechanic tests, a stress value above 20 MPa on sacrifice components is excessive for UHMWPE. However, many FEA carried on market-available designs still have higher peak values (26-36 MPa for Agitliy™ under 3330 N of axial load; 20 MPa for STAR™ under 3650) on similar loading conditions [160]. Reported values are smaller on both solid and structured proposed assembles.

From early attempts [182] it was shown that diminished stress levels are associated with widened support areas. TAA prosthesis design departing from original anatomy can impact beneficially on soft tissues as has been reported for BOX® [160], and the presence of total congruence for the cylindrical surfaces of talar and sacrifice component does reduce the existence of stress concentrators. This is supported by the obtained results of the solid equivalent sacrifice component.

The presence of internal gaps increased the stress peak values on sacrifice component, having a variation of over 25-27%, still under the material limit but certainly in detriment of the inner structure intended purpose.

In spite for this, a possible positive side effect is that wear debris would be isolated from the biological tissues, avoiding adverse reaction. However, this only could be confirmed by addition of a wear model for UHMWPE simulation properties.

It was found that tibial component had associated the highest stress values on the total assemble stress state. This trait is shared with some previous developments [50,161], and effects on bone should be further investigated, perhaps suggesting the need of a better anchoring method.

Proposed talar component is clearly a very robust design. In counterpart, a very massive design can be detrimental for a compromised talar bone.

6.4.4 Static safety factor

Failure theories are used in engineering to predict under which conditions will solid materials fail under the action of external loads [190].

For this purpose, material strength is usually derived from uniaxial loading testing data. In contrast, it is much more common to find a combination of multidimensional stresses on real designs. Thus, material failure theories are expressed mathematically as functions of stress and strain, while its physical interpretation will depend on current application.

As a result of their complex, non-linear behavior, polymer failure is harder to predict from simple uniaxial yielding stresses, in comparison with metals. However, semicrystalline polymers do present a similar behavior. UHMWPE can be considered as a ductile material, with a possible elongation up to 450% before rupture and a clear plateau on the evaluated stress-strain curve, as proved on Chapter 02 stress-strain graphics.

Under a multiaxial stress field on polymers, both Tresca and von Mises criterion are applicable. However, it is considered that the later adjusts slightly better to material data with a maximum difference of 15% on estimated failure [191]

Multidimensional von Mises stress in terms of components of stress deviation tensor σ_{ij} is given by Equation 6.3:

$$\sigma_v = \sqrt{\frac{(\sigma_{11}-\sigma_{22})^2 + (\sigma_{11}-\sigma_{22})^2 + (\sigma_{11}-\sigma_{22})^2 + 6(\sigma_{12}^2+\sigma_{23}^2+\sigma_{31}^2)}{2}} \qquad (6.3)$$

And failure is considered to occur when that equivalent stress reaches the same value of uniaxial yielding stress [192].

Von Mises theory is excellently suited for ductile metals [192], so it will be doubtlessly applied to the other TAA prosthesis components.

As programmed on the finite element software, von Mises theory was applied, using the maximum equivalent stress [107].

Safety factor drops (Figures 6.33-6.34, Table 6.7) are mostly, coincident with stress concentrators. almost all the ensemble operates with high safety values. Plantar flexion

operator gives the lowest safety values. Values for sacrifice component are based on adjusted stress values, with the same criteria described on section 6.3.3.

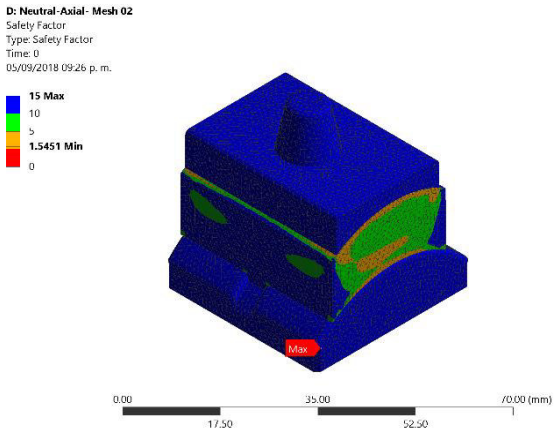

a) SOSA

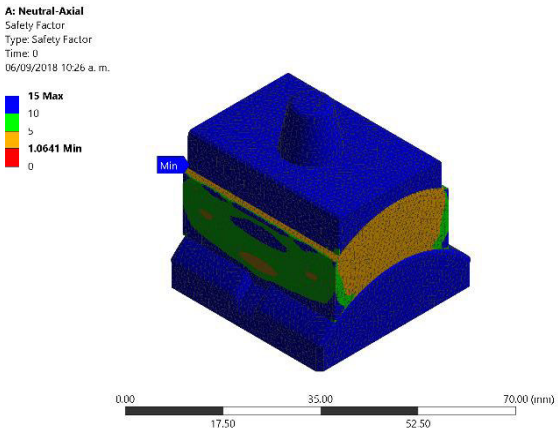

b) STSA

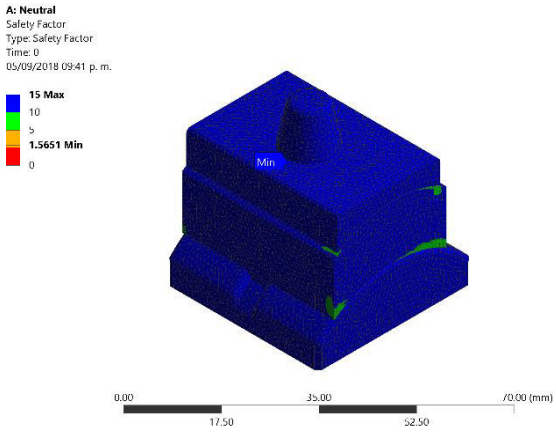

c) SON

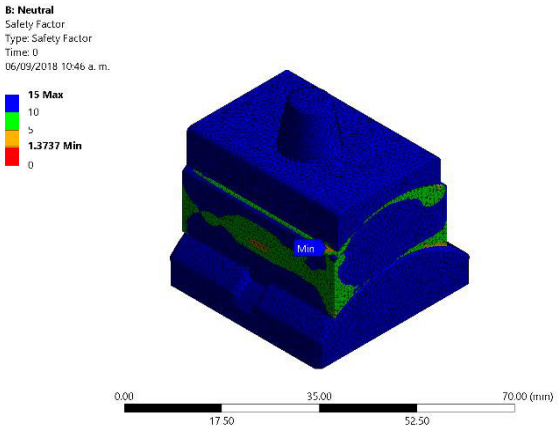

d) STN

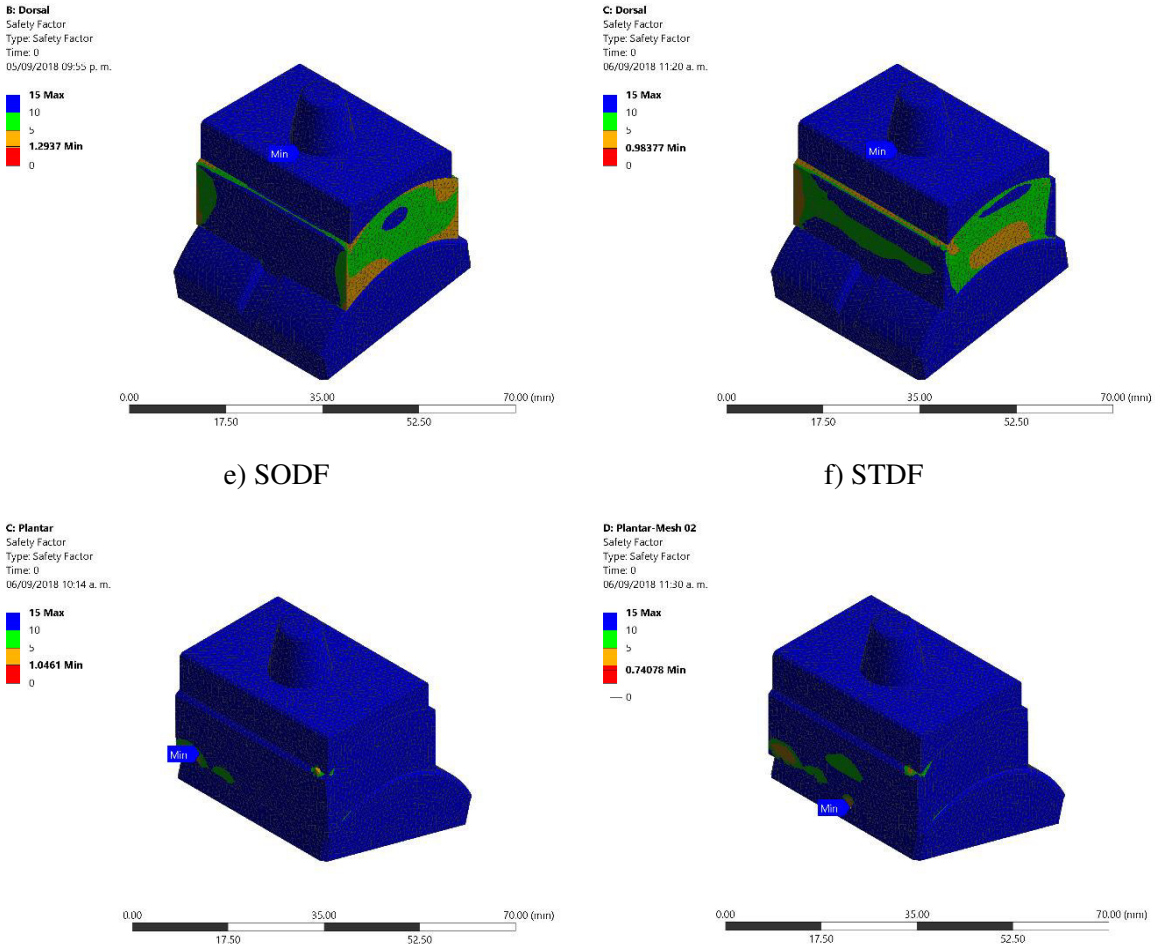

e) SODF f) STDF

g) SOPF h) STPF

Figure 6.33. Assemble static safety factor state.

It is evident on the previous images that safety factor is extremely high (10-15) on metallic components of TAA prosthesis and these are not a priority concern such as the UHMWPE component is.

Safety factors range among 1.1-1.5 for sacrifice components were obtained, as seen on Table

Table 6.7. Minimum static safety factor (adimensional).

Sacrifice component type	Component	Simple axial	Neutral	Dorsal flexion	Plantar flexion
Solid	Tibial	10.2430	13.8570	12.8230	5.0814
	Sacrifice	2.0580	2.0847	2.1526	1.3907
	Talar	15.0000	15.0000	15.0000	15.0000
Structured	Tibial	6.7931	5.4675	5.7748	5.3989
	Sacrifice	1.9251	5.0499	2.0354	2.2146
	Talar	15.0000	15.0000	15.0000	15.0000

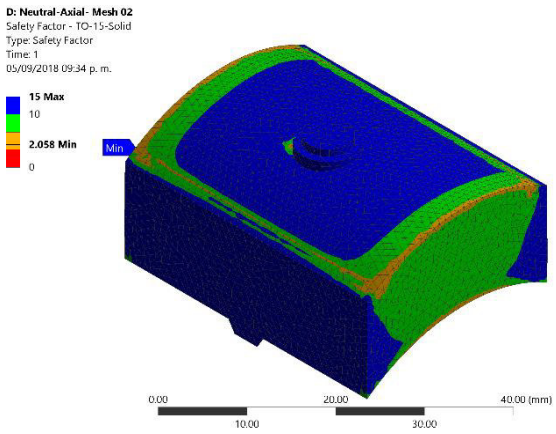

a) SOSA

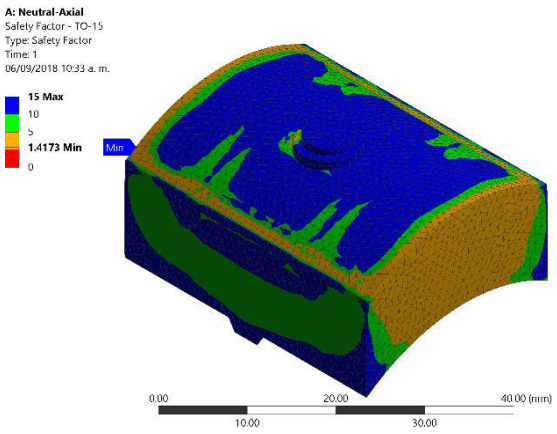

b) STSA

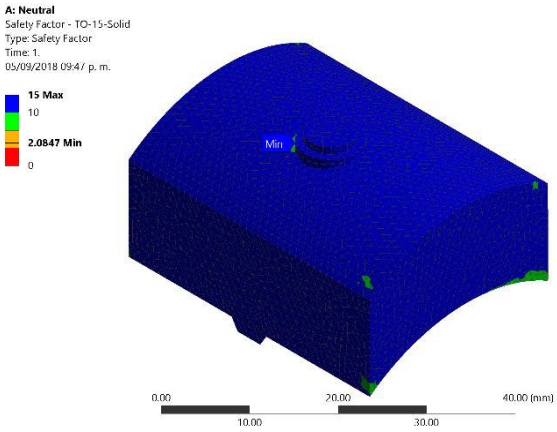

c) SON

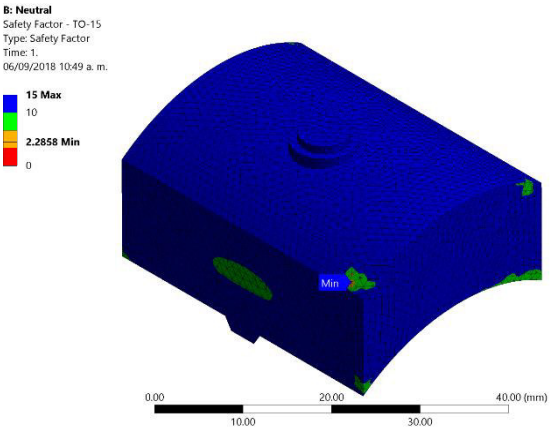

d) STN

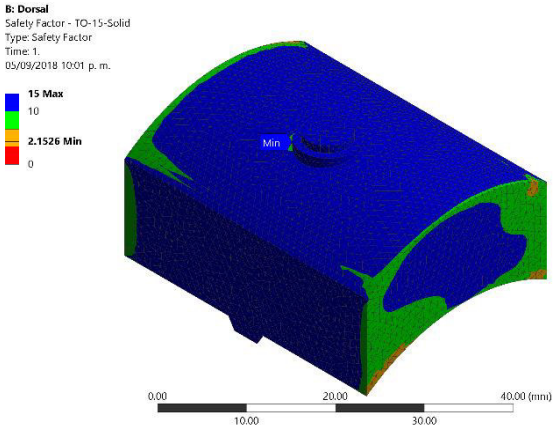

e) SODF

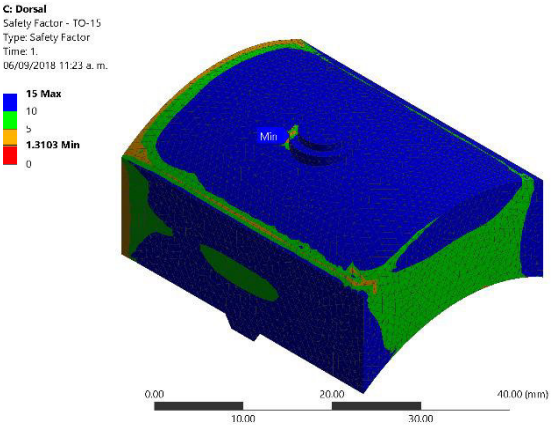

f) STDF

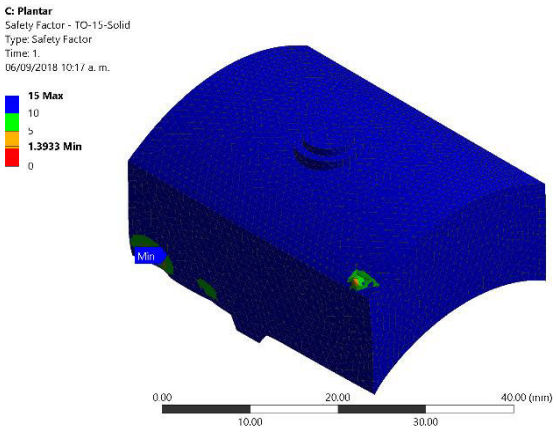

g) SOPF

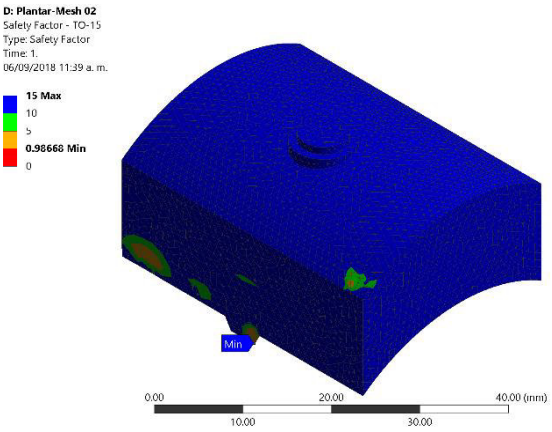

h) STPF

Figure 6.34. Static safety factor for sacrifice element

Although the safety values are above failure, the operation of sacrifice component is still very near. It should be remembered that excessive stress on this piece is the main problem that lead to failure of TAA [14] and that the relatively low yielding stress of UHMWPE (20 MPa) is the main limiting factor on prosthesis reliability.

6.4.5 Strain energy

In FEA, strain energy is an internal value relating stress and strain lectures for each element [156]. Having very similar mesh configurations, as seen on Figure 6.4 and Table 6.3, these were directly compared.

Although maximum and minimum values (Table 6.8) are dependent on element dimensions, the value distribution can give an idea of how the overall structure absorbs energy, as the most strained elements are the ones that may have energy-dissipating effects.

Table 6.8. Minimum and maximum strain energy values on sacrifice component (mJ).

Sacrifice component type	Value	Simple axial	Neutral	Dorsal flexion	Plantar flexion
Solid	Minimum	4.68E-06	3.29E-07	4.99E-07	8.47E-08
	Maximum	0.07392	0.05273	0.07210	0.09353
Structured	Minimum	2.34E-06	2.22E-07	2.96E-10	3.52E-08
	Maximum	0.40889	0.05589	0.34945	0.28374

Structured components account for more strain energy, as they are deformed easily.

Reported values on Table above are rather small, as stress strain value is directly linked with element size.

6.4.6 Fatigue

Failure to fatigue for UHMWPE was described on Chapter 02. A linear relation among yielding stress for GUR1050 and the number of cycles which it was subject was used.For the FEA, a zero- based stress was used, as the prosthesis works primarily on compression. Fatigue strength factor of choice was 1. Soderberg criterion on fatigue failure was used as mean stress theory, and so was the equivalent stress component [107]

About fatigue analysis and operative minimum life cycles (Table 6.9) sacrifice component on dorsal and plantar flexion cases, however, are near to the safety limit (Table 6.10), considering the decay of yielding stress through the number of applied cycles as expressed on Chapter 2.

Being subject to the same boundary conditions, the spatial distribution of safety factor is the same that the one shown on Figure 6.34, albeit the minimum safety factor changes

Table 6.9. Maximum estimated life cycles on respective boundary conditions (cycles)

Sacrifice component type	Component	Simple axial	Neutral	Dorsiflexion	Plantar flexion
Solid	Tibial	1.00E+07	1.00E+07	1.00E+07	1.00E+07
	Sacrifice	1.00E+06	1.00E+06	1.00E+06	1.00E+06
	Talar	1.00E+07	1.00E+07	1.00E+07	1.00E+07
Structured	Tibial	1.00E+07	1.00E+07	1.00E+07	1.00E+07
	Sacrifice	1.00E+06	1.00E+06	1.00E+06	1.00E+06
	Talar	1.00E+07	1.00E+07	1.00E+07	1.00E+07

Table 6.10. Minimum safety factor on fatigue (adimensional)

Sacrifice component type	Component	Simple axial	Neutral	Dorsiflexion	Plantar flexion
Solid	Tibial	7.5164	10.165	7.4314	3.7288
	Sacrifice	1.5451	1.5651	1.2937	1.0461
	Talar	15.0000	15.0000	15.0000	15.0000
Structured	Tibial	4.7458	2.9352	4.0345	3.7719
	Sacrifice	1.0641	1.3737	1.2484	1.4227
	Talar	15.0000	15.0000	15.0000	15.0000

It should be addresses that some of the early designs used structural steel properties on metallic components; having a greater elastic module, Ti6Al4V alloy can be subject to these cyclic loads without risk of failure.

Safety factors to fatigue are even lower, as seen on Table 6.9. It must be reminded that each assemble can bear the simulated loads for a million of cycles. Although it seems enough at glance, most fatigue tests and norms for orthopedic devices can range from 2-10 millions of load cycles [193-196], so further fatigue tests are required or at least additional information for this long-term operation.

Finally, the TAA simulations were carried as isolated systems. A future obligated approach will be the inclusion of the proposed TAA prosthesis in a suitable ankle joint model, not only including the osseous tissues [182] but at least the principal tendons and ligaments to see the effects of assembles on the ankle system.

6.5 Chapter conclusions

Finite Element Analysis (FEA) is nowadays a key tool on modern design engineering on biomechanics and medical applications.

A new TAA prosthesis design with a hollow, structured sacrifice element was tested by FEA to prove an energy absorbing effect. For the UHMWPE sacrifice component, a bilinear isotropic hardening model was implemented. Engineering decisions for model were explored for the other components. For comparison purposes, a solid sacrifice element was also tested as a control.

From the preliminary numerical results of static structural analysis, it is concluded that the proposed TAA prosthesis assemble is functional and can be operated safely at least for one million cycles. Stress distribution inside sacrifice component does change with the use of an inner structure. The proposed design is susceptible for further optimization and improvement. Experimental test on the manufactured design and the effect of the overall assemble on the joint also must be explored.

General conclusions

Main findings

TAA has been developed as a solution for the most severe cases of ankle cartilage degradation. Despite the beneficial results obtained, there are still issues with soft tissue overload, prosthesis loosening, premature wear and excessive stress transmission to the lower limb, having a window of opportunity on biomechanical applications development.

The architecture of joint prosthesis is clearly limited to anatomical dimensions; however, there is still the option of limited deviations from joint geometry while keeping the same functions, in order to reduce the impact on soft tissues.

In physical systems, damping is produced by processes that dissipate the energy stored in them. Although most investigation for this solutions have been oriented to material engineering and surface treatment for wear slowing on polymeric inserts on prosthesis, a mechanical focus is reputed as feasible.

Another important restriction was the use of biomechanical materials with the desired mechanical properties. While the metallic components have wider options or design, sacrifice component of TAA prosthesis are restricted to UHMWPE, at least by legal dispositions. This could change in the near future when other polymers are tested as possible substitutes.

Surgical grade UHMWPE, specifically the GUR1050 variety was tested from a rod segment. Sample manufacturing for tension and compression essays needs were clarifying for the future manufacturing of the physical prototype. Engineering stress-strain curves were generated and compared with previous work. The obtained data was qualitatively coincident with literature.

The obtained mechanical data was adjusted to a variety of material constitutive models. As it occurs on many polymers, relation among stress and strain on UHMWPE is non-linear and highly variable based on load rate, temperature changes and a myriad of controllable and

uncontrollable factors. As a consequence, a material model had to be chosen taking in consideration the best performance on the conditions closer to the physiological conditions and future prosthesis operation.

Design has been clearly aided by implementation of numerical simulations and finite element. This has allowed a quick and affordable recursive design technique. From a general idea, numerical results interpretation served to discard, complete and for the bettering the various prosthesis proposals.

For relevance, the choice of boundary conditions for the related FEA analysis should be close to the conditions found on natural ankle joint, in terms of carried loads and available degrees of freedom.

It should be noticed that the aforementioned anatomical limitations avoided the use of some primeval damping solutions, such as the use of fluids or negative-stiffness honeycomb structures, as seen.

One of the first explored options was the use of some damping, biologically compatible fluid, rather liquid or gas. On this early stage the use of FEA analysis for the design relied heavily on Fluid Solid Interaction (FSI); due the use of the tool, it was found that a solid UHMWPE structure with inner fluid embedded chambers could not be deformed enough to produce the required damping by frictional mechanisms.

The use of negative stiffness was also considered. Although the technology has been available for some time, most applications are related with vibrations control. The later focus was considered as a good option until it was found that strain was excessive for the chosen building material. Another cause of dissuasion for the implementation of this solution was the need of a viable manufacture design: chosen geometry should had been small enough to fit on the TAA prosthesis.

The use of simple hollow structures was formerly known on orthopedic applications for some similar, albeit different objectives, like weight reduction. It was found that this solution can be used for stress reduction within a limited space and restricted possible strain.

From the numerical results of FEA, it is concluded that the proposed TAA prosthesis assemble is functional and can be operated safely. Displacements and deformation parameters were compared with previous reports; while these were always higher for hollow designs, the associated change of stiffness allowed for more flexibility and energy absorption while still being close to original physiological behavior of the joint, avoiding a rigid load transfer to lower limb. Stress distribution and peak values inside sacrifice component change with the use of an inner hollow structure, being reduced in comparison with other TAA designs.

Future work

As a deliverable, a full prototype of a TAA prosthesis was developed. Simulation results are available for consult. However, only a rapid prototype was physically produced, with mechanical properties clearly different to the ones tested on simulations. A process of manufacturing should be found for creating the assemble as intended with enough competitive advantages to justify a future market development of the idea.

Prosthesis was tested as an isolated system, and it only took on account the osseous system during design stages. Even if it was demonstrated the safe operation under the average ankle loads, the effects on soft tissues are still in need of exploration. The nearest available solution is the inclusion of the prototype inside of a CAD model with at least the principal tendons and ligaments. In this sense, side work has been developed.

The proposed design is still susceptible for further optimization and improvement after an analysis on interaction within a virtual model of ankle joint. FEA will be a valuable tool for this purpose. In this line, new suggestions for prosthesis tibial and talar are of particular interest, as this work scope was mostly oriented to the polymeric sacrifice component. Changes on lighter biocompatible materials, new anchorage designs with less impact on osseous structure, ang geometrical optimization of these components are the most relevant options.

Another opportunity area and needed step is the design of a detailed description of surgical technique. and the needed instrumental for correct alignment and implementation of the prosthesis on a patient.

Experimental test on the manufactured design also must be explored. This would require a test bench, capable of operate within millions of cycles, following a correspondent norm for prosthesis testing, especially on fatigue.

With these additional elements, the possibility for seeking intellectual property protection for the proposed TAA prosthesis design and implementation is feasible. It also represents a prerequisite for further commercialization. As any medical equipment, the prosthesis should be tested for assuring safety in order to be certified by the competent authorities.

The use of highly crosslinked UHMWPE on prosthesis has slowly increased on commercial prosthesis. As a different focus for the solution of the same general problems of overstressed and over worn prosthesis, a combination of both seems at glance feasible and desired. Material characterization for a new material model is then required, in order to prove or not this possible bettering of the proposed design.

And finally, eve when the use of negative-stiffness honeycomb cells could not be applied on ankle prosthesis polymeric inserts, the idea for its use for damping on other biomechanical devices should be taken on consideration.

References

[1] Peyron JG. (1984) "The epidemiology of osteoarthritis" In: Moskowitz RW, Howell DS, Goldberg VM, Mankin HJ, eds. *Osteoarthritis. Diagnosis and Treatment*. Philadelphia, PA: WB Saunders; : pp. 9–27.

[2] World Health Organization (2013) "Priority Medicines for Europe and the World 2013 Update. Chapter 12: Osteoarthritis".

[3] Woolf DA, Erwin J, March L (2012) "The need to address the burden of musculoskeletal conditions" Best Pract Res Cl Rh, 2012, vol 26 (2), pp: 183-224 DOI: https://doi.org/10.1016/j.berh.2012.03.005

[4] Vos T, Flaxman AD, Naghavi M, Lozano R, Michaud C, Ezzati M, et al. (2012) "Years lived with disability (YLDs) for 1160 sequelae of 289 diseases and injuries 1990–2010: a systematic analysis for the Global Burden of Disease Study 2010" *Lancet*, vol 380 (9859), pp: 2163-2196 DOI: https://doi.org/10.1016/S0140-6736(12)61729-2

[5] Aofas.org. (2016). "Arthritis of the Foot and Ankle". [Access on 17/07/2016]. Available in: http://www.aofas.org/footcaremd/conditions/ailments-of-the-ankle/pages/arthritis.aspx.

[6] Osteoarthritis Research Society International (2016). "Osteoarthritis: A Serious Disease" U.S. Food and Drug Administration.

[7] International Osteoporosis Foundation. (2012) Latin American Regional Audit. "Epidemiología, costos e impacto de la osteoporosis en 2012".

[8] Maetzel A, L Li, J Pencharz, G Tomlinson, and C Bombardier (2004). "The economic burden associated with osteoarthritis, rheumatoid arthritis, and hypertension: a comparative study". *Ann Rheum Dis*, 2004, vol 63: pp. 395-401 DOI: 10.1136/ard.2003.006031

[9] Newsroom.aaos.org. (2016). "AAOS Online Newsroom | Despite Economic Times, U.S. Demand for Total Joint Replacement Remains Steady". [Access on 21/07 2016]. Available at: http://newsroom.aaos.org/media-resources/Press-releases/despite-economic-times-us-demand-for-total-joint-replacement-remains-steady.htm

[10] Kurtz S, Ong K, Lau E, Mowat F, Halpern M. "Projections of primary and revision hip and knee arthroplasty in the United States from 2005 to 2030". *J Bone Joint Surg Am*. 2007 Apr; 89(4):780-5. DOI:10.2106/JBJS.F.00222

[11] Orthopedic Prosthetics Market - Growth, Trends, and Forecast (2019 - 2024) [Access on 09/05/2019] Available at .https://www.mordorintelligence.com/industry-reports/orthopedic-prosthetics-market

[12] Orthopedic Medical Devices (2019). "Market 2019 Market Drivers, Trends and Issues forecast to 2024". Retrieved from https://www.marketwatch.com/press-release/orthopedic-medical-devices-market-2019-market-drivers-trends-and-issues-forecast-to-2024-2019-03-22 [Access on 07/05/2019].

[13] Mexico Orthopedic Devices Market Outlook to 2018 Available at https://www.marketresearch.com/product/sample-8042548.pdf

[14] Gougoulias N, Khanna A, Maffulli N. (2009) History and Evolution of the Total Ankle Replacement. British Medical Bulletin 2009; 89: 111–151 DOI: 10.1093/bmb/ldn039

[15] Vickerstaff JA, Miles AW, Cunningham JL. (2007) "A brief history of total ankle replacement and a review of the current status". *Medical Engineering & Physics* vol. 29;pp. 1056–1064 DOI: 10.1016/j.medengphy.2006.11.009

[16] Terrier A, Larrea X, Guerdat J, Crevoisier X. (2014) "Development and experimental validation of a finite element model of total ankle replacement". *Journal of Biomechanics* Vol. 47; pp. 742–745 DOI:

[17] Prissel MA, Roukis TS. (2013) "Managing Osteolysis Following A Failed Ankle Implant". *Podiatry Today* vol. 26(11). Available at https://www.podiatrytoday.com/managing-osteolysis-following-failed-ankle-implant

[18] Marieb EN. (2000). "Essentials of Human Anatomy and Physiology". San Francisco: Benjamin Cummings.

[19] Wikimedia Commons. "Lateral view of the human ankle". Available at https://commons.wikimedia.org/wiki/File:Ankle_en.svg [Access on 09/05/219]

[20] Kapandji AI. (2012) "Fisiología articular. Tomo 2. Miembro inferior". Quinta edición. Editorial Médica Panamericana.

[21] Soria C. (2016) "Tibia bone [CAD Model]" [Accessed on 19/08 2018].Available at https://grabcad.com/library/tibia-bone-1

[22] Wan L, de Asla RJ, Rubash HE, Li G. "In vivo cartilage contact deformation of human ankle joints under full body weight". *J Orthop Res*, Vol. 26(8): pp. 1081-1089. DOI: https://doi.org/10.1002/jor.20593

[23] Kimizuka M, Kurosawa H, Fukubayashi T. (1980) "Load-bearing pattern of the ankle joint. Contact area and pressure distribution". Arch Orthop Trauma Surg; vol 96(1): pp. 45-49. PMID: 7377925

[24] OpenStax College. Anatomy & Physiology, Connexions Web site. Jun 19, 2013. [Access on 07/05/219] Available at http://cnx.org/content/col11496/1.6/

[25] Vidal Lesso, A. (2012) "Caracterización biomecánica multifactorial numérica-experimental de osteoartritis en rodilla" [master's thesis. Universidad de Guanajuato.

[26] Delco ML, Kennedy JG, Bonassar LJ, Fortier LA (2017) "Post-Traumatic Osteoarthritis of the Ankle: A Distinct Clinical Entity Requiring New Research Approaches" J Orthop Res. 2017 Mar; 35(3): 440–453. DOI: 10.1002/jor.23462

[27] Schuh R, Hofstaetter J, Krismer M, Benovi R, Windhager R, Trnkla HJ. (2012) "Total ankle arthroplasty versus ankle arthrodesis. Comparison of sports, recreational activities and functional outcome". *Int Orthop* 36: pp. 1207-1214 DOI: : 10.1007/s00264-011-1455-8

[28] Abdo R, Wasilewski SA (1992) "Ankle arthrodesis: a long –term study". *Foot Ankle Int Vol 13*: pp. 307–312 PMID:1398357

[29]. Bonasia D, Dettoni F, Femino JE, Phisitkul P, Germano M, Amendola A. (2010) "Total Ankle Replacement: Why, When and How*?" Iowa Orthopaedics* J.; Vol. 30: pp. 119-30. PMID:21045984; PMCID: PMC2958283

[30] Park JS, Mroczek, KJ. (2011) "Total Ankle Arthroplasty". Bulletin of the NYU Hospital for Joint Diseases; vol 69(1); pp. 27-35 [Accessed on 09/05/2019] Available at: http://presentationgrafix.com/_dev/cake/files/archive/pdfs/239.pdf

[31] U.S. National Library of Medicine. "Ankle Replacement" MedlinePlus Medical Encyclopedia [Accessed on 09/05/2019] Available at: https://medlineplus.gov/ency/article/007254.htm

[32] Cleveland Clinic. "A Patient's Guide to Artificial Joint Replacement of the Ankle". Orthopod [Accessed on 09/05/2019] Available at: https://my.clevelandclinic.org/ccf/media/Files/Ortho/patient-education/total-joint-replacement-patient-guide.pdf?la=en

[33] Zhou H, Shaw J, Patel A, Li X, (2016) "In-patient Trends And Complications After Total Ankle Arthroplasty In The United States". *Orthopedics* vol. 39(1):e74-9. doi: 10.3928/01477447-20151228-05

[34] Arvind C. (2016) "Total Ankle Replacement Surgery". Royal Berkshire NHS [Accessed on 09/05/2019] Available at: http://www.royalberkshire.nhs.uk/patient-information-leaflets/Orthopaedics%20total%20ankle%20replacement.htm

[35] Orthopedics Today (2013) Total ankle arthroplasty shows promising results, but obstacles exist. [Accessed 09/075/2019] Available at: https://www.healio.com/orthopedics/foot-ankle/news/print/orthopedics-today/%7B730aa559-8135-4ce7-9903-ff5b5424d18e%7D/total-ankle-arthroplasty-shows-promising-results-but-obstacles-exist?page=5

[36] Greenfield S, Ellis S (2013) "The bright future for total ankle replacements" *Curr Rev Musculoskelet Med*; vol. 6(4): pp. 273–275. DOI: 10.1007/s12178-013-9189-4

[37] Glaister BC, Bernatz GC, Klute GK, Orendurff MS. (2007) "Video task analysis of turning during activities of daily living". *Gait Posture* vol 25(2): pp. 289-94. DOI: 10.1016/j.gaitpost.2006.04.003

[38] Which Medical Device™ Agility LP Total Ankle System. [Accessed on 21/07 2016]

Available at: http://www.whichmedicaldevice.com/by-manufacturer/86/171/agility-lp-total-ankle-system

[39] TotalAnkleJoint.com. "Ankle Replacement Solutions". [Accesed 21/06/2016]Available at: http://www.totalanklejoint.com/ankle_replacement_solutions.html

[40] Bonnin, M, Judet T, Colombier JA, Buscayret F, Graveleau N., Piriou P. (2004) "Midterm results of the Salto Total Ankle Prosthesis" *Clin Orthop Relat Res*. 424): pp. 6-18. DOI: 10.1097/01.blo.0000132407.75881.a0

[41] Wood PRL, Prem H, Sutton C. (2008) "Total Ankle Replacement. Medium term results in 200 Scandinavian Total Ankle Replacements" *J Bone Joint Surg Br*. 2008 vol 90(5): pp. 605-609. DOI: 10.1302/0301-620X.90B5.19677.

[42] Buechel FF, Pappas MJ. (2003) "Ten-Year Evaluation of Cementless Buechel-Pappas Meniscal Bearing Total Ankle Replacement" *Foot & Ankle International* vol 24(6): pp. 462-72 · DOI: 10.1177/107110070302400603

[43] Núñez-Sampera M. (2007) "Artroplastia modular de tobillo Modular ankle arthroplasty." *Revista Española de Cirugía Ortopédica y Traumatología*. Vol 51. Num 1. pp-51-58

[44] Hintermann B, Zwicky L, Knupp M, Henninger HB, Barg A "HINTEGRA Revision Arthroplasty for Failed Total Ankle Prostheses" J Bone Joint Surg Am, 2013 Jul 03; 95 (13): 1166 -1174 . http://dx.doi.org/10.2106/JBJS.L.00538

[45] Wood PLR, Karski MT, Watmough P (2010) "Total ankle replacement. The results of 100 Mobility Total Ankle Replacement" *J Bone Joint Surg Br*. 2010 Jul;92(7):958-62. DOI: 10.1302/0301-620X.92B7.23852

[46] Giannini S, Romagnoli M, O'Connor JJ, Malerba F, Leardini A. (2010) "Total Ankle Replacement Compatible with Ligament Function Produces Mobility, Good Clinical Scores, and Low Complication Rates. An Early Clinical Assessment". *Clinical Orthopedic Related Results*. vol 468: pp 2746–2753 DOI: 10.1007/s11999-010-1432-3

[47] Stryker (2017) STAR Surgical Technique. [Accessed 09/05/2019] Available at http://az621074.vo.msecnd.net/syk-mobile-content-cdn/global-content-system/SYKGCSDOC-2-42232/QEQdB2-cT87Q4a5nq7YCzPKdMMvSsg/STAR_ST_2.pdf

[48] Henricson A, Skoog A, Carlsonn A. (2007) "The Swedish Ankle Arthroplasty Register. An analysis of 531 arthroplasties between 1993 and 2005". *Acta Orthopaedica 2007*; vol. 78 (5): pp. 569-574 DOI: https://doi.org/10.1080/17453670710014248

[49] Mendiola G, Talus Group (1997) "The Ramses Ankle Replacement: Design – Surgical Technique- Results: A report of the First 38 Cases". *Maîtrise Orthopédique n° 61*.

[50]. Ianuzzi A, Mkandawire C. "Applications of UHMWPE in total ankle replacements" in Kurtz, S.M. ed., *UHMWPE Biomaterials Handbook*, 2nd ed, 2009, San Diego, California: Academic Press Elsevier, pp. 153-169.

[51] Stein HL (1998). "Ultrahigh molecular weight polyethylenes" (UHMWPE). *Engineered Materials Handbook* pp. 167-171

[52] Kurtz, S. (2009). "A primer on UHMWPE." In: Kurtz, S., ed., *UHMWPE Biomaterials Handbook*, 2nd ed. San Diego, California: Academic Press Elsevier, pp.1-6.

[53] Li S, Burstein AH. (1994) "Current Concepts Review: Ultra High Molecular Weight Polyethylene". *The Journal of Bone and Joint Surgery* vol.76-A (7): pp. 1080–1090

[54] Sobieraj MC, Rimnac CM. (2008). "Ultra high molecular weight polyethylene: mechanics, morphology, and clinical behavior". *Journal of the mechanical behavior of biomedical materials* vol. 2(5), 433–443. DOI:10.1016/j.jmbbm.2008.12.006

[55] Bowden AE, Oneida E, Bergström J. (2009). "Computer Modeling and Simulation of UHMWPE" S. Kurtz, ed., *UHMWPE Biomaterials Handbook*, 2nd ed. San Diego, California: Academic Press Elsevier, pp.519-531. DOI: 10.1016/S0142-9612(01)00265-4

[56] Harris J. "A study of the mechanical properties of Ultra High Molecular Weight Polyethylene (UHMWPE)". University of Pittsburgh. Department of Mechanical Engineering

[57] Musib M. (2012). "A Review of the History and Role of UHMWPE as A Component in Total Joint Replacements". International Journal of Biological Engineering vol 1(1), pp.6-10.

[58] Kurtz S. (2009). "From Ethylene Gas to UHMWPE Component: The Process of Producing Orthopedic Implants". In: S. Kurtz, ed., UHMWPE Biomaterials Handbook, 2nd ed. San Diego, California: Academic Press Elsevier, pp.8-18.

[59] Plasticsmag.com. (2003). Fabricating & Machining UHMW-PE: Plastic Distributor & Fabricator. [online] [Access on 18/01/2017]. Available at: http://www.plasticsmag.com/features.asp?fIssue=sep/oct-03&aid=3862

[60] Fulín P, Šlouf M, Vlková H, Kredatusová J, Pokorný D. (2019) "Comparison of the Quality of the Most Frequently Used New UHMWPE Articulation Inserts of the Total Hip Replacement" Acta Chir Orthop Traumatol Cech. 2019; vol 86(2): pp.101-109. PMID: 31070568

[61] Baker DA, Hastings RS, Pruitt LA. (2000) "Compression and tension fatigue resistance of medical grade ultra-high molecular weight polyethylene: the effect of morphology, sterilization, aging and temperature" Polymer vol. 41, pp. 795-808. DOI: https://doi.org/10.1016/S0032-3861(99)00199-8

[62] ASTM (2004) "Specification for Ultra-High-Molecular Weight Polyethylene Powder and Fabricated Form for Surgical Implants (F0648-04)" ASTM International, West Conshohocken, PA, USA

[63] Spiegelberg S. (2001), "Analytical techniques for assessing the effect of radiation on UHMWPE", http://www.campoly.com/notes/008. pdf, Presented at Soc. for Biomaterials Annual Conference, St. Paul MN Cam. Polym. Gr.

[64] Spiegelberg S. (2009). "Characterization of Physical, Chemical, and Mechanical Properties of UHMWPE". En: Kurtz, S. ed., UHMWPE Biomaterials Handbook, 2nd ed. San Diego, California: Academic Press Elsevier, pp.355-367.

[65] Kurtz S. (2009). "Compendium of Highly Crosslinked UHMWPEs". In: Kurtz, S., ed., UHMWPE Biomaterials Handbook, 2nd ed. San Diego, California: Academic Press Elsevier, pp.291-308.

[66] Federal Register. (2017). "Characterization of Ultrahigh Molecular Weight Polyethylene Used in Orthopedic Devices; Draft Guidance for Industry and Food and Drug Administration Staff" [Access on 18/01/2017]. Available at: https://www.federalregister.gov/documents/2016/02/12/2016-02879/characterization-of-ultrahigh-molecular-weight-polyethylene-used-in-orthopedic-devices-draft

[67] Oral E, Wannomae KK, Bichara DA, Micheli B, Doshi BN, O'Brien C, Nielsen GP, Muratoglu OK. (2018). "An antioxidant stabilized, chemically cross-linked UHMWPE with superior toughness". J Biomed Mater Res B Part B. 2018: 9999:9999: 1– 8. DOI: https://doi.org/10.1002/jbm.b.34287

[68] Addiego F, Buchheit O, Ruch D, Ahzi, S., & Dahoun, A. (2011). "Does texturing of UHMWPE increase strength and toughness? A pilot study". Clinical orthopaedics and related research, vol 469(8), pp. 2318–2326. DOI: 10.1007/s11999-010-1716-7

[69] Oral E, Orhun KM. (2009). "Compendium of Highly Crosslinked UHMWPEs".I: Kurtz S. ed., UHMWPE Biomaterials Handbook, 2nd ed. San Diego, California: Academic Press Elsevier, pp.221.

[70] Turner A, Okubo Y, Teramura S, "The antioxidant and non-antioxidant contributions of vitamin E in vitamin E blended ultra-high molecular weight polyethylene for total knee

replacement" J Mech Behav Biomed Mater. 2014 Mar; vol. 31: pp.21-30 DOI: 10.1016/j.jmbbm.2012.12.006

[71] Solapur D, Journal I. (2015). "Tribological wear investigation of UHMWPE and PEEK for artificial hip joint". Industrialscience.org. [Accessed 23/01/2017]. http://www.industrialscience.org/Article.aspx?aid=74&vid=12

[72] Brockett C, Carbone S, Fisher J, Jennings L. (2017). "PEEK and CFR-PEEK as alternative bearing materials to UHMWPE in a fixed bearing total knee replacement: An experimental wear study". Sciencedirect.com. [Accessed on 24/01/201] Available at: http://www.sciencedirect.com/science/article/pii/S0043164816307499

[73] Dahl M, Jacobsen S, Metcalf N, Sasso R, Ching R. (2011). "A comparison of the shock-absorbing properties of cervical disc prosthesis bearing materials". SAS Journal vol 5(2); pp. 48-54 DOI: https://doi.org/10.1016/j.esas.2011.01.002

[74]. Matweb.com. (2017). "MatWeb - The Online Materials Information Resource" [online] [Accessed 20 Dec. 2017]. Available at: http://www.matweb.com/search/datasheet.aspx?matguid=0a722163160c4c53b7f40e1efb71c291&ckck=1

[75]. Pruitt LA. (2005) "Deformation, yielding, fracture and fatigue behavior of conventional and highly cross-linked ultra-high molecular weight polyethylene" Biomaterials 26(8) pp. 905-915

[76] ASTM (2004) Standard Test Method for Tensile Properties of Plastics (Metric) (D638M-96) ASTM International, West Conshohocken, PA, USA

[77] ASTM (2004) Standard Test Method for Compressive Properties of Rigid Plastics (D695-02) ASTM International, West Conshohocken, PA, USA

[78] Available at: https://www.ebay.com/itm/Used-Fadal-VMC-3016-L-CNC-Vertical-Machining-Center-Mill-88HS-Rigid-Tap-CT-1999-/263901840301

[79] Available at: https://www.instron.es/es-es/products/testing-systems/dynamic-and-fatigue-systems/servohydraulic-fatigue/8802

[80] Turell MB, Bellare A. (2004) "A study of the nanostructure and tensile properties of ultra-high molecular weight polyethylene". Biomaterials. 2004 Aug; vol 25(17): pp. 3389-3398. DOI:10.1016/j.biomaterials.2003.10.027

[81] Kurtz S, Pruitt L, Jewett CW, Crawford RP, Crane DJ, Edidin AA. (1998) "The yielding, plastic flow, and fracture behavior of ultra-high molecular weight polyethylene used in total joint replacements". Sciencedirect.com. [Accessed on 24/01/201] Available at: http://www.sciencedirect.com/science/article/pii/S0142961298001124

[82] Hernández-Gómez O. (2015) Caracterización mediante pruebas de tensión, relajación de esfuerzos y tenacidad del UHMWPE (Pre-grade Thesis) Universidad Autónoma de México. Facultad de Ingeniería. Ciudad Universitaria, México

[83] Medel FJ, Furmanski J. (2009). "Fatigue and Fracture of UHMWPE" In: S. Kurtz, ed., UHMWPE Biomaterials Handbook, 2nd ed. San Diego, California: Academic Press Elsevier, pp.519-531.

[84] ASTM (2000) ASTM Standard Test Method for Measurement of Fatigue Crack Growth Rates (E647-00). ASTM International, West Conshohocken, PA, USA

[85] Kozak A, Leisinger S, Spiegelberg S, Narayan V. (2016) "Fatigue Crack Propagation Testing in UHMWPE" Cambridge Polymer Group [Accessed on 02/06/2019] Available at: http://www.campoly.com/files/2114/4673/7871/UHMWPE_2015_poster.pdf

[86] Ansari F, Gludovatz B, Kozak A, Ritchie RO, Pruitt LA. (2016) "Notch fatigue of ultrahight molecular weight polyethylene (UHMWPE) used in total joint replacements". Journal of the Mechanical Behavior of Biomedical Materials 60, pp. 267-279. DOI: 10.1016/j.jmbbm.2016.02.014

[87] Azam AM, Ali A, Khan H, Yasin T, Mehmood MS (2016) "Analysis of degradation in UHMWPE a comparative study among the various commercial and laboratory

grades UHMWPE" IOP Conf. Series: Materials Science and Engineering 146 (2016) 012025 DOI:10.1088/1757-899X/146/1/012025

[88] Gul RM, Fung K, Doshi BN, Oral E, Muratoglu OK (2017) "Surface cross-linked UHMWPE using peroxides" Journal of Orthopaedic Design vol. 35 (11): pp 2551-2556 DOI: https://doi.org/10.1002/jor.23569

[89] Zhang H, Liang Y (2017) "Extrusion Processing of Ultra-High Molecular Weight Polyethylene" in Qamar SZ, ed. Extrusion of Metals, Polymers and Food Products. Intech Open DOI: 10.5772/intechopen.72212

[90] Estupiñán JE, Baldini TH, Bartel DL, Wright TM (1999) "Recoverable and unrecoverable creep on UHMWPE" 45th Annual Meeting, Orthopaedic Research Society, February 1-4, 1999, Anaheim, California.

[91] Metin F, Cengil S (2016) "Short-term creep and recovery behavior of medical grade ultra-high molecular weight polyethylene (UHMWPE)" *JAMME* vol.78; pp. 65-70. DOI:10.5604/01.3001.0010.1496.

[92] Regis M, Bracco P, Giorgini L, Fusi S, Dalla Pria P, Costa L, Schmid C. (2014) "Correlation between in vivo stresses and oxidation of UHMWPE in total hip arthroplasty" *J Mater Sci Mater Med*. 2014; vol. 25(9): pp. 2185-2192. DOI: 10.1007/s10856-014-5254-9

[93] Edidin AA.; Jewett CW.; Kalinowski A, Kwarteng K, Kurtz SM. Degradation of mechanical behavior in UHMWPE after natural and accelerated aging. *Biomaterials* 2000, 21, 1451–1460. DOI: https://doi.org/10.1016/S0142-9612(00)00021-1

[94]. Bergström JS, Kurtz SM, Rimmac CM, Edidin AA. (2002) "Constitutive modeling of ultra-high molecular weight polyethylene under large-deformation and cyclic loading conditions" *Biomaterials* vol. 23(11), pp. 2329-2343 DOI: https://doi.org/10.1016/S0142-9612(01)00367-2

[95]. Martins-Barata, AM. (2014) "Bone Remodeling Analysis After Total Ankle Arthroplasty" Instituto Superior Técnico, Universidade Técnica de Lisboa. [Access on 28/06/2019] Available at: https://fenix.tecnico.ulisboa.pt/downloadFile/1970719973965836/resumo%20corrigido.pdf

[96]. Capitanu L, Vladarenau L. Florescu V. (2015) "The Knee Wear Prediction of UHMWPE Tibial Inset Using VIPRO Platform" *Journal of Mechanics Engineering and Automation* 55 pp. 591-600 DOI:10.17265/2159-5275/2015.11.001

[97]. Suchocki,C., Pawlikowski,M., Skalski, K. (2013) "Determination of material parameters of quasi-linear viscoelastic rheological model for thermoplastics and resins" *Journal of Theoreitcal and Applied Mechanics* 51,3, pp.569-580

[98]. Bergström JS, Boyce MC (1998) "Constitutive modeling of the large strain time–dependent behavior of elastomers," *J Mech Phys Solids*, vol. 46, pp. 931–954 DOI: https://doi.org/10.1016/S0022-5096(97)00075-6

[99]. J.S. Bergström JE. Bischoff (2010) "An Advanced Thermomechanical Constitutive Model for UHMWPE," *Int J Struct Changes Sol*, vol. 2: pp.31–39

[100] Singh KV, Khan F (2014) "Interactive Module for Biomaterial Modeling and Characterization" *Proceedings of 121st ASEE Annual Conference & Exposition*, Indiannapolis, IN, June 15-18

[101] Elliot BJ., Gundapaneni, D, Goswami, T. (2014) "Finite element analysis of stress and wear characterization in total ankle replacements". *Journal of the Mechanical Behavior of Biomedical Materials* vol. 34, June 2014, pp.134-145 DOI: https://doi.org/10.1016/j.jmbbm.2014.01.020

[102] Chen PC, Colwell CW, D'Lima DD (2011) "A nonlinear viscoelastic finite element model of polyethylene". *Mol Cell Biomech*. 2011 Jun; vol. 8(2): pp. 135-48 PMID: 21608414

[103] Thompson MK, Thompson JM, (2017). "Defining Material Properties" In Thompson MK, Thompson JM (Ed.), *ANSYS Mechanical APDL for Finite Element Analysis* pp. 147-161 Butterworth-Heinemann, DOI: https://doi.org/10.1016/B978-0-12-812981-4.00005-8

[104]. Slaughter WS. (2002) *The Linearized Theory of Elasticity* Birkhauser Verlag. AG, Basel. Switzerland.

[105]. Matweb.com. (2017). "MatWeb - The Online Materials Information Resource" [online] [Access on 20/12/2017]. Available at: http://www.matweb.com/search/datasheet.aspx?matguid=0a722163160c4c53b7f40e1efb71c291&ckck=1

[106]. Bower AF. (2012) "Constitutive Models-Relations between Stress and Strain" Bower, A.F. Applied Mechanics of Solids.

[107] ANSYS User's Guide Ansys 15. Educational version. Program documentation. SAS IP, Inc.; 2015

[108] Bergstöm J (2015) "Elasticity/Hyperelasticity" in Bergström J (Ed.) *Mechanics of solid polymers.Theory and Computational Modeling* pp. 209-307. William Andrew Applied Science Publishers

[109] Ranganatham R, Verdant B, Zhao, R (2014) "Bilinear isotropic hardening behavior" Cornell University College of Engineering. [Access on 28/06/2019] Available at: https://es.scribd.com/document/287234770/Bilinear-Isotropic-Hardening-Behavior

[110] Wright TM, Gunsallus KL, Rimnac CM et al (1991). "Design considerations from an acetabular component made from an enhanced form of ultra-high molecular weight polyethylene". *Transactions of the 37th Orthopedic Research Society 1991*; 248

[111]. Kelly PA. (2015) "Solid Mechanics Part II: Engineering Solid Mechanics – small strain." Solid Mechanics Part III, Department of Engineering Science, University of Auckland [Access on 28/06/2019] Available at:

http://homepages.engineering.auckland.ac.nz/~pkel015/SolidMechanicsBooks/Part_II/index.html

[112] Basan R, Marohnić T. (2016) "Constitutive model and material behavior" Scientific Project Number IP-2014-09-4982, Croatian Science Foundation Development of evolutionary procedures for characterization of biological tissues behavior BIOMAT University of Rijeka. Faculty of Engineering [Access on 28/06/2019] Available at: http://www.riteh.uniri.hr/media/filer_public/c7/b4/c7b4b975-9474-4b66-a04f-ff3597ba61e7/d711_constitutive_modeling_and_material_behavior_interim_report.pdf

[113] Bergstöm J (2015) "Plasticity Models" in Bergström J (Ed.) *Mechanics of solid polymers.Theory and Computational Modeling* pp. 353-369 William Andrew Applied Science Publishers

[114] Kang G, Ohno N, Nebu A (2003) "Constitutive modeling of strain range dependent cyclic hardening". *International Journal of Plasticity* vol. 19 (2003) pp. 1801–1819 DOI: https://doi.org/10.1016/S0749-6419(03)00016-0

[115]. Arruda EM., Boyce MC (1993) "A three-dimensional constitutive model for the large stretch behavior of rubber elastic materials". Journal of the Mechanics and Physics of Solids, Elsevier, 41 (2), pp.389-412. DOI: https://doi.org/10.1016/0022-5096(93)90013-6

[116]. Johansson H, Runesson, K. (2005) "Calibration of the Bergströn-Boyce model: Explicit expressions" Department of Applied Mechanics. Division Material & Computational Mechanics. Chalmers University of Technology. [Access on 28/06/2019] Available at https://core.ac.uk/download/pdf/70560937.pdf

[117]. Brinson HL., Brinson LC. (2008). "Polymer Engineering Science and Viscoelasticity", Springer Verlag (New York). I SBN 978-1-4899-7485-3

[118]. Lopes Pacheco JE. Bavastri CA, Pereira JT. (2015). "Viscoelastic Relaxation Modulus Characterization Using Prony Series". *Latin American Journal of Solids and Structures*, vol. 12(2), pp. 420-445. DOI: 10.1590/1679-78251412

[119] Dal H, Kaliske M (2009) "Bergström–Boyce model for nonlinear finite rubber viscoelasticity: theoretical aspects and algorithmic treatment for the FE method" *Comput Mech* vol. 44: pp. 809–823 DOI 10.1007/s00466-009-0407-2

[120] Steidel RF (1971). "An Introduction to Mechanical Vibrations". John Wiley & Sons. pp. 37 ISBN: 978-0-471-84545-4

[121] Geethamma VG, Asaletha R, Kalarikkal N,Thomas S (2014)"Vibration and sound damping in polymers" Resonance vol. 9 (14) pp 821–833 DOI: https://doi.org/10.1007/s12045-014-0091-1

[122] Sophia Fox AJ, Bedi A, Rodeo SA. (2009). "The Basic Science of Articular Cartilage: Structure, Composition, and Function". Sports Health, vol. 1(6), pp. 461–468. DOI: 10.1177/1941738109350438

[123] Lee JD, Mooney LM, Rouse EJ. (2017) "Design and Characterization of a Quasi-Passive Pneumatic Foot-Ankle Prosthesis". IEEE Transactions on Neural Systems and Rehabilitation Engineering vol: 25(7), pp. 823 – 831 DOI: 10.1109/TNSRE.2017.2699867

[124] Bungartz HJ, Schäfer M (2006). "Fluid-structure Interaction" In Bungartz HJ, Schäfer M *Fluid-structure Interaction: Modelling, Simulation, Optimization*. Springer-Verlag. ISBN 978-3-540-34595-4.

[125] Sigrist JF (2015). "Fluid-structure Interaction" In Sigrist *JF Fluid-Structure Interaction: An Introduction to Finite Element Coupling*. Wiley ISBN 978-1-119-95227-5

[126] Morand H, Ohayon R (1979) "Substructure variational analysis of the vibrations of coupled fluid–structure systems. Finite element results" International Journal for Numerical Methods in Engineering vol. 14(5):741 - 755 · DOI: 10.1002/nme.1620140508

[127] Dowell HE, Hall KC (2011) "Modeling of Fluid-Structure Interaction" Annual Review of Fluid Mechanics vol. 33(1); pp. 445-490 DOI: 10.1146/annurev.fluid.33.1.445

[128] Cengel YA, Boles MA. Thermodynamics: An Engineering Approach (4th ed.). pp. 89. ISBN 0-07-238332-1.

[129] Morrison SF. “Regulation of body temperature”. In: Boron WF, Boulpaep EL, eds. Medical Physiology. 3rd ed. Philadelphia, PA: Elsevier; 2017:chap 59.

[130] Zite JL, Ahmadkhanlou F, Neelakantan VA, Washington GN (2006) "A magnetorheological fluid based orthopedic active knee brace", Proc. SPIE 6171, Smart Structures and Materials 2006: Industrial and Commercial Applications of Smart Structures Technologies, 61710H (30 March 2006); https://doi.org/10.1117/12.658693

[131]. Dong L, Lakes RS. (2012) “Advanced damper with negative structural stiffness elements”, Smart Materials and Structures 21(7) p.075026 DOI: 10.1088/0964-1726/21/7/075026

[132].Jaglinski TM, Lakes RS. (2007) “Negative Stiffness and Negative Poisson's Ratio in Materials which Undergo a Phase Transformation, in Adaptive Structures: Engineering Applications” (eds D. J. Wagg, I. P. Bond, P. M. Weaver and M. I. Friswell), John Wiley & Sons, Ltd, Chichester, UK.

[133]. Kashdan LD, Seepersad CC, Haberman M, Wilson SP (2012) “Design, fabrication and evaluation of negative stiffness elements using SLS” Rapid Prototyping Journal 2012 18:3 , pp. 194-200 DOI: https://doi.org/10.1108/13552541211218108

[134]. Lakes RS (2001) “Extreme Damping in Composite Materials with a Negative Stifness Phase”, Physical Review Letters 86 (13) pp. 2897-2900 DOI: 10.1103/PhysRevLett.86.2897

[135] Dong L, Lakes R. (2013) “Advanced damper with high stiffness and high hysteresis damping based on negative structural stiffness” International Journal of Solids and Structures, 50(2013) pp. 2416-2423. DOI: https://doi.org/10.1016/j.ijsolstr.2013.03.018

[136] Platus DL (1993) "Smoothing out bad vibres", Machine Design, Penton,Inc. Cleveland, US, vol. 65, no. 4, 26 February 1993 (1993-02-26), pp. 123 - 126,128,13, XP000355854, ISSN: 0024-9114

[137] Minus K® Technology [online], Available at:. http://www.minusk.com/index.html [Accessed 22 Feb. 2018]

[138] Tolu N, Smit G, Nikooyan AA, Plettenburg D, Herder J.L. (2012) "Stiffness compensation mechanism for body powered hand prostheses with cosmetic covering". Journal of Medical Devices vol. 6(1):011004 DOI: 10.1115/1.3443321

[139] Smit G, Plettenburg D, Van der Helm F (2014) "A mechanism to compensate undesired stiffness in joints of prosthetic hands" Prosthetics and Otrhotics International 2014, Vol 38(2) pp. 96-102. DOI: 10.1177/0309364613488620.

[140] Dahiya A, Braun DJ. (2017) "Efficiently tunable positive-negative stiffness actuator," 2017 IEEE International Conference on Robotics and Automation (ICRA), Singapore, 2017, pp. 1235-1240 DOI: 10.1109/ICRA.2017.7989146

[141] Correa DM., Klatt T, Cortes S et al (2015) 'Negative stiffness honeycombs for recoverable shock isolation', Rapid Prototyping Journal, vol 21(2), pp. 193–200. DOI: https://doi.org/10.1108/RPJ-12-2014-0182

[142] Correa DM (2015) "Design and Evaluation of Negative Stiffness Honeycombs for Recoverable Shock Isolation" M.S.E. thesis University of Texas, Austin,TX.

[143] Bathe K. (1996) Finite element procedures in engineering analysis. Englewood Cliffs, N.J. Prentice Hall

[144]. Zhang Q, Yang X, Li P, Huang G, Feng S, Shen C, Han B, Zhang X, Jin F, Xu F, Lu TJ. (2015) "Bioinspired engineering of honeycomb structure – Using nature to inspire human innovation" Progress in Material Science 27 pp. 332-400 DOI: https://doi.org/10.1016/j.pmatsci.2015.05.001

[145] Corro-Hernández H, Vidal-Lesso A, Ledesma-Orozco ER "Mechanical Energy Absorption in Polyethylene Cell Pattern Structures for Biomedical Uses." *Proceedings of the ASME 2017 International Mechanical Engineering Congress and Exposition* vol. 3: Biomedical and Biotechnology Engineering. Tampa, Florida, USA. November 3–9, 2017. V003T04A015. ASME. https://doi.org/10.1115/IMECE2017-70345

[146] Lord G, Marotte JH (1973) "Total ankle prosthesis. Technique and first results. Apropos of 12 cases", *Rev Chir Orthop Reparatrice Appar Mot*, 1973, vol. 59 (pg. 139-151)

[147] Narayan, K. Lalit (2008). Computer Aided Design and Manufacturing. New Delhi: Prentice Hall of India. pp. 3. ISBN 978-8120333420.

[148] Total Ankle Institute (2017) The INFINITY™ Total Ankle System. [Access on 30/06/2019] Available at http://www.totalankleinstitute.com/infinity-products/infinity-ankle/

[149] Mann RA, Harrison MJ (2012) "Total Ankle Arthroplasty: A Brief Review" *Journal of Orthopaedics, Trauma and Rehabilitation* vol 16 (2) pp. 42-44 DOI: https://doi.org/10.1016/j.jotr.2011.12.001

[150] Global Market Insights (2017) Orthopedic Devices Market Size by Product. [Access on 30/06/2017] Available at https://www.orthoconnections.com/news/orthopedic-devices-market-to-reach-53bn-by-2024

[151] Polguj M, Bliźniewska KM, Jędrzejewski K, Majos A (2013) "Morphological study of linea aspera variations - proposal of classification and sexual dimorphism" *Folia morphologica* vol. 72(1): pp. 72-7 DOI: 10.5603/FM.2013.0012

[152] Van Dijk CN, Reilingh ML, Zengerink M, Van Bergen CJ. (2010). "Osteochondral defects in the ankle: why painful?". *Knee surgery, sports traumatology, arthroscopy : official journal of the ESSKA,* vol. 18(5), 570–580. DOI:10.1007/s00167-010-1064-x

[153] ISO 10993-1, "Biological evaluation of medical devices - Part 1: Evaluation and testing within a risk management process"(ISO, 2016)

[154] Alonso-Maturana A. Inventor. Sistema amortiguador para prótesis de rodilla y cadera. Comercial Maturana. SL ES 2538013B1 Spain. 2014 Dec. 30. [Access on 30/06/2019] Available at: https://patentados.com/2015/sistema-amortiguador-para-protesis

[155]. Araiko M.” Joint Forces within the Ankle During Level Walking”. Paper presented on ANSYS conference &26th CADFEM User’s Meeting 2008. October 22-24, 2008-darmstadium wissenschaft/ kongresse, Dramstadt, Germany.

[156] Corro-Hernández H, Vidal-Lesso A, Ledesma-Orozco ER, Palacios-Pineda LM (2019). “Structural analysis of a new total ankle replacement prosthesis with internal structure”. *DYNA* vol. 95: pp 192-197. DOI: http://dx.doi.org/10.6036/9267

[157]. Henricson A, Nilsson JA, Carlsson A. “10-year survival of total ankle arthroplasties: a report on 780 cases from the Swedish Ankle Register”. *Acta Orthop*. 2011 Vol 82(6): p. 655–659 DOI: https://doi.org/10.3109/17453674.2011.636678

[158]. Rippstein PF, Huber M, Coetzee JC, Naal FD (2011) “Total ankle replacement with use of a new three-component implant”. *J Bone Joint Surg* [Am] 2011; Vol. 93-A: p. 1426–1435. DOI: https://doi.org/10.1016/j.biomaterials.2004.03.022

[159]. Total Ankle Institute. 2018. “INBONE™ Total Ankle System - Total Ankle Institute”. [Accessed 20 Aug. 2018]. Available at: http://www.totalankleinstitute.com/inbone-products/inbone-ankle/

[160]. Kakkar R, Siddique MS.” Stresses in the ankle joint and total ankle replacement design”. *Foot Ankle Surg,* Vol. 17(2): p. 58 – 63. DOI: https://doi.org/10.1016/j.fas.2011.02.002

[161] Sopher RS, Amis AA, Calder JD, Jeffers JRT. (2017) “Total ankle replacement design and positioning affect implant-bone micromotion and bone strains”. *Medical Engineering & Physics* vol. 42, pp. 80-90 DOI:10.1016/j.medengphy.2017.01.022

[162] Manvi M., Kharvi PS, Savadi R. (2016) “Finite Element Analysis on Stainless Steel and Titanium Alloy Used as Ankle Joint Replacement Implant Materials*”. International Journal of Engineering Development and Research*. Vol. 4 (1); pp. 586-592

[163] Zhu J, Xu L. Inventors. All-organic high molecular material ankle joint prosthesis. CN105030385 A, China, 2015. [Access on 30/06/2019] Available at https://patents.google.com/patent/CN105030385A/en

[164] Exatech® (2018) Vantage ® Total Ankle System. A New Perspective in Total Ankle [Access on 30/06/2019] Available at https://www.exac.com/foot-and-ankle/vantage-total-ankle-system/

[165] Wagener J, Gross CE, Schweizer C1, Lang TH, Hintermann B. (2017) "Custom-made total ankle arthroplasty for the salvage of major talar bone loss." *Bone Joint J.* vol. ;99-B (2): pp. 231-236. DOI: 10.1302/0301-620X.99B2.BJJ-2016-0504.R2.

[166] Amazing AM, LLC (2018) [Access on 30/06/2019] Available at http://additivemanufacturing.com/basics/

[167] [Access on 30/06/2019] Available at https://articulo.mercadolibre.com.mx/MLM-603482947-impresora-replicadora-3d-negra-makerbot-_JM?matt_tool=43729882&matt_word&gclid=Cj0KCQjwu-HoBRD5ARIsAPIPeneLCneEiUi2bSa-_HOWufn6mqX5ypnJddRX6rGQJJsil9QW-kZKJoMaAulfEALw_wcB&quantity=1

[168] Belvedere C, Siegler S, Fortunato A, Caravaggi P, Liverani E, Durante S, Ensini A, Konow T, Leardini A (2018) "New comprehensive procedure for custom-made total ankle replacements: Medical imaging, joint modeling, prosthesis design, and 3D printing" *Journal of Orthopaedic Research* vol. 37(3); pp. 760-768 DOI: https://doi.org/10.1002/jor.24198

[169] Thomas RH, Daniels TR (2003) "Ankle arthritis" *J Bone Joint Surg Am*. 2003 May;85(5): pp. 923-36.

[170] Fraldi M, Esposito L, Perrella G, Cutolo A, Cowin SC (2010) "Topological optimization in hip prosthesis design". *Biomech Model Mechanobiol*. 2010 Aug;9(4):389-402. DOI: 10.1007/s10237-009-0183-0.

[171] 3D Printed PCU/UHMWPE Araujo-Borges R. "Polymeric Blends for Artificial Knee Meniscus" [Master's Thesis] University of Arkansas, Fayetteville, 2017

[172] Logan DL (2011). A first course in the finite element method. Cengage Learning

[173] Huiskes R., Chao EYS. (1983) *A survey of finite element analysis in orthopedic biomechanics: The first decade.* Journal of Biomechanics, Volume 16, Issue 6, pp. 385-4

[174] Stops A, Wilcox R, Jin Z. (2012) *Computational modelling of the natural hip: a review of finite element and multibody simulations*. Computer Methods in Biomechanics and Biomedical Engineering Volume 15, Issue 9 pp. 963-979

[175] Kang KT, Kim SH, Son J, ,Lee YH, Chun HJ. (2015) "In vivo evaluation of the subject-specific finite element model for knee joint cartilage contact area". *International Journal of Precision Engineering and Manufacturing*. June 2015, Volume 16, Issue 6, pp. 1171-1177

[176] Wong DWC, Wang Y, Chen TLW, Leung AKL, Zhang M. (2017) "Biomechanical consequences of subtalar joint arthroereisis in treating posterior tibial tendon dysfunction: a theoretical analysis using finite element analysis". *Computer Methods in Biomechanics and Biomedical Engineering* Volume 20, 2017, Issue 14, pp. 1525-1532

[177] Campbell B, Abramowitch,S, Anderst W. (2018) *A Comparison of the In Vivo Contact Pressure at the Tibiotalar Joint During Walking and Running*. Foot & Akle Orthopaedics Volume 3, Issue 3

[178] Chitsazana A, Rohui G, Abbasi M, Pezeshki,S, Tavakoli, SAH. (2015) "Assessment of stress distribution in ankle joint: simultaneous application of experimental and finite element methods*". Int. J. Experimental and Computational Biomechanics*, Vol. 3, No. 1, pp. 45-61

[179] Anderson DD, Goldsworthy JK, Li W, Rudert J, Togichi Y, Brown TD. (2007) "Physical validation of a patient-specific contact finite element model of the ankle". *Journal of Biomechanics* vol 40 (8), pp. 1662-1669

[180] Anderson DD, Goldsworthy JK, Shivanna K, Grosland, NM, Pedersen DR, Thomas, TP, Brown TD. (2006*). "*Intra-articular Contact Stress Distributions at the Ankle throughout Stance Phase – Patient-Specific Finite Element Analysis as a Metric of Degeneration Propensity". *Biomechanics and Modeling in Mechanobiology*, Vol. *5*(2-3), pp. 82–89.

[181] Terrier A, Fernandes CS, Guillemin M, Crevoisier X (2017) "Fixed and mobile-bearing total ankle prostheses: Effect on tibial bone strain". *Clin Biomech* Vol. 48: pp. 57-62 DOI: https://doi.org/10.1016/j.clinbiomech.2017.07.009

[182] Rodrigues, DSOS. "Biomechanics of the Total Ankle Arthroplasty: Stress Analysis and Bone Remodeling" [Master's Thesis] Instituto Superior Técnico. Universidad Técnica de Lisboa. 2013

[183] McInnes K, Oxland T, Younger A. (2012) "Micromotion patterns at the bone-implant interface of a mobile-bearing and a semi-constrained total ankle replacement: an in vitro biomechanical study". AOFAS

[184] Espinosa,N, Walti M, Favre P, Snedeker JG (2010) "Misalignment of total ankle components can induce high joint contact pressures". *J Bone Joint Surg Am*, vol. 92: pp.1179-1187,

[185] McIff TE, Saltzman C, Brown T. (2001) "Contact pressure and internal stresses in a mobile bearing total ankle replacement". Paper presented at *45th Annual Meeting of the Orthopaedic Research Society*. San Francisco, CA; 2001 Feb. 25–28.

[186] Park JB, Kim YK. "Metallic Biomaterials" in Wong, JY., Bronzino, JD., ed. *Biomaterials* 1st ed., 2007, Boca Raton, Florida. CRC Press Taylor & Francis Group pp. 6-10

[187] Matweb.com. (2018). MatWeb - The Online Materials Information Resource" [online] Available at: http://asm.matweb.com/search/SpecificMaterial.asp?bassnum=MTP641 [Accessed 02/09 2018].

[188] Reggiani B, Leardini A, Corazza F, Taylor M (2006) "Finite element analysis of a total ankle replacement during the stance phase of gait". *J Biomech*, 2006. Vol. 39(8): pp. 1435-1443. DOI: https://doi.org/10.1016/j.jbiomech.2005.04.010

[189] Miller MC et al. "Stresses in polyethylene liners in a semiconstrained ankle prosthesis". *J Biomech Eng*. 2004 Oct; Vol. 126(5): pp. 636-40. DOI: https://doi.org/10.1115/1.1798011

[190] Christesen RM (2019) "Failure Theory for Materials Science and Engineering" [Access on 04/11/2019] Available at: https://www.failurecriteria.com/index.html

[191] Lampman S "Mechanical behavior and wear" in Lampman S *Characterization and Failure Analysis of Plastics* 1st ed, 2003, Materials Park, Ohio, ASM International, pp. 202

[192] McGinty R (2012) "Von Mises Stress" [Access on 04/11/2019] Available at: https://www.continuummechanics.org/vonmisesstress.html

[193] Postak P, Rosca M, Greenwald A (2008) "Evaluation of the STAR total ankle replacement: an evolution in design." *Orthop Res Lab* 2008; Vol. 3: pp.180–182

[194] Smyth A, Fisher J, Suñer S, Brockett C. (2017) "Influence of kinematics on the wear of a total ankle replacement". *J Biomech* 53: pp. 105-110 DOI: https://doi.org/10.1016/j.jbiomech.2017.01.001

[195] *Standard Specification for Total Ankle Replacement Prosthesis*, ASTM International. ASTM F2665.

[196] Kincaid B, Fryman JC, Gillard D, Wentorf F, Popoola O, Bischoff J (2013). "Gravimetric Wear Testing of a Fixed-Bearing Bicondylar Total Ankle Replacement". Poster session presented on *ORS 2013 Annual Meeting* San Antonio, TX Jan 26-29, 2013. Poster No: 1161

Annex- Associated congress dissertations and journal publications

As products of the presented thesis, the following articles were published or part of conference memories.

- Corro-Hernández H, Vidal-Lesso A, Ledesma-Orozco ER "Mechanical Energy Absorption in Polyethylene Cell Pattern Structures for Biomedical Uses." *Proceedings of the ASME 2017 International Mechanical Engineering Congress and Exposition* vol. 3: Biomedical and Biotechnology Engineering. Tampa, Florida, USA. November 3–9, 2017. V003T04A015. ASME. https://doi.org/10.1115/IMECE2017-70345
- Corro-Hernández H, Vidal-Lesso A, Ledesma-Orozco ER, Balvantín-García AJ "Biomaterial Models Adjustment and Comparison for Ultra High Molecular Weight Polyethylene in Finite Element Models." *Proceedings of the ASME 2018 International Mechanical Engineering Congress and Exposition* vol. 3: Biomedical and Biotechnology Engineering. Pittsburgh, Pennsylvania, USA. November 9-15, 2018. V003T04A009. ASME. https://doi.org/10.1115/IMECE2018-87719
- Corro-Hernández H, Vidal-Lesso A, Ledesma-Orozco ER, Palacios-Pineda LM (2019). "Structural analysis of a new total ankle replacement prosthesis with internal structure". DYNA vol. 95: pp 192-197. DOI: http://dx.doi.org/10.6036/9267

The first pages of these publications are shown as annexes

Proceedings of the ASME 2017 International Mechanical Engineering Congress and Exposition
IMECE2017
November 3-9, 2017, Tampa, Florida, USA

IMECE2017-70345

MECHANICAL ENERGY ABSORPTION IN POLYETHYLENE CELL PATTERN STRUCTURES FOR BIOMEDICAL USES

Humberto Corro-Hernández
División de Ingenierías Campus Irapuato-Salamanca. Universidad de Guanajuato.
Carretera Salamanca-Valle de Santiago km 3.5 + 1.8 km. Comunidad de Palo Blanco
Salamanca, Guanajuato, México C.P. 36885. Tel. (464) 647 9940, ext. 2389
humbertocorrohdez@hotmail.com

Agustín Vidal-Lesso
División de Ingenierías Campus Irapuato-Salamanca. Universidad de Guanajuato.
Carretera Salamanca-Valle de Santiago km 3.5 + 1.8 km. Comunidad de Palo Blanco
Salamanca, Guanajuato, México C.P. 36885. Tel. (464) 647 9940, ext.2368
agustin.vidal@ugto.mx, agusvile@yahoo.com.mx

Elías R. Ledesma-Orozco
División de Ingenierías Campus Irapuato-Salamanca.
Universidad de Guanajuato.
Carretera Salamanca-Valle de Santiago km 3.5 + 1.8 km.
Comunidad de Palo Blanco
Salamanca, Guanajuato, México
C.P. 36885. Tel. (464) 647 9940, ext. 2306
elias@ugto.mx

ABSTRACT

Energy absorption and dissipation are characteristics that can be used to protect and extend the useful life of many systems. Two new models of shock absorption structures are proposed. These are based on honeycomb cell patterns with inherent negative stiffness, in theory enabling a large amplification of their damping and recoverability capabilities within a limited space.

A 2D finite element analysis (FEA) is carried on as a first approach for testing this concept. The reduction of kinetic energy of a falling block above the structure is taken as the main indicator of energy absorption.

After some verifications 3D models are developed and tested analogously. Numerical results are obtained with polyethylene (PE) material properties, looking forward for development of future applications in biomechanics.

INTRODUCTION

Negative stiffness is understood as the occurrence of a force in the same direction as the imposed deformation [1-2] in a certain element, in contrast with the usual phenomena. This can be explained as most of these elements have been previously buckled or strained, thus they store internal energy, assisting rather than resisting deformation [3]. It is known that heterogeneous systems with one constituent of negative stiffness are predicted to give rise to high damping and stiffness [4].

In other idea, honeycomb-like structures are traditionally used for a variety of applications as they support loads very efficiently [5], with a low material density, and still keeping great shock resistance and energy absorption [5-6]

Combining both concepts, the use of a repetitive pattern with inherent negative stiffness allows for even more energy absorption, giving it a good shape restoration capacity in spite of suffering great strain [7]. These characteristics have been of interest in such applications as damping and vibration control [1, 3, 7-8]. Previous work by Correa et. al. [7-8] was focused on

Proceedings of the ASME 2018
International Mechanical Engineering Congress and Exposition
IMECE2018
November 9-15, 2018, Pittsburgh, PA, USA

IMECE2018-87719

BIOMATERIAL MODELS ADJUSTMENT AND COMPARISON FOR ULTRA-HIGH MOLECULAR WEIGHT POLYETHYLENE IN FINITE ELEMENT MODELS

Humberto Corro-Hernández
División de Ingenierías Campus Irapuato-Salamanca. Universidad de Guanajuato.
Carretera Salamanca-Valle de Santiago km 3.5 + 1.8 km. Comunidad de Palo Blanco
Salamanca, Guanajuato, México C.P. 36885.
Tel. (464) 647 9940, ext. 2389

Agustín Vidal-Lesso
División de Ingenierías Campus Irapuato-Salamanca. Universidad de Guanajuato.
Carretera Salamanca-Valle de Santiago km 3.5 + 1.8 km. Comunidad de Palo Blanco
Salamanca, Guanajuato, México C.P. 36885.
Tel. (464) 647 9940, ext.2388

Elías Ledesma
División de Ingenierías Campus Irapuato-Salamanca. Universidad de Guanajuato.
Carretera Salamanca-Valle de Santiago km 3.5 + 1.8 km. Comunidad de Palo Blanco
Salamanca, Guanajuato, México C.P. 36885.
Tel. (464) 647 9940, ext. 2306

Antonio de Jesús Balvantín-García
División de Ingenierías Campus Irapuato-Salamanca. Universidad de Guanajuato.
Carretera Salamanca-Valle de Santiago km 3.5 + 1.8 km. Comunidad de Palo Blanco
Salamanca, Guanajuato, México C.P. 36885.
Tel. (464) 647 9940, ext. 2363

ABSTRACT

GUR1050 is a medical grade variety of ultra-high molecular weight polyethylene (UHMWPE) intended for use on total joint prosthesis and implants. Probes of this material were characterized on a compression test following ASTM norms and lineaments.

Available data from these mechanical tests is fitted on multiple material models. Achieved results on numerical solutions of finite element modeling (FEM) of the tests are discussed, looking for the best one available in order to simulate with accuracy GUR1050 behavior, with specific interest on the load curve results, showing the pertinence of using certain models on different conditions.

It was found that the use of a bilinear isotropic hardening model assures the best fit for GUR1050 behavior in uniaxial compression under a constant strain rate.

INTRODUCTION

GUR1050 or medical grade Lennite UHMWPE is produced from premium resins in accordance with ASTM specification F648 and International Standard ISO 5834-1 for surgical implants [1]. This material is used mostly for total joint replacements on hip and knee, among other medical devices and various implants, due for being biocompatible and having a great resistance to wear [2-3].

As it is reported, the particular molecular structure of UHMWPE [2] is the origin of physical phenomena such as viscoelastic behavior on small deformations, distributed fluency and viscoplastic flow on higher loads, and a noticeable stiffness rise before rupture. The material behavior is also heavily influenced by the strain rate and temperature: a slower strain rate and/or lower test temperatures both increment UHMWPE stiffness [4].

UHMWPE mechanical properties are also affected by sterilization and aging for its application on biomechanical devices [5].

Simulation of UHMWPE is limited by many assumptions if a simpler material model is used [4]. However, if chosen wisely, their use can give accurate answers for a particular problem [6-9] where the approximations are close enough to the real described phenomenon.

In contrast, several robust, non-linear material models specifically designed for UHMWPE have been developed [4, 10-11]. Their main disadvantage for use is that they require a lot of experimental tests in order to make a fit, and a precise adjustment can be hard to get [4].

Análisis estructural de una nueva prótesis para reemplazo de tobillo con estructura interna

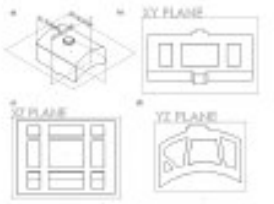

Structural analysis of a new total ankle replacement prosthesis with internal structure

Humberto Corro-Hernández, Agustín Vidal-Lesso, Elías Ledesma-Orozco y Luis-Manuel Palacios-Pineda

Universidad de Guanajuato. Departamento de Ingeniería Mecánica. División de Ingenierías. Campus Irapuato-Salamanca.
Valle de Santiago Km. 3.5 + 1.8885 Comunidad de Palo Blanco, Salamanca, Gto. (México)

DOI: http://dx.doi.org/10.6036/9267 | Recibido: 21/05/2019 • Inicio Evaluación: 04/06/2019 • Aceptado: 30/08/2019

ABSTRACT

A new prosthesis design for total ankle arthroplasty, with an internal damping structure for the sacrifice component is proposed and analyzed considering experimental data for the material model.
Engineering parameters for prosthesis designs are proposed and discussed and physiological load conditions for ankle joint are applied for numerical simulation.
Performance of total deformation, strain, safety factors and equivalent stress of structured prosthesis are compared versus a common solid model and literature findings for market-available prosthesis.
Results showed that the proposed design can be deformed up to 52.85% compared to the solid model and operated safely on simulated cases. Prosthesis deformation generates a damped load transmission rather than a rigid one, closer to the natural ankle joint behavior.

Keywords: ankle joint prosthesis; finite element analysis; computer aided design; orthopedics.

RESUMEN

Se propone y analiza un nuevo diseño de prótesis para la artroplastia total del tobillo, con una estructura de amortiguación interna para el componente de sacrificio, teniendo en cuenta los datos experimentales del modelo de material.

Se proponen y discuten los parámetros de ingeniería para los diseños de prótesis y se aplican condiciones de carga fisiológicas para la articulación del tobillo para la simulación numérica.

Los resultados para deformación total, deformación unitaria, los factores de seguridad y el esfuerzo equivalente de las prótesis estructuradas se comparan con un modelo sólido genérico y los reportes de literatura para las prótesis disponibles en el mercado.

Los resultados mostraron que el diseño propuesto puede deformarse hasta un 52.85% en comparación con el modelo sólido y operarse de manera segura en los casos simulados. La deformación de la prótesis genera una transmisión amortiguada de carga en vez de rígida, más cercana a la operación natural de la articulación del tobillo.

Palabras clave: prótesis articular de tobillo; análisis de elementos finitos; diseño asistido por computadora; ortopedia.

1. INTRODUCCIÓN

La artroplastia total de tobillo (ATT) es una intervención quirúrgica para el tratamiento de casos avanzados de degradación del cartílago en el mismo. La ATT requiere la exposición de la articulación, separando los tendones, nervios y vasos sanguíneos para extirpar el hueso y el cartílago dañado. Tras dicha extracción, sustitutos artificiales son anclados al hueso remanente. Un tercer elemento, más suave, es ensamblado posteriormente, cuidando de tener el mejor ajuste y alineación. Por último, los tejidos blandos se colocan en su sitio y se sutura la herida [1]. Conforme el promedio de edad de la población va en aumento, la necesidad de ATT y otras intervenciones relacionadas aumentará [2] y por tanto el trabajo requerido para la obtención de nuevas soluciones de ingeniería en el diseño de prótesis.

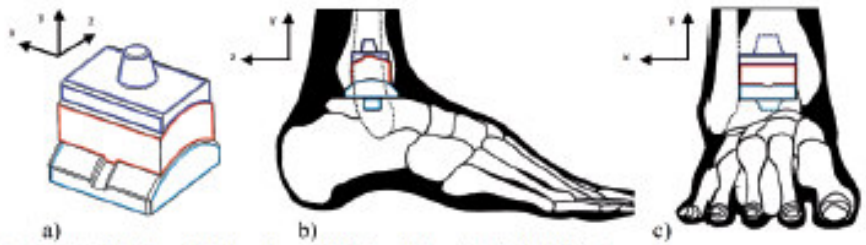

Fig. 1: Diseño de prótesis ATT a) Diseño b) Vista lateral externa c) Vista frontal de la articulación del tobillo derecho